

A CONTINENTAL SHELF BOTTOM BOUNDARY LAYER MODEL:  
DEVELOPMENT, CALIBRATION AND APPLICATIONS TO SEDIMENT  
TRANSPORT IN THE MIDDLE ATLANTIC BIGHT

by

RICHARD BRENT STYLES

A Dissertation submitted to the  
Graduate School-New Brunswick  
Rutgers, The State University of New Jersey  
in partial fulfillment of the requirements

for the degree of


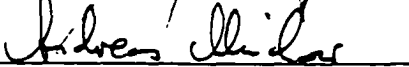
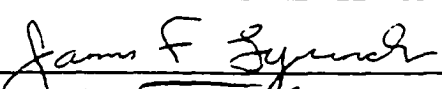

Doctor of Philosophy

Graduate Program in Oceanography

written under the direction of

Scott M. Glenn

and approved by

New Brunswick, New Jersey

May 1998

**UMI Number: 9900705**

---

**UMI Microform 9900705**  
**Copyright 1998, by UMI Company. All rights reserved.**

**This microform edition is protected against unauthorized  
copying under Title 17, United States Code.**

---

**UMI**  
**300 North Zeeb Road**  
**Ann Arbor, MI 48103**

## ABSTRACT OF THE DISSERTATION

A Continental Shelf Bottom Boundary Layer Model:  
Development, Calibration and Applications to Sediment Transport  
in the Middle Atlantic Bight

by

RICHARD BRENT STYLES

Dissertation Director:

Scott M. Glenn

A continental shelf bottom boundary layer model is presented for use over a non-cohesive movable sediment bed. Model features include a continuous eddy viscosity, a correction for suspended sediment-induced stratification and improved bottom roughness and reference concentration models. Predicted concentration and current profiles are sensitive to changes in selected internal model parameters and grain size.

High-resolution current and concentration profile data collected simultaneously over a 6-week summer deployment in 1995 off the southern coast of New Jersey are used to calibrated sensitive model coefficients and to determine the accuracy of the model at predicting the shear velocity and hydrodynamic roughness. Calibration of the internal parameters  $\alpha$ , which regulates the cutoff point of the eddy viscosity near the bed, and  $\gamma$ , which regulates the vertical decay of the suspended sediment concentration, are shown to be consistent with past estimates obtained in the field. Estimates of ripple height,  $\eta$ , and ripple length,  $\lambda$  are also shown to give good agreement with available field data.

Bottom roughness is shown to be a function of not only ripple height, but also of the angle between the wave and combined wave and current shear stress components.

Nearly two-years of current and wave data collected on the inner shelf offshore of New Jersey are used to run the model to investigate long-term sediment transport. Model results indicate that all transport events are related to waves and that the seasonal distribution includes a number of summer storms that are comparable in sediment transport potential to other systems in the spring and fall. Modes of longshore transport follow established patterns for a wide, gently sloping continental shelf with the transport directed primarily alongshore. Cross-shore patterns exhibit an onshore bias which may be caused by multi-scale topographic features that may introduce 3-dimensional flow effects.



## ACKNOWLEDGMENTS

I would first like to thank the Office of Naval Research/Augmentation Awards for Science and Engineering Research Training (ONR/AASERT) and the National Oceanographic and Atmospheric Administration National Undersea Research Program (NOAA/NURP) for providing funding to support this research. I also wish to thank Drs. Dale Haidvogel, James Lynch and Andreas Münchow for serving on my thesis committee and reviewing my dissertation in a professional and objective manner.

I would like to thank Mr. Peter Traykovski of the Woods Hole Oceanographic Institution for graciously providing the suspended sediment concentration and the ripple geometry data. These datasets contributed significantly to the quality of the work presented in these pages.

I would like to thank my family for their support of my career choice and for patiently waiting for my commencement to finally arrive.

I want to thank the staff and research faculty of the Institute of Marine and Coastal Sciences, Rutgers University for providing an atmosphere teeming with a collaborative spirit and enthusiasm for the ocean sciences. The inaugural days of the marine science program at Rutgers are sure to be regarded as a mile stone in the shifting focus to coastal oceanography that has recently swept through the U.S. oceanographic community.

I want to pay special tribute to my advisor and friend Dr. Scott Glenn. Scott has served as a source of inspiration since the conception of this dissertation. He has demonstrated impeccable leadership and has given me a strong foundation on which to

build my own independent research program. My career as an oceanographer will always reflect what I have learned as a student from Scott.

I would finally like to thank my wife Renée for her support, patience and comfort during this trying odyssey known as graduate school.

## TABLE OF CONTENTS

ABSTRACT OF THE DISSERTATION .....	ii
ACKNOWLEDGMENTS .....	iv
LIST OF TABLES .....	xi
LIST OF ILLUSTRATIONS .....	xii
1.0 INTRODUCTION .....	1
1.1 Objective of present study .....	6
2.0 BACKGROUND .....	8
2.1 Historical development of bottom boundary layer models .....	8
2.2 Observational studies of boundary layer processes .....	9
2.3 Related calibration studies of key model parameters .....	12
2.4 Justification and need .....	14
3.0 THEORETICAL MODEL DEVELOPMENT .....	16
3.1 Governing equations .....	16
3.1.1 Eddy viscosity .....	28

3.1.2	Stability parameter	31
3.2	Solution for the wave	34
3.3	Wave friction factor and the determination of the bottom stress	43
3.4	Solution for the mean current and suspended sediment concentration	58
3.5	Determination of the stability parameter	62
3.5.1	Stability parameter convergence tests	73
3.6	Solution procedure for the mean current and concentration	81
3.7	Theoretical model comparisons	84
3.8	Influence of multiple sediment grain size classes	91
3.8.1	Effect of reducing particle size	91
3.8.2	Effect of increasing the number of grain size classes	95
3.9	Sensitivity of the solution to $\beta$ and $\gamma$	98
3.9.1	Sensitivity to $\beta$ with $\gamma$ held fixed	99
3.9.2	Sensitivity to $\gamma$ with $\beta$ held fixed	102
3.9.3	Effect of varying $\gamma$ and grain size	104
3.10	Summary	107
4.0	MODEL AND DATA COMPARISONS	110
4.1	Study site and instrumentation	110
4.1.1	BASS current meter array	111
4.1.2	ABS sediment concentration profiler	113
4.1.3	SSS acoustic imaging system	114

4.2	Bed reference concentration	114
4.3	Determination of model input parameters	118
4.4	Field estimates of $\gamma_0$ , $\gamma$ and $\alpha$	120
4.4.1	Reference concentration model	122
4.4.2	Estimates of $\gamma$ reported in the past	123
4.4.3	Estimates of $\alpha$ reported in the past	123
4.4.4	Statistical methods	123
4.4.5	Flow and concentration data	127
4.4.6	Current data	128
4.4.7	Suspended sediment concentration data	129
4.4.8	$u_{*c}$ and $b_1$ statistics and raw data for the chosen bursts	131
4.4.9	Field estimates for $\gamma$ and $\alpha$	132
4.4.10	Estimates of $\gamma_0$	143
4.4.11	Summary of $\gamma$ , $\gamma_0$ and $\alpha$ estimates	143
4.5	Models of wave-formed ripples	145
4.5.1	Recalibration of $\eta$ and $\lambda$	148
4.6	Bottom roughness for combined wave and current flows	151
4.6.1	Review of bottom roughness models	153
4.6.2	Bottom roughness in the presence of a near-bed transport layer	155
4.7	Field estimates for $k_b$	157
4.7.1	Flow data	158
4.7.2	Bottom roughness estimates for the 1994 experiment	158

4.7.3	Bottom roughness estimates for 1995 experiment . . . . .	163
4.7.4	Reevaluation of bottom roughness for a rippled bed . . . . .	168
4.7.5	Summary and discussion of $k_b$ estimates . . . . .	174
4.8	Directions for future research . . . . .	175
4.8.1	Estimates for $\gamma_0$ , $\gamma$ and $\alpha$ . . . . .	175
5.0	MODEL APPLICATIONS: LONG-TERM SEDIMENT TRANSPORT AT LEO-15 . . . . .	180
5.1	Input model data . . . . .	182
5.1.1	Input wave and current data . . . . .	183
5.1.2	Input sediment data . . . . .	193
5.1.3	Sediment transport event criteria . . . . .	194
5.1.4	Qualitative assessment of sediment transport events . . . . .	196
5.1.5	Dominant forcing agents driving sediment resuspension . . . . .	200
5.2	Model results: Annual sediment transport at LEO-15 . . . . .	203
5.2.1	Estimates of $\Gamma_f$ and erosion depth . . . . .	209
5.2.2	Relationship between event duration, $\Gamma_{fm}$ and $\Gamma_{ft}$ . . . . .	210
5.2.3	Cross-shore and longshore transport . . . . .	213
5.2.4	The relationship between $\Gamma_f$ and sediment grain size. . . . .	220
5.2.5	Comparison of neutral and stratified models . . . . .	220
5.3	Discussion . . . . .	221
5.3.1	Mechanisms influencing cross-shore transport . . . . .	230
5.4	Summary . . . . .	237

6.0	SUMMARY AND CONCLUSIONS .....	239
	APPENDIX: LIST OF PRINCIPAL SYMBOLS .....	245
	REFERENCES .....	252
	Curriculum Vita .....	261

## LIST OF TABLES

Table 3.1	List of input values for stability parameter convergence tests. . . . .	74
Table 3.2	Input parameters for theoretical model comparisons. . . . .	85
Table 4.1	Values for the resuspension coefficient, $\gamma_o$ , reported by previous investigators. . . . . .	121
Table 4.2	Statistics showing errors associated with the Rouse parameter ( $b_1$ ) and $u_{*c}$ . . . . .	131
Table 4.3	Various calculated model parameters and statistics for the 6 chosen bursts. . . . . .	138
Table 5.1	Sediment transport model results categorized by transport events for 1994. . . . . .	197
Table 5.2	Sediment transport model results categorized by transport events for 1995. . . . . .	197
Table 5.3	Cross-correlation coefficient relating total depth-integrated sediment flux, maximum instantaneous depth-integrated sediment flux and event duration derived from 1994 sediment transport events. . . . .	227
Table 5.4	Cross-correlation coefficient relating total depth-integrated sediment flux, maximum instantaneous-depth integrated sediment flux and event duration derived from 1995 sediment transport events. . . . .	227



## LIST OF ILLUSTRATIONS

Figure 3.1 Comparison of the wave friction factor, $f_w$ , calculated using the 3-layer model developed for this study and the Grant and Madsen (1986) model. . . . .	51
Figure 3.2 Sensitivity test showing the wave friction factor calculated using the 3-layer model as a function of the parameters $\epsilon$ (a) and $\alpha$ (b). . . . .	53
Figure 3.3 Three-dimensional grided mesh plot showing $C_R$ as a function of $\epsilon$ and $\phi_{cw}$ . . . . .	55
Figure 3.4 Comparison between the kinematic flux ( $u'w'$ ) defined in (3.104) (solid) and the analytical solution (dashed). . . . .	66
Figure 3.5 Vertical profiles of the stability parameter for the three wave and current scenarios representing low (solid), medium (dash) and high (dash/dot) wave cases. . . . .	75
Figure 3.6 Vertical profiles of the stability parameter error, $\epsilon_{Np}$ for the high wave case. . . . .	78
Figure 3.7 Same as Figure 3.6 showing the error for the medium wave case. . . . .	79
Figure 3.8 Same as Figure 3.6 showing the error for the low wave case. . . . .	80
Figure 3.9 Normalized CPU runtime as a function of stability parameter maximum error, $\epsilon_n$ , for the Chebyshev approximation (solid) and the trapezoidal method (dash). . . . .	82
Figure 3.10 Sensitivity of calculated model parameters to changes in $\alpha$ . . . . .	86
Figure 3.11 Same as Figure 3.10 but with a grain-size of 0.01 cm. . . . .	92

Figure 3.12 Vertical profiles of calculated model parameters using three different grain size classes consisting of 0.01 <i>cm</i> (solid), 0.021 <i>cm</i> (dashed) and 0.04 <i>cm</i> (dash/dot) grains. . . . .	96
Figure 3.13 Sensitivity of calculated model parameters to changes in the stratification parameter $\beta$ . . . . .	100
Figure 3.14 Sensitivity of calculated model parameters to changes in the sediment concentration parameter $\gamma$ . . . . .	103
Figure 3.15 Same as Figure 3.14 but with a sediment grain size of 0.04 <i>cm</i> . . .	106
Figure 4.1 LEO-15 study site and bathymetry. (a) New York Bight showing large-scale bathymetry along the New Jersey coast. (b) Expanded view of the LEO-15 research area. Node A is located on the southern end of a distinctive shore oblique sand ridge. . . . .	112
Figure 4.2 Comparison of particle settling velocity as a function of grain size between the empirical formula (4.13) developed by Gibbs et al. (1971) and that determined by Madsen and Grant (1977). . . . .	125
Figure 4.3 Selected high quality concentration (a) and current profile (b) data used to determine the sediment reference concentration and $\gamma$ . . . . .	133
Figure 4.4 Same as Figure 4.3 for year day 242.67. . . . .	134
Figure 4.5 Same as Figure 4.3 for year day 247.71. . . . .	135
Figure 4.6 Same as Figure 4.3 for year day 247.96. . . . .	136
Figure 4.7 Same as Figure 4.3 for year day 248.58. . . . .	137
Figure 4.8 First of two selected bursts used to calculate the parameter $\alpha$ and the resuspension coefficient $\gamma_0$ . . . . .	141

Figure 4.9 Second selected burst used to calculate the parameter $\alpha$ and the resuspension coefficient $\gamma_0$ .	142
Figure 4.10 (a) Relative ripple height, $\eta/A_b$ , as a function of the non-dimensional wave and sediment parameter, $\chi$ .	150
Figure 4.11 Time series of $u_b$ and $u_r$ for the 1994 deployment.	159
Figure 4.12 Comparison of measured and modeled $u_{*c}$ and $z_{0c}$ for bursts that indicate $R^2 > 0.99$ for the 1994 deployment using the Sorenson et al. (1995) bottom roughness equation.	161
Figure 4.13 Same as Figure 4.12 but with the parameter $\beta_0$ set equal to 0.5 to give a better comparison between the model and data during the storm.	162
Figure 4.14 Time series of $u_b$ and $u_r$ for the 1995 deployment.	164
Figure 4.15 Comparison of $u_{*c}$ and $z_{0c}$ for the 1995 deployment using the modified Sorenson et al. (1995) bottom roughness equation.	166
Figure 4.16 Same as Figure 4.15 using the directionally independent bottom roughness model ( $k_r = 3\eta$ ).	167
Figure 4.17 Non-dimensional bottom roughness $k_r/\eta$ as a function of the $\cos\phi$ derived from chosen bursts in 1994 and 1995.	171
Figure 4.18 Reevaluation of (a) $u_{*c}$ and (b) $z_{0c}$ estimates for 1994 using the modified ripple roughness modified described in the text.	172
Figure 4.19 Same as Figure 4.18 for the 1995 experiment.	173
Figure 5.1 Maximum near-bottom wave orbital velocity, $u_b$ , derived from S4 current meters for 1994.	185
Figure 5.2 Same as Figure 5.1 for 1995.	186

Figure 5.3 Equivalent wave radian frequency, $\omega_r$ , calculated using the 1994 S4 current data. . . . .	187
Figure 5.4 Same as Figure 5.3 for 1995. . . . .	188
Figure 5.5 18-minute average current speed, $u_r$ , derived from S4 current meter for 1994. . . . .	189
Figure 5.6 Same as Figure 5.5 for 1995. . . . .	190
Figure 5.7 Angle between the wave and current, $\phi_{cw}$ , derived from S4 records during 1994. . . . .	191
Figure 5.8 Same as Figure 5.7 for 1995. . . . .	192
Figure 5.9 (a) Distribution of sediment transport occurrences for the two-year time period. . . . .	195
Figure 5.10 Backscatter time series in formazin turbidity units (FTU) derived from S4 OBS sensor for 1994. . . . .	198
Figure 5.11 Same as Figure 5.10 for 1995. . . . .	199
Figure 5.12 Significant wave height, $H_r$ , derived from S4 pressure sensor for 1994. . . . .	201
Figure 5.13 Same as Figure 5.12 for 1995. . . . .	202
Figure 5.14 Predicted combined wave and current shear velocity, $u_{*cw}$ , for 1994 model run. . . . .	204
Figure 5.15 Same as Figure 5.14 for 1995. . . . .	205
Figure 5.16 Predicted time average shear velocity, $u_{*c}$ , for 1994 model run. . . . .	206
Figure 5.17 Same as Figure 5.16 for 1995. . . . .	207

Figure 5.18 Predicted maximum depth-integrated transport (a) and erosion depth (b) for the 1994 sediment transport study. . . . .	211
Figure 5.19 Same as Figure 5.18 for 1995. . . . .	212
Figure 5.20 Maximum instantaneous depth-integrated transport, $\Gamma_{fm}$ total depth-integrated transport, $\Gamma_{fr}$ and event duration for the 11 events identified in 1994. . . .	214
Figure 5.21 Maximum instantaneous depth-integrated transport, $\Gamma_{fm}$ total depth-integrated transport, $\Gamma_{fr}$ and event duration for the 8 events identified in 1995. . . . .	215
Figure 5.22 Progressive trajectories of sediment transport for events identified in 1994. . . . .	216
Figure 5.23 Hodograph showing transport trajectories for events identified in 1995. . . . .	217
Figure 5.24 Cross-shore, $\Gamma_{fr-x}$ and longshore, $\Gamma_{fr-y}$ total depth-integrated sediment transport for each of the 11 events identified for 1994. . . . .	218
Figure 5.25 Cross-shore, $\Gamma_{fr-x}$ and longshore, $\Gamma_{fr-y}$ total depth-integrated sediment transport for 1995. . . . .	219
Figure 5.26 Comparison of total depth-integrated transport, $\Gamma_{fr}$ for neutral and stratified versions of the model for 1994. . . . .	222
Figure 5.27 Same as Figure 5.26 for 1995. . . . .	223
Figure 5.28 (a) Combined wave and current, $u_{cw}$ , and (b) time average, $u_c$ , shear velocities calculated by the model for 1994. . . . .	225
Figure 5.29 Same as Figure 5.28 for 1995. . . . .	226
Figure 5.30 Comparison of longshore and cross-shore wind speeds between Tuckerton wind sensor and Delaware Bay buoy. . . . .	232

Figure 5.31 Polar grid depicting wind and current vectors for 1994 transport events.

..... 234

Figure 5.32 Polar grid depicting wind and current vectors for 4 of the 1995 transport events. .... 235

## 1.0 INTRODUCTION

Boundary layers develop at the surface and bottom of the ocean due to the frictional drag experienced by the viscous fluid as it encounters the atmosphere or sea-bed. The surface boundary layer, which separates the interior from the atmosphere, is often characterized as a layer well mixed in density and momentum, but can experience significant vertical shear as in a surface Ekman layer. In contrast, friction induced by flow over a rough fixed bottom typically makes the bottom boundary layer a turbulent, sheared flow region where exchanges of mass, heat and momentum between the interior fluid and the sea-bed occur. In relatively shallow areas, such as the continental shelf, wind-waves propagating on the surface drive oscillatory currents that can extend to the sea-bed, generating a thin, highly sheared wave boundary layer. If both currents and waves are present, the wave boundary layer will be embedded within the thicker current boundary layer. In coastal areas, storm or tidal driven flows can sometimes produce boundary layers that are in excess of the Ekman layer depth, so that the bottom boundary layer can occupy a major fraction of the water column and even extend to the surface. The fact that the bottom boundary layer can sometimes extend over a large fraction of the water column (Lentz and Trowbridge 1991), and is directly influenced by wind-waves, indicates that a thorough description of the dynamical fields in the ocean should include accurate descriptions of physical processes occurring in boundary layers.

The bottom boundary layer on the continental shelf can be segmented into an outer region where the current is described by a velocity defect law, and an inner constant stress region where the current varies logarithmically with height (Tennekes and Lumley (1972). In the outer boundary layer, the effects of the earth's rotation and mean

horizontal pressure gradients become important. Typical examples of the steady horizontal flow in this region include the turning of the velocity vector with depth and the presence of vertical shear. Because the scale height of the wave boundary layer is much less than the scale height of the current boundary layer, the wave is adequately described by potential theory.

The constant stress region forms the lower part of the bottom Ekman layer and includes the wave boundary layer. Differences in the characteristic length and time scales for waves and currents leads to a complicated boundary layer structure for combined flows. For example, high frequency wave motion, which reverses direction each half wave cycle, induces time-dependent changes in the shear that maintains the turbulence transporting eddies. This effectively limits wave boundary layer growth as these eddies vary in intensity over a wave cycle. Depending on the local wave characteristics, the wave boundary layer thickness on the continental shelf can range between a few to tens of centimeters. For the current, the time scale of the motion is much greater than the wave so that the mean current shear is maintained well above the wave boundary layer height. Correspondingly, the current boundary layer extends further up into the water column. If the individual velocity scales for waves and currents are of the same order of magnitude, the maximum shear stress generated by the wave will have a greater magnitude than the shear stress for the current. Because the individual bed shear stress components are proportional to the square of the flow speed, the total bed shear stress will be a nonlinear function of the contributions from the wave and current. In the combined flow, the maximum shear stress associated with the wave will advect low momentum fluid away from the bed more vigorously than if the wave were



not present. This has the effect of reducing the current shear in the wave boundary layer and can distort the current profile from the classic logarithmic variation with height. Above the wave boundary layer, the shear stress is associated only with the current and the logarithmic velocity profile is recovered. In addition, the embedded structure of the wave boundary layer leads to an apparent hydraulic roughness, as seen by the current above the wave boundary layer, that is much larger than the physical bed roughness, which itself is a function of the unevenness of the seabed. This is similar to steady flow behind upstream bumps where the roughness experienced by the current is enhanced due to the presence of the extrusion.

If the sea-bed consists of loosely packed sediment, the combined wave and current shear stress can scour the bottom and resuspend bed material. This process leads to a suspended sediment concentration gradient, where the upward flux of sediment due to flow turbulence is balanced by the tendency for the particles to fall out of suspension under the action of gravity. As the sediment is entrained by the wave, the mean current transports it horizontally. Obviously, the net horizontal transport will depend on the relative magnitude of the near-bed wave and current velocities. During storms when both waves and currents are strong, large amounts of sediment are entrained by the wave and then steadily transported horizontally by the current. Critical to the accurate description of sediment resuspension is the definition of the reference concentration defined at the bed. This is of particular concern since the concentration at any level is directly related to the reference concentration.

When sediment is resuspended, it often is unevenly distributed in the water column resulting in the potential for flow stratification. A large vertical concentration

gradient results in a reduction in vertical turbulent transport efficiency, where a fraction of the turbulence kinetic energy is removed by the buoyancy flux induced by the stratified layer. The reduction in transport efficiency is associated with a corresponding reduction in mixing efficiency for mass, heat and momentum. Thus, stratification can reduce the vertical flux of momentum and sediment mass from the neutral case and, therefore, must be considered in boundary layer studies where the presence of a suspended sediment layer is probable.

Another important aspect of a movable sediment bed is the uneven redistribution of bed material under the action of the individual wave and current flows or by biological activity. Flow instabilities arising from the presence of turbulence, and flow over loosely consolidated, uneven sand bottoms, can lead to the formation of sand ripples. Biological organisms can rework the sediment bed through activities like mound building and burrowing, and modify sediment characteristics through adhesion and vertical mixing of particles. The mere presence of biological organisms and individual grains can further contribute to the unevenness of the sea-bed. The presence of these bedforms constitutes a hydrodynamically rough bottom which can enhance the spatially averaged bottom roughness experienced by the current. For extreme flow conditions over a movable sediment bed, a near-bed transport layer can develop that will also contribute to the roughness of the bed. Each of these sources of flow roughness will have a distinct influence on the spatially averaged bed roughness and an associated mathematical description which depends on the forces that generate the bedforms and/or their physical characteristics. Thus, accurate estimates of the geometrical properties and

relation to the roughness of these various bed forms is critical when modeling near-bed flow or sediment resuspension.

The need to understand processes occurring in boundary layers arises from a variety of historic and contemporary topics in physics and oceanography. For example, boundary layers are turbulent, and the description of turbulent flow is one of the unsolved problems remaining in classical mechanics from over a century ago. Self stratification due to suspended sediment, and how it affects the flow and sediment transport, is an important and still not well understood feature of boundary layers. As mentioned above, bottom boundary layers are regions where mass, momentum and heat are exchanged with the sea-bed. Chemical constituents including aquatic contaminants, decaying organic matter, oxygen and nutrients are passed from water column to sea-bed through the bottom boundary layer. In engineering applications, the design of pipelines, oil rig foundations, caissons and other sub-sea structures all require knowledge of the flow near the bed to ensure safe operation and structural integrity. The ultimate fate of dredge material and riverine discharges, both of which sometimes contain toxic elements, are highly dependent on the flow characteristics of the continental shelf bottom boundary layer. Long-term beach erosion, littoral drift and the formation and maintenance of sand ridges are all highly dependent on processes occurring in the bottom boundary layer. With these concerns in mind, it becomes clear that a greater understanding of boundary layer processes in the field through observation and prediction remains an important area of research.

## **1.1 Objective of present study**

The objective of this study is to develop, calibrate and apply a continental shelf bottom boundary layer model for combined wave and currents over a non-cohesive, movable sediment bed. Model features include the prediction of the wave and current shear stresses, the bed reference concentration, the bottom roughness, and the vertical distribution of the mean current and suspended sediment concentration for a fluid stratified by the resuspension of sediment. The model is self-contained in that a minimum of external mean flow and wave parameters are needed to initialize and run the model. The simple, analytic formulation allows the model to be constructed in a modular fashion so that it is easily modified for coupling with large-scale shelf circulation models.

Models that do not incorporate all the physics of the system being investigated are limited in their accuracy, and it is important to obtain detailed observations to gauge model performance. Therefore, a secondary objective is to calibrate model coefficients and compare predicted variables with data obtained in the field through a consistent statistical analysis which provides a quantitative framework from which to judge these calibrations and comparisons. The use of field data to gauge model performance is highly desirable since many past studies have relied extensively on laboratory measurements. Finally, the completed boundary layer model will be used to predict long-term sediment transport emphasizing the seasonal response of the bottom boundary layer to various degrees of forcing and the corresponding impact on sediment resuspension and net horizontal flux.

In Section 2, a brief review of relevant theoretical and experimental investigations are presented in order to place the present work in an appropriate context. Section 3 presents a detailed derivation of the governing equations with emphasis on the sensitivity of the solution to various experimentally determined free parameters. In Section 4, field data are used to calibrate model coefficients and gauge the accuracy of the model developed in Section 3. To illustrate the utility of the model, Section 5 presents results from a long-term study of sediment transport patterns off the New Jersey shelf using 2 years of current and wave measurements. Finally, Section 6 provides a brief summary of the results and directions for future research.

## **2.0 BACKGROUND**

### **2.1 Historical development of bottom boundary layer models**

Modern theoretical studies of combined wave and current flows can be traced back to Lundgren (1972) who developed a simple model for the mean current in the presence of waves but did not include the nonlinear interaction between the wave and current stress components. The first study to include the non-linear interaction was achieved, independently, by Smith (1977) and Grant (1977). The work of Grant (1977) was later reported in Grant and Madsen (1979). Both the Smith (1977) and Grant and Madsen (1979) models used simple, time-invariant, linear eddy viscosities and concentrated on flows very near the bed. The Smith (1977) model was developed for waves and currents flowing in the same direction, while Grant and Madsen (1979) included waves and currents at arbitrary angles. Since then, numerous investigators have developed more sophisticated boundary layer models that include other processes. For example, Grant and Madsen (1982) developed a bottom roughness model for a movable, non-cohesive sediment bed, for pure waves. Grant and Madsen (1986) introduced a simplification for calculating the wave friction factor solution in the Grant and Madsen (1979) model. Madsen and Wikramanayake (1991) added a more realistic continuous eddy viscosity to the Grant and Madsen (1986) model.

Sediment transport models similarly have evolved over the past few decades. Unlike the non-linear boundary layer theories posed by Smith (1977) and Grant and Madsen (1979) in the 1970s, modern theories on the resuspension of sediment can be traced back to Rouse (1937). Rouse (1937) assumed that if the only difference between the sediment and fluid velocity is the particle settling velocity, then the upward turbulent

flux of sediment balances the settling of particles under the action of gravity. This greatly simplified the governing equations for particles mixed in fluid and laid the foundation for modern studies of sediment transport. Lumley (1976) established quantitative guidelines to identify conditions for which the Rouse (1937) theory could be applied. Smith (1977) also included in his combined wave and current flow model algorithms to compute suspended sediment concentration profiles using the original theories introduced by Rouse (1936). Wiberg and Smith (1983) included a correction for suspended sediment-induced stratification to the Smith (1977) model, while Glenn and Grant (1987) did the same for the Grant and Madsen (1979) model. Wikramanayake and Madsen (1992) derived a suspended sediment concentration model under neutral conditions for use with the Madsen and Wikramanayake (1991) wave and current model.

## **2.2 Observational studies of boundary layer processes**

In conjunction with modeling studies of flow and sediment transport for combined waves and currents, a number of related observational programs have been conducted over the past several decades. One of the first large-scale studies of flow in boundary layers was conducted as part of the Coastal Ocean Dynamics Experiment (CODE-1) during the spring and summer of 1981 (Allen et al. 1982). During early June of that year, instrumented bottom boundary layer tripods equipped with state-of-the-art current sensors were deployed at depths of 30 and 90 *m* off the northern California coast. Results from the 90 *m* deployment reported by Grant et al. (1984) demonstrated the importance of wave/current interaction in determining bottom stress and confirmed the presence of logarithmic velocity profiles for a natural wave and current flow environment. Grant et al. (1984) also showed that bottom stress estimates using the

Grant and Madsen (1979) model were typically within 10-15% of those measured. Also on the northern California shelf, but during a winter storm in December 1979, Cacchione et al. (1987) measured highly logarithmic velocity profiles near the bed in 85 *m* of water, and suggested that high shear stress events due to combined wave and current flow could be a major factor in controlling the distribution of surficial sediment in that area. Estimates of shear velocity obtained from a bottom boundary layer tripod were similarly shown to be in good agreement with the Grant and Madsen (1979) model.

A decade after CODE, researchers returned to the northern California shelf as part of The Sediment TRansport on Shelves and Slopes (STRESS) experiment (Sherwood et al. 1994; Wiberg et al. 1994; Lynch et al. 1997). Occupying some of the original mooring sites used during CODE, researchers engaged in a comprehensive investigation of sediment resuspension and flux using state-of-the-art optical, acoustical and current sensors. These instruments measured current and suspended sediment concentration profiles, particle size spectra, particle settling velocity, and micro-topography (Sherwood et al. 1994). Unlike CODE, which was conducted during the spring and summer upwelling season, the initial phase of STRESS focused in on the storm season during the winter months of 1990-1991. Information obtained on the resuspension of sediment during storms in a water depth of 90 *m* confirmed the importance of wave/current interaction on the vertical distribution of suspended sediment (Lynch et al. 1997), and revealed a distinct transition layer in the measured profiles similar to that predicted in the Wikramanayake and Madsen (1992) suspended sediment concentration model. Additionally, instruments were used to determine suspended sediment particle size distribution and showed good agreement with both grab samples obtained from near the



tripod and laser diffraction instruments designed to measure particle size spectra (Lynch et al. 1994).

Although the CODE, and STRESS experiments successfully increased present theoretical and experimental knowledge on flow and sediment transport in boundary layers, both were conducted in relatively deep water with bottom sediment comprised mostly of silt. Studies with the same scope as CODE and STRESS for shallow, wide continental shelves, like that observed off the east coast of the United States, are less common. One of the earlier studies for the New Jersey coast was conducted by McClennen (1973). McClennen (1973) deployed individual current meters offshore of New Jersey in water depths ranging from 20 to 140 *m*, to obtain velocity data to calculate sediment transport in combined wave and current flows. Using wave data from NOAA buoys in conjunction with his measured currents, McClennen (1973) calculated empirical relationships to describe the threshold of sand movement in combined wave and current flows. McClennen further alluded to the now well understood process of sediment transport in combined wave and current flows, where the waves act to suspend sediment while the mean current transports it horizontally. More recently, Wright et al. (1991) deployed boundary layer tripods in the Middle Atlantic Bight over a 3-year period in a depth of 7-17 *m* at two locations offshore of North Carolina to study cross-shore transport for a variety of conditions ranging from fair weather to storms. Currents were measured at 4 heights off the bed using two-component ECMs at a sampling rate of 1 *Hz*, and suspended sediment was measured at 5 heights off the bed using Optical Backscatter Sensors (OBS), which also sampled at 1 *Hz*. Madsen et al. (1993) deployed boundary layer tripods offshore of North Carolina in a water depth of 13 *m* using the

same instrument package as Wright et al. (1991). Although the OBS sensors in both these experiments provide vertical profiles at 5 discrete heights, acoustic instruments, like the 5 *MHz* ABS deployed during STRESS (Lynch et al. 1994), provide individual concentration estimates in 1 *cm* bins ranging from the sea bed up to about 50 *cm*. Lee and Haynes (1996) deployed a horizontal cross-bar attached to two vertical posts jettied into the sand in 3–4 *m* of water off the Atlantic coast of Florida using OBS and acoustic sediment profiling instruments but only one ECM. In their experiment, the sediment concentration was adequately resolved but the shear stress was calculated using the Madsen and Wikramanayake (1991) bottom boundary layer model. During high wave conditions, measured concentrations from the acoustic profiler showed fair agreement with the Wikramanayake and Madsen (1992) suspended sediment transport model. Trowbridge and Agrawal (1995) deployed a bottom boundary layer tripod off Duck, North Carolina in a water depth of approximately 6 *m* and obtained current profile measurements from 5 to 16 *cm* above the bed, but did not investigate sediment resuspension. Although these studies were conducted in relatively shallow water, none possessed the variety of instrumentation or the comprehensive scope of either CODE or STRESS.

### **2.3 Related calibration studies of key model parameters**

In addition to the field experiments described above, a number of related field and laboratory experiments have recently advanced our understanding of key physical processes related to boundary layer flows. Included are the specification of the bottom roughness, the determination of the bed reference concentration, and the accuracy of accepted turbulence closure schemes.

As mentioned above, bottom roughness on continental shelves is related to a number of bed attributes including sand grains, wave-formed ripples and, for extreme flow conditions, a highly-concentrated near-bed sediment transport layer. On wave dominated shelves, ripples are known to play an important role in controlling the spatially averaged roughness for the mean flow, and the relationship between the geometrical properties of ripples, such as ripple height, and the roughness is still an active area of research (Wikramanayake and Madsen 1991; Tolman 1994; Mathisen and Madsen 1996). Emerging trends indicate that bottom roughness is more related to the height of the ripples (Wikramanayake and Madsen 1991). Similarly, the description of bottom roughness has been expanded to include waves and currents flowing at arbitrary angles (Sorenson et al. 1995), which previously has been virtually unexplored.

Another important area is the specification of the reference concentration defining the suspended sediment concentration at the bed. Historically, progress in this area has been severely limited by a lack of high-quality in situ measurements very near the bed. Instruments like the ABS described above can now provide concentration measurements very close to the bottom so that the reference concentration can be measured more accurately than was previously possible.

A third area that has received more attention lately is the optimal choice of the eddy viscosity formulation needed to describe the turbulence Reynolds fluxes. For neutral conditions, Lynch et al. (1989) identified a transition layer near the top of the wave boundary layer in their suspended sediment concentration measurements that was not consistent with previous eddy viscosity formulations adopted by Grant and Madsen (1979) and Glenn and Grant (1987). They showed that the Wikramanayake and Madsen

(1992) continuous eddy viscosity model predicted the cutoff point identifying the edge of the transition layer, and was more accurate than the Grant and Madsen (1986) discontinuous eddy viscosity model. For stratified flows, the functional form of the correction to the eddy viscosity originally suggested by Businger et al. (1971), who developed their eddy viscosity for thermally stratified atmospheric boundary layers, has recently been verified for suspended sediment-induced stratification by Villaret and Trowbridge (1991).

## **2.4 Justification and need**

The lack of comprehensive measurements of flow and sediment resuspension in a high energy shallow water environment, combined with recently advanced theories on key physical parameters directly related to modeling boundary layer flows, led a team of scientists from Rutgers University, Woods Hole Oceanographic Institution (WHOI), and Sequoia Scientific to conceive and execute one of the most intensive shallow water observational studies of boundary layer flow and sediment transport to date. During the summer months of 1994 and 1995, instrumented bottom boundary layer tripods were deployed on the shallow continental shelf offshore New Jersey as part of the National Undersea Research Program's Boundary Layer Stress and Sediment Transport (NURP/BLASST) experiment. The primary goals of this study were to use state-of-the-art acoustical and optical sensors to measure current and suspended sediment concentration profiles, particle size spectra, particle settling velocity, and micro-topography of the sea-floor to produce a comprehensive data set on flow and sediment transport for this shallow water environment. The availability of these high-resolution measurements, combined with updated theories on the physics of flow and sediment

transport, provide the means for upgrading existing boundary layer models and to gauge model performance using data obtained exclusively in a natural, shallow water environment consisting primarily of medium sized sand.

### 3.0 THEORETICAL MODEL DEVELOPMENT

#### 3.1 Governing equations

The horizontal equations of motion for a viscous, incompressible, rotating fluid can be written as

$$\begin{aligned} \frac{\partial u}{\partial t} + u \frac{\partial u}{\partial x} + v \frac{\partial u}{\partial y} + w \frac{\partial u}{\partial z} - f v &= -\frac{1}{\rho} \frac{\partial p}{\partial x} + \frac{1}{\rho} \left[ \frac{\partial \tau_{xx}}{\partial x} + \frac{\partial \tau_{yx}}{\partial y} + \frac{\partial \tau_{zx}}{\partial z} \right] \\ \frac{\partial v}{\partial t} + u \frac{\partial v}{\partial x} + v \frac{\partial v}{\partial y} + w \frac{\partial v}{\partial z} + f u &= -\frac{1}{\rho} \frac{\partial p}{\partial y} + \frac{1}{\rho} \left[ \frac{\partial \tau_{xy}}{\partial x} + \frac{\partial \tau_{yy}}{\partial y} + \frac{\partial \tau_{zy}}{\partial z} \right] \end{aligned} \quad (3.1)$$

where  $u$  and  $v$  are the horizontal components of velocity in the  $x$  and  $y$  directions, respectively,  $w$  is the vertical component of velocity with  $z$  positive upwards from the bed,  $t$  is the time,  $f$  is the Coriolis parameter,  $\rho$  is the fluid density,  $p$  is the pressure and  $\tau$  is the viscous shear stress. The first indices on the shear stress components indicates the direction perpendicular to the plane of the applied stress and the second indicates the direction that the shear stress acts (Dean and Dalrymple 1991). The hydrostatic approximation can be used to reduce the vertical equation of motion to

$$\frac{\partial p}{\partial z} = -\rho g \quad (3.2)$$

where  $g$  is the acceleration due to gravity.

For the flows considered here, the fluid motion is assumed to be turbulent, which is defined in terms of the wave Reynolds number,  $R_e = u_b A_b / \nu$ , where  $u_b$  is the maximum

near-bottom wave orbital velocity,  $A_b$  is the maximum near-bed wave excursion amplitude and  $\nu$  is the kinematic viscosity of water. Nielsen (1992) notes that for the field  $R_\tau$  is likely to be greater than  $10^5$  which shows that the boundary layer can be assumed turbulent. Under the turbulent flow assumption, (3.1) is modified by partitioning the  $u$ ,  $v$ ,  $w$  and  $p$  variables into mean,  $U$ , and turbulent,  $u'$ , quantities ( $u = U + u'$ ,  $v = V + v'$ ,  $w = W + w'$  and  $p = P + p'$ ). Employing the Reynolds averaging procedure (Hinze 1975), (3.1) now becomes

$$\begin{aligned}
 \frac{\partial U}{\partial t} + U \frac{\partial U}{\partial x} + V \frac{\partial U}{\partial y} + W \frac{\partial U}{\partial z} - fV &= -\frac{1}{\rho} \frac{\partial P}{\partial x} \\
 &\quad - \frac{\partial \overline{u'u'}}{\partial x} - \frac{\partial \overline{u'v'}}{\partial y} - \frac{\partial \overline{u'w'}}{\partial z} \\
 \frac{\partial V}{\partial t} + U \frac{\partial V}{\partial x} + V \frac{\partial V}{\partial y} + W \frac{\partial V}{\partial z} + fU &= -\frac{1}{\rho} \frac{\partial P}{\partial y} \\
 &\quad - \frac{\partial \overline{v'u'}}{\partial x} - \frac{\partial \overline{v'v'}}{\partial y} - \frac{\partial \overline{v'w'}}{\partial z}
 \end{aligned} \tag{3.3}$$

where the overbar indicates the Reynolds averaged quantity and the viscous shear stresses have been neglected assuming fully rough turbulent flow.

Near the bottom, the turbulent motion can act to entrain sediment, causing the particles to mix with the fluid. The dynamics controlling the sediment motion are complex, but can be greatly simplified if it is assumed that concentrations of suspended material are low enough to neglect particle interactions. Lumley (1976) suggests that for volumetric concentrations less than about  $3 \times 10^{-3}$ , which is expected for many

continental shelf flow fields outside the surf-zone, individual particle interactions are negligible and the equations governing particle momentum reduce to

$$\begin{aligned} (u_p, v_p) &= (u, v) \\ w_p &= w - w_f \end{aligned} \quad (3.4)$$

where the subscript  $p$  denotes particle velocity and  $w_f$  is the particle fall or settling velocity. This implies that the only difference between the fluid and sediment motion is the particle fall velocity, which greatly simplifies the analysis. For concentrations low enough to neglect particle-particle interactions, yet large enough to treat the sediment particles as a continuum (Lumley 1976), the equation governing conservation of sediment mass becomes,

$$\frac{\partial c_n}{\partial t} + \frac{\partial c_n u}{\partial x} + \frac{\partial c_n v}{\partial y} + \frac{\partial c_n w}{\partial z} = 0 \quad (3.5)$$

where  $c_n$  is the volumetric concentration in  $cm^3$  of sediment per  $cm^3$  of the mixture for each size/density class  $n$ . A similar expression can be obtained for fluid mass,

$$\frac{\partial c_f}{\partial t} + \frac{\partial c_f u}{\partial x} + \frac{\partial c_f v}{\partial y} + \frac{\partial c_f w}{\partial z} = 0 \quad (3.6)$$

where  $c_f$  is the volumetric concentration of fluid. Following Glenn (1983), (3.4) is substituted into (3.5), giving



$$\frac{\partial c_n}{\partial t} + \frac{\partial c_n u}{\partial x} + \frac{\partial c_n v}{\partial y} + \frac{\partial c_n w}{\partial z} - \frac{\partial c_n w_{f_n}}{\partial z} = 0 \quad (3.7)$$

where the subscript  $n$  on  $w_{f_n}$  indicates that the fall velocity will vary between each sediment class. Using (3.6) and (3.7), and noting that

$$c_f + \sum_{n=1}^N c_n = 1 \quad (3.8)$$

where  $N$  indicates the total number of sediment size/density classes, conservation of fluid mass becomes

$$\frac{\partial u}{\partial x} + \frac{\partial v}{\partial y} + \frac{\partial w}{\partial z} - \sum_{n=1}^N w_{f_n} \frac{\partial c_n}{\partial z} = 0 \quad (3.9)$$

The last term on the left-hand side of (3.9) indicates that vertical fluid velocities will be produced by sediment falling through the water column as the fluid must move in the opposite direction of the sediment to conserve fluid mass. For small concentrations, which is the case considered here, the vertical fluid velocity induced by the sediment falling out of suspension will be small so that the usual continuity equation is recovered,

$$\frac{\partial u}{\partial x} + \frac{\partial v}{\partial y} + \frac{\partial w}{\partial z} \sim 0 \quad (3.10)$$

The concentrations in (3.7) are divided into mean,  $C_n$ , and turbulent,  $c_n'$ , quantities, and then Reynolds averaged giving

$$\begin{aligned} \frac{\partial C_n}{\partial t} + U \frac{\partial C_n}{\partial x} + V \frac{\partial C_n}{\partial y} + W \frac{\partial C_n}{\partial z} - w_{fn} \frac{\partial C_n}{\partial z} = \\ - \frac{\partial \overline{c_n' u'}}{\partial x} - \frac{\partial \overline{c_n' v'}}{\partial y} - \frac{\partial \overline{c_n' w'}}{\partial z} \end{aligned} \quad (3.11)$$

Because the interest here is to study low-frequency current motion on continental shelves in the presence of high-frequency wind-waves, the mean velocity components and pressure in (3.3), and the sediment concentrations in (3.11), are divided into current and wave components:

$$\begin{aligned} U &= u_c + u_w \\ V &= v_c + v_w \\ W &= w_c + w_w \\ P &= p_c + p_w \\ C_n &= C_{nm} + C_{np} \end{aligned} \quad (3.12)$$

where the subscripts  $c$ ,  $w$ ,  $m$  and  $p$  denote the current, wave, mean concentration and periodic concentration, respectively. The justification and consequences of this separation will be addressed after presenting further scaling of the governing equations. Assuming that the appropriate length and time scales of the motion are the wavelength,  $L_w$ , and wave period,  $T_w$ , of the wind-waves, the governing equations (3.3) and (3.11) are

scaled to eliminate the advective terms. The  $x$ -momentum equation is chosen to illustrate the scaling procedure with similar arguments applying to the  $y$ -momentum and sediment mass equations. Inserting (3.12) into (3.3), and assuming quasi-steady motion ( $\partial u_c / \partial t \approx 0$ ), the local acceleration term for the  $x$ -momentum equation scales as

$$\frac{\partial u_w}{\partial t} \sim O\left(\frac{u_0}{T_w}\right) \quad (3.13)$$

where, in the most general case, the wave and current velocities are assumed to be the same order of magnitude, and are represented by the single velocity scale  $u_0$ . The advective term similarly scales as

$$u_w \frac{\partial u_w}{\partial x} + v_w \frac{\partial u_w}{\partial y} \sim O\left(\frac{u_0^2}{L_w}\right) \quad (3.14)$$

Using the definition of the wave phase speed,  $c_p = L_w/T_w$ , (3.13) and (3.14) indicate that if  $u_0 \ll c_p$ , the advective terms in (3.3) and (3.11) can be neglected with respect to the local acceleration of the wave. This assumption, that the fluid velocities are much less than the wave phase speed, is the same scaling argument leading to linear wave theory and is adopted here. Since the horizontal scale of the current motion is assumed to be much greater than  $L_w$ , this argument equally is valid for the mean quantities.

Further simplification of the governing equations is possible through the boundary layer approximation. The primary assumption common to all boundary layer flows is that the characteristic length scale of the motion parallel to the boundary is much greater

than the length scale normal to it (Hinze 1975). An immediate consequence of this result is that the horizontal gradients in the Reynolds stress terms in (3.3), and the corresponding Reynolds flux terms in (3.11), can be neglected with respect to the vertical gradients. Furthermore, the boundary layer approximation can be used in conjunction with the continuity relation to scale the vertical fluid velocity. Using (3.10), which assumes that the contribution from the suspended load is negligible, the continuity equation is written in terms of the wave and current components,

$$\begin{aligned} \frac{\partial u_c}{\partial x} + \frac{\partial v_c}{\partial y} + \frac{\partial w_c}{\partial z} + \\ \frac{\partial u_w}{\partial x} + \frac{\partial v_w}{\partial y} + \frac{\partial w_w}{\partial z} = 0 \end{aligned} \quad (3.15)$$

Time averaging (3.15) over a wave period gives

$$\frac{\partial u_c}{\partial x} + \frac{\partial v_c}{\partial y} + \frac{\partial w_c}{\partial z} = 0 \quad (3.16)$$

Subtracting (3.16) from (3.15) shows that the wave satisfies the continuity relation independent of the current. Using the continuity equation for the wave provides a relation between the velocity and length scales of the flow,

$$\frac{u_0}{L_w} \sim \frac{w_0}{l_w} \quad (3.17)$$

where  $w_0$  is the velocity scale of the vertical motion and  $l_w$  is the scale height of the wave boundary layer. From (3.17),  $l_w/L_w \sim w_0/u_0$ , which implies that  $u_0 \gg w_0$ . The relation (3.17), combined with (3.14), also implies that terms like  $W\partial u/\partial z$  will be much smaller than, say,  $\partial u_w/\partial t$ . Thus, terms involving products of the vertical velocity can be neglected in this boundary layer approximation.

In light of the boundary layer approximation, it is now possible to justify separating the flow into wave and mean quantities for implementing the Reynolds averaging procedure. Within the wave boundary layer, the relevant length scale for the momentum transporting eddies is the distance from the bed. Therefore, near the top of the wave boundary layer, a logical turbulence length scale is  $l_w$ . Because  $l_w$  is much less than  $L_w$ , the turbulence transporting eddies have characteristically higher wave numbers than the surface wind-waves. This ensures adequate spectral separation between the wave and turbulence, and a corresponding sufficiently wide spectral gap for implementation of the averaging procedure. Above the wave boundary layer, the wave motion is irrotational so that products like  $\overline{u'u_w}$  are uncorrelated. As a result, the turbulence is associated only with the mean current. In this region, the length scale of the turbulence transporting eddies typically will be larger than in the wave boundary layer. This means that the peak in the turbulence kinetic energy spectrum is shifted to lower wave numbers. The energy spectrum of the mean flow, however, is expected to

peak at even lower wave numbers. In either case, a sufficiently wide spectral gap exists to justify separating the Reynolds averaged variables into wave and current components.

Finally, the remaining Reynolds stresses are expressed as the product of an isotropic eddy viscosity,  $K$ , and the vertical shear of the current,

$$\begin{aligned} -\overline{u'w'} &\equiv K \frac{\partial U}{\partial z} \\ -\overline{v'w'} &\equiv K \frac{\partial V}{\partial z} \end{aligned} \quad (3.18)$$

A similar expression is adopted for the Reynolds fluxes for sediment mass,

$$-\overline{c'_n w'} \equiv K_s \frac{\partial C_n}{\partial z} \quad (3.19)$$

where  $K_s$  is the eddy diffusivity for suspended sediment under neutral conditions.

Applying the boundary layer and linear approximations, and assuming that  $f$  is small compared to  $1/T_w$ , the equations governing fluid momentum and sediment mass reduce to

$$\begin{aligned}
\frac{\partial u_w}{\partial t} - f v_c &= -\frac{1}{\rho} \left[ \frac{\partial p_c}{\partial x} + \frac{\partial p_w}{\partial x} \right] + \frac{\partial}{\partial z} K \frac{\partial}{\partial z} (u_c + u_w) \\
\frac{\partial v_w}{\partial t} + f u_c &= -\frac{1}{\rho} \left[ \frac{\partial p_c}{\partial y} + \frac{\partial p_w}{\partial y} \right] + \frac{\partial}{\partial z} K \frac{\partial}{\partial z} (v_c + v_w) \\
\frac{\partial C_{np}}{\partial t} + w_w \frac{\partial C_{nm}}{\partial z} - w_{f_n} \frac{\partial}{\partial z} (C_{nm} + C_{np}) &= \frac{\partial}{\partial z} K_s \frac{\partial}{\partial z} (C_{nm} + C_{np})
\end{aligned} \tag{3.20}$$

where the Reynolds stress and flux terms have been replaced by the appropriate eddy viscosity and eddy diffusivity formulations. Time averaging (3.20) over a wave period gives the equations governing the mean flow and mean concentration,

$$\begin{aligned}
-f v_c &= -\frac{1}{\rho} \frac{\partial p_c}{\partial x} + \frac{\partial}{\partial z} \left( K \frac{\partial u_c}{\partial z} \right) \\
+f u_c &= -\frac{1}{\rho} \frac{\partial p_c}{\partial y} + \frac{\partial}{\partial z} \left( K \frac{\partial v_c}{\partial z} \right) \\
w_{f_n} \frac{\partial C_{nm}}{\partial z} + \frac{\partial}{\partial z} K_s \frac{\partial C_{nm}}{\partial z} &= 0
\end{aligned} \tag{3.21}$$

Subtracting (3.21) from (3.20) gives the equations for the periodic motion and concentration,

$$\begin{aligned}
\frac{\partial u_w}{\partial t} &= -\frac{1}{\rho} \frac{\partial p_w}{\partial x} + \frac{\partial}{\partial z} \left( K \frac{\partial u_w}{\partial z} \right) \\
\frac{\partial v_w}{\partial t} &= -\frac{1}{\rho} \frac{\partial p_w}{\partial y} + \frac{\partial}{\partial z} \left( K \frac{\partial v_w}{\partial z} \right) \\
\frac{\partial C_{np}}{\partial t} + w_w \frac{\partial C_{nm}}{\partial z} - w_{f_n} \frac{\partial C_{np}}{\partial z} &= \frac{\partial}{\partial z} \left( K_s \frac{\partial C_{np}}{\partial z} \right)
\end{aligned} \tag{3.22}$$

In the immediate vicinity of the bed, the effects of the earth's rotation and horizontal pressure gradients are negligible compared to the frictional term. Under these conditions, the last term on the right hand side of (3.21) must identically vanish as  $z \rightarrow 0$ . In this limit, it is seen that the usual constant stress assumption is recovered. The equation governing the mean current very close to the bed becomes

$$\begin{aligned}
\tau_{bx} &= K \frac{\partial u_c}{\partial z} \bigg|_{z=0} \\
\tau_{by} &= K \frac{\partial v_c}{\partial z} \bigg|_{z=0}
\end{aligned} \tag{3.23}$$

where  $\tau_{b(x,y)}$  represents the component of the shear stress in the given direction and the subscript  $b$  indicates that the stress is evaluated at the bed. For points outside the constant stress layer,  $z$  is no longer small and the remaining terms in (3.21) for the current must be retained. It is suspected that (3.23) is valid over the lower 10 to 20%



of the bottom boundary layer, which, in the coastal ocean, may typically represent a range from a few to tens of meters above the bottom (Grant and Madsen 1986).

The concentration equation in (3.21) along with (3.23) for the mean current and (3.22) for the wave constitute the governing equations to be solved for the constant stress region of the bottom boundary layer. Two important, yet independent, limiting assumptions have been applied to reduce the equations of motion to the form chosen for this investigation - the boundary layer and linear approximations. The analysis has shown that linearization of the governing equations is justified if the scale of the horizontal velocity for the combined wave and current motion is small with respect to the wave phase speed. This approximation is consistent with linearized wave theory, which is the case considered here. Additionally, the boundary layer approximation, which is defined in terms of the wave parameters  $L_w$  and  $l_w$ , also has been used to justify neglecting the vertical velocity and the horizontal gradients of the Reynolds stresses in the current boundary layer. Through both approximations it is seen that the wave is the central measure from which all scaling parameters are defined, and it is within the context of the linearized wave solution that applications of this theory must be understood. This is an important distinction since the scaling is not valid if the roughness elements are of the same order of magnitude as the wave boundary layer height. Under these conditions, the wavelength is no longer the appropriate horizontal length scale, and must be replaced with the characteristic scale of the bottom topography. As an example, wave-formed ripples can have characteristic length scales comparable to the boundary layer height. For such conditions, the above approximations may not be valid. It is expected, however, that when the ripples are on the order of the wave

boundary layer height, sediment transport is weak, as relatively large ripples form at the onset of sediment motion. Since the primary interest is to model sediment transport during high flow events, this is not a concern for the present study. At the other extreme, when flow conditions are strong, sediment resuspension is high, and ripples are washed out leaving a relatively flat bed. Under these conditions, the boundary layer assumption presented here is valid and use of the present model is justified.

### **3.1.1 Eddy viscosity**

The first order solution of flow in turbulent bottom boundary layers for both waves and currents has been described remarkably well using only simple closure models based primarily on time-invariant, linear eddy viscosities that scale with the vertical coordinate and the bottom shear stress. The ability of these simple closure schemes to provide reliable estimates of the mean structure of processes in boundary layers has contributed to their continued use and expansion into more sophisticated models of turbulent flow. Proof of the successfulness of these models is provided in the vast literature on modeling and observational studies of combined wave and current flow in boundary layers (Smith 1977; Smith and McLean 1977; Grant and Madsen 1979, 1986; Wiberg and Smith 1983; Grant et al. 1984; Christoffersen and Jonsson 1985; Glenn and Grant 1987; Sleath 1991; Madsen and Wikramanayake 1991; Drake et al. 1992; Trowbridge and Agrawal 1995). In order to describe more fully the use of eddy viscosities in modeling turbulent flow, and to introduce important definitions, a brief review of past work relevant to this study is presented.

Grant and Madsen (1979) suggest the following simple, two-layer eddy viscosity to close the fluid momentum equation,

$$\begin{aligned}
 K &= \kappa u_{*cw} z & z \leq \delta_w \\
 K &= \kappa u_{*c} z & z > \delta_w
 \end{aligned}
 \tag{3.24}$$

where  $\kappa$  is von Karman's constant (0.4) and  $\delta_w$  is the wave boundary layer height. The friction velocity,  $u_* = \sqrt{|\tau_b|/\rho}$ , is defined in terms of the magnitude of the turbulent shear stress at the bed,  $\tau_b$ , and fluid density. Within the wave boundary layer, the total shear stress will be the sum of the shear stress associated with the wave plus the low frequency current. Because most of the momentum transfer occurs during the maximum stress portion of the wave cycle, Grant and Madsen (1979) use the maximum instantaneous shear stress associated with the wave,  $\tau_{wm} = \rho u_{*wm} u_{*wm}$  to represent the wave contribution to the eddy viscosity. They further define the eddy viscosity in (3.24) in terms of the maximum instantaneous shear stress,  $\tau_{cw} = \rho u_{*cw} u_{*cw}$ , which is the sum of  $\tau_{wm}$  plus the time average of the instantaneous shear stress,  $\tau_c = \rho u_{*c} u_{*c}$ . Outside the wave boundary layer,  $\tau_{wm}$  is negligible, and the eddy viscosity is defined using only  $\tau_c$ .

One weakness in the Grant and Madsen (1979) model is the discontinuity in the eddy viscosity at the top of the wave boundary layer. In modeling real turbulent flows, studies have shown that an eddy viscosity that increases linearly does not accurately reflect turbulent mixing in the outer wave boundary layer, since it is known that turbulence production by shear is reduced (Jonsson and Carlsen 1976; Sleath 1987; Jensen et al. 1989). Trowbridge and Madsen (1984a,b), in a modeling study of turbulent wave boundary layers, recognized the need for different mixing scales within the inner and outer wave boundary layer and chose the following simple eddy viscosity model,

$$\begin{aligned}
K &= \kappa u_{*f} z & z \leq \delta_I \\
K &= \kappa u_{*f} \delta_I & z \geq \delta_I
\end{aligned} \tag{3.25}$$

where  $u_{*f}$  is the shear velocity associated with the time-averaged shear stress over one wave period in the absence of a steady current and  $\delta_I$  is the height at which the eddy viscosity reaches a maximum. Below  $\delta_I$ , the eddy viscosity is scaled by  $u_{*f}$  and the vertical coordinate, giving an eddy viscosity similar to that used by Grant and Madsen (1979). Above  $\delta_I$ , a constant length scale is used to represent the reduction in turbulence transport efficiency due to the reduced production of turbulence kinetic energy. For this study, the following 3-layer eddy viscosity model is chosen that combines the methods of Grant and Madsen (1979) and Trowbridge and Madsen (1984a),

$$\begin{aligned}
K &= \kappa u_{*cw} z & z_0 \leq z \leq z_1 \\
K &= \kappa u_{*cw} z_1 & z_1 \leq z \leq z_2 \\
K &= \kappa u_{*c} z & z_2 \leq z
\end{aligned} \tag{3.26}$$

where  $z_0$  is the hydrodynamic roughness,  $z_1$  is an arbitrary scale that is some fraction of the wave boundary layer height and  $z_2 = z_1 u_{*cw} / u_{*c}$ , which is determined by matching the eddy viscosities at  $z = z_2$ . Like the Grant and Madsen (1979) eddy viscosity model, the characteristic velocity scale in the lower and upper layers are  $u_{*cw}$  and  $u_{*c}$  respectively. To remove the discontinuity, an additional layer is inserted between the upper and lower layers that scales with  $u_{*cw}$ , reflecting the contribution to the turbulence transport by the

combined wave and current motion, while ensuring that the decrease in production of turbulence kinetic energy associated with the wave is represented through the constant length scale  $z_1$ . The 3-layer eddy viscosity model for this application was first proposed by Glenn (1983) and later revisited by Madsen and Wikramanayake (1991).

### 3.1.2 Stability parameter

In anticipation of self-stratification due to suspended sediment, the 3-layer eddy viscosity model is modified to incorporate the effects of vertical stratification,

$$K_{strat} = \frac{K}{1 + \beta \frac{z}{L}} \quad (3.27)$$

with a similar modification for suspended sediment,

$$K_{s\,strat} = \frac{K}{\gamma + \beta \frac{z}{L}} \quad (3.28)$$

where  $\gamma$  and  $\beta$  are constants and the ratio  $z/L$  is the stability parameter described below. Based on estimates obtained from thermally stratified flows in the atmospheric boundary layer (Businger et al. 1971), Glenn and Grant (1987) (hereafter, GG) adopt values of  $\gamma = 0.74$  and  $\beta = 4.7$ . Even though similarity arguments suggest that the stratified flow analogy should apply to continental shelf boundary layers, caution must be used when assuming that empirically determined coefficients derived for thermally stratified flows will apply to flows stratified by suspended sediment. Villaret and Trowbridge (1991)

addressed this issue by comparing previously reported laboratory measurements of suspended sediment concentration and current profiles with a theoretical model that incorporates the effects of suspended sediment-induced stratification in much the same way as presented here. They found that the stratified flow analogy for suspended sediment-induced stratification was valid, and that empirically derived coefficients were consistent with what had been reported for thermally stratified atmospheric boundary layers. Thus, the use of a neutral eddy viscosity modulated by a buoyancy term to represent the effects of suspended sediment-induced stratification is consistent with existing theories and, therefore, adopted for this study.

In (3.27) and (3.28),  $L$  is the Monin-Obukov length defined as

$$L = \frac{[\overline{u'w'}]^{3/2} \overline{\rho}}{\kappa g \overline{\rho'w'}} \quad (3.29)$$

where  $\overline{\rho}$  is the Reynolds averaged density and  $\rho'$  is the turbulent density fluctuation (Turner 1979; Stull 1988). In the constant stress layer, it is assumed that temperature and salinity are well-mixed so that the only source of flow stratification is suspended sediment, allowing  $\rho'$  to be written explicitly in terms of  $c'_n$ . Following Glenn (1983), the total density,  $\rho_T$ , of the fluid-sediment mixture is

$$\rho_T = c_f \rho + \sum_{n=1}^N c_n \rho_{sn} \quad (3.30)$$

where  $\rho_{sn}$  is the sediment density for each size class  $n$ . Recalling that

$$c_f + \sum_{n=1}^N c_n = 1 \quad (3.31)$$

the total density can be written as

$$\rho_T = \rho \left[ 1 + \sum_{n=1}^N c_n (s_n - 1) \right] \quad (3.32)$$

where  $s_n = \rho_{sn}/\rho$  is the relative sediment density. Applying the Reynolds averaging procedure to (3.32), and recalling that  $C_n \ll 1$ , gives the following mean and fluctuating density equations,

$$\begin{aligned} \overline{\rho_T} &= \rho \left[ 1 + \sum_{n=1}^N (s_n - 1) C_n \right] \approx \rho \\ \rho'_T &= \rho \sum_{n=1}^N (s_n - 1) c'_n \end{aligned} \quad (3.33)$$

The stability parameter is now expressed in terms of the suspended sediment concentration,

$$\frac{z}{L} = \frac{\kappa z}{[\overline{u'w'}]^{3/2}} \sum_{n=1}^N g(s_n - 1) \overline{c'_n w'} \quad (3.34)$$

where  $\rho_T$  has replaced  $\rho$  in (3.29). Rewriting (3.19) using the stratified eddy diffusivity to represent the Reynolds flux in (3.34), the following expression for the stability parameter results,

$$\frac{z}{L} = -\frac{\kappa z}{[\overline{u'w'}]^{3/2}} \sum_{n=1}^N g(s_n - 1) K_{s \text{ strat}} \left[ \frac{\partial C_{nm}}{\partial z} + \frac{\partial C_{np}}{\partial z} \right] \quad (3.35)$$

With the stability parameter written in terms of the mean and periodic concentration gradient, it is possible to examine how stratification influences mixing through the eddy viscosity and eddy diffusivity. Because the stability parameter appears in the denominator of (3.27) and (3.28), it will tend to reduce  $K_{\text{strat}}$  and  $K_{s \text{ strat}}$  for large, negative values of the suspended sediment concentration gradient. The sharper the gradient, the smaller are  $K_{\text{strat}}$  and  $K_{s \text{ strat}}$ , leading to the suppression of vertical mixing of momentum and suspended sediment. If the vertical concentration gradients are very small, the stratification correction is negligible and the neutral eddy viscosity and eddy diffusivity are recovered.

### 3.2 Solution for the wave

Outside the wave boundary layer, the stress term in (3.22) can be neglected so that the usual linearized potential flow solution applies,

$$u_w = \frac{gHk \cosh kz}{2\omega \cosh kh} e^{i(\omega t - kx)} \quad (3.36)$$

where  $H$  is the wave height,  $k$  is the wave number in the  $x$  direction,  $\omega = 2\pi/T_w$  is the wave radian frequency,  $i$  is the imaginary unit,  $h$  is the water depth and, for convenience, the  $x$ -axis has been aligned with the direction of wave propagation (Mei 1990). For irrotational flows, the pressure under the wave can similarly be written as



$$p = -\rho g(z - h) + \rho g \frac{H}{2} \frac{\cosh kz}{\cosh kh} e^{i(\omega t - kx)} \quad (3.37)$$

where the pressure has arbitrarily been set equal to 0 at the surface (Mei 1990). The first expression on the right-hand side of (3.37) represents the hydrostatic term and the second represents the dynamic pressure due to the wave. For constant depth ( $h \neq h(x)$ ), (3.36) and (3.37) can be combined to show that,

$$\frac{\partial u_w}{\partial t} = -\frac{1}{\rho} \frac{\partial p_w}{\partial x} \quad (3.38)$$

Equations (3.36)-(3.38) apply to the irrotational part of the wave outside the wave boundary layer. Because the wave boundary layer is assumed to be very thin with respect to the total water depth, it is customary to apply the lower boundary condition for the irrotational part of the wave at  $z = 0 \approx \delta_w$ , which represents the outer edge of the wave boundary layer (Grant and Madsen 1979, Glenn 1983). Taking the derivative of (3.37) with respect to  $z$  gives

$$\frac{\partial p}{\partial z} = -\rho g + \rho g k \frac{H}{2} \frac{\sinh kz}{\cosh kh} e^{i(\omega t - kx)} \quad (3.39)$$

which, when evaluated at  $z = 0 \approx \delta_w$  gives

$$\frac{\partial p}{\partial z} = -\rho g \quad (3.40)$$

Although suspended sediment-induced stratification will alter the vertical density structure, the boundary layer approximation adopted here assumes that horizontal variations in density are negligible. Taking the horizontal derivative of (3.40) gives

$$\frac{\partial}{\partial x} \frac{\partial p}{\partial z} = \frac{\partial}{\partial z} \frac{\partial p}{\partial x} = 0 \quad (3.41)$$

which shows the horizontal pressure gradient is independent of depth. Since the height  $z = 0 \approx \delta_w$ , corresponds to the edge of the wave boundary layer, the horizontal pressure gradient within the wave boundary layer is independent of  $z$ . This means that the pressure gradient term in the wave boundary layer is the same as the pressure gradient for the linearized potential wave solution evaluated at  $z = 0$ . Evaluating (3.36) at  $x = 0$  and  $z = \delta_w$  gives the solution for the wave at the outer edge of the wave boundary layer,

$$u_w = u_b e^{i\omega t} \quad (3.42)$$

where  $u_b$  is the maximum near-bottom wave orbital velocity and is equal to  $gHk/[2\omega \cosh(kh)]$ , since  $\cosh(k\delta_w) \cong 1$ . Inserting (3.42) into (3.38) to define the horizontal pressure gradient, the governing equation (3.22) within the wave boundary layer becomes

$$\frac{\partial u_w}{\partial t} - \frac{\partial u_w}{\partial t} = \frac{\partial}{\partial z} \left( K \frac{\partial u_w}{\partial z} \right) \quad (3.43)$$

The general solution for  $u_w$  should incorporate both a periodic component to represent the oscillatory wave motion and a vertically dependent function to satisfy the

no-slip condition at the bed. Defining  $u_w$  as  $f(z)e^{i\omega t}$ , where  $f(z)$  is a general function to be determined, and inserting this expression into (3.43) gives

$$i\omega Q = \frac{\partial}{\partial z} \left( K \frac{\partial Q}{\partial z} \right) \quad (3.44)$$

where  $Q = f(z) - u_b$ . The task is now to find solutions for  $Q$  using the eddy viscosities given in (3.26).

The solution to (3.44) is facilitated by non-dimensionalizing the vertical coordinate, i.e.,  $\xi = z/l_{cw}$ , where  $l_{cw} = \kappa u_{*cw}/\omega$  is the scale height of the wave boundary layer for combined flows. For  $\xi$  less than  $\xi_1 = z_1/l_{cw}$ , the eddy viscosity is given by  $K = \kappa u_{*cw} \xi l_{cw}$ , and (3.44) becomes

$$iQ - \frac{\partial}{\partial \xi} \left( \xi \frac{\partial Q}{\partial \xi} \right) = 0 \quad (3.45)$$

with the general solution

$$Q = A (Ber 2\sqrt{\xi} + iBei 2\sqrt{\xi}) + B (Ker 2\sqrt{\xi} + iKei 2\sqrt{\xi}) \quad (3.46)$$

where *Ber*, *Bei*, *Ker* and *Kei* are Kelvin functions of order zero and  $A$  and  $B$  are complex constants (Abramowitz and Stegun 1964). For  $\xi_1 \leq \xi \leq \xi_2 = z_2/l_{cw}$ , the eddy viscosity is constant and (3.44) becomes

$$iQ - \xi_1 \frac{\partial^2 Q}{\partial \xi^2} = 0 \quad (3.47)$$

with the general solution

$$Q = C e^{m\xi} + D e^{-m\xi} \quad (3.48)$$

where

$$m = \sqrt{\frac{i}{\xi_1}} \quad (3.49)$$

and  $C$  and  $D$  are complex constants. For  $\xi \geq \xi_2$ , (3.44) becomes

$$iQ - \frac{\partial}{\partial \xi} \left( \frac{\xi}{\epsilon} \frac{\partial Q}{\partial \xi} \right) = 0 \quad (3.50)$$

with the general solution,

$$Q = F (Ber 2\sqrt{\epsilon\xi} + iBei 2\sqrt{\epsilon\xi}) + G (Ker 2\sqrt{\epsilon\xi} + iKei 2\sqrt{\epsilon\xi}) \quad (3.51)$$

where  $\epsilon = u_{*cw}/u_{*c}$  and  $F$  and  $G$  are complex constants. The constants are determined by boundary conditions and matching of the solutions in the interior. At the bed,  $u_w = 0$ , which gives  $Q = u_w - u_b = -u_b$ . As  $\xi \rightarrow +\infty$ , where the limit  $+\infty$  is taken in the usual boundary layer sense in that it refers to a distance much greater than  $\delta_w$ ,  $u_w$  should approach the solution for irrotational flow so that  $Q = u_w - u_b = 0$ . At the points  $\xi_1$  and  $\xi_2$ , the matching condition that  $u_w$  and the shear stress,  $K\partial u_w/\partial \xi$ , be continuous is imposed. Since for this model the eddy viscosity is continuous throughout the boundary

layer, the matching condition reduces to the requirement that the velocity  $Q$  and the shear  $\partial Q/\partial \xi$  be continuous across  $\xi_1$  and  $\xi_2$ . Applying the matching and boundary conditions gives the following set of algebraic equations to determine the six constants,

$$Q_0 = AB_0 + BK_0 \quad (3.52a)$$

$$AB_1 + BK_1 = CP_1 + DM_1 \quad (3.52b)$$

$$AB_1^{(1)} + BK_1^{(1)} = m(CP_1 - DM_1) \quad (3.52c)$$

$$CP_2 + DM_2 = GK_2 \quad (3.52d)$$

$$m(CP_2 - DM_2) = GK_2^{(1)} \quad (3.52e)$$

$$F = 0 \quad (3.52f)$$

where the requirement that  $F = 0$  has been imposed because  $Ber$  and  $Bei$  increase without bound as  $\xi = z/l_{cw} \rightarrow +\infty$ . The terms in (3.52) are defined as follows:

$$Q_0 = -u_b$$

$$B_0 = \text{Ber } 2\sqrt{\xi_0} + i \text{Bei } 2\sqrt{\xi_0}$$

$$K_0 = \text{Ker } 2\sqrt{\xi_0} + i \text{Kei } 2\sqrt{\xi_0}$$

$$B_1 = \text{Ber } 2\sqrt{\xi_1} + i \text{Bei } 2\sqrt{\xi_1}$$

$$K_1 = \text{Ker } 2\sqrt{\xi_1} + i \text{Kei } 2\sqrt{\xi_1}$$

$$B_1^{(1)} = \frac{\partial}{\partial \xi} \left( \text{Ber } 2\sqrt{\xi} + i \text{Bei } 2\sqrt{\xi} \right) \Big|_{\xi = \xi_1} \quad (3.53)$$

$$K_1^{(1)} = \frac{\partial}{\partial \xi} \left( \text{Ker } 2\sqrt{\xi} + i \text{Kei } 2\sqrt{\xi} \right) \Big|_{\xi = \xi_1}$$

$$P_1 = e^{m\xi_1} \quad P_2 = e^{m\xi_2}$$

$$M_1 = e^{-m\xi_1} \quad M_2 = e^{-m\xi_2}$$

$$K_2 = \text{Ker } 2\sqrt{\epsilon\xi_2} + i \text{Kei } 2\sqrt{\epsilon\xi_2}$$

$$K_2^{(1)} = \frac{\partial}{\partial \xi} \left( \text{Ker } 2\sqrt{\epsilon\xi} + i \text{Kei } 2\sqrt{\epsilon\xi} \right) \Big|_{\xi = \xi_2}$$

The method to solve for the constants in (3.52) is to first eliminate  $G$  to give an equation in terms of  $C$  and  $D$ , then to eliminate  $C$  and  $D$  to give an equation in terms of  $A$  and

B. Solving for  $G$  in (3.52d) and (3.52e) gives the following relationship between  $C$  and  $D$ ,

$$C P_2 \left( 1 - \frac{m K_2}{K_2^{(1)}} \right) = -D M_2 \left( 1 + \frac{m K_2}{K_2^{(1)}} \right) \quad (3.54)$$

or

$$C P_2 = D M_2 \bar{H} \quad (3.55)$$

where

$$\bar{H} = \frac{m K_2 + K_2^{(1)}}{m K_2 - K_2^{(1)}} \quad (3.56)$$

Solving for  $C$  in (3.55), and inserting into (3.52b) and (3.52c), gives

$$A B_1 + B K_1 = \frac{D M_2 \bar{H} P_1}{P_2} + D M_1 \quad (3.57)$$

and

$$A B_1^{(1)} + B K_1^{(1)} = m \left( \frac{D M_2 \bar{H} P_1}{P_2} - D M_1 \right) \quad (3.58)$$

respectively. Eliminating  $D$  from (3.57) and (3.58) gives the following expression for  $A$  in terms of  $B$ ,

$$A \left( \frac{B_1}{I} - \frac{B_1^{(1)}}{J} \right) = B \left( \frac{K_1^{(1)}}{J} - \frac{K_1}{I} \right) \quad (3.59)$$

where

$$I = \frac{M_2 P_1 \bar{H}}{P_2} + M_1 \quad (3.60)$$

$$J = \frac{m M_2 P_1 \bar{H}}{P_2} + m M_1$$

Finally, (3.52a) along with (3.59) can be used to solve for  $A$  and  $B$  in terms of  $Q_0$ ,

$$A = \frac{Q_0 N}{B_0 N + K_0 L} \quad (3.61)$$

$$B = \frac{Q_0 L}{B_0 N + K_0 L}$$

where

$$N = \frac{K_1^{(1)}}{J} - \frac{K_1}{I} \quad (3.62)$$

$$L = \frac{B_1}{I} - \frac{B_1^{(1)}}{J}$$

Once  $A$  and  $B$  are known, the solutions for  $C$ ,  $D$  and  $G$  can be determined from (3.52). Multiplying (3.52b) by  $m$  and adding to (3.52c) gives  $C$  in terms of  $A$  and  $B$ ,



$$C = \frac{(AB_1 + BK_1)m + (AB_1^{(1)} + BK_1^{(1)})}{2mP_1} \quad (3.63)$$

Similarly, multiplying (3.52b) by  $m$  and subtracting from (3.52c) gives  $D$  in terms of  $A$  and  $B$ ,

$$D = \frac{(AB_1 + BK_1)m - (AB_1^{(1)} + BK_1^{(1)})}{2mM_1} \quad (3.64)$$

Finally, (3.52d) and (3.52e) are added to express  $G$  in terms of  $C$  and  $D$ ,

$$G = \frac{CP_2(1 + m) + DM_2(1 - m)}{K_2 + K_2^{(1)}} \quad (3.65)$$

If the flow parameters  $u_{*cw}$ ,  $u_{*c}$ ,  $z_0$ ,  $z_1$ ,  $u_b$  and  $\omega$  are specified,  $Q$  can be determined from Equations (3.46), (3.48) and (3.51)-(3.65), which then can be used to determine the wave velocity profile for the bottom boundary layer. The solutions for the Kelvin functions must be determined numerically, and polynomial expansions, with associated errors for arguments ranging from 0 to  $\infty$ , are given in Abramowitz and Stegun (1964). Methods to determine the shear velocities are discussed next.

### 3.3 Wave friction factor and the determination of the bottom stress

As mentioned above, the maximum instantaneous shear stress is the vector sum of the time-average of the instantaneous shear stress plus the maximum instantaneous shear stress associated with the wave,

$$\tau_{cw} = \tau_c + \tau_{wm} \quad (3.66)$$

Writing (3.66) in terms of the shear velocities and noting that the stresses are vector quantities gives

$$\mathbf{u}_{*cw} \mathbf{u}_{*cw} = u_{*c}^2 (\cos \phi_{cw} \hat{i} + \sin \phi_{cw} \hat{j}) + u_{*wm}^2 \hat{i} \quad (3.67)$$

where  $\phi_{cw}$  ( $0^\circ \leq \phi_{cw} \leq 90^\circ$ ) is the angle between the mean current and the wave,  $\hat{i}$  and  $\hat{j}$  are unit vectors in the  $x$  and  $y$  directions, respectively, and the bold face  $\mathbf{u}_{*cw}$  is a vector quantity. Taking the magnitude of (3.67) gives the following relationship between the three shear velocities,

$$u_{*cw}^2 = C_R u_{*wm}^2 \quad (3.68)$$

where

$$C_R = \left[ 1 + 2 \left( \frac{u_{*c}}{u_{*wm}} \right)^2 \cos \phi_{cw} + \left( \frac{u_{*c}}{u_{*wm}} \right)^4 \right]^{1/2} \quad (3.69)$$

As the current decreases, the time average shear stress,  $\tau_c$ , decreases. In the limit,  $u_{*c} \rightarrow 0$ ,  $C_R \rightarrow 1$ , which means that  $u_{*cw} \rightarrow u_{*wm}$ , as would be expected for wave motion in the absence of a mean current. As  $\tau_c$  increases,  $C_R$  becomes larger so that  $u_{*cw}$  becomes greater than  $u_{*wm}$ , reflecting the contribution from the mean current to the total maximum shear stress.

The calculation of the bed shear stress is aided by the introduction of a wave

friction factor,  $f_w$  (Jonsson 1966), that relates  $\tau_{wm}$  to  $u_b$ ,

$$\tau_{wm} = \frac{1}{2} f_w \rho u_b^2 \quad (3.70)$$

Although (3.70) is applicable only for pure wave motion, Grant and Madsen (1986), in a novel approach, suggest that a modified wave-current friction factor may be constructed if the magnitude of  $\tau_c$  is small relative to  $\tau_{wm}$ . Under these conditions, they suggest  $\tau_{wm}$  can be expressed as

$$\tau_{wm} = \frac{1}{2} f_w C_R \rho u_b^2 \quad (3.71)$$

Thus, the shear stress experienced by a wave in the presence of a mean current is modified from the pure wave case by the factor  $C_R$ . When  $u_{*c} \rightarrow 0$ ,  $C_R \rightarrow 1$ , and (3.70) is recovered, giving the correct expression for the shear stress for pure wave motion. As  $C_R$  increases, which for this study is expected only to be slightly larger than unity,  $\tau_{wm}$  also becomes larger, representing the contribution from the time averaged current.

The maximum instantaneous shear stress for the wave also can be expressed as

$$\tau_{wm} = \lim_{z \rightarrow z_0} \left( \rho K \left| \frac{\partial u_w}{\partial z} \right| \right) \quad (3.72)$$

where  $| |$  indicates the modulus. Near the bed, the equations for the wave and eddy viscosity are

$$u_w = [u_b + A(Ber\,2\sqrt{\xi} + i\,Bei\,2\sqrt{\xi}) + B(Ker\,2\sqrt{\xi} + i\,Kei\,2\sqrt{\xi})] e^{i\omega t} \quad (3.73)$$

and  $K = \kappa u_{*cw} z$ , respectively. Substituting the nondimensional vertical coordinate into (3.72), along with (3.73) for the wave, gives

$$\tau_{wm} = \rho \kappa u_{*cw} \xi_0 \left| (A B_0^{(1)} + B K_0^{(1)}) \right| \quad (3.74)$$

where

$$B_0^{(1)} = \frac{\partial}{\partial \xi} (Ber\,2\sqrt{\xi} + i\,Bei\,2\sqrt{\xi}) \Big|_{\xi = \xi_0} \quad (3.75)$$

$$K_0^{(1)} = \frac{\partial}{\partial \xi} (Ker\,2\sqrt{\xi} + i\,Kei\,2\sqrt{\xi}) \Big|_{\xi = \xi_0}$$

For convenience, (3.74) is written as

$$\tau_{wm} = \rho u_{*cw} u_b \Gamma_w \quad (3.76)$$

where the non-dimensional function  $\Gamma_w$  is defined as

$$\Gamma_w = -\kappa \xi_0 \left| \frac{B_0^{(1)} N + K_0^{(1)} L}{B_0 N + K_0 L} \right| \quad (3.77)$$

and (3.61) has been used to substitute for  $A$  and  $B$ . An expression for the wave friction factor can be obtained by substituting (3.68) into (3.76),

$$\frac{\tau_{wm}}{\rho} = u_{*wm}^2 = (\sqrt{C_R} u_b \Gamma_w) u_b \Gamma_w \quad (3.78)$$

so that

$$u_{*wm} = \sqrt{C_R} u_b \Gamma_w \quad (3.79)$$

which, using (3.71), gives

$$\sqrt{\frac{f_w}{2}} \sqrt{C_R} u_b = \sqrt{C_R} u_b \Gamma_w \quad (3.80)$$

or

$$\frac{f_w}{2} = \Gamma_w^2 \quad (3.81)$$

Inspection of the terms that define  $\Gamma_w$  shows that  $f_w$  is only a function of  $\xi_0$ ,  $\xi_1$  and  $\xi_2$ .

$$z_0 = \frac{k_b}{30} \quad (3.82)$$

Using the Nikuradse equivalent sand grain roughness,  $z_0$  can be written as where  $k_b$  is the physical bottom roughness length and serves as a convenient scale to represent the combined effect of various roughness types encountered on the continental shelf. These typically include sand grains, wave-generated ripples and bedforms

associated with biological activity (Grant and Madsen 1986). Using (3.82), along with the definition of  $l_{cw}$ , (3.68), (3.79) and (3.81), the equation for  $\xi_0$  becomes

$$\begin{aligned}
 \xi_0 &= \frac{k_b}{30 l_{cw}} \\
 &= \frac{k_b \omega}{30 \kappa u_{*cw}} \\
 &= \frac{k_b \omega}{30 \kappa C_R \sqrt{f_w/2} u_b} \\
 &= \frac{k_b}{30 \kappa C_R \sqrt{f_w/2} A_b}
 \end{aligned} \tag{3.83}$$

where  $A_b = u_b/\omega$  is the maximum bottom excursion amplitude of the wave motion.

Up to this point,  $z_1$  has remained arbitrary, however, GG suggested that  $z_1 \approx 0.15 l_{cw}$  based on theoretical arguments for waves. Madsen and Wikramanayake (1991), in a study that compared the same 3-layer model to flume measurements of combined wave and current flows, found that  $z_1 \cong 0.5 l_{cw}$  for a steady current in the presence of waves. For waves in the presence of a current, they found  $z_1 \cong 0.15 l_{cw}$  gave the best fit to available wave profile data. They further conducted sensitivity tests on the wave friction factor allowing  $z_1$  to vary from 0.25 to  $2.0 l_{cw}$ . More recently, Lynch et al. (1997) set  $z_1 = 2.0 l_{cw}$  based on sediment concentration profiles they measured in the field. Because  $z_1$  remains undetermined, the more general expression,  $z_1 = \alpha l_{cw}$  is temporarily chosen for this study. The nondimensional parameter  $\xi_1$  is now equal to  $\alpha$ ,

which gives  $\xi_2 = \xi_1 \epsilon = \alpha \epsilon$ , so that the friction factor in (3.81) becomes a function of  $k_b / A_b$ ,  $\alpha$ ,  $\epsilon$  and  $C_R$ .

Due to the complicated form of  $\Gamma_w$ , an explicit expression for  $f_w$  cannot be derived from (3.81). Therefore,  $f_w$  is determined numerically as a function of  $A_b/k_b$ ,  $\alpha$ ,  $\epsilon$  and  $C_R$ . Similar procedures have been used by other investigators to construct wave friction factor diagrams which are useful in applications and provide a common framework from which various theoretical and experimental methods to determine  $f_w$  can be judged. For example, Grant and Madsen (1986) use (3.24) as their eddy viscosity model to derive a wave friction factor equation. For this choice of eddy viscosity, the solution for the wave-induced velocity becomes

$$u_w = u_b \left[ 1 - \frac{Ker 2\sqrt{\xi} + i Kei 2\sqrt{\xi}}{K_0} \right] \quad (3.84)$$

so that the shear velocity associated with  $\tau_{wm}$  is

$$u_{wm}^2 = -\kappa u_{cw} u_b \xi_0 \left| \frac{K_0^{(1)}}{K_0} \right| \quad (3.85)$$

Following the same procedures as equations (3.76)-(3.81),  $f_w$  is found to be a function of  $\xi_0$  only, i.e.,

$$f_w = 2 \Delta_w^2 \quad (3.86)$$

where

$$\Delta_w = -\kappa \xi_0 \left| \frac{K_0^{(1)}}{K_0} \right| \quad (3.87)$$

Figure 3.1 shows  $f_w$  as a function of  $C_R A_b/k_b$  for  $\epsilon = 2.1$  and  $\alpha = 0.5$ , along with the Grant and Madsen (1986) wave friction factor for comparison. The value  $\alpha = 0.5$  has been suggested by Madsen and Wikramanayake (1991) for modeling currents in the presence of waves, and  $\epsilon = u_{*cw}/u_{*c}$  represents a medium range where the relative magnitude of the wave and current velocities outside the wave boundary layer are about the same. The sensitivity of the wave friction factor to these parameters will be explored in Section 3.7. For large values of  $C_R A_b/k_b$ , which can be interpreted as energetic waves in the presence of small roughness elements, the wave senses a relatively smooth bed so that the friction factor is small. As this ratio becomes smaller, the influence of the roughness elements becomes greater, leading to an increase in frictional drag associated with the wave, which explains why  $f_w$  increases with decreasing  $C_R A_b/k_b$ . Comparison of the Grant and Madsen (1986) wave friction factor to the one presented here shows that the two methods give nearly identical results for large values of  $C_R A_b/k_b$  but then diverge as  $C_R A_b/k_b$  approaches unity. Grant and Madsen (1982), in a detailed study of bottom roughness associated with wave-induced, fully rough turbulent flow, hypothesize that for  $A_b/k_b \leq 1$ , the proper length scale for the turbulent eddies becomes  $A_b$  and not  $k_b$ . In this limit,  $f_w$  is constant and can be determined by setting  $C_R A_b/k_b = 1$ . Of the two plots shown in Figure 3.1, the 3-layer eddy viscosity model shows this limiting behavior, suggesting that this model better agrees with the theory.



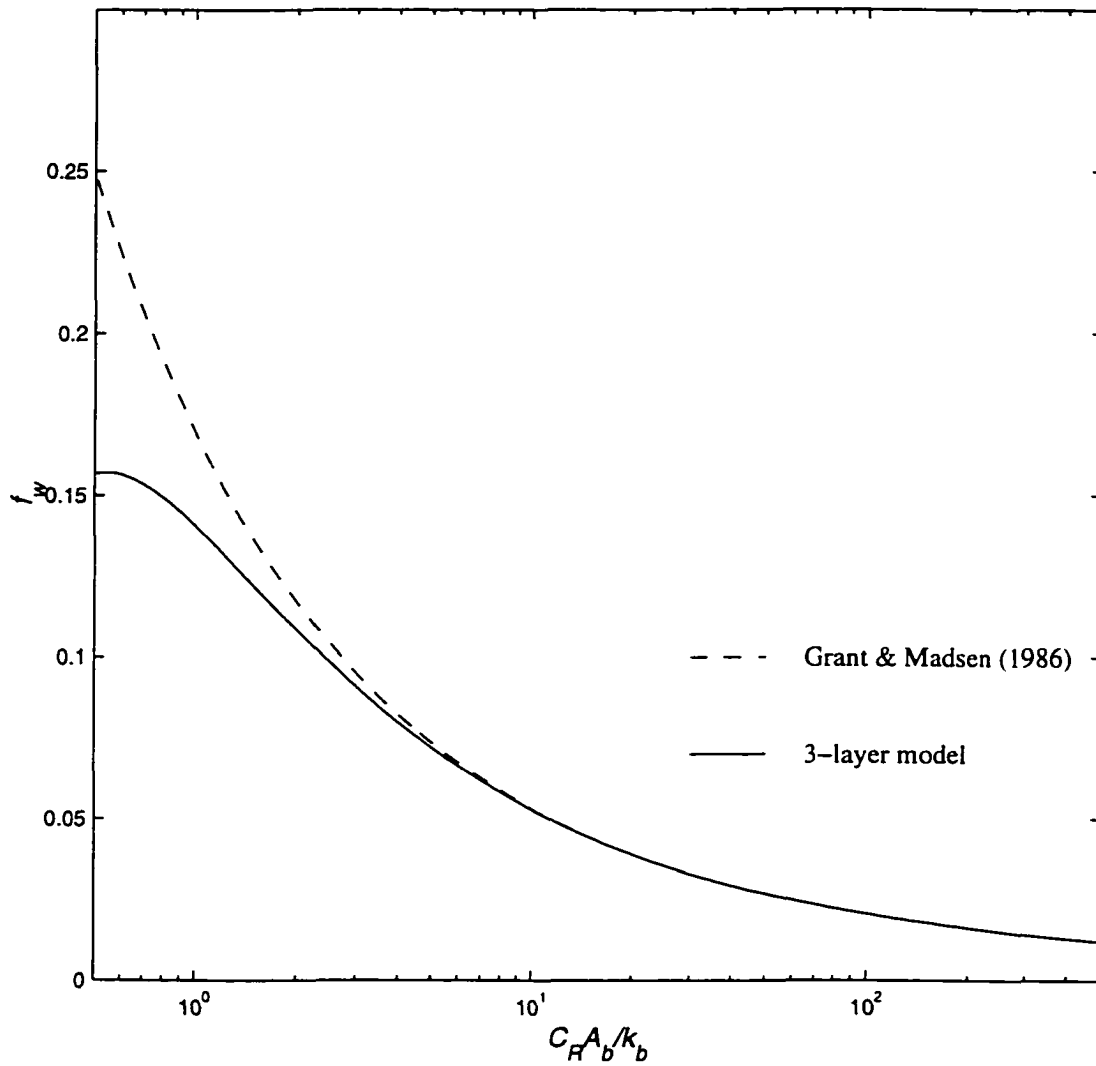


Figure 3.1 Comparison of the wave friction factor,  $f_w$ , calculated using the 3-layer model developed for this study and the Grant and Madsen (1986) model.

For the 3-layer model,  $f_w$  is also a function of  $\alpha = z_i/l_{cw}$  and  $\epsilon = u_{*cw}/u_{*c}$ , and a test to determine the sensitivity of the solution to changes in these two parameters is informative. Figure 3.2(a) shows  $f_w$  for different values of  $\epsilon$  with  $\alpha = 0.5$ , and Figure 3.2(b) shows the same but with  $\epsilon = 2.1$  and  $\alpha$  variable. The solutions are only weakly influenced by changes in  $\epsilon$  except when  $C_R A_b/k_b$  is less than about 1.0, in which smaller  $\epsilon$  tends to produce higher  $f_w$ . This suggests that the influence of the current is minimal except for large roughness configurations ( $C_R A_b/k_b < 1$ ), where increasing the contribution from the current increases the friction factor. For  $C_R A_b/k_b > 10$ , the effect of changing  $\alpha$  appears minimal for the  $\alpha = 0.5$  and 1.0 cases (Figure 3.2b). When this ratio approaches its minimum value shown,  $f_w$  begins to level off in agreement Grant and Madsen (1982) who suggested that  $f_w$  approaches a constant value for large roughness configurations. For  $C_R A_b/k_b \leq 1.0$ , however,  $f_w$  identified by  $\alpha = 0.15$  begins to increase. A similar pattern occurs for  $\alpha = 0.5$  when  $C_R A_b/k_b \leq 0.2$ . Measurements in rough turbulent oscillatory flow for  $A_b/k_b < 1$  (Simons et al. 1988; Rankin 1997) have indicated that  $f_w$  does not asymptotically steer toward a constant, but can increase in a manner consistent with the plots identified as  $\alpha = 0.15$  and 0.5 in Figure 3.2(b). It should be noted that for large roughness configurations, when  $k_b$  is on the order of the wave boundary layer height, the boundary layer theory presented in Section 3.1 is not formally valid.

From this analysis, the quantitative features of the wave friction factor under small roughness configurations is not influenced by changes in either  $\alpha$  or  $\epsilon$ . This was confirmed in similar sensitivity tests conducted by Madsen and Wikramanayake(1991). When the ratio  $C_R A_b/k_b$  is small, the wave friction factor becomes more sensitive to

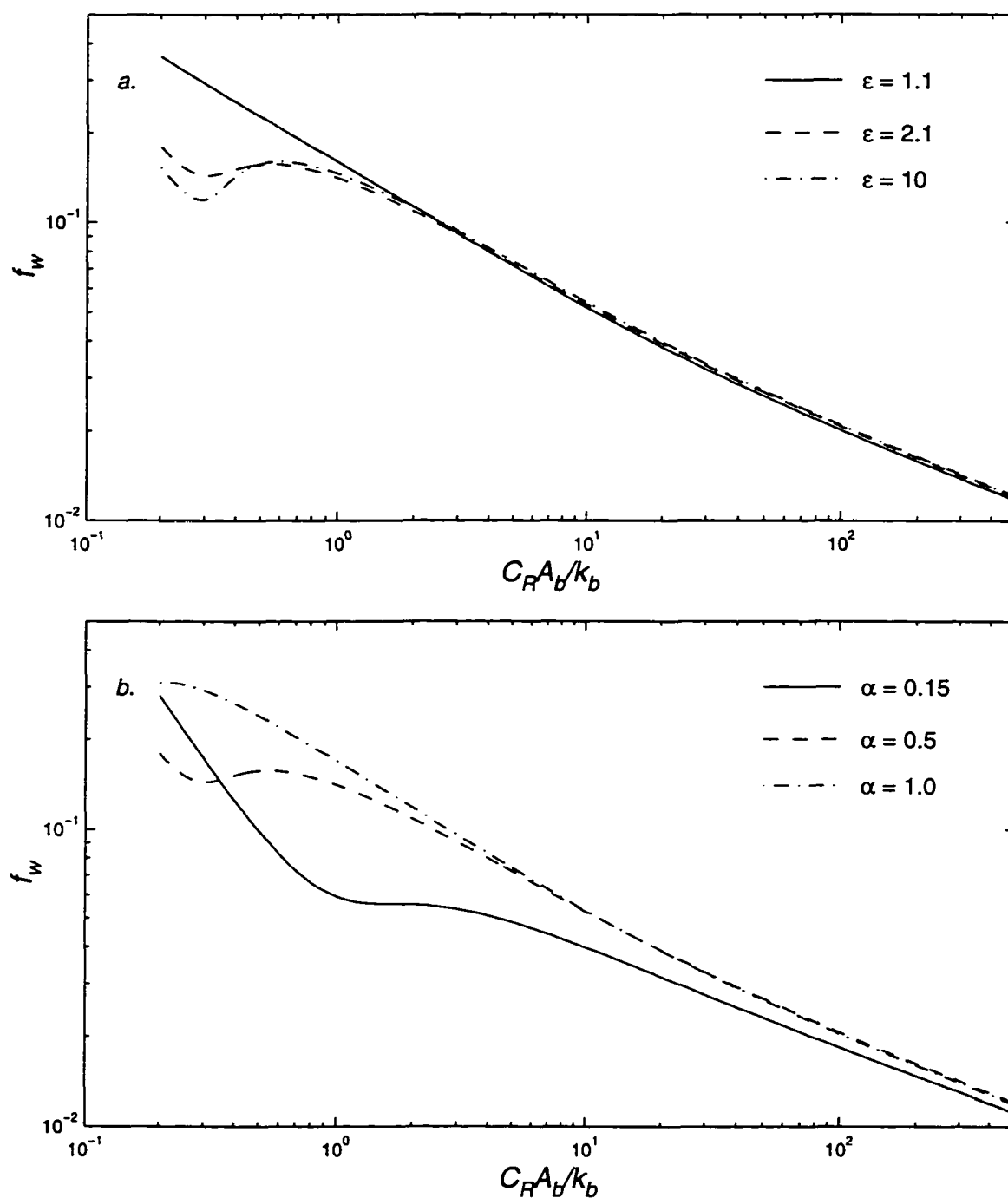


Figure 3.2 Sensitivity test showing the wave friction factor calculated using the 3-layer model as a function of the parameters  $\epsilon$  (a) and  $\alpha$  (b). In (a)  $\alpha = 0.5$  and in (b)  $\epsilon = 2.1$ .

changes in  $\alpha$ . It is reemphasized that under these conditions, the applicable range of the theory is near its asymptotic limit, and as such, the model may not accurately represent the functional relationship between  $f_w$  and  $C_R A_b/k_b$ .

Grant and Madsen (1986) derived their wave friction factor solution under the assumption that  $C_R$  is close to unity, but neglected to perform sensitivity tests to identify conditions for which  $C_R$  is greater than 1. Therefore, a closed expression for  $C_R$  is derived, and sensitivity of the solution to changes in  $\epsilon$  and  $\phi_{cw}$  is examined. Recalling that  $\epsilon = u_{*cw}/u_{*c}$ , (3.68) is substituted into (3.69) giving

$$(1 - \epsilon^4) C_R^2 + 2 \cos \phi_{cw} \epsilon^2 C_R + \epsilon^4 = 0 \quad (3.88)$$

Equation (3.88) is quadratic in  $C_R$  with the solution

$$C_R = \frac{-2 \cos \phi_{cw} \epsilon^2 \pm \sqrt{4 \cos^2 \phi_{cw} \epsilon^4 - 4(1 - \epsilon^4) \epsilon^4}}{2(1 - \epsilon^4)} \quad (3.89)$$

A 3-dimensional mesh plot showing the dependence of  $C_R$  on  $\epsilon$  and  $\phi_{cw}$  is depicted in Figure 3.3. For values of  $\epsilon$  greater than about 4,  $C_R$  is approximately equal to 1 regardless of  $\phi_{cw}$ . When  $\epsilon$  is large,  $\tau_{wm}$  constitutes a major fraction of the total shear stress so that  $C_R$  is a minimum. As  $\epsilon$  approaches 1,  $C_R \rightarrow \infty$ , which means that the contribution from  $\tau_{wm}$  is negligible and the solution approaches that of a pure current where the need to obtain a wave friction factor, which is coupled to the current through  $C_R$ , is no longer necessary. It is also interesting to examine how  $C_R$  varies with  $\phi_{cw}$  for small values of  $\epsilon$ . With  $\epsilon = 1.5$ , which corresponds to the lower limit in the figure,  $C_R$

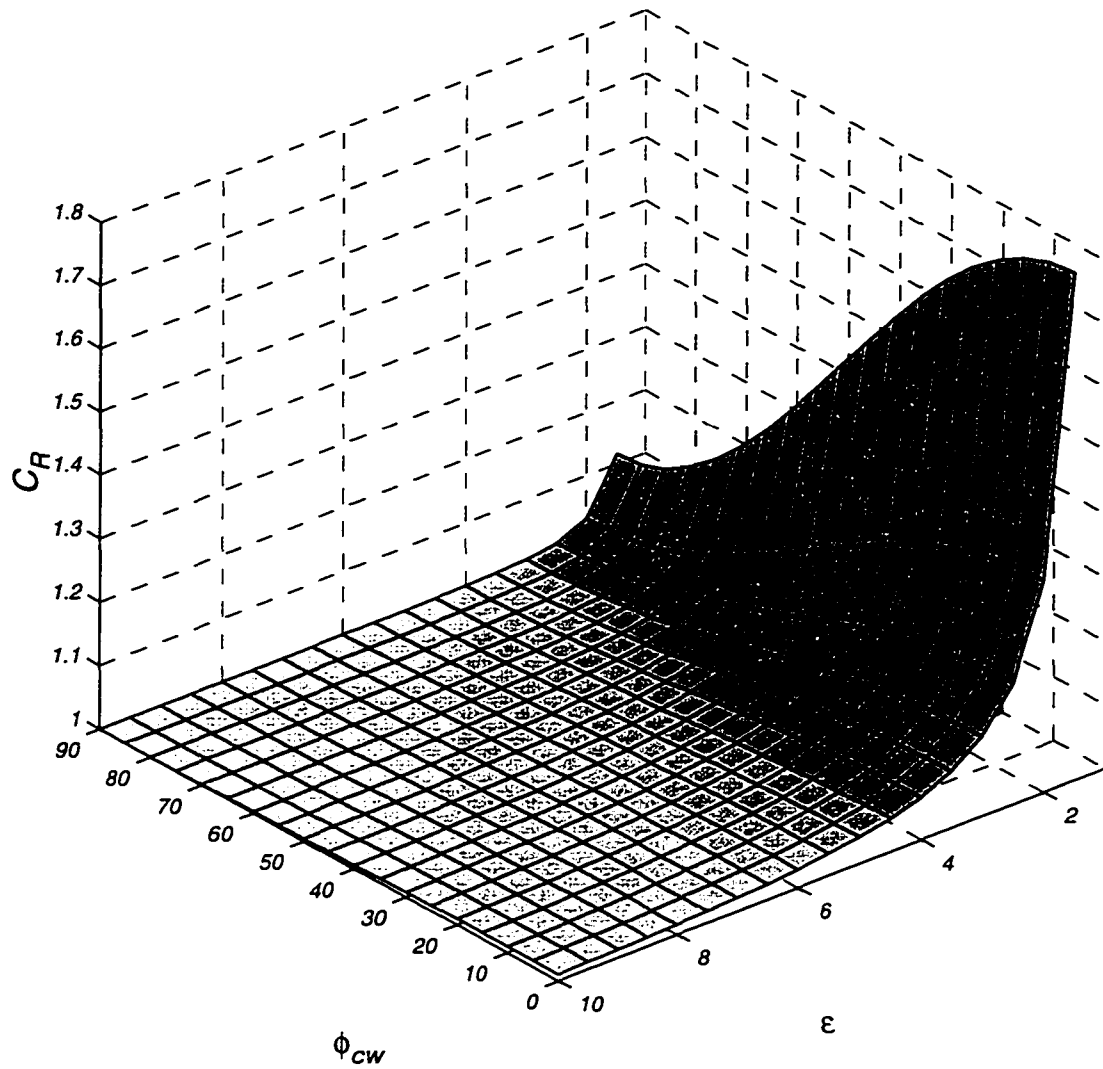


Figure 3.3 Three-dimensional grided mesh plot showing  $C_R$  as a function of  $\epsilon$  and  $\phi_{cw}$ .  $\epsilon$  ranges from a minimum of 1.5 to a maximum of 10. The grid is spaced in 1/2 increments for  $\epsilon$  and every 5 degrees for  $\phi_{cw}$ .

varies between 1.1 for  $\phi_{cw} = 90^\circ$ , and 1.8 for  $\phi_{cw} = 0^\circ$ . Thus, when the wave and mean current stresses are of the same order of magnitude, accurate estimates of  $\phi_{cw}$  become important. For larger values of  $\epsilon$ , the directional dependence is negligible, and accurate estimates of  $\phi_{cw}$  are not crucial since  $\tau_{wm}$  constitutes a major fraction of the combined wave and current shear stress.

The solution for the wave was derived using the neutral eddy viscosity, and it is important to examine the validity of this decision since the purpose here is to model stratified flows. If the maximum near-bed shear stress associated with the wave can be adequately described using the neutral theory, then the stratification correction for the wave can be neglected. The procedure is to calculate, for a given velocity profile, the change in shear stress that would be caused by the inclusion of the stratification correction, and to determine if this change is significant. For this application, the shear stresses associated with the wave for neutral and stratified flows are

$$\tau_w = \rho K \frac{\partial u_w}{\partial z} \quad (3.90)$$

and

$$\tau_{ws} = \rho K_{strat} \frac{\partial u_w}{\partial z} \quad (3.91)$$

respectively, where the subscript *ws* denotes the modified wave shear stress due to the

inclusion of the stability parameter. Dividing both sides of (3.90) and (3.91) by  $\rho$  and subtracting gives

$$\frac{\delta \tau_w}{\rho} = K \frac{\partial u_w}{\partial z} \left[ 1 - \frac{1}{1 + \beta \frac{z}{L}} \right] \quad (3.92)$$

where  $\delta \tau_w$  indicates the stress difference between the neutral and stratified cases. Near the bed,  $z$  is small so that the term in square brackets in (3.92) is near zero. At the top of the wave boundary layer, the shear stress for the wave goes to zero, so that the right hand side of (3.92) is small. In both cases,  $\delta \tau_w$  is small so that the wave shear stress is described adequately by (3.90). For  $z_0 \ll z \ll \delta_w$ , it is unclear whether the stability parameter is large or small.

Possible stratification effects in the central wave boundary layer are estimated by examination of the eddy viscosity in (3.26), which shows that changes in  $\alpha$ , which defines  $z_1$ , and  $\epsilon$ , which is used to define  $z_2$ , represent arbitrary changes to the neutral eddy viscosity. These arbitrary changes were shown not to affect the wave friction factor solution depicted in Figure 3.2 except for large roughness configurations. Thus, the wave stress at the bed  $\tau_{wm} = \rho \frac{1}{2} f_w C_R u_b^2$ , where  $C_R$  is also a function of  $\epsilon$ , is not affected by arbitrary changes in the neutral eddy viscosity except when  $\alpha$  and  $C_R A_b/k_b$  are small. The inclusion of a stability parameter also introduces arbitrary changes to the neutral eddy viscosity which also will not affect  $f_w$  unless  $\alpha$  and  $C_R A_b/k_b$  are small. For small  $C_R A_b/k_b$ , the roughness will be large indicating large ripples and low flow velocities. For large ripples and low flow, sediment transport is weak and very little will be in suspension. Under these conditions, stratification will be negligible and  $z/L$  will

be small. Because it is the bottom stress that is important to wave/current interaction, and is all that directly affects the current, the inclusion of  $z/L$  in the wave will not change the results for the current. Therefore,  $z/L$  in the wave stress calculation is neglected. Possible exceptions will include large roughness configurations when the model is not formally valid, or when  $\alpha \approx 0.15$ . As mentioned above, for currents in the presence of waves,  $\alpha = 0.5$  for data collected in the laboratory and  $\alpha = 2.0$  for data collected in the field. Thus, as long as  $\alpha \geq 0.5$ , the stability parameter can be neglected in the wave stress problem.

Because the height of the current boundary layer is much greater than the wave boundary layer, the vertical shear in the current does not vanish until much higher in the water column. This fact suggests that the stratification correction is important for the mean current, except possibly very near the bed where  $z$  is small.

### 3.4 Solution for the mean current and suspended sediment concentration

To simplify the derivation, only the solution for the magnitude of the mean current,  $U_0$ , is presented here. Once the magnitude is known, the current direction relative to the wave is given by  $\phi_{cw}$ . The magnitude of the bottom stress felt by the current is the magnitude of the time-average bottom stress,

$$\tau_c = |\tau_{bx} + \tau_{by}| = \rho u_{*c}^2 = \rho K_{strat} \frac{\partial U_0}{\partial z} \quad (3.93)$$

where the first equality comes from (3.23). Using (3.26) to represent the neutral portion of the eddy viscosity in each of the three layers, (3.93) is written as



$$\begin{aligned}
u_{*c}^2 &= \frac{\kappa u_{*cw} z}{1 + \beta \frac{z}{L}} \frac{\partial U_0}{\partial z} & z_0 \leq z \leq z_1 \\
u_{*c}^2 &= \frac{\kappa u_{*cw} z_1}{1 + \beta \frac{z}{L}} \frac{\partial U_0}{\partial z} & z_1 \leq z \leq z_2 \\
u_{*c}^2 &= \frac{\kappa u_{*c} z}{1 + \beta \frac{z}{L}} \frac{\partial U_0}{\partial z} & z_2 \leq z
\end{aligned} \tag{3.94}$$

Solving for the velocity gradient in (3.94), and then integrating, gives

$$\begin{aligned}
U_0(z) &= \frac{u_{*c}^2}{\kappa u_{*cw}} \left[ \ln \left( \frac{z}{z_0} \right) + \beta \int_{z_0}^z \frac{dz}{L} \right] & z_0 \leq z \leq z_1 \\
U_0(z) &= \frac{u_{*c}^2}{\kappa u_{*cw}} \left[ \frac{(z - z_1)}{z_1} + \frac{\beta}{z_1} \int_{z_1}^z \frac{z}{L} dz \right] + U_0(z_1) & z_1 \leq z \leq z_2 \\
U_0(z) &= \frac{u_{*c}^2}{\kappa} \left[ \ln \left( \frac{z}{z_2} \right) + \beta \int_{z_2}^z \frac{dz}{L} \right] + U_0(z_2) & z_2 \leq z
\end{aligned} \tag{3.95}$$

where the boundary condition  $U_0(z_0) = 0$  has been imposed along with the requirement that  $U_0(z)$  is continuous at  $z_1$  and  $z_2$ .

The current profile in (3.95) is controlled by the two factors appearing in square brackets. The first term represents the neutral solution, where the  $z$  dependence is described by a logarithmic function in the upper and lower layers and a linear function in the middle. The neutral solution is identical to that obtained by Madsen and Wikramanayake (1991). The second term represents the correction for suspended sediment-induced stratification, where the vertical variation is regulated by the integral of  $1/L$  in the upper and lower layers and by the integral of  $z/L$  in the middle. Examining the neutral solution in the lower two layers reveals the effect of the wave stress on the mean current. Because  $u_{*cw}$  appears in the denominator, the added affect of the wave is to reduce the slope of the current profile. This is consistent with enhanced vertical mixing associated with the wave shear stress, where, near the bed, low momentum fluid is diffused higher into the water column in the combined flow. A similar modulation is seen in the middle layer, with the exception that the current is now a linear function of  $z$ . Above  $z_2$ , the shear stress for the wave is negligible and the current is described by the classic "law of the wall".

For the mean suspended sediment concentration, the third equation in (3.21) is vertically integrated to give

$$w_{f_n} C_{nm} + K_{s \text{ strat}} \frac{\partial C_{nm}}{\partial z} = \text{constant} \quad (3.96)$$

where the constant is set equal to zero, since at the top of the boundary layer there is no upward turbulent flux out of the boundary layer, and there is no sediment falling

downward from above. Substituting (3.28) as the eddy diffusivity, and using (3.26) for each of the three layers, the solution to the concentration equation is given as

$$\begin{aligned}
 C_{nm}(z) &= C_{nm}(z_0) \left( \frac{z}{z_0} \right)^{\frac{-\gamma w_{fn}}{\kappa u_{*cw}}} \exp \left[ \frac{-\beta w_{fn}}{\kappa u_{*cw}} \int_{z_0}^z \frac{dz}{L} \right] & z_0 \leq z \leq z_1 \\
 C_{nm}(z) &= C_{nm}(z_1) e^{\frac{-\gamma w_{fn}(z - z_1)}{\kappa u_{*cw} z_1}} \exp \left[ \frac{-\beta w_{fn}}{\kappa u_{*cw} z_1} \int_{z_1}^z \frac{z}{L} dz \right] & z_1 \leq z \leq z_2 \\
 C_{nm}(z) &= C_{nm}(z_2) \left( \frac{z}{z_2} \right)^{\frac{-\gamma w_{fn}}{\kappa u_{*c}}} \exp \left[ \frac{-\beta w_{fn}}{\kappa u_{*c}} \int_{z_2}^z \frac{dz}{L} \right] & z_2 \leq z
 \end{aligned} \tag{3.97}$$

where the concentration at the lower boundary,  $C_{nm}(z_0)$ , equals an assumed reference value, and the requirement that the solution is continuous at  $z_1$  and  $z_2$  has been imposed.

The concentration equation is also modulated by two factors representing neutral and stratified solutions. The second term on the right-hand side of (3.97) represents the neutral model, where a classic Rouse-like profile in the upper and lower layers is separated by an exponential decay in the middle. This is similar to the concentration profile obtained by Wikramanayake and Madsen (1992). The second exponential term represents the stratification correction, where the vertical variation is controlled by the integral of  $1/L$  in the upper and lower layers and by the integral of  $z/L$  in the middle. Again the effects of  $u_{*cw}$  can be seen. For combined wave and current flows,  $u_{*cw}$  will be larger than for pure steady currents, so the exponent in the lower layer will be

smaller, reducing the vertical decay rate of the sediment concentration. A similar effect occurs in the middle layer. Like the mean current solution, the enhanced shear stress associated with the wave is seen to increase vertical mixing within the wave boundary layer, leading to greater concentrations of suspended material near the bed for the combined flow than for pure steady currents. Above  $z_2$ , the shear stress for the wave is negligible and the turbulent sediment flux will be forced only by the enhanced shear stress for the current.

### 3.5 Determination of the stability parameter

Further simplification of the stability parameter can be achieved by neglecting the periodic concentration. Within the wave boundary layer the periodic concentration gradient can be the same order of magnitude as the mean concentration gradient. However, the stability parameter will be small simply due to the smallness of  $z$  and will not effect the current solution. In the outer wave boundary layer and above, the periodic concentration gradient is an order of magnitude less than the mean concentration gradient (Glenn 1983). Even though the stability parameter is large enough to effect the solution in this region, the effect of the periodic concentration gradient is negligible. Therefore, the periodic concentration gradient is neglected in the stability parameter. With this further simplification, the stability parameter reduces to

$$\frac{z}{L} = - \frac{\kappa z}{[u'w']^{3/2}} \sum_{n=1}^N g(s_n - 1) K_s \frac{\partial C_{nm}}{\partial z} \quad (3.98)$$

Substituting (3.96) into (3.98), the alternative expression

$$\frac{z}{L} = \frac{\kappa z}{[\overline{u'w'}]^{3/2}} \sum_{n=1}^N g(s_n - 1) w_{f_n} C_{nm} \quad (3.99)$$

is obtained. As noted by GG, only certain combinations of the product  $w_{f_n} C_{nm}$  will produce a large value of  $z/L$ . If the sediment fall velocity is large, then the suspended material will tend to quickly fall out of suspension leading to low concentrations of suspended load in the water column so that stratification will be negligible. If  $w_{f_n}$  is small, then the sediment will be evenly distributed throughout the water column, and stratification will again be negligible. Thus, only an intermediate range of sediment fall velocities and concentrations will produce a stability parameter large enough to alter the momentum and mass balance of the fluid-sediment mixture from the neutral case.

The remaining step is to obtain appropriate representations for the kinematic flux  $\overline{u'w'}$ . By definition, the kinematic flux is the product of the eddy viscosity and the vertical shear of the velocity,

$$\overline{u'w'} = K \left[ \frac{\partial u_c}{\partial z} + \frac{\partial u_w}{\partial z} \right] \quad (3.100)$$

where the neutral eddy viscosity is chosen to preserve the traditional relation between the Richardson flux number and the stability parameter in the constant stress layer (Turner 1979). For  $z < z_1$ , the shear stress for the current is constant so that the first term in square brackets in (3.100) reduces to  $u_{*c}^2/u_{*cw}z\kappa$ , or when multiplied by the neutral eddy viscosity gives  $u_{*c}^2$ . In this region, the small argument approximation to the Kelvin

functions given by Abramowitz and Stegun (1964) can be used to define the wave solution (Glenn 1983),

$$u_w = u_b + A - \frac{B}{2} \left( \ln \xi + 1.154 + i \frac{\pi}{2} \right) \quad (3.101)$$

Taking the derivative of (3.101) gives the wave shear,

$$\frac{\partial u_w}{\partial z} = -\frac{B}{2\xi} \quad (3.102)$$

which, when multiplied by the eddy viscosity ( $K = \kappa u_{*cw} \xi l_{cw}$ ) shows that the wave shear stress is constant, and must equal the maximum near-bottom shear stress for the wave,  $\tau_{wm} = \rho u_{*wm}^2$ . Thus, for  $z < z_1$ , the kinematic flux is simply the sum of  $u_c^2 + u_{*wm}^2 = u_{cw}^2$ . For  $z > z_2$ , the shear stress associated with the wave is negligible, and the stress for the current is still assumed constant. In this region,  $\overline{u'w'} = u_{*c}^2$ . For the middle region,  $z$  is no longer small and it is no longer valid to use the small argument approximation to the Kelvin functions to obtain the solution for the wave. A formal approach would be to explicitly solve for the wave stress and substitute the values for the kinematic flux. This approach, however, is not in the spirit of the original goal of developing a simple analytical model that can be efficiently applied at every grid point in a 3-dimensional shelf circulation model. An approach that is consistent with the goals presented here and that preserves the wave contribution to the kinematic flux, at least to first order, is to approximate the flux in the region  $z_1 \leq z \leq z_2$  using a function that

maintains the general functional form of the wave stress, but with a much simpler expression that can be prescribed independent of the details of the wave solution. Inspection of (3.48), which represents the wave solution in the range  $z_1 \leq z \leq z_2$ , shows that the vertical decay for both the wave and the wave shear is exponential. Thus, the kinematic flux in the range  $z_1 \leq z \leq z_2$  is approximated as

$$\overline{u'w'} = c_1 e^{\xi} + c_2 e^{-\xi} \quad (3.103)$$

with the boundary conditions.  $\overline{u'w'} = u_{*cw}^2$  at  $\xi = \xi_1 = z_1/l_{cw}$ , and  $\overline{u'w'} = u_{*c}^2$  at  $\xi = \xi_2 = z_2/l_{cw}$ . Using the boundary conditions and solving for the constants in (3.103) gives

$$\overline{u'w'} = u_{*k}^2 = \frac{u_{*c}^2 \sinh(\xi - \xi_1) + u_{*cw}^2 \sinh(\xi_2 - \xi)}{\sinh(\xi_2 - \xi_1)} \quad (3.104)$$

At  $\xi = \xi_1$ , (3.104) equals  $u_{*cw}^2$ , and then continuously decays to  $u_{*c}^2$  at  $\xi = \xi_2$ . The full solution to the wave shear will depend on the parameters  $\alpha$  and  $\epsilon$ , both, as mentioned previously, influence  $z_1$  and  $z_2$ . Figure 3.4 shows  $u_{*c}^2 + u_{*wm}^2 = u_{*cw}^2$ , with  $u_{*wm}^2$  calculated analytically as described in Section 3.2, and the approximation (3.104) for the same values of  $\alpha$  used in the wave friction factor sensitivity discussion and  $\epsilon = 2, 5$  and 10. Recalling that  $\epsilon = u_{*cw}/u_{*c}$ , the approximation (3.104), which is primarily used to represent the wave stress, is only important when the wave stress makes a significant contribution to the total stress. For  $\epsilon \leq 2$ , it is expected that the contribution from the wave is less important. For  $\epsilon = 2$  the departure of the approximation from the exact solution is strongest in the upper boundary layer when  $\alpha = 0.15$ . The departure from the

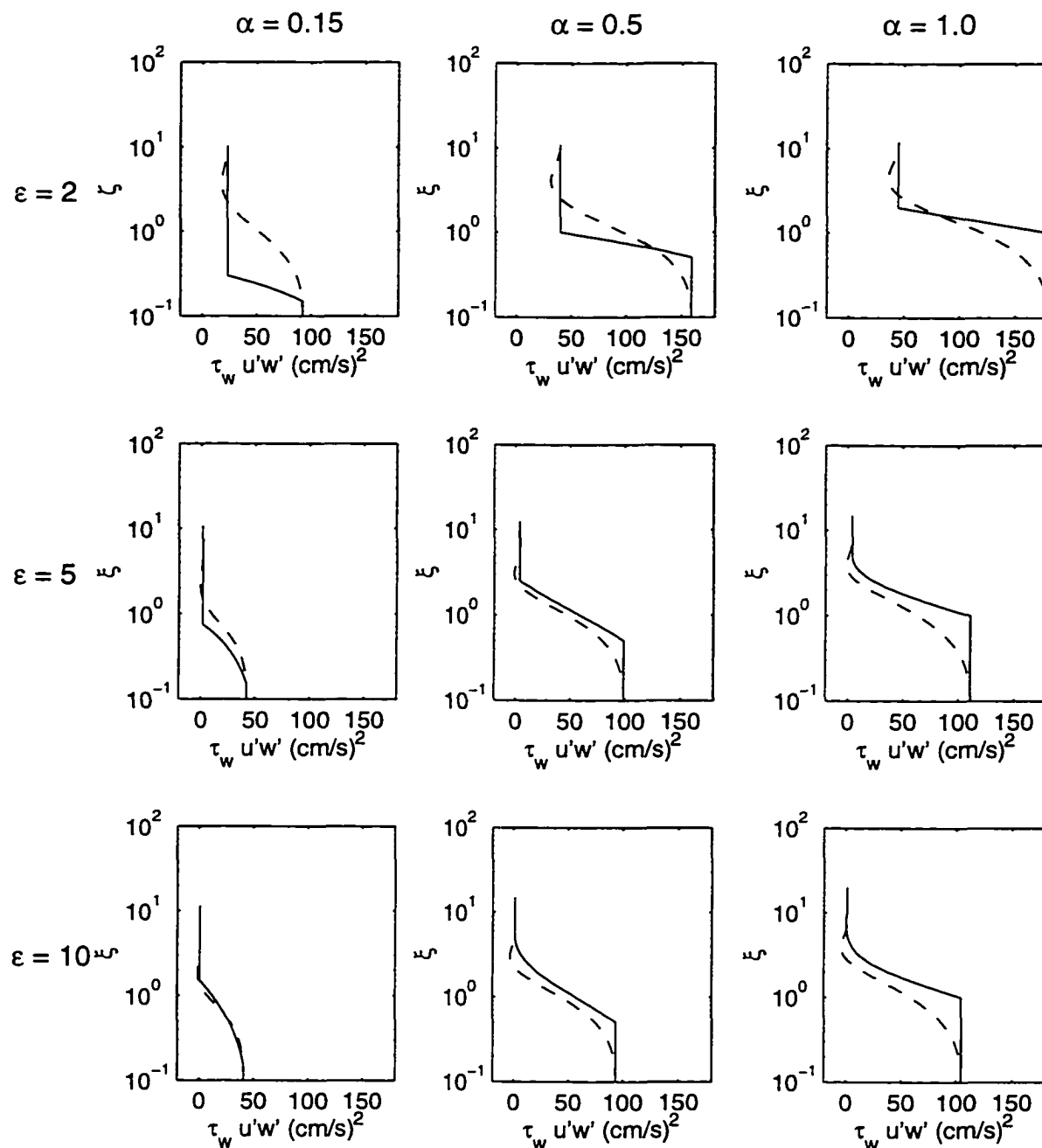


Figure 3.4 Comparison between the kinematic flux ( $u'w'$ ) defined in (3.104) (solid) and the analytical solution (dashed). The rows correspond to advancing  $\epsilon$ , which ranges from 2 at the top to 10 at the bottom. The columns correspond to advancing  $\alpha$ , which ranges from 0.15 on the left to 1.0 on the right.



exact solution is similarly large near the bed when  $\alpha = 1.0$ . As previously mentioned, for this case the contribution from the wave is relatively weak and the kinematic flux is primarily associated with the constant stress for the current. For  $\epsilon = 5$ , the match between the analytical solution and the approximation is improved for all  $\alpha$ . For  $\epsilon = 10$ , the comparison is further improved for  $\alpha = 0.15$  and  $0.5$ . In all 9 cases illustrated, the wave shear stress approaches a constant near the bed, supporting the use of (3.102) to represent the wave shear in the arguments that lead to the kinematic flux for  $z < z_1$ . In addition, the response of the approximate solution to changes in  $\alpha$  possesses a distinct pattern at the extremes  $z_1$  and  $z_2$ . For  $\alpha = 0.15$ , the approximate solution is more smooth at  $z = z_1$  and more kinked at  $z = z_2$ . For  $\alpha = 1.0$  the pattern is reversed. The smoothness is also improved with increases in  $\epsilon$ . Overall, the approximate solution ensures that the flux obtains appropriate values at  $z_1$  and  $z_2$ , and is a reasonable substitute for the more computationally demanding analytical solution. The fit is not as good for smaller  $\epsilon$ , but in this case, however, a major fraction of the kinematic flux is associated with the current and the details of the wave are less important.

The stability parameter in each of the three layers can now be written

$$\begin{aligned}
\frac{z}{L} &= \frac{\kappa z}{u_{*cw}^3} \sum_{n=1}^N g(s_n - 1) w_{f_n} C_{nm} & z_0 \leq z \leq z_1 \\
\frac{z}{L} &= \frac{\kappa z}{u_{*k}^3} \sum_{n=1}^N g(s_n - 1) w_{f_n} C_{nm} & z_1 \leq z \leq z_2 \\
\frac{z}{L} &= \frac{\kappa z}{u_{*c}^3} \sum_{n=1}^N g(s_n - 1) w_{f_n} C_{nm} & z_2 \leq z
\end{aligned} \tag{3.105}$$

To calculate the stability parameter, it is necessary to know in advance the concentration profile, and since the concentration profile depends explicitly on integrals related to  $z/L$ , the equation for the stability parameter has no simple algebraic solution. Under these conditions, a numerical solution is sought to approximate the vertical variation of the stability parameter. Numerical modeling of boundary layer processes usually requires a very fine grid to resolve the gradients of the pertinent variables in the immediate vicinity of the boundary, while a courser grid is adequate in the outer part of the boundary layer. Thus, a tradeoff exists between resolution and computational efficiency. To help maintain the necessary degree of resolution in both regions, a logarithmic transformation is employed so that a new non-dimensional coordinate may be formed,

$$\theta \equiv \ln \frac{z}{z_0} \tag{3.106}$$

with a corresponding differential,

$$\begin{aligned} d\theta &= \frac{dz}{z} \\ &= \frac{dz}{z_0 e^\theta} \end{aligned} \tag{3.107}$$

In the transformed coordinate system, the vertical spacing of the grid can remain uniform and still maintain adequate resolution throughout the boundary layer. Using (3.97) for the suspended sediment concentration, the stability parameter in the transformed coordinate system is

$$\begin{aligned}
\frac{z_0 e^\theta}{L} &= \frac{\kappa z_0 e^\theta}{u_{cw}^3} \sum_{n=1}^N g(s_n - 1) w_{f_n} C_{nm}(0) \cdot \\
&\quad e^{\frac{-\gamma w_{f_n} \theta}{\kappa u_{cw}}} \exp \left[ \frac{-\beta w_{f_n} z_0}{\kappa u_{cw}} \int_0^\theta \frac{e^\theta}{L} d\theta \right] \quad 0 \leq \theta \leq \theta_1 \\
\frac{z_0 e^\theta}{L} &= \frac{\kappa z_0 e^\theta}{u_k^3} \sum_{n=1}^N g(s_n - 1) w_{f_n} C_{nm}(\theta_1) \cdot \\
&\quad e^{\frac{-\gamma w_{f_n}}{\kappa u_{cw}} [e^{(\theta - \theta_1)} - 1]} \exp \left[ \frac{-\beta w_{f_n} z_0}{\kappa u_{cw} e^{\theta_1}} \int_{\theta_1}^\theta \frac{e^{2\theta}}{L} d\theta \right] \quad \theta_1 \leq \theta \leq \theta_2 \\
\frac{z_0 e^\theta}{L} &= \frac{\kappa z_0 e^\theta}{u_c^3} \sum_{n=1}^N g(s_n - 1) w_{f_n} C_{nm}(\theta_2) \cdot \\
&\quad e^{\frac{-\gamma w_{f_n} (\theta - \theta_2)}{\kappa u_c}} \exp \left[ \frac{-\beta w_{f_n} z_0}{\kappa u_c} \int_{\theta_2}^\theta \frac{e^\theta}{L} d\theta \right] \quad \theta_2 \leq \theta
\end{aligned} \tag{3.108}$$

where,  $\theta_1 = \ln(z_1/z_0)$  and  $\theta_2 = \ln(z_2/z_0)$ . Inspection of (3.108) reveals the equation governing the stability parameter is transcendental, justifying the need for a numerical solution.

For this study, the stability parameter is approximated using Chebyshev polynomials. These functions are chosen because they possess desirable error and

convergent properties, are easily discretized for numerical computation, are orthogonal, and admit continuous solutions (Atkinson 1989). For convergence and error, the Chebyshev polynomial approximation is closely related to the minimax approximation (Atkinson 1989) which, for a general polynomial of degree  $n$ , has the lowest maximum error for all approximating polynomials of degree less than or equal to  $n$ . Also, due to the equal oscillation theorem (see Atkinson 1989 p.224) the error is evenly distributed over the entire interval so that the approximation is more or less uniformly accurate throughout the domain. The Chebyshev polynomials also are easy to compute, in that each higher order polynomial can be written recursively as a function of lower order terms, i.e.,

$$T_{n+1}(x) = 2xT_n(x) - T_{n-1}(x) \quad (3.109)$$

where

$$T_0(x) \equiv 1 \quad T_1(x) = x \quad (3.110)$$

and  $T_n$  represents a Chebyshev polynomial of degree  $n$ . The orthogonality of the Chebyshev polynomials can be exploited to derive a method to approximate functions that are well represented by polynomials. For a general function  $g(x)$  defined on the interval  $[-1,1]$ , the Chebyshev polynomial approximation can be written discretely as

$$g(x) \approx \sum_{k=2}^M c_k T_{k-1}(x) - \frac{c_1}{2} \quad (3.111)$$

where

$$c_j = \frac{2}{M} \sum_{k=1}^M g(x_k) T_{j-1}(x_k) \quad j = 1, 2, \dots, M \quad (3.112)$$

and  $M$  is the total number of nodes in the interval  $-1 \leq x \leq 1$ . A simple linear coordinate transformation allows functions defined on arbitrary intervals ( $a \leq y \leq b$ ) to be expressed on the interval  $-1 \leq x \leq 1$ ,

$$x \equiv \frac{y - 0.5(b + a)}{0.5(b - a)} \quad (3.113)$$

where the coordinate  $x$  ranges between  $-1$  and  $1$  as  $y$  ranges between  $a$  and  $b$  (Press et al. 1986). Once the  $c_j$ 's are known, the integral is easily determined as

$$I = \int g(x) dx \approx \sum_{k=1}^M C_k T_{k-1}(x) \quad (3.114)$$

where

$$C_k = \frac{c_{k-1} - c_{k+1}}{2(k-1)} \quad (k > 1) \quad (3.115)$$

and  $C_1$  is an arbitrary constant of integration in (3.114).

Because the Chebyshev polynomial approximation does not require discretization of the function  $g(x)$ , a numerical grid in the formal sense is not required. This suggests that the added expense of employing a logarithmic coordinate transformation is

unnecessary. A test between both methods, however, showed that to obtain the same level of accuracy using either coordinate system, the total number of nodes  $M$  in the  $\theta$  coordinate system was much less than in the  $z$  coordinate system. Since the procedure to determine the  $c_j$ 's requires  $M^2$  operations, employing the coordinate transformation is computationally more efficient.

Application of the Chebyshev approximation procedure discussed here requires values of the stability parameter at discrete locations throughout the range of the boundary layer. Because  $e^\theta/L$  is initially unknown, an iterative procedure is employed to obtain the values at the discrete points. The iterative scheme is initiated by setting the stability parameter equal to zero ( $z/L = z_0 e^\theta/L = 0$ ), giving the concentration profile for a neutral boundary layer. The resulting concentration profile is substituted into (3.108) to determine an initial guess for  $e^\theta/L$ . These expressions are then integrated within their respective layers using (3.114) and (3.115) to give an estimate of the integral terms in (3.97). With a non-zero value for the integral terms, the suspended sediment concentration profile can be obtained from (3.97), which when inserted back into (3.108) gives an updated value for the stability parameter. The procedure is repeated until the stability parameter profile converges. Convergence is assumed when the absolute value of the difference between the present and previous iterate divided by the present iterate is less than 0.1% at all nodes.

### 3.5.1 Stability parameter convergence tests

Although the Chebyshev approximation is often a very accurate and robust numerical procedure for approximating functions, it can be computationally expensive. As previously mentioned, the procedure requires  $M^2$  operations, which rapidly increases

CPU run-time as the number of nodes are increased. Other methods, such as the trapezoidal method require only  $M$  operations, but are usually less accurate for a given number of nodes. Therefore, a comparison between these two methods provides a way to gauge the computationally expensive Chebyshev approximation in terms of the less accurate though efficient trapezoidal method. To encompass some of the possible ranges of the stability parameter, three wave and current configurations are chosen: high wave with low current, medium wave with medium current, and low wave with high current. Relevant input wave and current parameters are shown in Table 3.1. The relative

Table 3.1 List of input values for stability parameter convergence tests. Categories correspond to simulated low, medium and high wave conditions.

	$z_0$ (cm)	$z_1$ (cm)	$u_{*c}$ (cm/s)	$u_{*cw}$ (cm/s)	$u_{*cw}/u_{*c}$
Low wave	0.5	2.0	5.00	5.2	1.0
Med. wave	1.0	4.0	2.36	5.0	2.1
High wave	1.5	6.0	1.00	8.0	8.0

strength of the current and wave is measured in terms of the ratio  $u_{*cw}/u_{*c}$  shown in the last column of the table. When this ratio is large, the total shear stress is primarily associated with the wave. When this ratio is small, the total shear stress is primarily associated with the current. In addition, sediment input parameters are defined by a single grain size class of 0.01 cm with a reference concentration of  $C_m(z_0) = 1.0 \times 10^{-3}$  and density 2.65 gm/cm<sup>3</sup>. Figure 3.5 shows the three stability parameter profiles representing the three wave cases using the values listed in Table 3.1 as input. Also



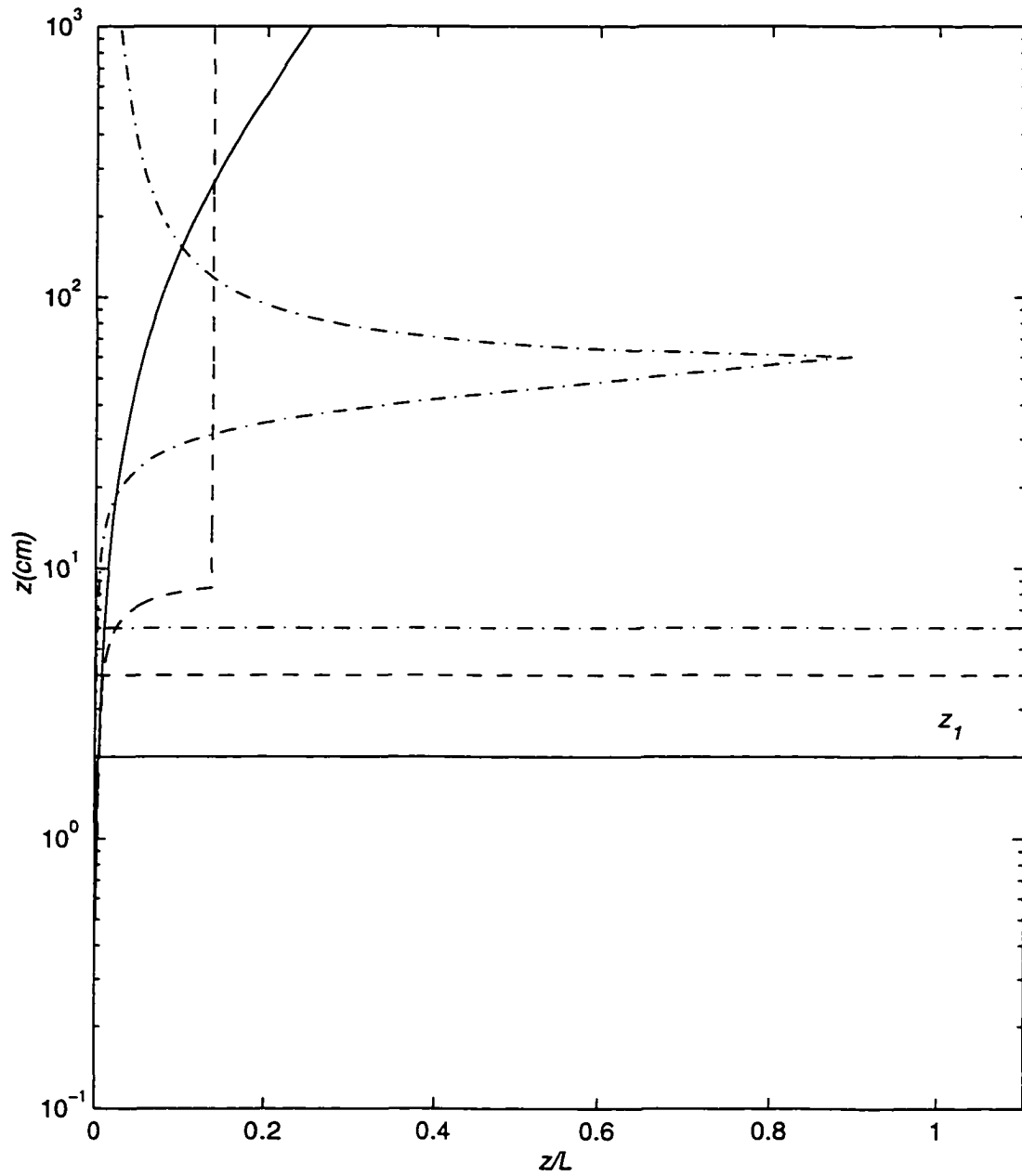


Figure 3.5 Vertical profiles of the stability parameter for the three wave and current scenarios representing low (solid), medium (dash) and high (dash/dot) wave cases. Also shown is the height  $z_1$  for each of the three cases.

shown, for reference, is the height  $z_1$ . For the low wave case,  $z/L$  is small near the bed, but then monotonically increases throughout the outer boundary layer. The stability parameter for the medium wave case also is small below  $z_1$  but then rapidly increases to about 0.18 at 8 cm, where it remains constant with height. For the high wave case, the stability parameter is, again, small below  $z_1$  but then rapidly increases to about 0.9 at 60 cm, and then monotonically decreases toward the top. In all three cases, the assumption that  $z/L$  is small in the lower and middle wave boundary layer ( $z \leq z_1$ ) is clearly seen. This is consistent with the present theory where the periodic concentration and stratification correction in the stability parameter and wave stress, respectively, have been neglected. In addition, for  $z \gg z_1$ , which more or less corresponds to outside the wave boundary layer, all three profiles exhibit the same asymptotic behavior predicted by GG for similar low, medium and high wave scenarios.

Reference stability parameter profiles calculated using the Chebyshev polynomial approximation with  $M = 2000$  form a basis from which the error for both methods are gauged. Defining the difference between profiles constructed with  $N$  nodes and the reference profile as

$$\epsilon_{N_i} = \left| \frac{z_i}{L(z_i)} \right|_N - \left| \frac{z_i}{L(z_i)} \right|_M \quad i = 1, \dots, \bar{N} \quad (3.116)$$

at selected node points  $i$ , gives a measure of the relative error as a function of the number of nodes. The overbar on  $N$  denotes that the total number of evaluation points does not necessarily coincide with the total number of nodes. For a given node density, the maximum error over a profile is defined as

$$\varepsilon_N = \text{Max}_{i=1, \dots, \bar{N}} \left( \varepsilon_{N_i} \right) \quad (3.117)$$

The number of nodes are systematically increased to provide a tangible measure of the relative error between the two integration methods. An acceptable error is assumed when  $\varepsilon_N \leq 1.0 \times 10^{-3}$  (0.1%). Figure 3.6(a) depicts the error for the high wave case calculated using the Chebyshev approximation with various node densities. To provide adequate coverage over the domain,  $\bar{N} = 3000$  for all Chebyshev error tests. For  $N = 200$ , it is seen that the maximum error is approximately  $1.8 \times 10^{-3}$ . As expected, the error decreases with increasing node density. Figure 3.6(b) shows the trapezoidal integration method for the same wave and current case. Because the trapezoidal method is a discrete approximation, the function is defined only at the node points, which gives  $\bar{N} = N$ . The most striking feature is the greater number of nodes required to obtain equivalent error as the Chebyshev approximation, where a maximum error of  $\sim 1.0 \times 10^{-3}$  requires 40,000 nodes. Figure 3.7 depicts the stability parameter errors for the medium wave case. The Chebyshev approximation again shows rapid decrease in  $\varepsilon_N$  as the number of nodes are doubled. Interestingly, to obtain equivalent error as the high wave case requires many fewer nodes. Also, the oscillation of the error associated with the Chebyshev approximation previously mentioned is clearly illustrated. The trapezoidal method also requires fewer nodes, where setting  $N = 500$  produces a maximum error of about  $0.95 \times 10^{-3}$ . Finally, Figure 3.8 shows  $\varepsilon_{N_i}$  for the low wave with high current case. For both methods the number of nodes required to obtain comparable accuracy is very small compared to the previous two cases.

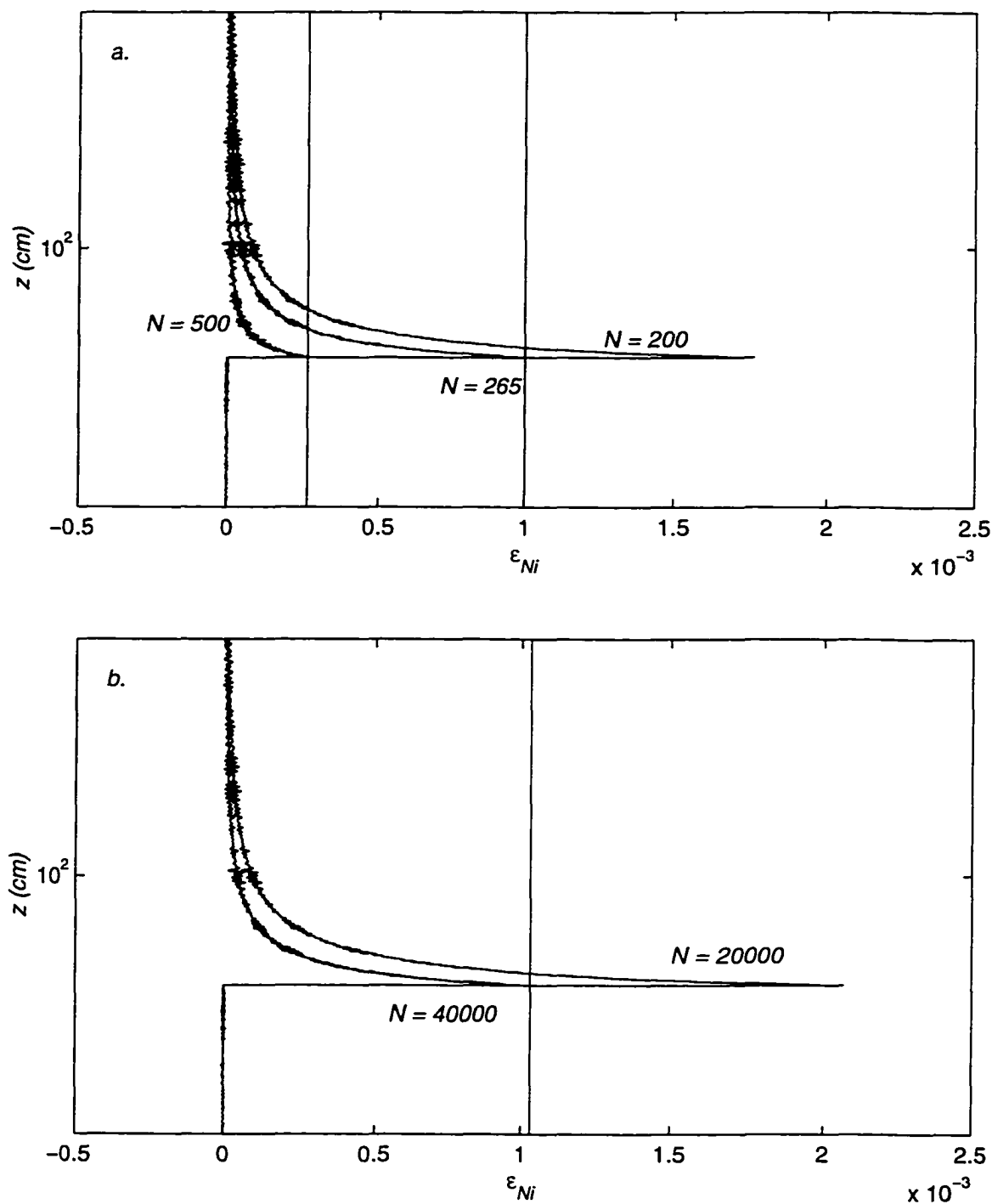


Figure 3.6 Vertical profiles of the stability parameter error,  $\epsilon_{Ni}$ , for the high wave case. (a) error for the Chebyshev method and (b) error for the trapezoidal method. Vertical lines indicate maximum error for nodes,  $N$ , indicated. Note the large number of nodes required in the trapezoidal method to obtain comparable accuracy as the Chebyshev approximation.

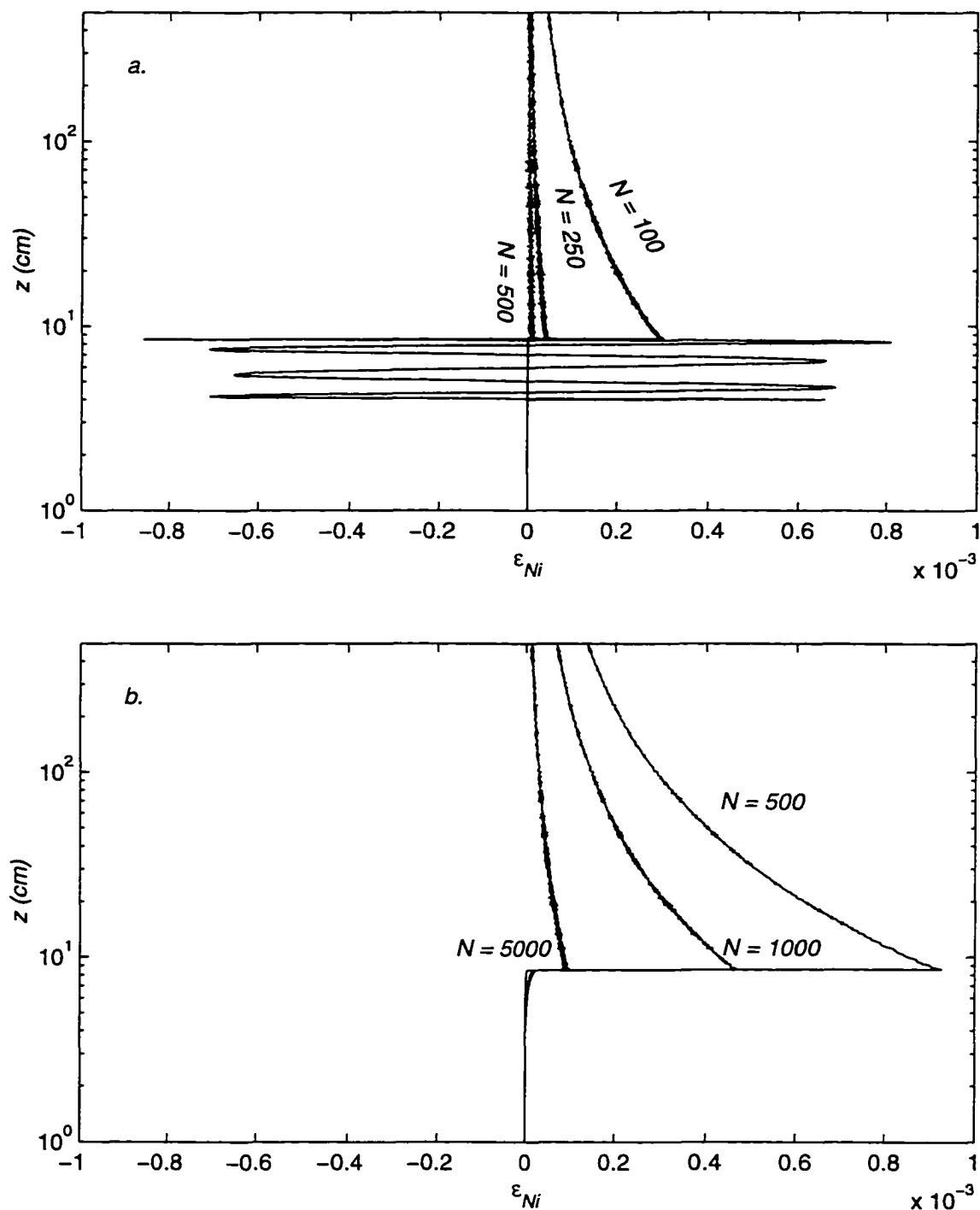


Figure 3.7 Same as Figure 3.6 showing the error for the medium wave case. Note the oscillation of the error for the Chebyshev approximation which is more or less evenly distributed over the range  $z_1 < z < z_2$ .

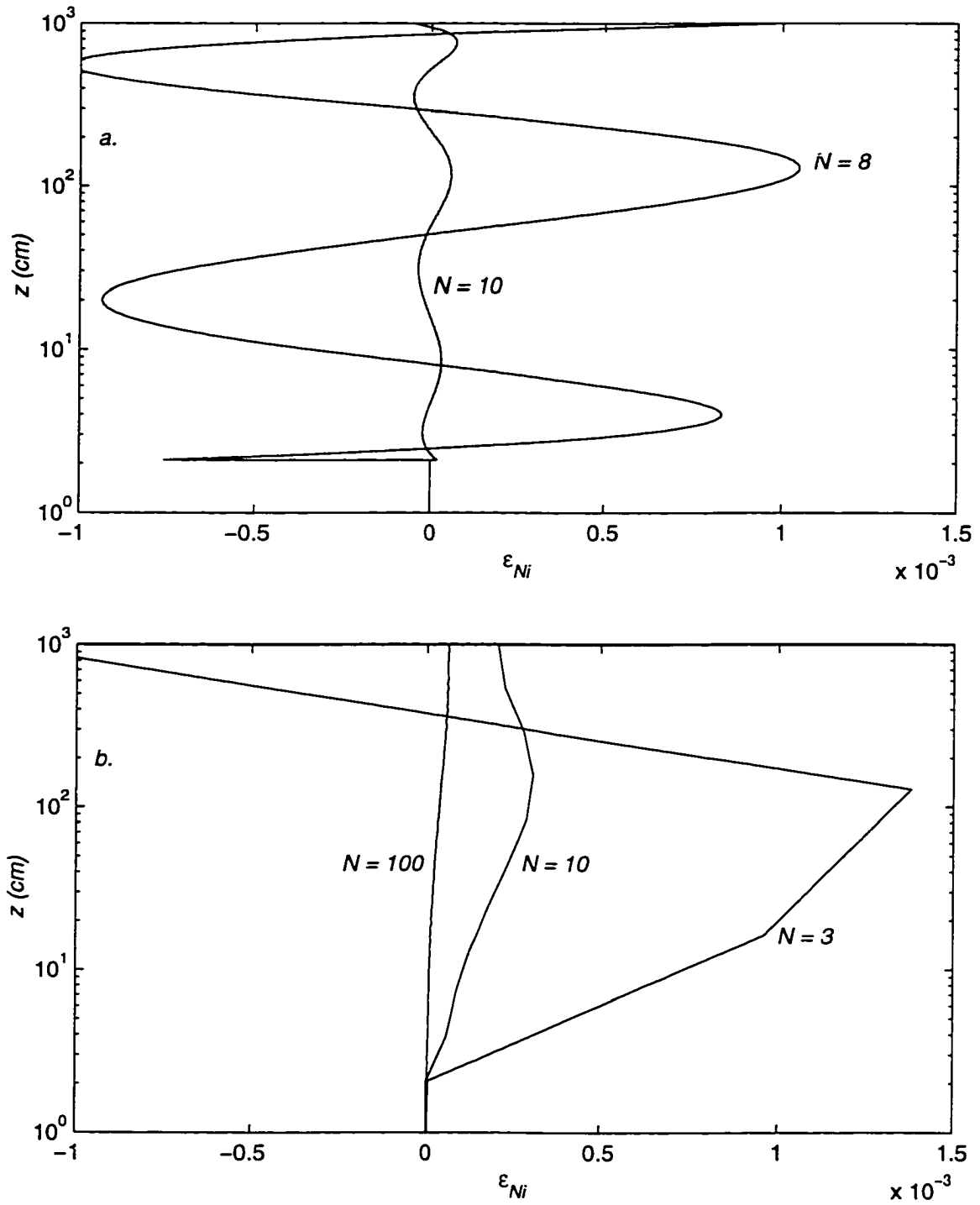


Figure 3.8 Same as Figure 3.6 showing the error for the low wave case. Upper panel shows Chebyshev approximation and lower panel shows the trapezoidal method. Compared to the high wave case the total number of nodes,  $N$ , required to obtain equivalent error for either method is much less.

For the high wave case, the trapezoidal method required 40,000 nodes to obtain the same level of accuracy as 280 nodes for the Chebyshev approximation. For many flows of interest on storm dominated continental shelves, it is expected that the high wave case will be the situation most realized. In addition, one of the applications is to couple the bottom boundary layer model (BBLM) to shelf circulation models. Under these circumstances efficiency is a major concern. Figure 3.9 shows normalized computer run time as a function of maximum error for the high wave case. At the 0.1% error level ( $\epsilon_N = 1.0 \times 10^{-3}$ ), the Chebyshev approximation converges nearly 5 times as fast as the trapezoidal method. This time difference rapidly increases as error thresholds become more stringent. For the other two cases the computer run time was over an order of magnitude faster than for the high wave case for equivalent error thresholds. As a result, the run time for these cases are negligible in comparison to the high wave case, so that efficiency is best gauged by the high wave model simulations. The results presented here confirm that the Chebyshev approximation is the better overall choice for these applications.

### 3.6 Solution procedure for the mean current and concentration

The solution for the current, and the mean suspended sediment concentration for a stably stratified bottom boundary layer can now be completely specified given the following set of input variables:  $C_{nm}(z_0)$ ,  $u_{*c}$ ,  $k_b$ ,  $A_b$ ,  $u_b$  and  $\phi_{cw}$ . Because application of this model for the continental shelf requires measurements of the near-bottom flow field to obtain the wave parameters, it is often more convenient to prescribe the mean current  $u_r$  at a known height above the bed,  $z_r$ , which, for computational purposes, is equivalent to specifying  $u_{*c}$ . With this substitution, the input variables now become

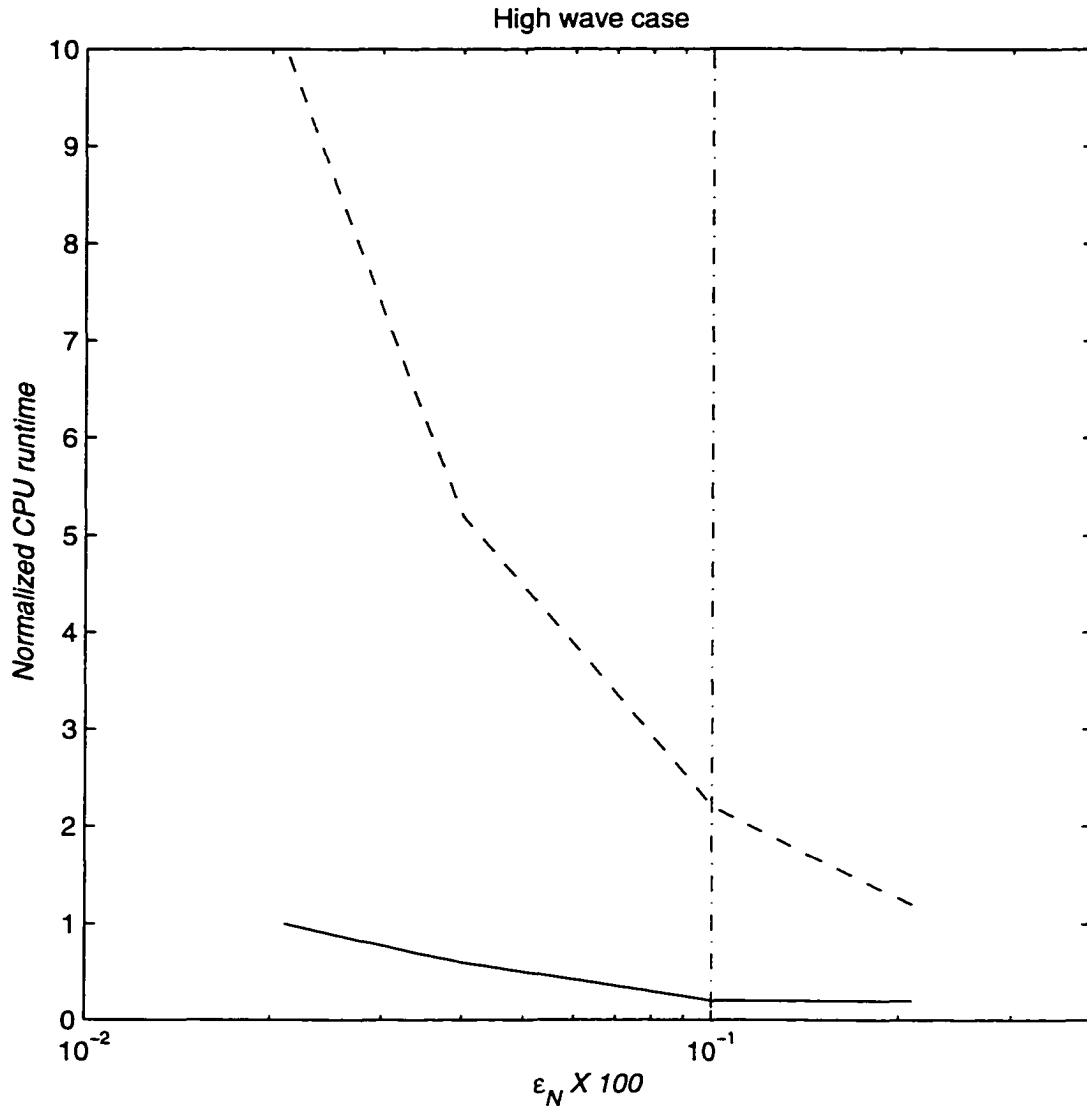


Figure 3.9 Normalized CPU runtime as a function of stability parameter maximum error,  $\epsilon_N$ , for the Chebyshev approximation (solid) and the trapezoidal method (dash). Vertical line indicates 0.1% error. Error is reduced by increasing the number of nodes, which increases computing time. Compared to the Chebyshev approximation, error associated with the trapezoidal method decreases at a much slower rate.



$C_{nm}(z_0)$ ,  $u_r$ ,  $z_r$ ,  $k_b$ ,  $A_b$ ,  $u_b$  and  $\phi_{cw}$ , all of which are measurable by a single, high-frequency current meter/pressure sensor combination except for the boundary values  $k_b$  and  $C_{nm}(z_0)$ . Given these boundary values from other sources, the solution for the coupled boundary layer equations is now presented.

The first step is to assign initial "guess" estimates for  $u_{*c}$  and  $u_{*cw}$ , and set  $C_R = 1$ . For conditions typically encountered in this study, a good initial guess is to set the ratio  $u_{*cw}/u_{*c} = 5$  and  $u_{*c} = 1$ . With these variables defined, the stability parameter profile is calculated using the procedures described above. Once the stability parameter is known,  $\xi_0$  is defined using the initial  $u_{*cw}$  through (3.82), and  $\xi_1$  and  $\xi_2$  are determined from  $\alpha$  and  $\epsilon$ , where  $\alpha$  is presumed known, and  $\epsilon = u_{*cw}/u_{*c}$ . The non-dimensional heights  $\xi_0$ ,  $\xi_1$  and  $\xi_2$  along with  $\epsilon$  are substituted into  $\Gamma_w$ , which is solved using the polynomial approximations of the Kelvin functions given by Abramowitz and Stegun (1964). Once  $\Gamma_w$  is known,  $f_w$  is determined from (3.81), which in turn is used to estimate  $u_{*wm}$  through (3.71) and update  $C_R$  and  $u_{*cw}$  through (3.69) and (3.68), respectively. The shear stresses, along with the stability parameter,  $z_r$  and the initial guess value of  $u_{*c}$ , are inserted into (3.95) to determine  $u_r$ . If the initial guess value for  $u_{*c}$  does not lead to the correct value of  $u_r$ , then the entire procedure is repeated with a new  $u_{*c}$  until the calculated current equals  $u_r$ . Because it is not possible to obtain an algebraic expression for  $u_{*c}$  using (3.95), the solution must be determined iteratively. For this study, the secant method is chosen because it is easy to implement and is rapidly convergent for many nonlinear problems if the initial "guess" is close to the actual value.

### 3.7 Theoretical model comparisons

The GG model is chosen for the comparison study because it uses a similar turbulence closure scheme and includes a stability parameter to parameterize the effects of suspended sediment-induced stratification. The major differences between the two models are the eddy viscosity formulation and the vertical range of the stability parameter, where GG use the Grant and Madsen (1979) two-layer discontinuous eddy viscosity and neglect the stability parameter in the wave boundary layer. To illustrate the differences resulting from these two modeling approaches, the comparisons will primarily focus on the predicted stability parameter, current, sediment concentration and sediment transport profiles. The input variables are listed in Table 3.2 and are representative of the high wave case previously discussed. The free parameter  $\alpha$ , which regulates the height  $z_1$ , is allowed to vary since it is the least well known of all independent model parameters. The grain diameter is set equal to 0.04 *cm*.

Figure 3.10(a) shows the stability parameters calculated from the GG model and the BBLM, or 3-layer model, as a function of height off the bed. Also shown are  $z_2$  and, for comparison,  $\delta_w$  as calculated by the GG model. The GG stability parameter is maximum at  $\delta_w$  and then monotonically decreases throughout the upper boundary layer. This is the same general behavior shown in Figure 3.5 for the high wave case. The stability parameters calculated from the 3-layer model are small near the bed, and then peak at  $z_2$  for  $\alpha = 0.15$  and 0.5, and just below  $z_2$  for  $\alpha = 1.0$ . Above  $z_2$ , all three rapidly decay throughout the upper boundary layer. The peak identified by  $\alpha = 1.0$  is smooth, while the peak for the other two values of  $\alpha$  are kinked. Inspection of Figure 3.4 shows that the kinematic flux (3.104) has a strong kink at  $z_2$  for  $\alpha = 0.15$  and 0.5.

Table 3.2 Input parameters for theoretical model comparisons.

Parameter	Value
<i>Wave</i>	
$A_b, cm$	119
$u_b, cm/s$	64
<i>Current</i>	
$u_r, cm/s$	23
$z_r, cm$	238
$\phi_{cw}, deg$	56
<i>Sediment/Fluid</i>	
$\rho_s, g/cm^3$	2.65
$\rho, g/cm^3$	1
$g, cm/s^2$	981
$w_f, cm/s$	7.142
$k_b, cm$	30.0
$C_{nm}(z_0)$	0.003
$c_b$	0.65

For  $\alpha = 1.0$ , (3.104) smoothly approaches  $u_{*c}^2$  as  $z \rightarrow z_2$ . This is reflected in the stability parameter profiles depicted in Figure 3.10(a), where the kink is most pronounced for the profiles associated with the lower two values of  $\alpha$ . All three profiles show similar peak magnitudes which shift according to changes in  $\alpha$ . For  $\alpha = 0.5$ , the point  $z_2$  compares reasonably well with  $\delta_w$  calculated from the GG model. This is the same value suggested by Madsen and Wikramanayake (1991) for the neutral version of (3.95) that they compared to laboratory flow data. The large difference in peak values is attributed to the assumption on the part of GG concerning the applicable range of the stability parameter and to the different eddy viscosity configurations.

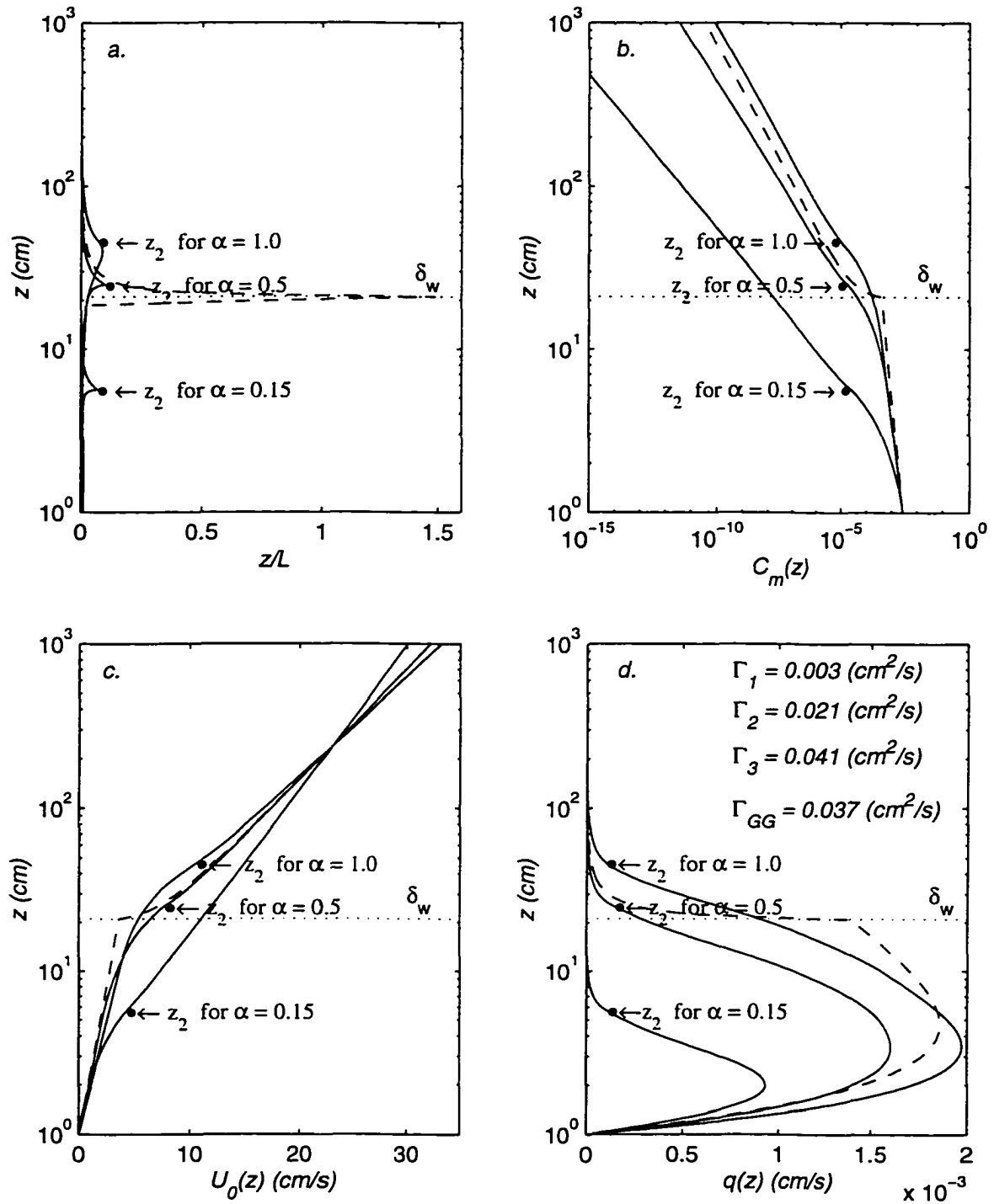


Figure 3.10 Sensitivity of calculated model parameters to changes in  $\alpha$ . (a) stability parameter, (b) suspended sediment concentration, (c) mean current and (d) sediment transport. Also shown are equivalent parameters calculated from the GG model (dash), including  $\delta_w$  for comparison.  $\Gamma$  is the depth-integrated sediment flux defined in (3.121). Numbers correspond, in increasing value, to  $\alpha = 0.15, 0.5$  and  $1.0$ .

GG chose to neglect the stability parameter in the wave boundary layer based on a systematic scaling analysis that showed  $z/L$  was at most  $O(10^{-2})$  for typical storm conditions expected in the field. Using these same arguments, order of magnitude estimates for the stability parameter in the 3-layer model are calculated, and results compared to GG. Below  $z_1$ , the two models are identical so that the scaling results obtained by GG, which show that  $z/L$  is small and can be neglected, apply equally well to the 3-layer model. For  $z_1 < z < z_2$  the stability parameter is found by inserting (3.97) into (3.105), giving

$$\frac{z}{L} = \frac{\kappa z}{u_{*k}^3} \sum_{n=1}^N g(s_n - 1) w_{f_n} C_{nm}(z_1) e^{\frac{-\gamma w_{f_n} (z - z_1)}{\kappa z_1 u_{*cw}}} \cdot \exp \left[ \frac{-\beta w_{f_n}}{\kappa u_{*cw} z_1} \int_{z_1}^z \frac{z}{L} dz \right] \quad (3.118)$$

Inspection of (3.118) shows that the vertical dependence is controlled by a production related term  $(u_{*k}^3/\kappa z)$  and two exponential terms. Regardless of the value of the production related term, the effect of the exponential functions is to cause the stability parameter to decrease with increasing  $z$ . Because the interest is to obtain an upper bound on  $z/L$ , the arguments of the exponential terms are set equal to 0. This defines the maximum stability parameter,

$$\left. \frac{z}{L} \right|_{\max} \equiv \frac{\kappa z}{u_{*k}^3} g(s - 1) w_f C_m(z_1) \quad z_1 \leq z \leq z_2 \quad (3.119)$$

where only one grain size class has been assumed to simplify the discussion. In their scaling analysis, GG adopt values of  $\kappa = 0.4$ ,  $z_0 = 0.1 \text{ cm}$ ,  $g = 980 \text{ cm/s}^2$ ,  $u_{*cw} = 5.0 \text{ cm/s}$ ,  $s = 2.65$ ,  $w_f = 1 \text{ cm/s}$  and  $C_m(z_0) = 1.0 \times 10^{-3}$ . In addition, typical values for the following variables must be defined for the 3-layer model:  $u_{*c} = 1.0 \text{ cm/s}$ ,  $\gamma = 0.74$ ,  $\alpha = 0.5$  and  $z_1 = 2.5 \text{ cm}$ . Inserting these values into (3.97) gives a suspended sediment concentration at  $z = z_1$ , of  $C_m(z_1) = 3.04 \times 10^{-4}$ . With (3.119), this translates to a stability parameter estimate of  $z_1/L = 3.9 \times 10^{-3}$ , which is similar in magnitude to GG who showed that  $z/L$  in the wave boundary layer is small and can be neglected. At  $z = z_2 = u_{*cw}/u_{*c} z_1$ ,  $u_{*k} = u_{*c}$ , so that (3.119) gives  $z_2/L = 2.5$ . For the 3-layer model used here, the stability parameter is  $O(1)$  for  $z_1 < z < z_2$  and, unlike GG, cannot be neglected in the outer wave boundary layer.

The order of magnitude differences in the outer wave boundary layer are a direct result of the two approaches to modeling the effects of turbulence. GG model their production related term in the stability parameter after the 2-layer discontinuous eddy viscosity, which assumes that  $u_{*cw}$  is the proper velocity scale for the kinematic flux for  $z \leq \delta_w$ . At  $z = z_2 \approx \delta_w$ , the production related term in the GG model is  $(u_{*cw}^3/\kappa\delta_w)$ . For  $z \geq z_2 \approx \delta_w$ , the production related term is  $u_{*c}^3/\kappa z$ , which also is in agreement with the 2-layer discontinuous eddy viscosity. By definition,  $u_{*c} < u_{*cw}$  which means that the production related term in the GG model is discontinuous at  $\delta_w$ . As  $u_{*cw} \gg u_{*c}$  the discontinuity in the GG production related term will lead to a correspondingly large discontinuity in the stability parameter. This is illustrated for the high wave case depicted in Figure 3.10(a), where the strong discontinuity at  $\delta_w$  is clearly indicated. For the 3-layer model, (3.104) is used to ensure continuity in the production related term by

forcing the velocity scale,  $u_* \rightarrow u_{*c}$  as  $z \rightarrow z_2$ . At  $z_2$ , the production related term for the 3-layer model is not discontinuous due to the imposed requirement that  $u_{*c}$  be the characteristic velocity scale at  $z_2$ . Thus, modeling the stability parameter after the eddy viscosity, as was done by GG, leads to a discontinuity at  $z = z_2 \approx \delta_w$ , but produces a scaling that ensures  $z/L$  is small and can be neglected. Keeping in the spirit of a continuous eddy viscosity, the stability parameter in the 3-layer model is forced to remain continuous throughout the boundary layer. This procedure leads to scaling arguments that show  $z/L$  is not small for the current in the outer wave boundary layer and, therefore, cannot be neglected.

The sensitivity of the stability parameter to  $\alpha$  is equally apparent in the concentration profiles. Figure 3.10(b) shows mean suspended sediment concentration,  $C_m(z)$ , corresponding to the stability parameters and  $\alpha$  values depicted in Figure 3.10(a). Within the lower section of the wave boundary layer, where  $z/L$  for both models is small, the concentration profiles are similar, but then begin to diverge as a function of  $\alpha$ . For  $\alpha = 0.15$ , the predicted concentration values at  $z_2$  are separated by two orders of magnitude. At  $\delta_w$ , this difference is over four orders of magnitude. For the three  $\alpha$ 's chosen, the 3-layer model is in closest agreement to the GG model for  $\alpha = 0.5$ . Also noticeable is the artificial kink at  $\delta_w$  in the GG model. This kink is a result of the discontinuous eddy viscosity and rationalizes the decision to adopt a more realistic continuous eddy viscosity.

The effect of altering the cutoff for  $z_1$  is equally apparent in the current profiles, where, for the three chosen values of  $\alpha$ , setting  $\alpha = 0.5$  leads to the best overall comparison between the two models (Figure 3.10c). The artificial kink again is clearly

indicated. At points very near and very far away from the bed, the two models give similar current speeds, indicating that model sensitivity to changes in  $\alpha$  in these two regions is relatively weak. In the middle region, ( $3 \text{ cm} \leq z \leq 100 \text{ cm}$ ) which roughly corresponds to the outer wave boundary layer and lower current boundary layer, the current profiles are most sensitive to changes in  $\alpha$ . For example, the current speed predicted by the GG model at  $z = \delta_w$  is only half the value obtained using the BBLM for  $\alpha = 0.15$ . Because it is expected that most of the suspended load is carried within the wave boundary layer or just above, accurate estimates of both the concentration and the current in this middle region are important for sediment transport studies. To illustrate this point, Figure 3.10(d) shows the sediment transport,  $q(z)$ , which is defined as the product of the suspended sediment concentration and velocity at a given level,

$$q(z) = C_m(z) U_0(z) \quad (3.120)$$

Like the current and concentration, the transport is heavily dependent on the parameter  $\alpha$ , with peak sediment transport increasing with increasing  $\alpha$ . Furthermore, nearly all the transport in this case is confined to the wave boundary layer where the effects of wave/current interaction are most prevalent. Also shown in the upper right quadrant of Figure 3.10(d) is the depth-integrated sediment transport defined as

$$\Gamma = \int_{z_0}^h q(z) dz \quad (3.121)$$

Like the transport,  $\Gamma$  increases with increasing  $\alpha$ .



The previous discussion has demonstrated that the BBLM is sensitive to changes in the parameter  $\alpha$ . Although a range of values have been reported, Madsen and Wikramanayake (1991) suggest that  $\alpha \approx 0.5$  based on current observations in the presence of waves. This value is also shown to give good agreement with the GG model. The fact that the Madsen and Wikramanayake (1991) data are derived exclusively from flume experiments, however, does not unequivocally establish  $\alpha$  for use with a model primarily designed to simulate continental shelf boundary layer flows.

### **3.8 Influence of multiple sediment grain size classes**

The seemingly small influence of the stratification correction, as seen in the small values for the stability parameter, is a consequence of the choice of sediment grain size class and input wave and current parameters. For the given high wave conditions, model runs using both a smaller sized grains and multiple grain size classes are presented to examine how these changes affect the stratified solution.

#### **3.8.1 Effect of reducing particle size**

For the first case, the parameter  $\alpha$  is allowed to vary using the same values presented in the comparison with the GG model. The grain size is reduced from 0.04 *cm* to 0.01 *cm*, and the input wave and current parameters remain the same as those listed in Table 3.2. Figure 3.11(a) shows the stability parameter with  $d = 0.01$  *cm*. The peak magnitude is an order of magnitude greater than for the 0.04 *cm* grains (Figure 3.10a). With all other parameters left unchanged, a reduction in grain size is seen to lead to order of magnitude changes in  $z/L$ . This is a testament to the sensitivity of the solution to particle size. The smaller grain sizes have a lower settling velocity which causes a weaker decay in concentration with height. This leads, on average, to higher

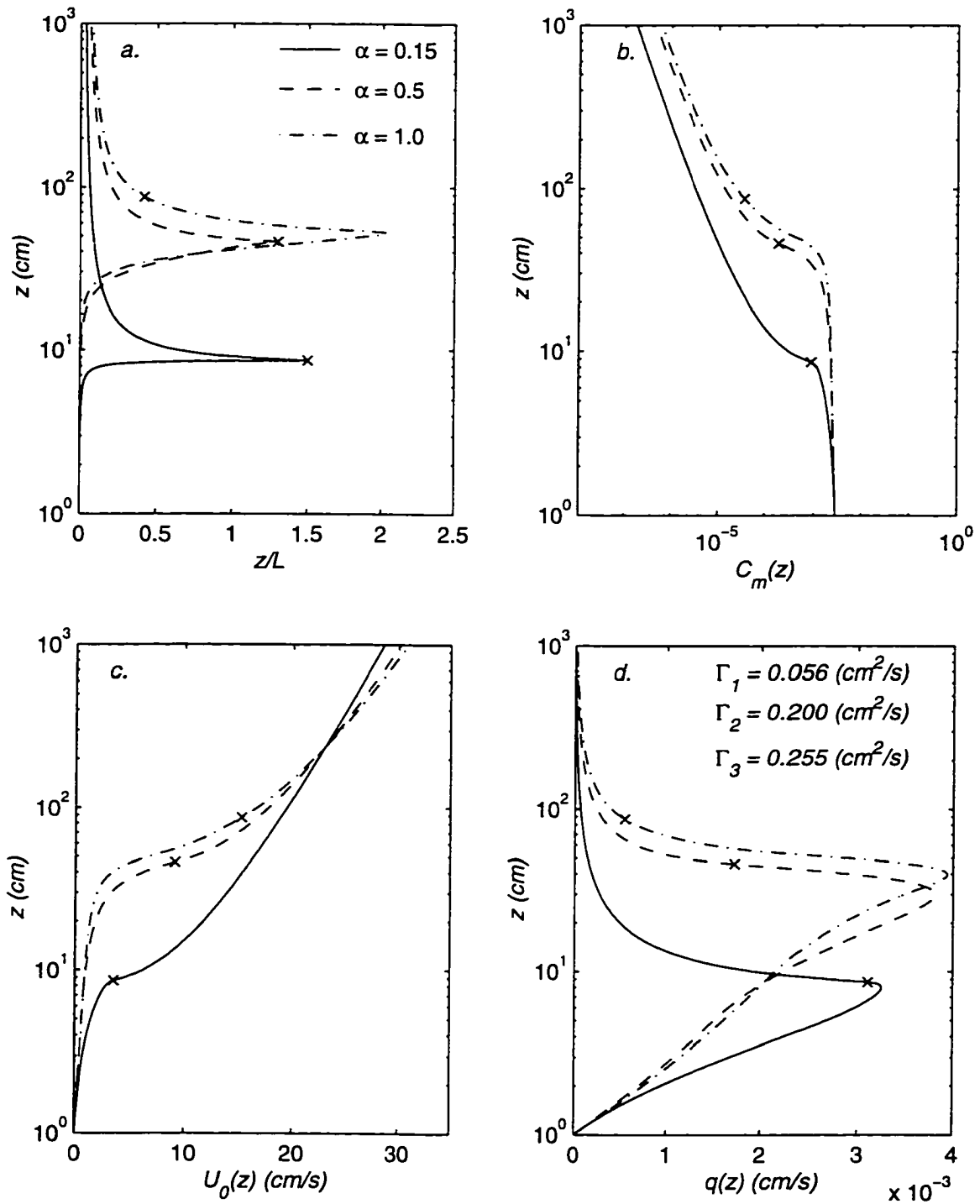


Figure 3.11 Same as Figure 3.10 but with a grain size of 0.01 cm. X's mark the height  $z_2$  for each value of  $\alpha$ .

concentrations in the lower water column and a correspondingly greater potential for a large buoyancy flux near the top of the wave boundary layer where production of turbulence kinetic energy is rapidly decreasing. In contrast, the larger grains are not mixed as high into the water column so that concentrations at  $\delta_w$  are generally too weak to produce a large buoyancy flux. This is illustrated in Figure 3.11(b) where the concentrations at  $z = 20 \text{ cm}$ , when  $d = 0.01 \text{ cm}$ , are an order of magnitude greater than in Figure 3.10(b), when  $d = 0.04 \text{ cm}$ .

The effect of the larger stability parameter associated with the smaller grain size is evident in the concentration profiles shown in Figure 3.11(b). For  $z$  less than the height associated with the stability parameter peak, the concentrations do not significantly depart from the log-log variation with height attributed to the neutral model. At a height consistent with the increase in the stability parameter, the concentrations start to show curvature away from this log-log behavior. The distortion is related to the integral terms in (3.97), which alter the vertical variation of the concentration from the strictly Rouse-like profile associated with the neutral model. The distortion is greatest at a height consistent with the stability parameter peak. Higher in the water column, where the stability parameter rapidly decreases, the concentrations begin to appear linear when drawn on a log-log axis. The height at which stratification becomes important is similarly related to  $\alpha$ , where lower  $\alpha$  causes the rapid drop off in concentration to occur lower in the water column. Because the vertical decay rate in the upper water column for all three values of  $\alpha$  is essentially the same, the overall concentration for  $\alpha = 0.15$  will always be less than the other two cases.

The effect of the larger stability parameter on the mean current is illustrated in Figure 3.11(c). Again for points below the stability parameter peak the current does not depart significantly from the classic logarithmic variation with height. For heights consistent with increases in the stability parameter, the current shows a definite upward curvature. This departure is a result of the stratification correction in (3.95) which distorts the neutral model from the classic logarithmic variation with height. In addition, the combined influence of the stratification correction and  $\alpha$  act to further the spread in current values in the lower water column so that at  $z = 20 \text{ cm}$  the difference in magnitude between  $\alpha = 0.15$  and  $\alpha = 1.0$  is a factor of 5 or so.

Figure 3.11(d) shows calculated sediment transport using (3.120). The larger stability parameter associated with the concentration and current profile used to calculate  $q(z)$  similarly distorts the transport shown here ( $d = 0.01 \text{ cm}$ ), from the transport depicted in Figure 3.10(d) ( $d = 0.04 \text{ cm}$ ). In the lower water column, where the stratification correction is weak, the flux rapidly increases with height as these smaller particles are more easily fluxed higher into the water column than the larger  $0.04 \text{ cm}$  grains. Because the stratification correction is not important near the bed, the peak transport values are nearly twice as high as the  $0.04 \text{ cm}$  sediment shown in Figure 3.10(d). At a height consistent with the peak in the stability parameter, the transport rapidly decays since the concentration is tapering off at a much faster rate than the current is increasing. Even though the stratification correction is more important for this case, the smaller grains are lifted higher into the water column causing a greater overall transport than the larger grains. This is illustrated in Figure 3.11(d) which shows  $\Gamma$  for corresponding  $\alpha$ . In each case,  $\Gamma$  is an order of magnitude greater than shown in Figure 3.10(d).

### 3.8.2 Effect of increasing the number of grain size classes

To further examine the stratification effect, the theoretical analysis is expanded to include multiple grain size classes. To keep the analysis relatively simple for this theoretical test, only 3 grain size classes consisting of 0.01, 0.025 and 0.04 *cm* grains are used. This range represents medium to fine sand which is expected for typical shallow continental shelves. The input parameters are the same as above, except that  $\alpha$  is set with the intermediate value of 0.5 and the reference concentration is allowed to vary between each grain size class. Assuming a near-Gaussian distribution, the middle grain size class constitutes 50% of the total reference concentration  $C_m(z_0) = 2.76 \times 10^{-3}$ , and the larger and smaller size classes each constitute 25% of the total.

Figure 3.12(a) depicts the stability parameter using the three grain size classes described above. Also shown for comparison are the heights  $z_1$  and  $z_2$ . Like Figure 3.11(a), the most obvious difference from Figure 3.10(a) is the maximum value, which is over an order of magnitude greater than the stability parameter calculated using only the 0.04 *cm* grains. In contrast, however, the value is less than half that for the single size class consisting of 0.01 *cm* grains for  $\alpha = 0.5$  shown in Figure 3.11(a). The reference concentration representing the 0.01 *cm* grains in Figure 3.12 is only 1/4 that used to calculate the stability parameter shown in Figure 3.11(a). Thus, it is seen that the stratification correction in this example is weighted by both grain diameter and reference concentration, with the smaller sized grains with the largest reference concentration producing the largest stability parameter. Like Figure 3.11, extending the number of sediment size classes to include smaller grains also significantly distorts the concentration profiles from the neutral case (Figure 3.12b). Concentration values

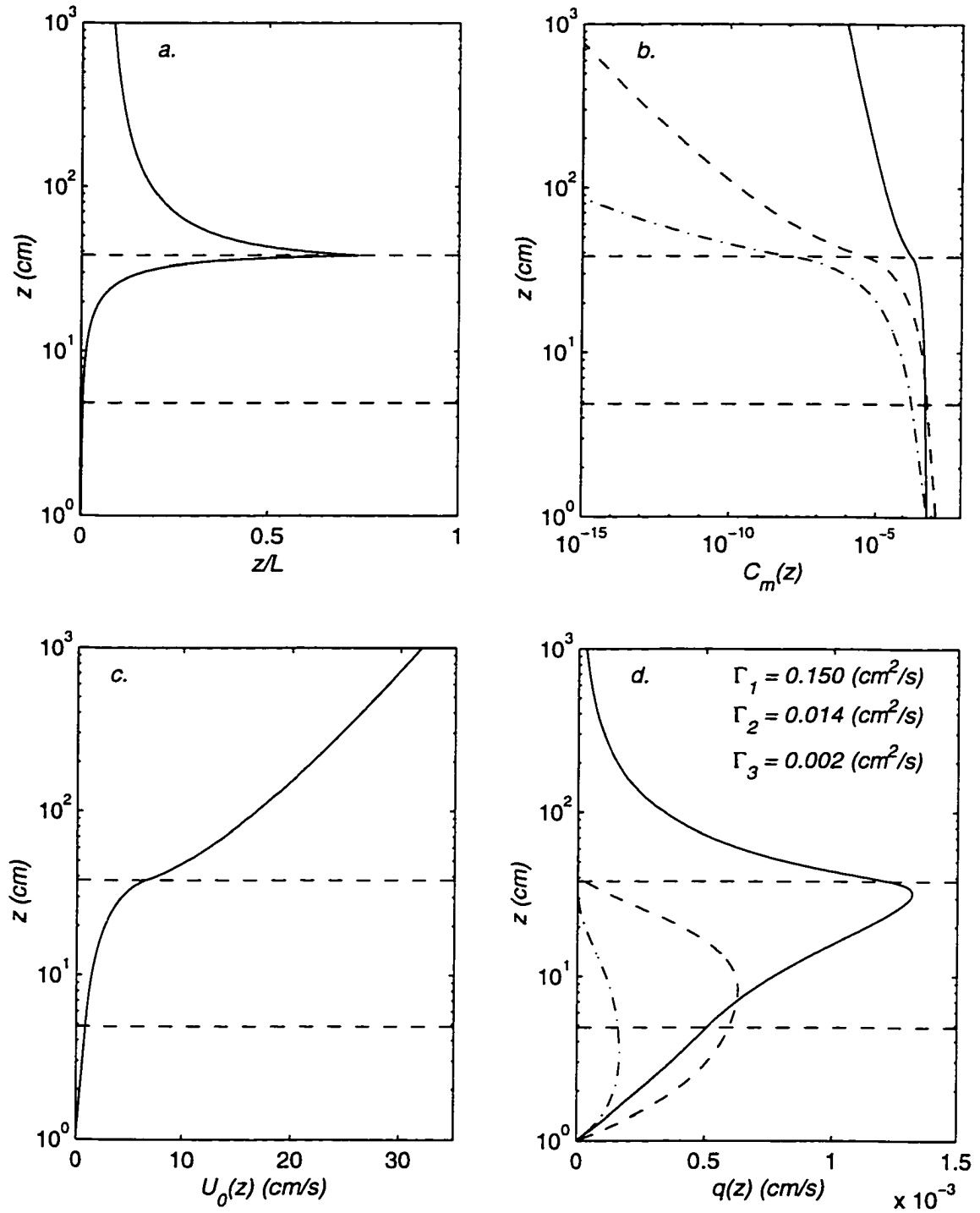


Figure 3.12 Vertical profiles of calculated model parameters using three different grain size classes consisting of  $0.01 \text{ cm}$  (solid),  $0.021 \text{ cm}$  (dashed) and  $0.04 \text{ cm}$  (dash/dot) grains. Lower horizontal dashed line marks  $z_1$  and upper dashed line marks  $z_2$ .

categorized by grain size also show a distinct divergent pattern for  $z$  greater than  $z_1$ , with values at  $z_2$  spanning over nine orders of magnitude between the largest and smallest grain size classes. The larger sediment is barely suspended above the wave boundary layer, rapidly falling out of suspension as the turbulent intensity decreases. The smallest sediment, although it starts off with a smaller concentration in the bed, is mixed more uniformly through the water column, so that above the wave boundary layer, it is the dominant size class. The effect of the stability parameter on the mean current also is illustrated in Figure 3.12(c). When plotted on a semi-logarithmic scale, the current shows an upward curvature for points greater than about  $z_2$  similar to the current shown in Figure 3.11(c). This is also a consequence of the integral terms in (3.95), which can alter the profile from the classic logarithmic variation with height.

As a final test to illustrate the effect of multiple grain size classes, Figure 3.12(d) shows the sediment transport for each of the three grain sizes. The largest sized grains show a vertical structure similar to Figure 3.10(d), and the smallest grains show a structure similar to Figure 3.11(d). For the two larger size classes, the sediment transport profiles are consistent with what would be expected, in that a balance exists between the increase in current speed with height and the corresponding decrease in suspended sediment concentration. Near the bed, the current is increasing at a rate faster than the suspended sediment is decreasing, so that the net effect is an increase in sediment transport with distance from the bottom. At points greater than about  $z_1$ , the concentration associated with the two largest grain size classes begins to decay at a much faster rate than the current is increasing. This leads to the rapid decay in the sediment transport profile near  $z_2$  for these two grain size classes. The smallest grain size class

shows very little variation in height for  $z$  less than about  $z_2$ , so that the product of the concentration and current speed over this region increases with height due to the continual increase in the current speed throughout the boundary layer. For points greater than  $z_2$ , the suspended sediment concentration for the smallest grain size class begins to decay, but at a slower rate than the largest two grain size classes. This leads to the slower decay of this grain size compared to the two larger grain sizes illustrated in the figure.

### 3.9 Sensitivity of the solution to $\beta$ and $\gamma$

It has been demonstrated that the model is sensitive to changes in the free parameter  $\alpha$ . It was also mentioned in Section 3.1.2 that the numerical value for  $\beta$ , which is important in the stratification correction, and  $\gamma$ , which is important in modulating the neutral concentration equation, are derived from experimental studies of stably stratified atmospheric boundary layers. Since  $\beta$  and  $\gamma$  are experimentally determined coefficients, it can be debated that values adopted here may not be appropriate for flows stratified by suspended sediment. In fact, for the atmosphere,  $\gamma$  takes on different values under neutral, stable or unstable conditions (Businger et al. 1971; Wieringa 1980; Högström 1987). Additionally, when the flow consists of water stratified by suspended sediment, the data have suggested that  $\gamma$  may be grain size dependent (Villaret and Trowbridge 1991). With these concerns in mind, model sensitivity studies are performed using a range of  $\beta$  and  $\gamma$  values reported in the past. The parameter  $\beta$  has been reported to range between about 2.3 and 10, and  $\gamma$  between 0.35 and 1.0 (see reviews by Businger et al. 1971, Wieringa 1980 and Högström 1987 for a thermally stratified atmosphere, and Hill et al. 1988, McLean 1992 and Villaret and



Trowbridge 1991 for suspended sediment-induced stratification in water). Using these values as a guide, the coefficients are set with  $\beta = 2, 4.7, 10$  and  $\gamma = 0.35, 0.74$  and  $1.0$ . To preserve continuity with previous sensitivity studies, the wave and current parameters shown in Table 3.2 will serve for all model runs. For wave dominated conditions, it was shown in Section 3.8 that the  $0.01 \text{ cm}$  grains lead to the largest stability parameter. Since  $\beta$  is important in the stratified version of the model, the  $0.01 \text{ cm}$  grains will be used in order to optimize the effect of the stratification correction.

### 3.9.1 Sensitivity to $\beta$ with $\gamma$ held fixed

For the initial case,  $\beta$  is allowed to vary while  $\gamma$  is fixed with the widely reported value  $0.74$ . Figure 3.13(a) shows stability parameter profiles for the three indicated  $\beta$ s. Also shown is  $z_2$  for  $\beta = 4.7$ , and provides a scale estimate of the approximate height of the wave boundary layer. An inverse relation, where increases in  $\beta$  correspond to decreases in the stability parameter, clearly is illustrated. Near the peak, which shifts to points higher in the water column with increasing  $\beta$ , doubling  $\beta$  reduces the magnitude by about one-half. Since  $\beta$  occurs in the argument of the second exponential function in (3.108), increasing  $\beta$  increases the vertical decay. Figure 3.13(b) shows suspended sediment concentration profiles. Below  $z_2$ , the three profiles give nearly identical results, but then diverge throughout the remainder of the boundary layer. Interestingly, the profile identified as  $\beta = 2.0$ , which is associated with the largest stability parameter, shows the slowest decay with height in the outer boundary layer. This inverse pattern, where the largest stability parameter ( $\beta = 2.0$ ) shows the weakest stratification effect in the concentration profiles, can be explained by examining the exponential term

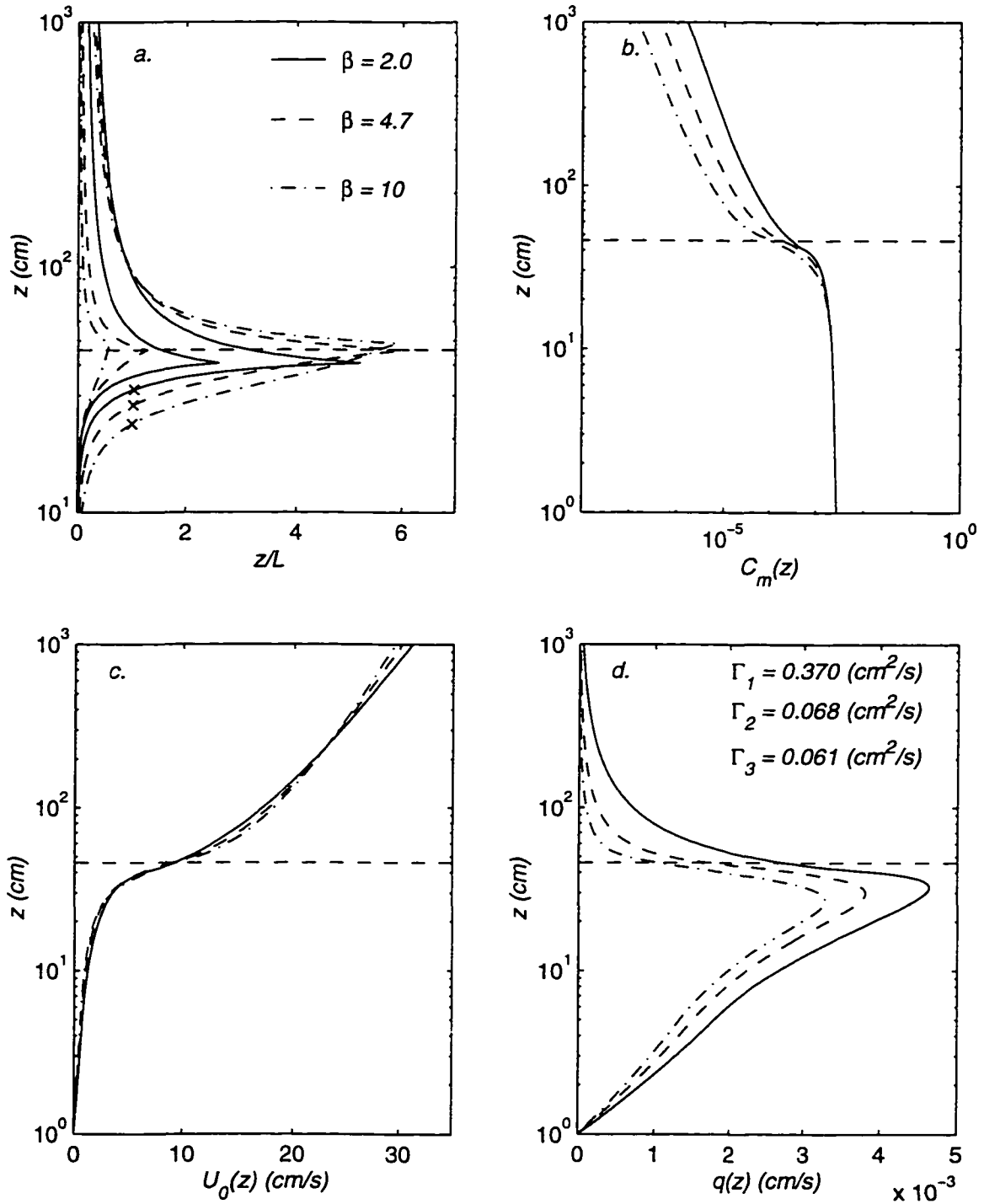


Figure 3.13 Sensitivity of calculated model parameters to changes in the stratification parameter  $\beta$ . Sediment grain size is set equal to  $0.01 \text{ cm}$ . Horizontal dashed line marks  $z_2$  calculated for  $\beta = 4.7$ . The 3 profiles in 3.13(a) marked by X's are the product of the stability parameter and corresponding  $\beta$ .

that represents the correction for suspended sediment-induced stratification in the current and concentration equations, i.e.,

$$\exp \left[ \frac{-\beta w_{fn}}{\kappa u_{*cw} z_1} \int_{z_1}^z \frac{z}{L} dz \right] \quad z_1 < z < z_2 \quad (3.122)$$

Assuming all other factors remain unchanged, inspection of (3.122) shows that the exponential function is modulated by  $\beta$  and the integral over the stability parameter. Multiplying each of the stability parameters in Figure 3.13(a) by their corresponding value of  $\beta$ , which is also depicted in figure, shows that the product  $\beta z/L$  generally increases with increasing  $\beta$ . This means that the integral in (3.122) is largest for  $\beta = 10$ , which explains why the largest  $\beta$  produces the slowest decay in concentration with height in the outer boundary layer. For the sensitivity tests presented here,  $\beta$  is clearly the dominant term in (3.122) that modulates the vertical dependence of the concentration under stratified conditions. This is an interesting consequence since inspection of the stability parameters in Figure 3.13(a) could be falsely interpreted as smaller  $\beta$  producing a larger stratification effect for the high wave case demonstrated here.

The effect of  $\beta$  on the current is relatively weak where profiles identified by  $\beta = 4.7$  and 10 show very similar trends (Figure 3.13c). For  $\beta = 2$ , the current within the wave boundary layer is slightly larger than the other two cases, but then becomes slightly smaller above the wave boundary layer up to  $z_n$  where all three must converge. For points greater than  $z_n$  the current identified by  $\beta = 2$  again slightly increases beyond

the other two. Since many of the above reported values suggest that  $\beta$  is between 5 and 10, the effect on the current profile under these conditions appears minimal. As a final look at the influence of  $\beta$ , sediment transport profiles are depicted in Figure 3.13(d). Patterns shown here mimic those of the concentration where smaller  $\beta$  leads to the largest transport values for a given height. The fact that the ordering of the transport according to  $\beta$  follows the same pattern associated with the concentration is not surprising given the relative insensitivity of the current to changes in  $\beta$ . The depth-integrated transport,  $\Gamma$ , also mimics  $q(z)$  where the smallest  $\beta$  shows the highest  $\Gamma$ . Unlike the current however,  $\Gamma$  is sensitive to changes in  $\beta$  where values range over an order of magnitude from smallest to largest  $\beta$ .

### 3.9.2 Sensitivity to $\gamma$ with $\beta$ held fixed

The focus now turns to the influence of  $\gamma$  with  $\beta$  held fixed. As a reminder, the parameter  $\gamma$  appears in the numerator of the Rouse parameter,  $R_s$ ,

$$R_s = \frac{-\gamma w_f}{\kappa u_*} \quad (3.123)$$

which is one of two terms that regulate the vertical structure of the suspended sediment concentration and stability parameter equations. In the concentration equation, the Rouse parameter serves as the argument of the vertically dependent function that represents the neutral solution. Therefore, increasing  $\gamma$  in the neutral model leads to a faster decay in concentration with height. Figure 3.14(a) shows stability parameters for  $\gamma = 0.35, 0.74$  and  $1.0$ , with  $\beta$  set at  $4.7$ . The profiles are clearly ordered, where larger  $\gamma$  predicts a smaller stability parameter, except near the peak where the pattern is reversed. The

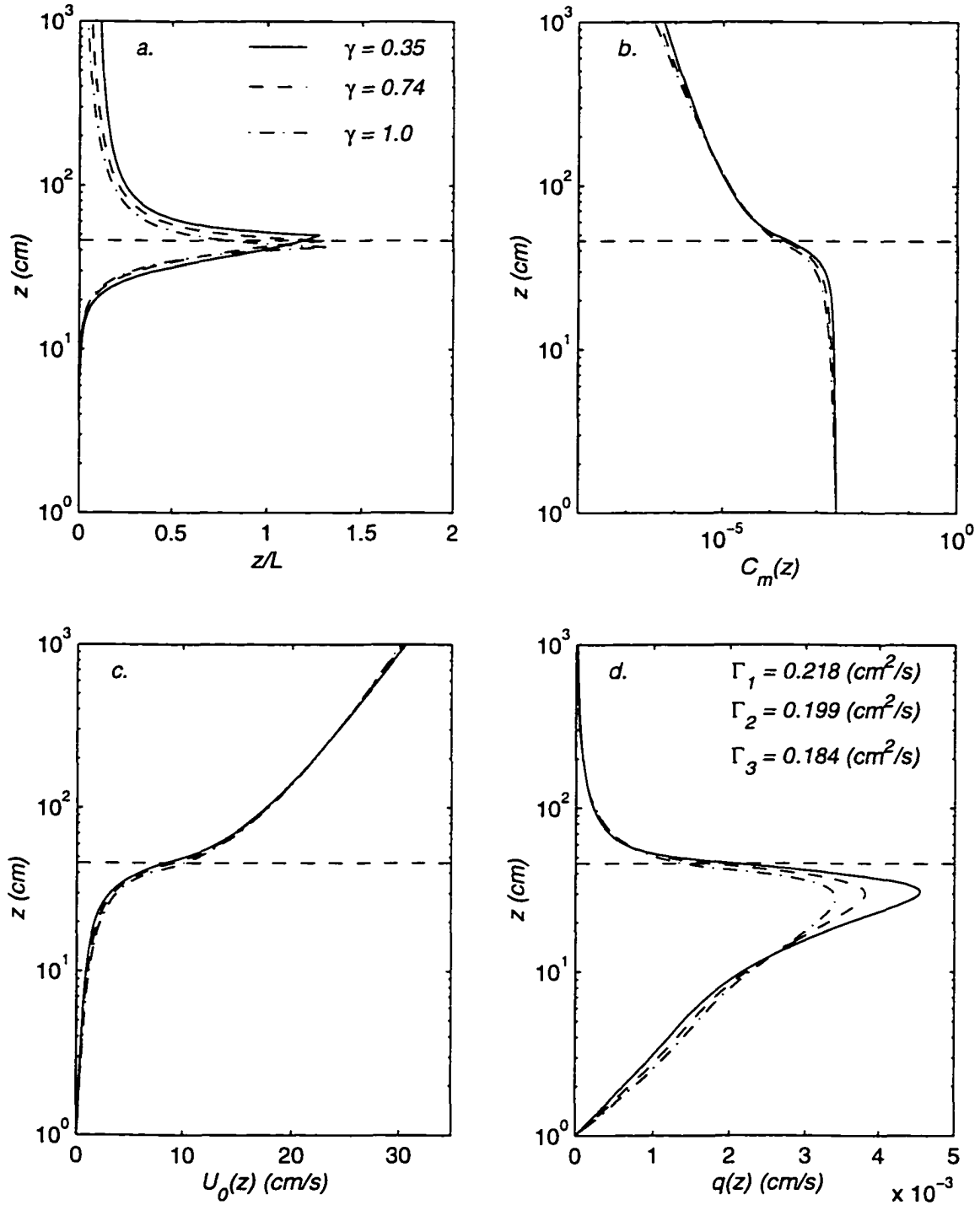


Figure 3.14 Sensitivity of calculated model parameters to changes in the sediment concentration parameter  $\gamma$ . Sediment grain size is set equal to 0.01 cm. Horizontal dashed line marks  $z_2$  calculated with  $\gamma = 0.74$ .

height of the stability parameter peak is also ordered, with the smallest  $\gamma$  shifted highest along the vertical axis. Overall differences between the three profiles, however, are minimal, indicating the stability parameter for these conditions is only weakly influenced by changes in  $\gamma$ . The influence on the concentration profiles also is weak, but not negligible (Figure 3.14b). Below  $z_2$ ,  $z/L$  is small, and the concentration is similar to the Rouse-like profile indicative of the neutral model. The profiles are, again, ordered with smaller  $\gamma$  predicting larger concentrations. At about  $z = z_2$ , the weak stratification effect is noticeable where the concentration identified by  $\gamma = 0.35$  decays at a faster rate than the other two profiles. This leads to a reversal in the ordering at about  $z = 60 \text{ cm}$ , which is barely visible in the figure. At about  $z = 100 \text{ cm}$ ,  $z/L$  becomes smaller and the stratification effect again is weak. This is indicated in the concentrations where at  $z = 200 \text{ cm}$  the ordering is again reversed so that the profile identified by  $\gamma = 0.35$  shows the largest concentrations. Figure 3.14(c) shows the current profile, where, again, the effect is minimal, with maximum differences between  $\gamma = 0.35$  and 1.0 being less than about  $1.0 \text{ cm/s}$ . This is not surprising since  $\gamma$  influences the current only through the stability parameter, which is shown in Figure 3.14(a) only to be weakly sensitive to changes in  $\gamma$ . Like the concentration, the flux profiles (Figure 3.14d) show the strongest divergence near  $z_2$ , with the smallest  $\gamma$  predicting the greatest transport. Values of  $\Gamma$  similarly are insensitive to changes in  $\gamma$  with a maximum relative difference between  $\Gamma_1$  and  $\Gamma_3$  of approximately 17%.

### 3.9.3 Effect of varying $\gamma$ and grain size

From the above analysis, it would seem that the solution is relatively insensitive to changes in  $\gamma$ . It must be reiterated, however, that the discussion here is restricted to

a very specific set of input wave, current and sediment parameters. For example, if the grain size is altered, then the influence of  $\gamma$  can become much more dramatic. Figure 3.15(a) shows the stability parameter for the same conditions above, but with  $d = 0.4 \text{ cm}$ . Compared to Figure 3.14(a) the stability parameter is much smaller, but still increases with decreasing  $\gamma$ . For the concentration, (Figure 3.15b), the differences in the three profiles is striking, with  $\gamma = 0.35$  predicting over an order of magnitude greater concentration at  $z = 10 \text{ cm}$  than for  $\gamma = 1.0$ . It is interesting that the concentration profile identified by  $\gamma = 0.35$  appears to be affected by the weak stratification conditions implied in the stability parameter profile. Because similar sensitivity tests with larger grains indicate that the stratification correction is virtually negligible, this is a surprising result. A clue as to why the stratification correction affects this concentration profile much more than the others is revealed in the Rouse parameter defined in (3.123). The larger grains ( $d = 0.04 \text{ cm}$ ) have a higher settling rate than the smaller grains ( $d = 0.01 \text{ cm}$ ). This means that  $w_f$  will be smaller for the smallest grains, leading to a smaller Rouse parameter and a corresponding slower decay in concentration with height. This is the same condition illustrated in Figure 3.11, which represents conditions for which the stratification correction is important. Equation (3.123) will also be small if  $w_f$  is larger, and  $\gamma$  is smaller. This is the situation depicted in Figure 3.15 for  $\gamma = 0.35$ , and explains why the presumably small stability parameter can lead to a stratification effect strong enough to alter this concentration profile from an otherwise neutral water column. A similar effect is seen in the current where the profile identified by  $\gamma = 0.35$  appears to exhibit similar, although not as strong, behavior

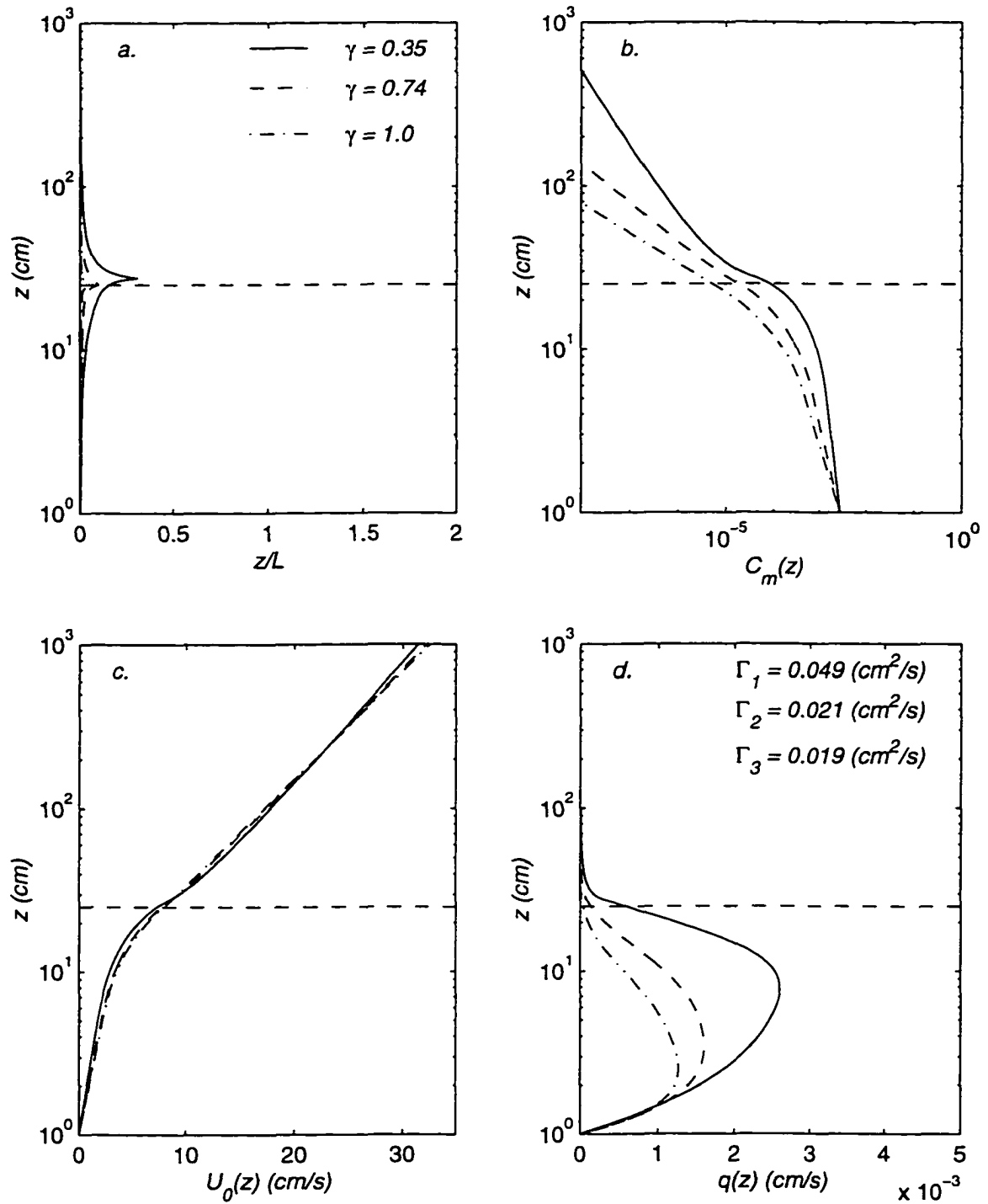


Figure 3.15 Same as Figure 3.14 but with a sediment grain size of 0.04 cm.



as the heavily stratified scenario in Figure 3.11. Because the effect is relatively weak, the ordering of the profiles is similar to Figure 3.14(c), which uses the same three values of  $\gamma$ . Finally, the transport profiles resemble those shown in Figure 3.10(d), with the largest transport associated with the smallest  $\gamma$ . Compared to Figure 3.14(d),  $\Gamma$  values are an order of magnitude lower which is expected for the larger sized grains used in this test case.

The varied profile structure shown in the four variables  $z/L$ ,  $C_m(z)$ ,  $U_0(z)$  and  $q(z)$ , for only one type of input wave and current condition, clearly reveals the sensitive nature of the BBLM to the internal parameters  $\alpha$ ,  $\beta$  and  $\gamma$  and the external parameter  $d$ . This suggests that applications to a wide range of sediment and current conditions can give very different results depending on changes in certain key coefficients. It also provides important calibration information since the sensitivity of the model to certain coefficients can be controlled. Careful manipulation of experimental conditions can reduce model sensitivity to certain parameters, while amplifying the sensitivity to other coefficients one wishes to calibrate.

### 3.10 Summary

A simple expression governing particle momentum, where the particle velocity differs from the fluid only through its tendency to fall out of suspension, was achieved by assuming that concentrations of suspended matter were low enough to neglect individual particle interactions. Under this assumption, the continuity equation was divided into fluid and solid phases which lead to a simple expression governing sediment concentrations. For fluid momentum, the usual linear and boundary layer approximations were invoked, leading to simple equations governing the wave and current velocities.

The momentum and mass conservation equations were coupled through an eddy diffusivity that scaled with the vertical coordinate, the shear velocity and a stability parameter. This simple turbulence closure scheme was considered adequate for modeling the constant stress region of the bottom boundary layer. Because both waves and currents were considered important, the constant stress layer was divided into an inner wave boundary layer where the wave shear stress contributed to the momentum balance, and an outer current boundary layer where the stress was associated only with the time averaged current. Within the wave boundary layer, the eddy viscosity was defined in terms of the sum of the time average of the shear stress plus the maximum instantaneous shear stress for the wave. This ensured that the non-linear coupling of the wave and current stress components would be retained in the description of the turbulence fluxes.

It was shown that if the kinematic flux term in the stability parameter was independent of height in the region  $z_1 \leq z \leq z_2$ , then the stability parameter was discontinuous at  $z = z_2$ . As a result, the kinematic flux was modified to ensure a continuous solution. This was achieved by assuming that the vertical dependence of the flux could be described by an exponential decay similar to the analytical solution for the wave shear. Because the stability parameter equation was transcendental, the solution was obtained numerically through application of the Chebyshev polynomial approximation. Convergence tests, comparing the Chebyshev approximation to the trapezoidal method, indicated that the Chebyshev formulation was more efficient for high wave conditions based on a predetermined 0.1% error threshold. Predicted stability parameter, concentration, current and flux profiles were compared with the GG bottom boundary layer model, and showed reasonable agreement when the free parameter  $\alpha$  was

set equal to 0.5. Model sensitivity tests were expanded to include the effects of varying grain size class on the stability parameter and associated current, suspended sediment concentration and transport profiles. For the cases presented, it was shown that smaller grains lead to larger stability parameters and distortion of the current and concentration from the classic log-linear and Rouse-like profiles derived for the neutral case. The effect of increasing the number of grain size classes to include 0.01, 0.025 and 0.04 *cm* grains gave similar results as the 0.01 *cm* tests, showing that for these conditions the smaller sized grains contribute the most to the stratification correction. Finally, sensitivity tests for  $\beta$  and  $\gamma$  indicated that the stratified model was strongly dependent on  $\beta$ , where increases in  $\beta$  lead to order of magnitude changes in concentration values above the wave boundary layer. The effect of altering  $\beta$  was minimal, however, on the current profile. For stratified conditions, model sensitivity to  $\gamma$  was weak for all profiles examined except near the edge of the wave boundary layer where smaller  $\gamma$  produced slightly higher concentrations and transports. It was shown, however, that  $\gamma$  was influential when the stratification correction was not important, and suggested that careful consideration of the possible values of all coefficients under a variety of wave, current and sediment conditions must be kept in mind during calibration studies.

## 4.0 MODEL AND DATA COMPARISONS

In this section, field data are used to calibrate model coefficients and to gauge the accuracy of the BBLM at predicting the shear stress and suspended sediment concentration profiles. Before discussing the parameter calibrations and model/data comparisons, a brief description of the study site and instrumentation is presented.

### 4.1 Study site and instrumentation

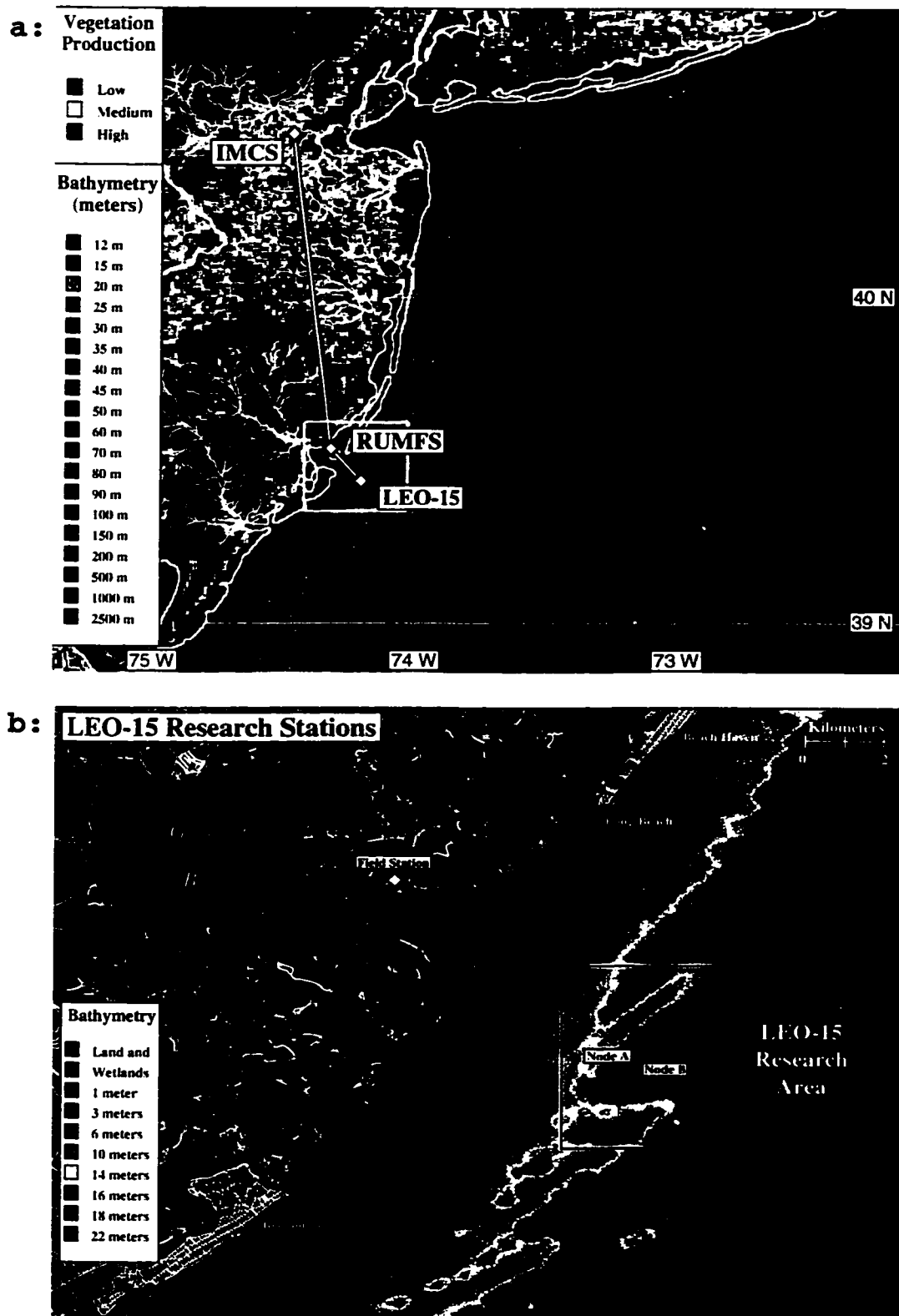
All field data for this study were collected at LEO-15, a Long-term Ecosystem Observatory located approximately 10 *km* off the southern coast of New Jersey in 15 *m* of water (von Alt and Grassle 1992; von Alt et al. 1997). LEO-15 serves as a natural, underwater environmental monitoring station to support multi-disciplinary research of coastal processes at an inner-shelf, shallow water site. The observatory presently consists of two undersea nodes connected to shore via an electro/fiber optic cable that serves dually as a power conduit and data transmission line. Tethered instruments only operate within a small radius centered on the nodes. To achieve greater spatial resolution, a multiplatform support network is in place that links the larger-scale processes to the spatially limited measurements available at the nodes. The network presently includes: (a) a Remote Sensing Laboratory in New Brunswick, New Jersey, (b) a meteorological tower at Rutgers University's Marine Field Station (RUMFS), in Tuckerton, New Jersey, (c) two research vessels, (d) shipboard towed CTD profilers and bio-optical sensors, (e) bottom mounted and towed profiling current meters, and (f) a suite of autonomous underwater vehicles.

During the summer months of 1994 and 1995, researchers from the Woods Hole Oceanographic Institution (WHOI), Rutgers University and Sequoia Scientific

participated in the National Undersea Research Program's Boundary Layer Stress and Sediment Transport (NURP/BLASST) experiment. The main objectives of this study were to identify dynamical processes related to: 1) the combined effect of waves and mean currents on bed shear stress; 2) the resuspension, grain size distribution, and vertical flux of sediment, and how this flux influences stratification; 3) the geometrical properties of wave-formed ripples, emphasizing the dynamical balance between near-bed flow and small-scale bedforms; and 4) the improvement of bottom boundary layer models based on results obtained from the observations. To achieve these goals, instrumented bottom boundary layer tripods equipped with state-of-the-art sensors were deployed at the present location of Node A (39.46 N - 74.26 W) centered within the larger LEO-15 research area (Figure 4.1). The primary instruments from this study relevant to the BBLM calibration and model/data comparisons presented here include the Benthic Acoustic Stress Sensor (BASS), deployed by Rutgers, the rotary SideScan Sonar (SSS), deployed by WHOI, and the Acoustic Backscattering System (ABS) also deployed by WHOI.

#### **4.1.1 BASS current meter array**

The BASS is a high-resolution current measuring system used to calculate shear stress in the bottom boundary layer. A typical BASS unit consists of a vertical array of four acoustic current meters along with individual temperature, salinity and pressure sensors, all connected to a submersible pressure housing containing the electronic components, tilt and roll sensors and a compass. The unit measures the current speed by calculating the round-trip travel time of a high-frequency acoustic pulse between two opposing transducer heads mounted 15 *cm* apart and oriented 45 degrees off the vertical.



**Figure 4.1 LEO-15 study site and bathymetry. (a) New York bight showing large scale bathymetry along the New Jersey Coast. (b) Expanded view of the LEO-15 research area. Node A is located on the southern end of a distinctive shore oblique sand ridge.**

The difference in travel time between what is measured and the known speed of sound in water gives the velocity of the fluid along each beam path. Each sensor contains 4 independent pairs of transducers, and velocities measured along the most accurate of any three axes are converted into  $u$ ,  $v$  and  $w$ . All sensors on the unit are programmed to sample at 4 Hz for a 15-minute burst each hour. This sampling scheme is chosen so that both high-frequency wave motion and low-frequency currents can be easily resolved, while insuring adequate battery power and data storage capacity for approximately 6 weeks. Information on the calibration and accuracy of the BASS can be found in Williams et al. (1987).

#### **4.1.2 ABS sediment concentration profiler**

The ABS is an acoustic transducer that calculates suspended sediment concentration profiles based on the scatter of sound by particles. The instrument operates by emitting a series of short acoustic pulses that scatter off the suspended material and then are sampled on the return. The intensity of the scattered beam is proportional to the grain size, which is assumed known, and concentration. Given the speed of the acoustic wave through water, each pulse is time sampled and then averaged to produce vertical range bins of 1 cm. Concentration measurements are recorded each ½-second for a 4-minute burst every 30 minutes. An important feature of systems like the ABS is that the flow and particle motion are not disturbed during operation. This nonintrusive method assures that ambient turbulent fluctuations are not contaminated by processes associated with the measuring unit. Information on using acoustic instruments to measure concentration and how they are calibrated for various grain size classes can be found in Thorne et al. (1991) and Lynch et al. (1994).

### 4.1.3 SSS acoustic imaging system

The SSS maps the micro-topography of the sea floor within a circular area of approximately 3 *m* radius. The unit emits an acoustic signal over a 30 degree swath 0.9 degrees wide centered on a 60 degree angle off the vertical. The transceiver rotates through 350 degrees forming an almost complete circular image of the sea floor. The intensity of the backscatter signal is proportional to the angle between the emitted beam and the geometric bedforms, with surfaces oriented perpendicular to the beam path producing the highest return intensity. Bedform features are easily determined by visual inspection of the shaded image, where surfaces oriented toward the beam appear lighter and surfaces oriented away from the beam appear darker (P. Traykovski, WHOI, personal communication). Because the beam intensity becomes more diffuse with increasing angle off the vertical, a unit placed 1 *m* off the bottom optimally gives a resolution of 1.4 X 2.0 *cm*<sup>2</sup> near the inner edge of the beam, and a resolution of 1.1 X 5.1 *cm*<sup>2</sup> near the outer edge. This degree of resolution is adequate for identifying bedforms such as wave-formed ripples but cannot distinguish individual sand particles. Applications of this instrument for the continental shelf can be found in Hay (1994) and Traykovski et al. (1998).

## 4.2 Bed reference concentration

Because the sediment concentration and concentration flux go to zero as  $z \rightarrow +\infty$ , the suspended sediment concentration solution is completely determined by the bed reference concentration. Studies on the entrainment of sediment reveal a highly complex process in which near-bed sediment motion is controlled by both individual particle interactions and advective/diffusive processes associated with the turbulent flow and



gravity. It is known that within only a few grain diameters of the bed, particles essentially are transported either as bedload, or by saltation (Wiberg and Smith 1985; Madsen 1991). In this region, forces associated with gravity and individual particle interactions such as rolling and jumping are primarily balanced by fluid drag. Further from the bed, these interactions are negligible and the sediment motion is adequately described by the continuum hypothesis presented in Section 3. Obviously, the boundary separating these two regions is not well defined since the sediment dynamics are described by a combination of the continuum assumption and the momentum equation governing individual grains. The dynamical processes associated with this transition layer are not well understood, making it difficult to define a reference concentration for the suspended load.

Models to describe the reference concentration for combined wave and current flows primarily associate entrainment of sediment to the local bed shear stress (Smith 1977). In order for entrainment to occur, the local shear stress must exceed the minimum required for initiation of motion,  $\tau_{cm}'$ , where the prime indicates that the stress is based on skin friction associated with the individual grains rather than form drag associated with ripples. Using the Shield's criteria for the initiation of motion developed for steady flows, Madsen and Grant (1977) extended the theory to oscillatory boundary layers, and developed empirical expressions that relate the critical Shields parameter,

$$\psi_{cm}' = \frac{|\tau_{cm}'|}{\rho (s_n - 1) g d_n} \quad (4.1)$$

to the non-dimensional sediment parameter  $S_n$ ,

$$\tau_n = \frac{d_n}{4\nu} [(s_n - 1) g d_n]^{1/2} \quad (4.2)$$

where  $\nu$  is the kinematic viscosity of the water. In the immediate vicinity of the bed, it is hypothesized that the flow will only sense a roughness due to the individual grains since the hydrodynamic roughness due to wave-formed ripples affects only the large-scale spatially averaged flow. The fact that the stress due to the individual grains is responsible for the initiation of sediment motion, rather than the much stronger bottom stress associated with the ripples, is well supported by experimental evidence (Nielsen 1992).

Assuming that sediment entrainment is a function of the bed shear stress associated with skin friction, Smith (1977) developed the following empirical reference concentration model for steady boundary layer flows,

$$\begin{aligned} C_n(z_0) &= \frac{c_b \gamma_0 \bar{S}_n}{1 + \gamma_0 \bar{S}_n} & \bar{S}_n > 0 \\ C_n(z_0) &= 0 & \bar{S}_n \leq 0 \end{aligned} \quad (4.3)$$

where  $c_b$  is the bed concentration ( $\sim 0.65$ ),  $\gamma_0$  is the resuspension coefficient,  $\bar{S}_n$  is the normalized excess skin friction for steady flows,

$$\overline{S}_n = \frac{|\tau_n'| - |\tau_{cn}'|}{|\tau_{cn}'|} \quad (4.4)$$

and  $\tau_n'$  is the steady shear stress based on skin friction for each sediment size class  $n$ . Grant and Madsen (1982) showed that the time for sediments to accelerate from rest to the fluid velocity in oscillatory flows was much less than the wave period. This lead GG to hypothesize that for oscillatory flows, (4.4) could be modified by simply replacing  $\tau_n'$  with the instantaneous shear stress for skin friction, giving

$$C_n(z_o) = \frac{c_b \gamma_o S_n'}{1 + \gamma_o S_n'} \quad S_n' > 0$$

$$C_n(z_o) = 0 \quad S_n' \leq 0 \quad (4.5)$$

where  $S_n'$  is the normalized excess skin friction for combined wave and current flows, defined as

$$S_n' = \frac{|\tau_{bn}'| - |\tau_{cn}'|}{|\tau_{cn}'|} \quad (4.6)$$

and  $\tau_{bn}'$  is the instantaneous shear stress for combined wave and current flows based on skin friction.

The term in the denominator of (4.5) was originally included by Smith (1977) to ensure that  $C_n(z_o)$  did not exceed the concentration in the bed. Wikramanayake and Madsen (1992) noted, however, that for most flows of interest on the continental shelf,

the product  $\gamma_o S_n'$  was  $O(10^{-2})$ , and could be neglected in the denominator. This approximation reduces (4.5) to

$$\begin{aligned} C_n(z_o) &= c_b \gamma_o S_n' & S_n' > 0 \\ C_n(z_o) &= 0 & S_n' \leq 0 \end{aligned} \quad (4.7)$$

which will serve as the reference concentration model for this study. To obtain the mean reference concentration,  $C_{nm}(z_o)$ , (4.7) is time averaged over a wave period.

The procedure to calculate the shear stress based on skin friction is identical to the methods described in Section 3, except that the bottom roughness,  $k_b$ , defined in (3.83) is set equal to the sediment grain diameter.

### 4.3 Determination of model input parameters

The independent input parameters for the BBLM include  $u_r$ ,  $z_r$ ,  $\phi_{cw}$ ,  $A_b$  and  $u_b$  which, as mentioned above, can be derived from a current/meter pressure sensor combination. For this study, these parameters are calculated from BASS data obtained during NURP/BLASST as described in Section 4.1. The mean current is obtained by simply time-averaging the individual  $u$  and  $v$  records over each 15-minute burst sampling period, and  $z_r$  is determined by measuring the height of the current meter relative to the base of the tripod prior to deployment. The calculation of  $u_b$ ,  $A_b$  and  $\omega$  is less direct.

The multi-directional and spectral characteristics of the ocean wave field make it difficult to isolate any one wave amplitude, direction and period that accurately represents the wave field as a whole. Unfortunately, there are many instances in practice when a simple description of the random wave field is essential if quantitative results are

to be obtained. In order to obtain a suitable representation of the wave field, while maintaining a relatively simple mathematical description, statistical procedures have been employed and provide the accuracy required for applications. The statistical variable of primary importance for this study is the near-bottom orbital velocity spectrum,  $S_{u_b}(\omega)$ , which is based on the Fourier transform of the near-bottom wave pressure. An important property of  $S_{u_b}(\omega)$  is that when integrated over all frequencies, the variance of the original time series record is obtained. In order to determine  $u_b$  for a spectral sea, Madsen et al. (1988) define an equivalent wave that has the same variance as the spectral representation, i.e.,

$$u_b \equiv \sqrt{2 \int_0^{\infty} S_{u_b}(\omega) d\omega} = \sqrt{2} \sqrt{\text{wave variance}} \quad (4.8)$$

where the  $\sqrt{2}$  factor comes from the fact that the variance of a sine wave is equal to the amplitude squared divided by 2. Thus, the amplitude of the equivalent wave bottom velocity,  $u_b$ , which must possess the same variance as the spectral wave, is correctly expressed in (4.8). This is an important distinction since many authors use the root-mean-square wave, which does not include the  $\sqrt{2}$  factor. The equivalent wave radian frequency is given by

$$\omega_r = \frac{\int_0^{\infty} \omega S_{u_b}(\omega) d\omega}{\int_0^{\infty} S_{u_b}(\omega) d\omega} \quad (4.9)$$

so that  $A_b$  can be determined as  $u_r/\omega_r$  (Madsen 1991). It is important to note that for a broad banded spectrum,  $\omega_r$  does not necessarily coincide with the spectral peak. Wikramanayake and Madsen (1992) showed that under these circumstances,  $\omega_r$  better represented the actual wave radian frequency when measured in terms of the zero down crossing of the original time series. As the wave spectrum becomes narrow banded,  $\omega_r$  converges to the radian frequency associated with the spectral peak, as expected.

Finally, the Fourier expansion method given by Longuet-Higgins et al. (1963) is used to determine the wave direction. The directional spectrum,  $S(\omega, \theta)$ , is expressed as the product of a frequency spectrum,  $S(\omega)$ , and a direction spreading function,  $D(\omega, \theta)$ , where  $\theta$  is the direction of an individual wave component. At each frequency, the directional spreading function can be expanded as a Fourier series. Using linear wave theory, the coefficients of the first term of the Fourier expansion can be written in terms of the cross-spectra of the observed pressure and velocity time series. The inverse tangent of the ratio of these coefficients gives the mean wave direction at each frequency. The mean wave direction of the spectrum is a weighted averaged based on  $S(\omega)$ . This method is in wide use, and a detailed explanation on the theory and applications to ocean waves can be found in Longuet-Higgins et al. (1963) and Bowden and White (1966).

#### **4.4 Field estimates of $\gamma_0$ , $\gamma$ and $\alpha$**

The dynamics controlling particle-fluid interactions near the bed are complex, making it impossible to determine  $\gamma_0$  theoretically for the variety of flow and roughness configurations found on the continental shelf. Attempts to determine  $\gamma_0$  in both the field and the laboratory have been extensive, but, due to the wide range of values reported,

the collective results of these studies has only complicated the issue. Table 4.1 lists estimates of  $\gamma_0$  that have been obtained in the past from a series of independent studies for a variety of flow and sediment conditions. The reported values range from  $10^{-3}$  to

Table 4.1 Values for the resuspension coefficient,  $\gamma_0$ , reported by previous investigators.

Investigator	$\gamma_0$
Smith (1977)	$2.0 \times 10^{-3}$
Dyer (1980)	$7.8 \times 10^{-5}$
Wiberg & Smith (1983)	$1.6 \times 10^{-5}$
Glenn & Grant (1987)	$2.0 \times 10^{-3}$
Hill et al. (1988)	$1.3 \times 10^{-4}$
Drake & Cacchione (1989)	$1.5 \times 10^{-5} - 3.0 \times 10^{-4}$
Vincent & Green (1990)	$3.7 \times 10^{-4} - 8.7 \times 10^{-4}$
Wikramanayake & Madsen (1992)	$1.8 \times 10^{-4} - 1.8 \times 10^{-3}$
Madsen et al. (1993)	$4.0 \times 10^{-4}$

$10^{-5}$ , which suggests that the underlying theory that relates the reference concentration to the excess boundary shear stress may neglect some crucial process describing sediment flux near the bed. Discussions on how the values indicated in the table were obtained, however, lead to at least two other reasons why the spread in  $\gamma_0$  is so large. First, as indicated by Madsen et al. (1993), the height at which  $C_m(z_0)$  is evaluated varies between each of the studies. This would certainly lead to different values for  $\gamma_0$  since the concentration gradient near the bed can vary greatly depending on the bed shear stress

and grain size. Second, most of the instruments used were placed at heights much greater than the reference level so that estimates had to be extrapolated to  $z_0$ . In addition, estimates of the reference concentration and bed shear stress were obtained from models that could not be verified with both current and concentration profile measurements (see references listed in Table 4.1 for experimental details). To address these concerns, and establish a consistent procedure for calculating the reference concentration,  $\gamma_0$  is determined using the semi-empirical reference concentration model developed by Wikramanayake and Madsen (1992) described below. Their model is chosen because it is intended for use in combined wave and current flows on the continental shelf and normalizes all  $\gamma_0$  estimates to a common reference level.

#### **4.4.1 Reference concentration model**

Wikramanayake and Madsen (1992) set the reference height equal to  $7d$ , based on Madsen's (1991) estimate of the height of the saltation layer derived from his conceptual model of bedload transport. They also noted that the height  $7d$  was a better choice than  $z_0$ , since for non-rippled beds,  $z_0$  could be less than the grain diameter. For the study here, the reference height is also set to  $7d$ , and the extrapolation to  $z_0$  is accomplished using (3.97). Using the data sets of Vincent and Green (1990), Wright et al. (1991), Hanes (1991), Bedford et al. (1990), and the unpublished data of Vincent and Osborne, Wikramanayake and Madsen (1992) concluded that  $\gamma_0 = 1.8 \times 10^{-3}$  for rippled beds and  $1.8 \times 10^{-4}$  for flat beds (sheet flow). The criteria to distinguish between rippled and flat beds is the ratio of the Shield's parameter based on skin friction for the wave to  $S_*$ . If this ratio is less than 0.18, the bed is assumed to be rippled and the value



$1.8 \times 10^{-3}$  is used; otherwise  $\gamma_0 = 1.8 \times 10^{-4}$ . For this study,  $\gamma_0$  is determined from field data using the time average of (4.7) to represent the reference concentration.

#### **4.4.2 Estimates of $\gamma$ reported in the past**

As discussed in Section 3, limited theoretical and experimental studies have suggested that  $\gamma$ , which helps regulate the vertical decay rate for the concentration, may be a function of grain size, with increases in grain diameter producing decreases in  $\gamma$  (Hill et al. 1988; Villaret and Trowbridge 1991). Other studies, however, have suggested that  $\gamma$  may be closer to 0.74 (Vincent and Green 1990), which is the value generally reported for neutral atmospheric boundary layers (Businger et al. 1971). It is important to note that these investigators could not establish to a satisfactory degree of certainty whether  $\gamma$  is constant or a function of grain size or, equivalently, settling velocity. As a result, a second task is to attempt to better define this parameter.

#### **4.4.3 Estimates of $\alpha$ reported in the past**

As described in Section 3, values of  $\alpha$ , which determines the height  $z_1$  in the eddy viscosity equation, range from about 0.15 for waves (Madsen and Wikramanayake 1991), to as large as 2.0 for suspended sediment concentration measurements reported in the field (Lynch et al. 1997). Thus, a third task is to determine  $\alpha$  using the concentration profile estimates collected in the field.

#### **4.4.4 Statistical methods**

Taking the log of both sides of the neutral version of the third equation in (3.97) gives the following linear equation to describe the concentration profile,

$$\ln[C_{nm}(z)] = \frac{-\gamma w_{f_n}}{\kappa u_{*c}} \ln \left[ \frac{z}{z_2} \right] + \ln[C_{nm}(z_2)] \quad (4.10)$$

or

$$Y = b_1 X + b_0 \quad (4.11)$$

where  $b_1$  is the familiar Rouse parameter defined in Section 3,

$$b_1 = R_s = \frac{-\gamma w_{f_n}}{\kappa u_{*c}} \quad (4.12)$$

The four terms appearing in (4.12) are  $\gamma$ , the von Karman's constant  $\kappa = 0.4$ , the settling velocity for each grain size class  $w_{f_n}$ , and the time average of the shear stress  $u_{*c}$ . For  $w_{f_n}$ , a common approach is to express the settling rate of various sized particles in still water in terms of grain size. For sediment grains in the range  $0.0063 \text{ cm} < d < 1.0 \text{ cm}$ , the following empirical equation developed by Gibbs et al. (1971) provides a convenient formula for computing  $w_{f_n}$ ,

$$w_{f_n} = \frac{-3 \nu + \sqrt{9 \nu^2 + g d_n^2 (s_n - 1)(0.003869 + 0.02480 d_n)}}{0.011607 + 0.07440 d_n} \quad (4.13)$$

where the constants in (4.13) are expressed in cgs units. Figure 4.2 shows (4.13) along with the empirical relation used by GG for  $s = 2.65$  and  $\nu = 0.0119 \text{ cm}^2/\text{s}$ , which is the kinematic viscosity of water at  $15^\circ\text{C}$ . The comparison between the two methods is good

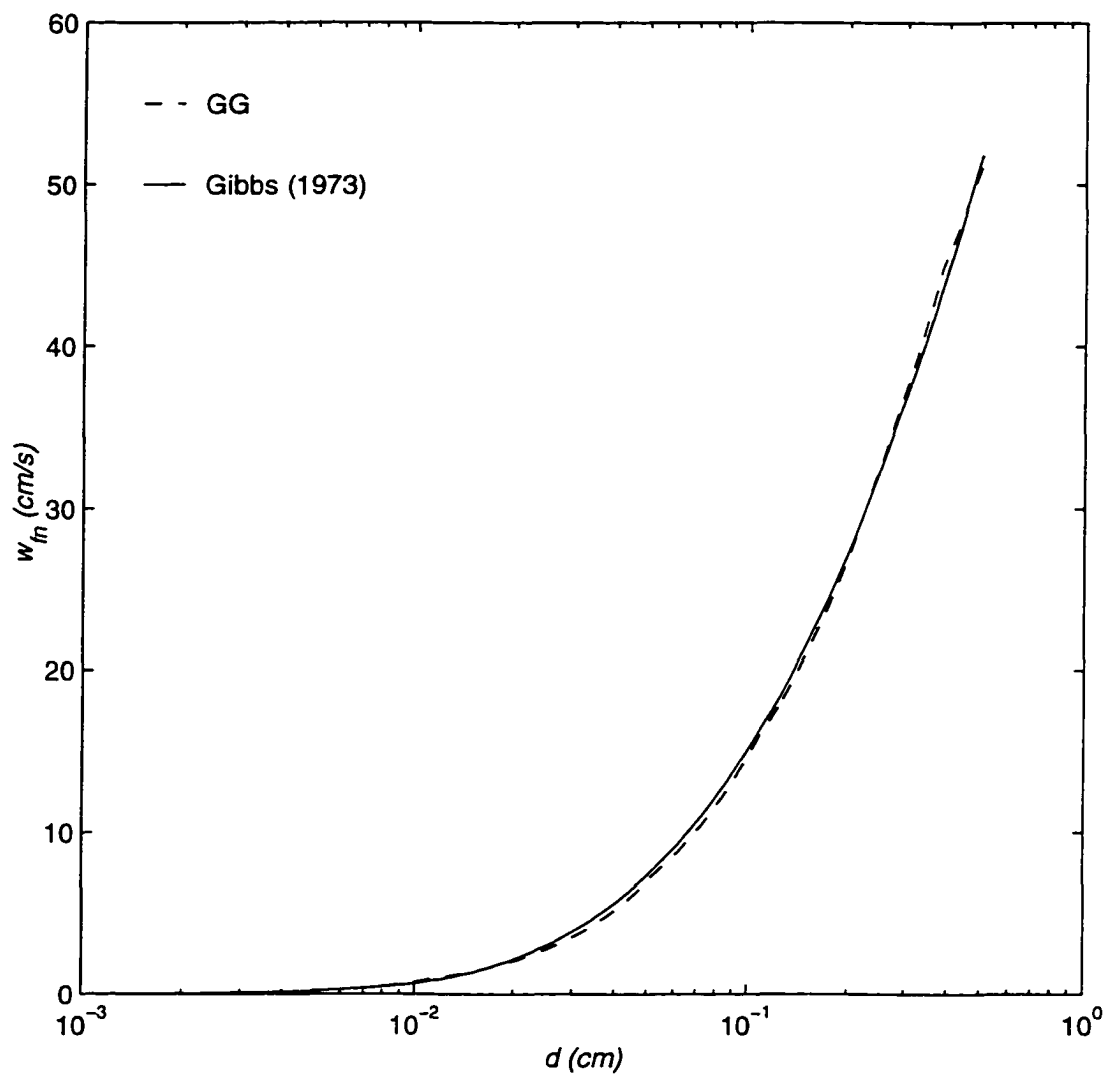


Figure 4.2 Comparison of particle settling velocity as a function of grain size between the empirical formula (4.13) developed by Gibbs et al. (1971) and that determined by Madsen and Grant (1977)

with a maximum difference of 12%. Given the uncertainty on the settling rate of particles in natural flow environments, this difference is low, so (4.13) will be used for all studies with this boundary layer model.

Assuming that the mean current in the bottom boundary layer varies logarithmically with height, mean current velocities can be reconstructed from all four BASS sensors and compared to the current profile derived from a model. The model equation is the classic "law of the wall", which expresses the mean current as a simple logarithmic function of height,

$$U(z) = \frac{u_{*c}}{\kappa} \ln \left( \frac{z}{z_{0c}} \right) \quad (4.14)$$

$$\ln(z) = \frac{\kappa}{u_{*c}} U(z) + \ln(z_{0c}) \quad (4.15)$$

where  $z_{0c}$  is the apparent hydraulic roughness for the mean current in the presence of waves. Algebraic manipulation of (4.14) allows it to be written in linear form, or

$$Y = a_1 X + a_0 \quad (4.16)$$

Both  $u_{*c}$  and  $z_{0c}$  can be estimated from the linear regression analysis since  $a_1 = \kappa/u_{*c}$  and  $a_0 = \ln(z_{0c})$ . The regression analysis also provides a convenient and simple method to quantify the error associated with the shear stress estimates by calculating the correlation coefficient ( $R$ ) to test goodness-of-fit, and by constructing confidence limits to establish the error bound on individual  $u_{*c}$  and  $z_{0c}$  estimates. Assuming the system can be

accurately described using the above regression model, a confidence interval for  $u_{*c}$  is determined from

$$\overline{u_{*c}} (1 - e) \leq \overline{u_{*c}} \leq \overline{u_{*c}} (1 + e) \quad (4.17)$$

where the over bar represents the estimate of  $u_{*c}$  obtained from the data, and

$$e = (t_{\alpha/2, N-2}) \left[ \frac{1}{N-2} \left( \frac{1 - R^2}{R^2} \right) \right]^{1/2} \quad (4.18)$$

where  $t$  is the Student's  $t$  distribution for the  $(1 - \alpha)$  confidence interval with  $(N - 2)$  degrees of freedom, and  $N$  is the number of current meters (Gross and Nowell 1983; Grant et al. 1984). Equations (4.17) and (4.18) can also be used to estimate errors associated with the Rouse parameter in (4.12) by simply replacing  $u_{*c}$  with  $b_1$  (Neter et al. 1989).

With the slope represented by  $b_1$ , and  $u_{*c}$ ,  $w_{f_n}$  and  $\kappa$  defined as described above,  $\gamma$  can be estimated from (4.12). This value can then be used to set the slope of the concentration profile in the model. Once the slope has been determined, the profile is shifted along the concentration axis until the model passes through the measured concentration. This then defines the reference concentration, and associated  $\gamma_0$ . The parameter  $\alpha$  is determined by matching the measured and modeled profiles in the range  $z_1 < z < z_2$ .

#### 4.4.5 Flow and concentration data

Current and suspended sediment concentration profile data obtained using a BASS and ABS, respectively, at LEO-15 during a 6-week deployment beginning August 23,

1995 are used to estimate  $\gamma_0$ ,  $\gamma$  and  $\alpha$  for the field. The instruments and the LEO-15 study sight are discussed in Section 4.1.

#### 4.4.6 Current data

Current data obtained using a BASS deployed simultaneous with an ABS on a single tripod were used to reconstruct vertical profiles of the current and to determine estimates of  $u_{*c}$  and  $z_{0c}$  as described above. Current meters were positioned at 45, 80, 165 and 250 *cm* above the bottom which was considered close enough to the bed to occupy the constant stress region during high wave and current activity, yet far enough away so that the effects of local bathymetric features such as ripples were not directly affecting the flow measured by the BASS. A pressure sensor was positioned at 416 *cm* directly above the highest BASS sensor. As mentioned above, the BASS samples at 4 *Hz* for a 15-minute burst each hour. The mean current was extracted by averaging the 4 *Hz* record over each 15-minute burst and wave parameters were calculated using the individual 4 *Hz* current and pressure records. For this deployment, the mean current and wave parameters were calculated using the lowest pod located 45 *cm* above the bottom.

During the course of the deployment, some tripod settling may occur causing the heights of the individual sensors to shift. In addition, bedforms such as ripples will migrate past the instrument causing the distance between the bed and the sensors to change over time (Traykovski et al. 1998). Because of these processes, the measurements made prior to deployment may need to be adjusted to provide an accurate estimate of the sensor heights. Grant et al. (1984), in a similar study using a BASS array, stated that shifts of up to  $\pm 5$  *cm* are possible based on estimates of the standard deviation in pod heights obtained from both a mechanical gauge and an echo sounder.

For this study, no such exact measurements are available so that the maximum acceptable range for the spatially averaged height of each current sensor is defined as  $\pm 5 \text{ cm}$  criteria set by Grant et al. (1984). This may underestimate the variance in ripple height at LEO-15, in a depth of approximately 11 *m*, where the ripples are probably much larger than bedforms measured off northern California by Grant et al. (1984), in a water depth of 90 *m*. Reevaluation of the current profile data using vertical shifts of up to  $\pm 5 \text{ cm}$  in the individual pod heights produced no significant improvement in the  $R^2$  values. The lack of significant settling at LEO-15 may be a result of the different substrates, i.e., Grant et al. (1984) deployed on a silty bottom, whereas LEO-15 is mostly a medium sand. In any event, the possibility of tripod settling is noted but considered negligible.

#### **4.4.7 Suspended sediment concentration data**

Peter Traykovski of WHOI (personal communication) calibrated the ABS using surface sediment obtained by divers from underneath the tripod equipped with the ABS. In analyzing the data, he determined that the major fraction of sediment consisted of medium sand with an average grain diameter of 0.04 *cm* and a distribution, based on one standard deviation, of approximately  $\pm 0.02 \text{ cm}$ . Based on his calibration, a single grains size class consisting of 0.04 *cm* grains with a density of 2.65  $\text{gm/cm}^3$  is used in this analysis. The ABS was mounted 109 *cm* off the bottom looking downwards and produced concentration measurements ranging from 1 *cm* above the bottom to approximately 100 *cm* above the bottom in 1 *cm* increments. Inspection of (4.10) shows that the comparison points are limited to heights greater than  $z_2$ . Because the exact height of  $z_2$  cannot be determined prior to running the model, an initial value of 25 *cm* is chosen. In addition, a number of bursts showed that the upper 20 *cm* or so displayed

a sharp departure from the Rouse-like profile assumed in the statistical model. One possible explanation is that the ABS instrument does not provide consistently accurate estimates of concentration near the instrument head. As an acoustic pulse is emitted, the transducer vibrates for a very short time afterwards. Any acoustic energy returned from particles very near the instrument will not be accurately recorded due to the instrument still ringing from the initial transmitted signal. Therefore, in the near field of the instrument, concentration estimates may be contaminated and are not reliable. As a result, concentration measurements within 20 *cm* of the instrument are neglected in the calibration procedure. Removing the first 25 *cm* from the bottom and the last 20 *cm* from the top gives approximately 55 concentration values for each profile. For  $N = 55$ , a minimum  $R^2$  value of 0.967 gives a confidence band of approximately  $\pm 4.7\%$ , which will serve as the limiting criteria for extracting appropriate bursts. Limiting the statistical analysis to heights greater than  $z_2$  is also consistent with the shear stress estimates obtained from current measurements at heights greater than 44 *cm* above the bottom. Of the total bursts, 48 concentration profiles produced  $R^2 \geq 0.97$ . For these 48 bursts, the BASS data were used to identify current profiles that produced  $R^2 \geq 0.96$ . Extracting only profiles with both  $R^2 \geq 0.969$  for the concentration and  $R^2 \geq 0.96$  for the current further reduced the total number of bursts to 9.

Examination of the tripod upon recovery revealed dense patches of hydrozoan (*Tubularia crocea*) growth on the superstructure as well as on the BASS transducers. Because the exact time bio-fouling began to interfere with the operation of the sensors could not be determined, the mean current records were consulted and an approximate cutoff date was obtained by visual inspection of the recorded time series. Significant



bio-fouling of pod 1 (45 *cm* above the bottom) and pod 3 (165 *cm* above the bottom) was suspected to have begun around year day 255, where the current magnitudes, as compared to the other BASS sensors and an acoustic doppler current profiler that was deployed near the tripods, showed significant deviations from the data obtained from these other sensors. As a precaution, data obtained only before year day 250 is used in the calibration study. This further restriction limits the number of available high quality bursts to 5.

#### 4.4.8 $u_{*c}$ and $b_1$ statistics and raw data for the chosen bursts

Error estimates and  $R^2$  for both the Rouse parameter and  $u_{*c}$  are shown in Table 4.2 for the 5 chosen bursts. Errors for the Rouse parameter,  $b_1$ , range from  $\pm 2.3\%$  to  $\pm 4.5\%$  at the 95% level of significance, which is a consequence of the relatively stringent  $R^2$  criteria used to extract appropriate bursts. The estimates of  $u_{*c}$  show errors that range from a low of  $\pm 31\%$  to a high of  $\pm 54\%$  at the 95% level of significance.

Table 4.2 Statistics showing errors associated with the Rouse parameter ( $b_1$ ) and  $u_{*c}$ . Error bounds indicate confidence limits, expressed in percent, at the 95% level of significance.

Year day	$R^2 (b_1)$	error ( $b_1$ )	$R^2 (u_{*c})$	error ( $u_{*c}$ )
241.29	0.98	$\pm 3.7\%$	0.98	$\pm 44\%$
242.67	0.98	$\pm 3.7\%$	0.97	$\pm 54\%$
247.71	0.97	$\pm 4.6\%$	0.99	$\pm 31\%$
247.96	0.98	$\pm 3.7\%$	0.97	$\pm 54\%$
248.58	0.99	$\pm 2.6\%$	0.98	$\pm 44\%$

This is a direct consequence of using only 4 current meters where inspection of (4.18) shows that error bounds, for a given  $R^2$ , are inversely proportional to the square root of the number of current profile measurements. Figures 4.3 through 4.7 show the raw profile data for both the current and concentration for the 5 chosen bursts, along with the slope estimates which helps to visually illustrate the accuracy of the fit. Most concentration profiles appear relatively linear on a log-log plot in the range  $25\text{ cm} < z < 80\text{ cm}$ , which is the range used to identify log-log profiles. For points lower than about  $20\text{ cm}$ , the data begins to curve away from the log-log behavior. In addition, all the profiles show at least a slight increase in concentration in the top few centimeters, which, as previously discussed, represents the near field of the ABS instrument, and occupies the region where the ABS is suspected to be the least accurate.

#### 4.4.9 Field estimates for $\gamma$ and $\alpha$

Of the 5 chosen bursts,  $u_{*c}$  and Rouse parameter estimates were used to calculate  $\gamma$ , and the results are shown in Table 4.3. Estimates range from 0.26 to 0.85 with a mean of 0.43. Because  $\gamma$  is directly proportional to  $u_{*c}$  through the Rouse parameter, the error will be at least as large as that associated with  $u_{*c}$ . These errors are also shown in the table. Since the average is well below the widely reported value of 0.74 for stratified atmospheric boundary layers are also shown in the table. Since the average is well below the widely reported value of 0.74 for stratified atmospheric boundary layers (Businger et al. 1971), it seems likely that  $\gamma$  may be grain size dependent.

The 5 bursts were also used to calculate  $\alpha$ . This was achieved by running the BBLM with  $u_{*c}$  and  $z_{0c}$  estimates derived from the data, and back calculating  $k_b$ . In this procedure,  $u_{*c}$  and  $z_{0c}$  were given and  $k_b$  was the initially unknown parameter which was

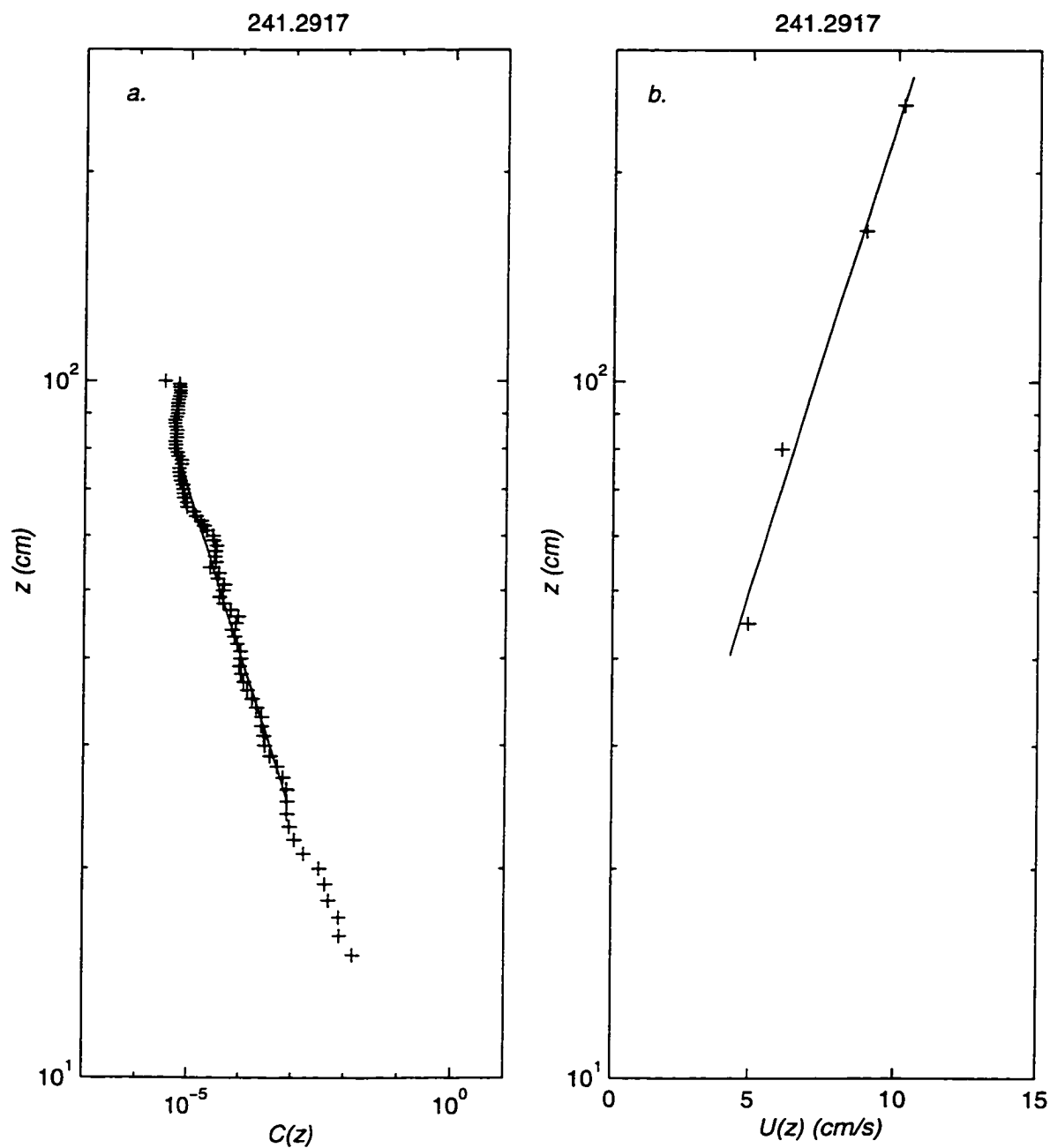


Figure 4.3 Selected high quality concentration (a) and current profile (b) data used to determine the sediment reference concentration and  $\gamma$ . Lines indicate best fit as described in the text.

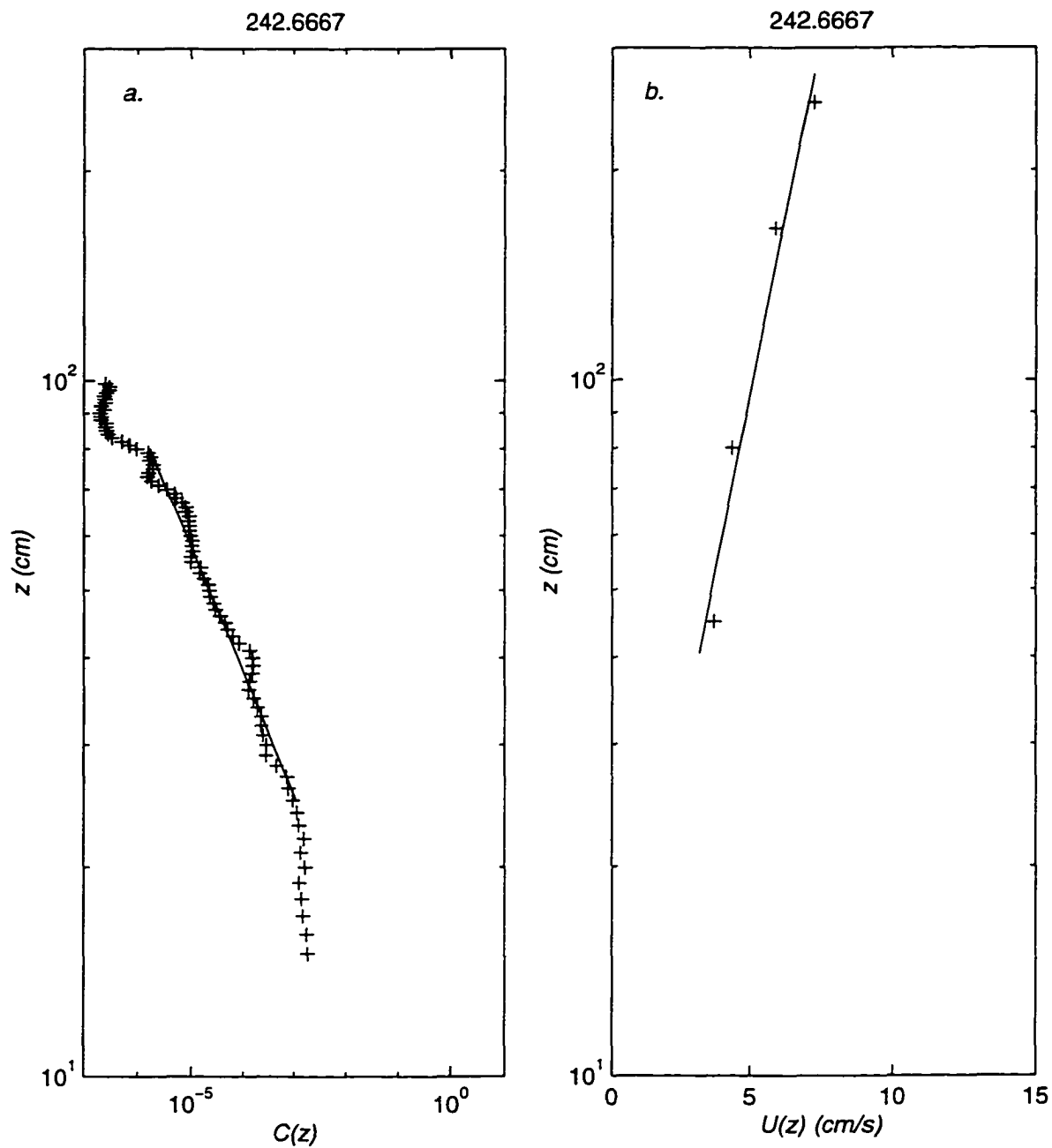


Figure 4.4 Same as Figure 4.3 for year day 242.67.

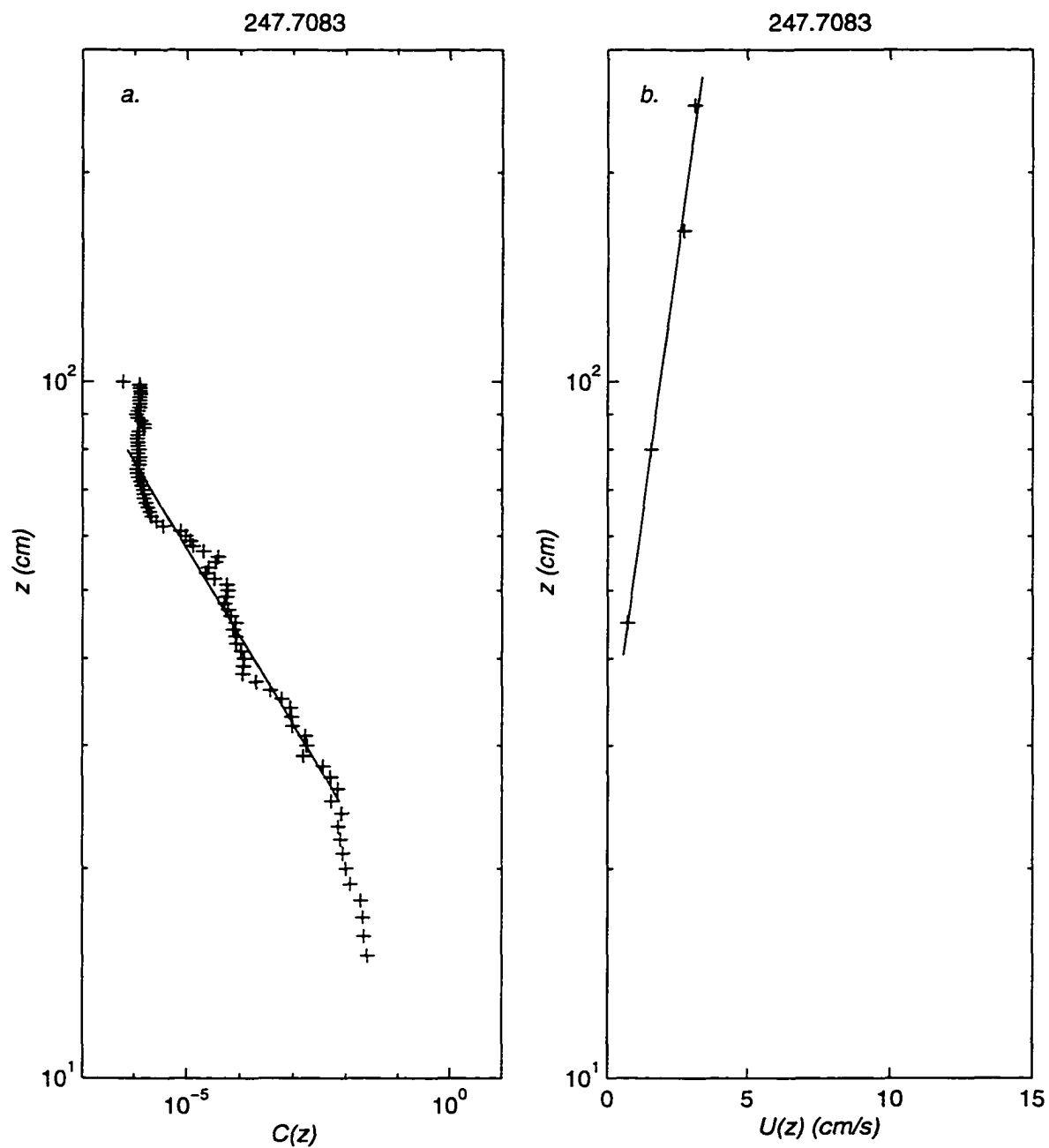


Figure 4.5 Same as Figure 4.3 for year day 247.71.

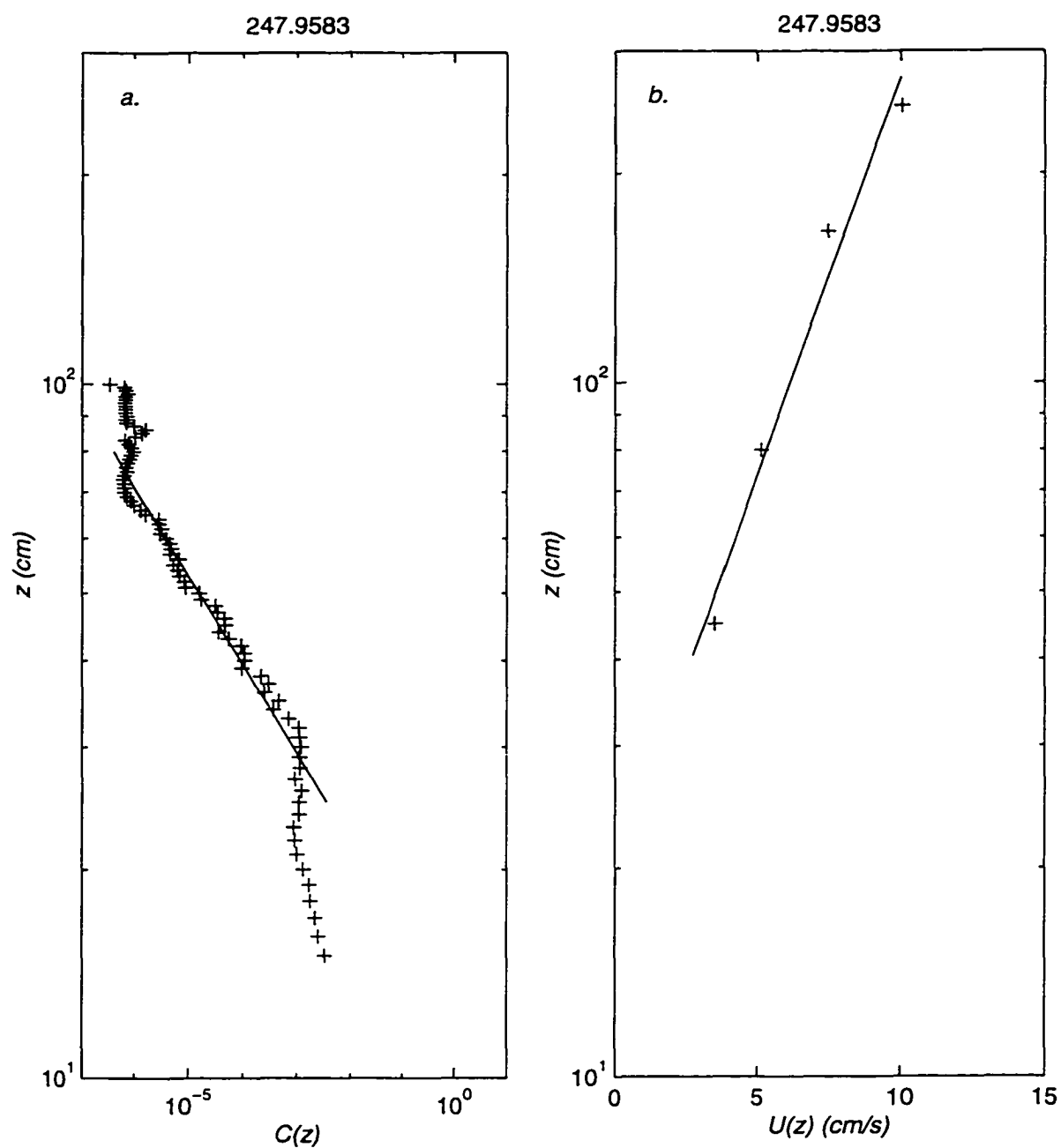


Figure 4.6 Same as Figure 4.3 for year day 247.96.

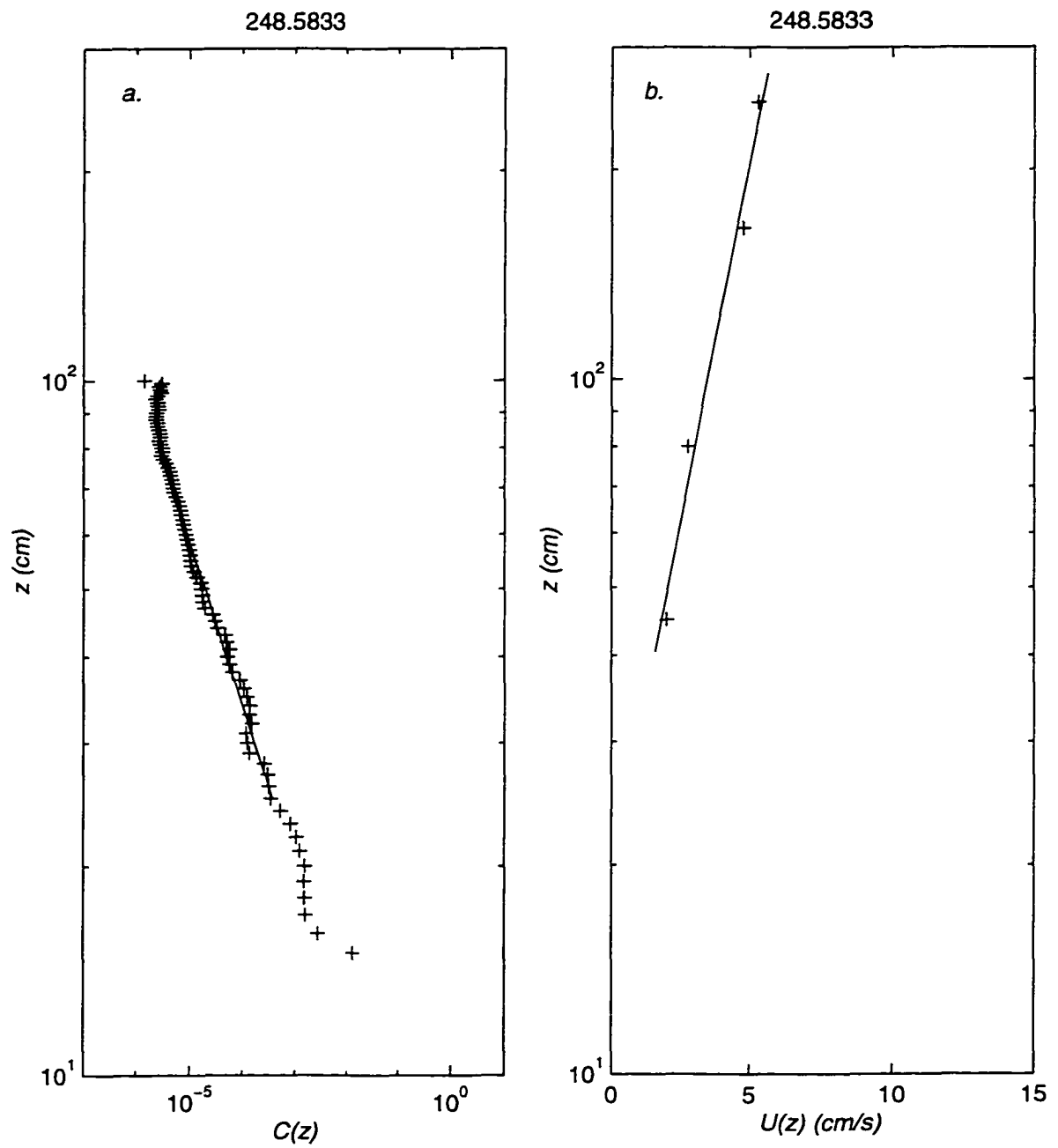


Figure 4.7 Same as Figure 4.3 for year day 248.58.

Table 4.3 Various calculated model parameters and statistics for the 6 chosen bursts.

Year day	$\gamma$	$\alpha$	$\gamma_0$
241.29	0.40 ( $\pm 44\%$ )	0.9	$4.78 \times 10^{-4}$
242.67	0.34 ( $\pm 54\%$ )	2.2	$2.38 \times 10^{-2}$
247.71	0.33 ( $\pm 31\%$ )	-	-
247.96	0.85 ( $\pm 54\%$ )	-	-
248.58	0.26 ( $\pm 44\%$ )	-	-
mean	0.43	1.55	$3.1 \times 10^{-3}$

solved through iteration until  $z_{0c}$  calculated from the model matched that measured by the BASS. This produced estimates of  $u_{*cw}$  needed to reconstruct concentration profiles. Because the slope of the concentration profiles above  $z_2$  was provided from estimates of  $b_1$ , along with concentration estimates from the best fit line to define the concentration at a known reference height, it was possible to reconstruct the concentration profile over the entire boundary layer. This provided estimates of the concentration in the region  $z_1 < z < z_2$  so that  $\alpha$  could be adjusted to give the best overall fit between the modeled and measured concentration.

For each of the 5 bursts,  $\alpha$  was varied to produce a family of concentration profiles. The difference between the measured and modeled concentration at each point was determined, and then used to calculate the relative error defined as



$$\ln(e) = \left[ \frac{1}{N} \sum_{i=1}^N (\ln(Y_i) - \ln(\bar{Y}_i))^2 \right]^{\frac{1}{2}} \quad (4.19)$$

where  $Y$  is the measured data point and  $\bar{Y}$  is the corresponding best fit. As noted by Wikramanayake and Madsen (1991), when  $e$  is minimized, (4.19) is a least squares fit on a log-log plot. In addition, (4.19) provides a good method to determine the error for variables that span several orders of magnitude, as is the case here. As an example of how (4.19) can be used to interpret the error, a value of  $e = 1.23$  gives an error of ~21%.

An optimal value of  $\alpha$  was determined by consulting the relative error from the family of  $\alpha$  values and choosing the one that was the lowest. In some instances, however, the error continued to decrease until  $\alpha$  became so small that  $z_1 = \alpha l_{cw}$  became less than  $z_0$ . Under these conditions, a natural extension of the three layer eddy viscosity would be to reduce the model to a 2-layer eddy viscosity, where the eddy viscosity is constant with height for  $z < z_2$  ( $K = \kappa u_{*cw} z_0$ ), and then reverts to a linear increase with height like the 3-layer model above  $z_2$  ( $K = \kappa u_{*c} z$ ). For this eddy viscosity, the model is no longer dependent on  $\alpha$ . For cases where the minimum relative error asymptotically decreases but does not reach a minimum before  $z_1$  becomes less than  $z_0$ , it is not possible to determine  $\alpha$ . Bursts identified as year day 247.71, 247.96 and 248.58 all showed this behavior and therefore cannot be used to define  $\alpha$ . It is interesting to note that Davies and Villaret (1997), and others, have suggested that, for a rippled bed, the eddy viscosity should be constant with height. When  $z_0$  is larger than  $z_1$ , this usually indicates that wave-formed ripples are large. For example, for year day 247.71, 247.96 and 248.58,

in which  $\alpha$  could not be determined,  $z_0$  was 4.77, 7.71 and 5.27 *cm*, respectively. During the bursts on year day 241.29 and 242.67, where  $\alpha$  could be determined,  $z_0$  was 2.23 and 0.35 *cm*, respectively. The higher  $z_0$  values during the three bursts that could not be used to calibrate  $\alpha$ , suggests the possibility that a different eddy viscosity should be used in these instances.

Figures 4.8(a) and 4.9(a), show the concentration data along with the best fit obtained by varying  $\alpha$  in the model. Figures 4.8(b) and 4.9(b) show the BASS current data along with the current profile obtained by adjusting  $k_b$  until the measured  $z_{\alpha c}$  matched that obtained from the BASS data. The horizontal line on the concentration plots indicate twice the ripple height,  $\eta$ , which was also measured during the deployment (see Section 4.5 for details of ripple height measurements). For both plots, the fit above  $2\eta$  is good, but then begins to show a strong divergence from the best fit line for points lower. Past studies of flow over uneven bottoms have indicated that local effects due to the presence of variable topography generally extend 2 to 5 times the height of the individual bedforms (Wiberg and Nelson 1992). As a result, measurements of mean properties made less than twice the height of ripples may be directly influenced by variations in topography. In this region, a single point estimate may not be representative of the spatially averaged flow and therefore should not be used in a model that does not take into account horizontal variability. As a result, only data obtained for points greater than  $2\eta$  are used to calibrate  $\alpha$ . As an upper bound, the modeled concentration is, by definition, already a best fit above  $z_2$ , so that the calibration is restricted to measured profiles in the range  $2\eta < z < z_2$ . For the profile identified as year

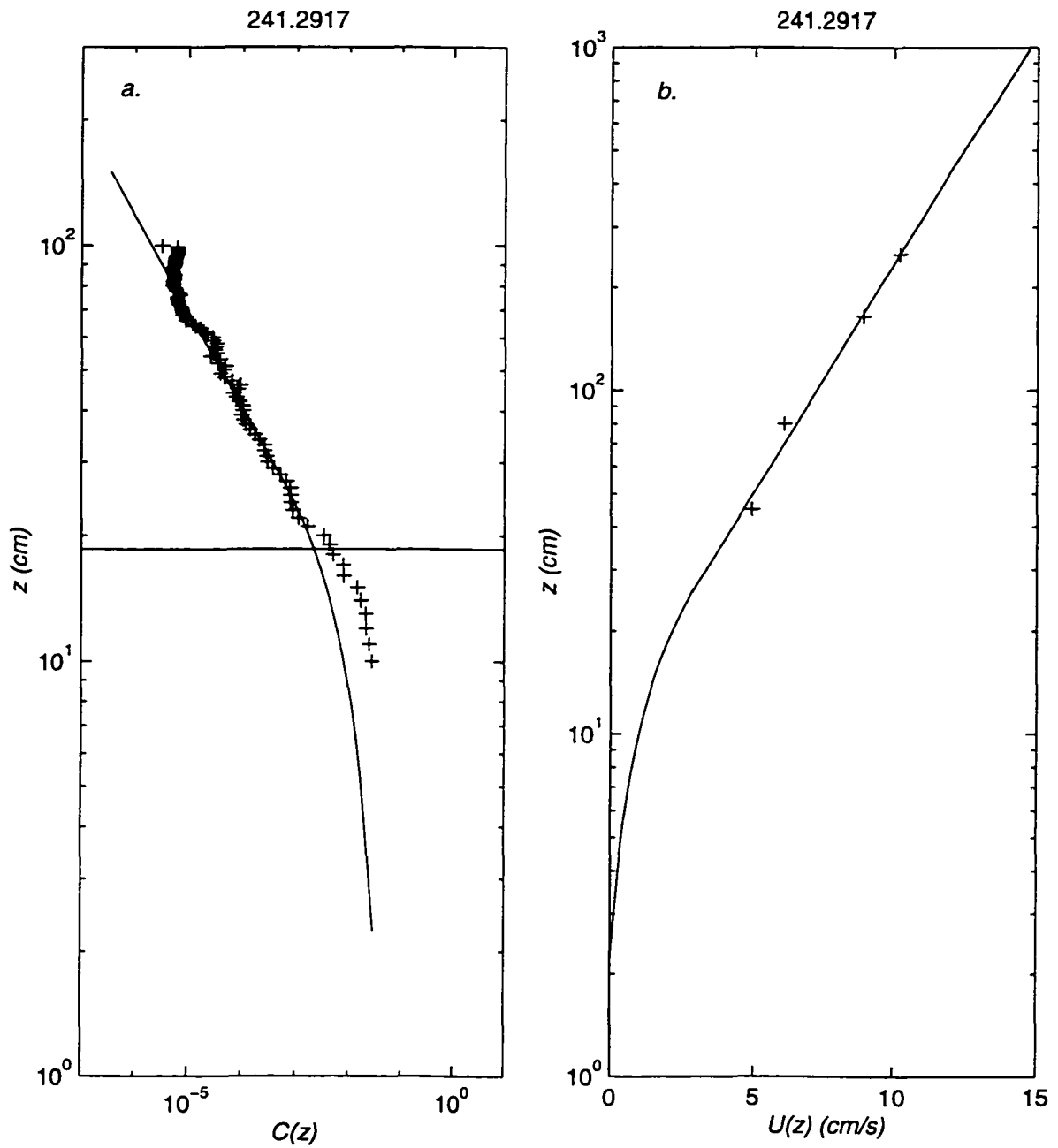


Figure 4.8 First of two selected bursts used to calculate the parameter  $\alpha$  and the resuspension coefficient  $\gamma_0$ . (a) shows the best fit profile by adjusting  $\alpha$  to minimize the difference between the model and measured data in the region  $2\eta < z < z_2$ . The height  $2\eta$  is marked by the horizontal line in the plot. (b) shows the corresponding best fit current profile based on measured  $u_{*c}$  and  $z_{0c}$ .

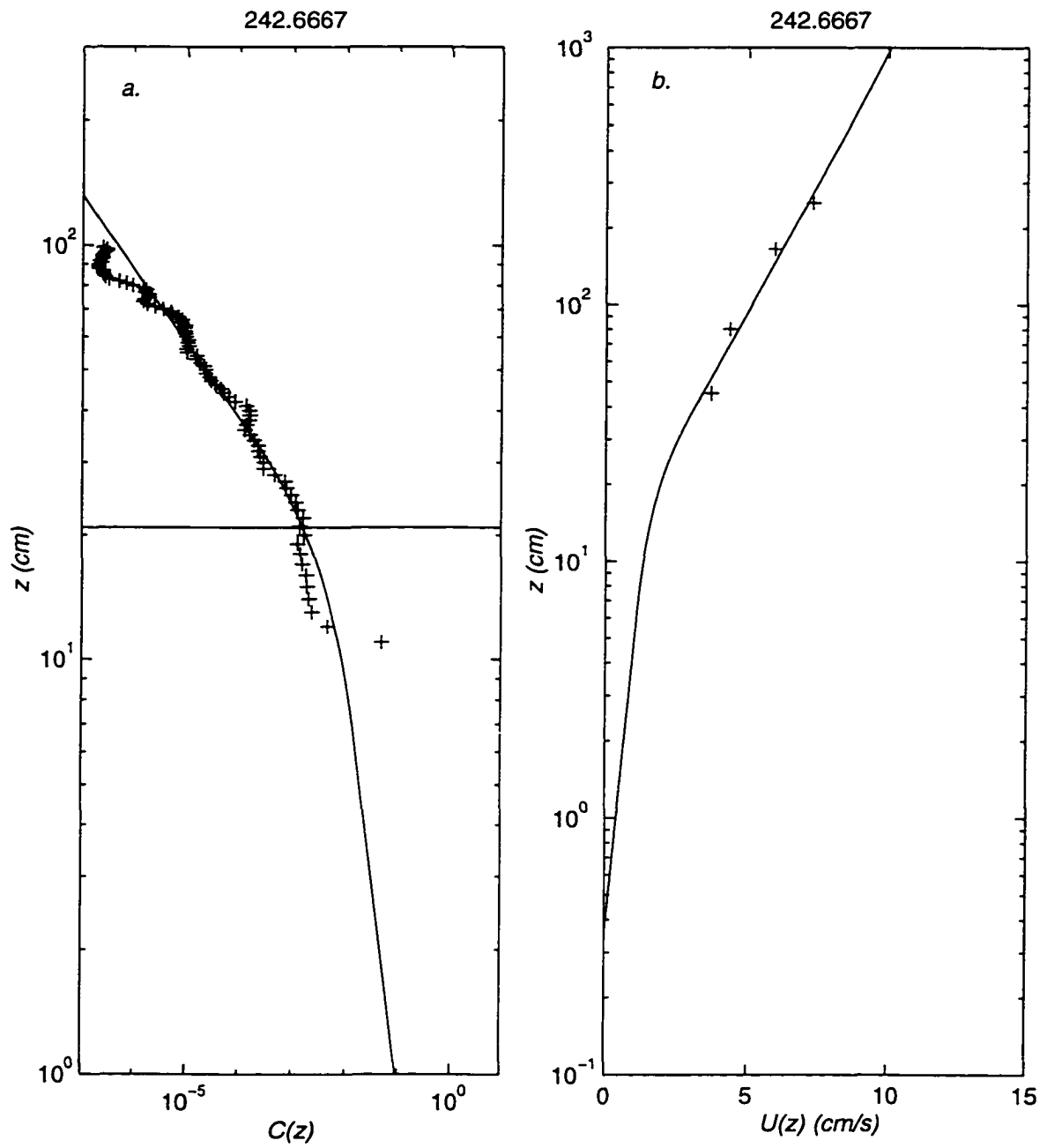


Figure 4.9 Second selected burst used to calculate the parameter  $\alpha$  and the resuspension coefficient  $\gamma_0$ . Plots are the same as described in Figure 4.8.

day 241.29 this gives 10 data points and for year day 242.67 this gives 16 data points. The two  $\alpha$  values are 0.9 and 2.2, and are listed in Table 4.3.

#### 4.4.10 Estimates of $\gamma_0$

With  $\gamma$  determined from (4.12), and  $\alpha$  determined by minimizing the error between modeled and measured concentration profiles, it is possible to obtain an optimal estimate of  $\gamma_0$  by comparing the reference concentration obtained from the time average of (4.6) times  $c_b$  with that obtained by extending the profiles calculated in Section 4.4.9 to the reference level. The ratio of the time average of (4.6) times  $c_b$  to the concentration evaluated at the reference level gives  $\gamma_0$ . Because (4.6) is dependent on the critical shear stress for the initiation of sediment motion, there is no a priori guarantee that threshold conditions will be exceeded. Under such circumstances, an estimate of  $\gamma_0$  is not possible. Model estimates of the reference concentration for the two bursts that gave  $\alpha$  estimates both produced a non-zero reference concentration. The values of  $\gamma_0$  for the two bursts are  $4.97 \times 10^{-4}$  and  $1.91 \times 10^{-2}$ . These span several orders of magnitude so that a procedure consistent with the above  $\alpha$  calibration, where the relative error was used to identify the best fit value, is to express the mean reference concentration as the geometric average from the two bursts. This gives a geometric mean  $\gamma_0$  of  $3.1 \times 10^{-3}$ .

#### 4.4.11 Summary of $\gamma$ , $\gamma_0$ and $\alpha$ estimates

The suggested method to calibrate  $\gamma$  presented in Section 4.4.3 was to obtain  $u_{*c}$  and  $b_1$  from the data, and then use (4.12) to derive an estimate. It should be noted, however, that the error in  $\gamma$  is directly proportional to the error in  $u_{*c}$  derived from (4.15) and  $b_1$  derived from (4.12). Essentially,  $\gamma$  is a function of the product  $u_{*c}$  and  $b_1$ , both

of which have quantifiable errors. Examination of Table 4.2 shows that the errors in  $u_{*c}$  range between  $\pm 31\%$  and  $\pm 54\%$  at the 95% level of significance. Errors associated with  $b_1$  also are shown, and range between  $\pm 3\%$  and  $\pm 5\%$  at the 95% level. For all cases, the error bound on  $u_{*c}$  is much greater than for  $b_1$ . Thus, the error for the product will be at least as great as the error for  $u_{*c}$ . The large errors associated with  $u_{*c}$  must be kept in mind in this calibration procedure; especially since it was shown in Section 3.9 that the neutral concentration solution is sensitive to changes in  $\gamma$ . In support of the estimates presented in Table 4.3, however, other studies have suggested that  $\gamma$  may be a function of grain size, with increases in grain diameter corresponding to decreases in  $\gamma$  (Hill et al. 1988; Villaret and Trowbridge 1991). Hill et al. (1988) reported 5 experiments where the grain size ranged from a minimum of 0.02 *cm* to a maximum of 0.032 *cm*, which represents grains slightly smaller than used to calibrate  $\gamma$  in this study. Taking the average of the Hill et al. (1988) equivalent of  $\gamma$  for these 5 experiments gives a mean of  $\gamma = 0.55$ , which is slightly higher than the average value 0.43 taken from Table 4.3. Because the Hill et al. (1988) values are for  $d \approx 0.03$  *cm* it is expected that their estimate of  $\gamma$  would be slightly larger than for the 0.04 *cm* grains used in this study.

Comparison of the measured and modeled concentration profiles further indicates that some previously reported values of  $\alpha$  may be too low for use in the field. Because  $\alpha$  is a free parameter, it must be verified through detailed profile comparisons which should include measurements within the transition layer as well as the current boundary layer. Even though a larger sample of high quality current and concentration measurements within the wave boundary layer are needed to better define  $z_1$ , and

associated  $\alpha$ , it is encouraging that the mean of 1.55 obtained from the data lies between 0.5 obtained by Madsen and Wikramanayake (1991) based on laboratory current measurements and 2.0 suggested by Lynch et al. (1997) based on field concentration measurements.

As previously mentioned, values of  $\gamma_0$  obtained in the past have spanned several orders of magnitude. This notwithstanding, it is encouraging that the average value of  $\gamma_0 = 3.1 \times 10^{-3}$  is close to the value suggested Wikramanayake and Madsen (1992). In their analysis they claimed that for  $\psi'/S_* < 0.18$ , where  $\psi'$  is based on the skin friction for the wave in the presence of a rippled bed,  $\gamma_0 = 1.8 \times 10^{-3}$ . In this study,  $\psi'$  is determined using the skin friction for combined wave and current flows, which is expected to dominate in the field. For both bursts,  $\psi'/S_*$  is less than 0.06, so that the order of magnitude estimate of  $\gamma$  for rippled beds is in accordance with the theory on which this analysis is based.

#### **4.5 Models of wave-formed ripples**

The instability mechanisms that govern the formation and evolution of wave-formed ripples is a process still not well understood; however, the geometrical characteristics of these ripples and how they respond to varying flow intensities has been studied extensively in the past (Bagnold 1946; Carstens et al. 1969; Mogridge and Kamphuis 1972; Inman 1957; and Dingler 1974). For oscillatory flow over a loose sediment bed, ripples begin to form once the flow strength increases beyond the minimum required to initiate sediment motion. Typically, these ripples appear as sharp crested, highly symmetrical, two-dimensional bedforms with crests aligned perpendicular to the direction of wave propagation. The above ripple studies have shown that ripple

length,  $\lambda$  (defined as the distance from crest to crest), scales with  $A_b$ , and that ripple steepness (defined as the ratio of ripple height,  $\eta$ , to  $\lambda$ ) is nearly constant. The range of flow conditions for which this scaling holds is called the equilibrium range. If the flow continues to increase, a thin, near-bed sediment transport layer forms and  $\eta$  and  $\lambda$  no longer scale with  $A_b$ . Grant and Madsen (1982) defined this as the breakoff region. At even higher flow rates ripples wash out leaving only the thin, near-bed transport layer.

For wave-dominated shelves during small storms, ripples are usually in equilibrium with the wave, and it is expected that  $k_b$  is a function of the ripple dimensions only. Due to the high correlation between ripple dimensions and wave parameters, a number of competing ripple geometry models have emerged (Nielsen 1981; Grant and Madsen 1982; Wikramanayake and Madsen 1991; Wiberg and Harris 1994; Traykovski et al. 1998). Wiberg and Harris (1994), using data sets obtained from both field (Inman 1957; Dingler 1974) and laboratory (Carstens et al. 1969; Kennedy and Falcon 1965; Mogridge and Kamphuis 1972; Dingler 1974) studies, concluded that for equilibrium conditions, which more or less corresponded to what they termed orbital ripples,  $\lambda$  scaled with the wave orbital diameter,  $d_o$  ( $\lambda = 0.62d_o$ , where  $d_o = 2A_b$ ) and ripple steepness was constant ( $\eta/\lambda = 0.17$ ). Traykovski et al. (1998) obtained similar results for ripples they measured at LEO-15 using an SSS, but with different values for the constants,  $\lambda = 0.75d_o$  and  $\eta/\lambda = 0.15$ . For stronger flows, Wiberg and Harris (1994) showed ripple length was proportional to grain size ( $\lambda = 535d$ ) and ripple steepness decreased with increasing flow intensity. Based on the available data, they developed a parametric model that related ripple steepness to  $d_o$  under these conditions. The end



result was a ripple geometry model valid for a wide range of flow conditions, with wave orbital diameter and sediment grain size the only needed input parameters.

Although the Wiberg and Harris (1994) model approximates ripple length and steepness reasonable well for a wide range of flow conditions, dimensional analysis suggests that other factors such as sediment size and type ( $d$  and  $\rho_s$ ) and fluid properties ( $\rho_w$  and  $\nu$ ) are also important in determining ripple geometry. Wikramanayake and Madsen (1991) reviewed several fundamental non-dimensional parameters commonly used in ripple geometry studies and found that the ratio of the mobility number,

$$\theta_m = \frac{u_b^2}{(s - 1) g d} \quad (4.20)$$

to the non-dimensional sediment parameter defined previously,

$$S_* = \frac{d}{4 \nu} [(s - 1) g d]^{1/2} \quad (4.21)$$

was well correlated with available field data, i.e.,

$$\frac{\eta}{A_b} = \begin{cases} 0.27 X^{-0.5} & X \leq 3 \\ 0.52 X^{-1.1} & X \geq 3 \end{cases} \quad (4.22)$$

$$\frac{\lambda}{A_b} = \begin{cases} 1.7 X^{-0.5} & X \leq 3 \\ 2.1 X^{-0.7} & X \geq 3 \end{cases}$$

where the non-dimensional wave and sediment parameter,  $X$ , is defined as

$$X = \frac{\theta_m}{S_*} = \frac{4 \nu u_b^2}{d [(s-1)g d]^{1.5}} \quad (4.23)$$

For  $X < 3$  in the above formulations, the  $-0.5$  exponent for  $X$  results in expressions for  $\eta$  and  $\lambda$  that are independent of water depth and  $A_b$ , and become functions only of the wave period. This is a physically unreasonable result for the continental shelf under equilibrium conditions when the ripples are known to scale with  $A_b$ . As a result,  $\eta/A_b$  and  $\lambda/A_b$  are recalibrated using the field data obtained by Traykovski et al. (1998) at LEO-15 and the data used by Wikramanayake and Madsen to obtain (4.22).

#### 4.5.1 Recalibration of $\eta$ and $\lambda$

Wikramanayake and Madsen (1991) used three independent field data sets to arrive at (4.25). The data sets, originally collected by Inman (1957), Dingler (1974) and Nielsen (1984), were reproduced in tabular form in Wikramanayake and Madsen (1991). Each of the three investigators collected sediment grain size, ripple height and length, wave height and period, and Dingler (1974) and Nielsen (1984) also recorded water temperature. Wikramanayake and Madsen (1991) converted the originally measured wave heights to  $A_{brms}$ , which is the root mean square maximum near bottom orbital amplitude. The *rms* maximum bottom orbital amplitude is easily converted to the equivalent near bottom wave orbital amplitude since  $A_b = \sqrt{2} A_{brms}$ . This, along with  $\omega$ , are used to compute  $u_b$  in (4.23). The experimental details of how these data sets were collected can be reviewed by consulting the original references.

During the 1995 deployment, measurements of ripple height and length were obtained using an SSS (Traykovski et al. 1998). The instrument recorded sea-floor images every 30 minutes during the course of the deployment. Peter Traykovski of the WHOI analyzed the images to produce time series of both ripple height and ripple length. A description of the methods used to convert images to ripple geometry estimates is found in Traykovski et al. (1998). Supporting wave, current and sediment measurements from the 1995 experiment needed to calculate (3.23) are described in Section 4.4. All four data sets are combined into one representative data set to determine  $\eta/A_b$  and  $\lambda/A_b$  as a function of  $X$ . The method to determine the best fit is adopted from Wikramanayake and Madsen (1991) who used the relative error as defined in (4.19).

As part of the recalibration study, the cutoff,  $X = 3$ , determined by Wikramanayake and Madsen (1991) was varied between a maximum of 5 and a minimum of 0.5. The value that produced the lowest  $e$ , as measured from (4.19), was designated the new cutoff point. The results of the recalibration are depicted in Figure 4.10. Noticeable is the natural extension of the Traykovski et al. (1998) data set for smaller  $X$  where the data used by Wikramanayake and Madsen (1991) are more scarce. A natural cutoff at  $X = 2$  gives the lowest overall error for both  $\eta/A_b$  and  $\lambda/A_b$ , with values of 1.31 and 1.25, respectively. Equivalent errors calculated by Wikramanayake and Madsen (1991) for  $X = 3$  are 1.88 for  $\eta/A_b$  and 1.75 for  $\lambda/A_b$ . Close inspection of the best fit curve at  $X = 2$  reveals a slight discontinuity for lines calibrated using the data less than and greater than 2. The error at the matching point, however, is less than 0.01% for  $\eta/A_b$  and less than 5% for  $\lambda/A_b$ . Therefore, the best fit curve shown in Figure

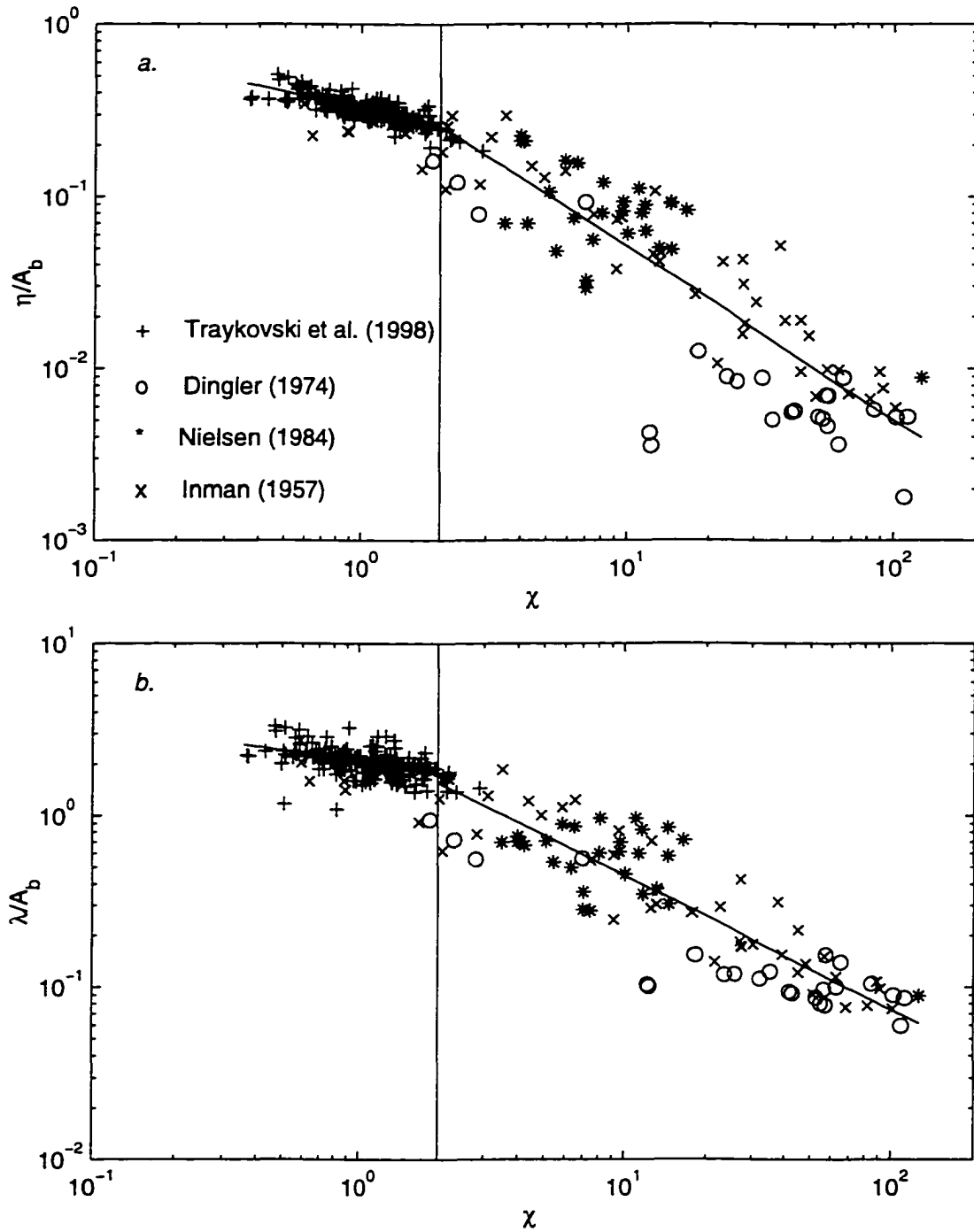


Figure 4.10 (a) Relative ripple height,  $\eta/A_b$ , as a function of the non-dimensional wave and sediment parameter,  $\chi$ . Solid line indicates best-fit curve for the data sets listed. (b) Same as (a) showing relative ripple wavelength ( $\lambda/A_b$ ) as a function of  $\chi$ . Vertical line marks  $\chi = 2$ .

4.10 replaces the original equation developed by Wikramanayake and Madsen (1991) and is given by,

$$\frac{\eta}{A_b} = \begin{cases} 0.32 X^{-0.34} & X \leq 2 \\ 0.52 X^{-1.01} & X \geq 2 \end{cases} \quad (4.24)$$

$$\frac{\lambda}{A_b} = \begin{cases} 2.04 X^{-0.23} & X \leq 2 \\ 2.70 X^{-0.78} & X \geq 2 \end{cases}$$

Because none of the exponents of  $X$  in (4.24) are  $-0.5$ ,  $\eta$  and  $\lambda$  remain functions of  $A_b$  as expected. As an upper bound, Wikramanayake and Madsen (1991) state that (4.22) is valid for  $X$  as large as 50. For the plot shown in Figure 4.10, however, it appears that (4.24) is valid up to about  $X = 100$ . In addition, for  $X > 2$ , the decay in  $\eta$  is nearly proportional to  $1/A_b$ . Thus, above the cutoff point,  $X = 2$ , ripple height begins to decay as the wave becomes stronger. This is consistent with earlier statements concerning the measured behavior of wave-formed ripples for conditions beyond the equilibrium range. For such conditions, a point will be reached where  $\eta$  no longer scales with  $A_b$  but begins to decay with increasing wave energy. This is exactly the behavior of  $\eta$  when  $X$  is greater than 2, and provides a possible first look at the functional relationship between  $\eta$  and  $A_b$  for conditions beyond the equilibrium range.

#### 4.6 Bottom roughness for combined wave and current flows

In general, sources of flow roughness on the continental shelf can be categorized as either skin friction associated with flow over individual sediment grains, or form drag

associated with flow over bedforms. Typical examples of form drag in the marine environment include wave-formed ripples and biologically generated bedforms. The degree to which biological activity can significantly influence the spatially averaged hydrodynamic roughness is difficult to quantify for all continental shelf regions. It is generally believed, however, that bedforms associated with biological activity are more prominent in areas comprised of soft silt or mud, i.e.,  $d \leq 0.006 \text{ cm}$ , where  $d$  is the sediment grain diameter (Grant et al. 1982; Nowell et al. 1981; Rhodes and Boyer 1982). Beds comprised of coarser sediment usually occupy high energy flow environments, and it is suspected that bottom roughness is dominated by processes associated with the flow. At LEO-15, the bed is primarily composed of medium sized sand ( $d \cong 0.02\text{-}0.05 \text{ cm}$ ), so the effects of biologically generated bedforms on bottom roughness are probably less important. This would certainly be true during storms when such bedforms would be quickly eroded. In the absence of wave-formed ripples, sand grains are considered the dominant roughness elements and  $k_b$  is proportional to  $d$ . For most continental shelf flows of interest, however, wave action at the surface causes ripples to form on the bottom. In general, these ripples are several orders of magnitude greater in height than  $d$  so that bottom roughness on wave dominated shelves is usually scaled by the ripples. During extreme events, ripples wash out so that the characteristic length scale of the ripples is no longer an adequate measure of  $k_b$ . Under these conditions, a thin, heavily concentrated near-bed sediment transport layer develops, and bottom roughness becomes a function of the thickness of this layer.

#### 4.6.1 Review of bottom roughness models

Past studies of oscillatory flows over a movable bed for equilibrium conditions reveal that bottom roughness is proportional to the ripples created by the wave motion (Grant and Madsen 1982; Wikramanayake and Madsen 1991). To calculate  $k_b$  under these conditions, independent estimates of  $z_0 = k_b/30$  and the ripple parameters  $\eta$  and  $\lambda$  are required. In laboratory experiments,  $\eta$  and  $\lambda$  are easily obtained by visual inspection of the wave-generated bedforms, while in the field, ripple geometry can be measured accurately using acoustical instruments like the SSS, or directly by underwater cameras or divers. Because  $z_0$  is a function of the hydrodynamic characteristics of the flow, direct measurements are difficult to make, and investigators typically must rely on some supporting flow or wave energy dissipation model (Wikramanayake and Madsen 1991). As a result, most bed roughness models are derived using directly measured bedforms with  $z_0$  determined from an independent flow model.

Models that express bottom roughness exclusively in terms of ripple geometry are generally of two basic forms. The first relates bottom roughness to the product of ripple height and ripple steepness ( $\eta\eta/\lambda$ ), while the second relates bottom roughness to ripple height only. For equilibrium conditions, it has been noted that ripple steepness is nearly constant, suggesting that the only relevant length scale is the height of the ripples. Wikramanayake and Madsen (1991) reviewed available ripple and oscillatory flow data and found that  $k_b$  was well represented by the simple formula  $k_b = 4\eta$ . This expression was obtained for regular waves in a flume with both artificial and natural bottom roughness elements using the Grant and Madsen (1986) wave friction factor model to calculate  $k_b$ . Rankin (1997), using a shear plate to measure bottom stress in a sand laden

wave flume, showed good agreement between her  $f_w$  measurements and the theoretical friction factor curve obtained by Grant and Madsen (1979) using  $k_b = 4\eta$  for  $A/k_b \geq 1$ . Mathisen and Madsen (1996a) conducted a detailed laboratory experiment to determine  $k_b$  for pure waves, pure currents and waves in the presence of currents. Using artificial roughness elements for co-directional flow only, along with the Grant and Madsen (1986) bottom boundary layer model and a wave energy dissipation model based on second-order Stokes' theory, they found that  $k_b$  was proportional to the height of the roughness elements and that a single length scale was valid for pure waves, pure currents, and waves in the presence of currents. In a companion paper, Mathisen and Madsen (1996b) further showed that the same roughness length could be used to describe the current roughness in the presence of waves if the wave boundary layer height was adjusted, and the steady streaming at the edge of the wave boundary layer due to the waves was taken into account. In all their experiments for currents, it was found that  $k_b$  was proportional to  $\eta$  with the proportionality constant ranging between 7-16. Although this range is somewhat higher than suggested above, it should be noted that they used artificial roughness elements which may produce a larger roughness than expected for equilibrium ripples. The point is that a single length scale proportional to the height of the roughness elements provides an accurate model for pure waves, pure currents, waves in the presence of currents and currents in the presence of waves for unidirectional flows using artificial roughness elements that approximate the geometry of wave-formed ripples.

On the continental shelf, irregular waves and directional spreading are prominent and may affect the bottom roughness in a manner not measurable within a laboratory flume. For example, ripples in the field formed by irregular waves are usually more



round crested, and it is hypothesized that the roughness due to these generally smoother bedforms will differ from values obtained in the laboratory. In addition, waves flowing at arbitrary angles to the current will influence the roughness experienced by the mean flow in a manner not consistent with unidirectional flows, since the effective wavelength of the ripples, as viewed by the mean current, can be much greater than  $\lambda$ . Under these conditions, a directionally independent roughness model that is uniquely a function of  $\eta$  may not accurately represent the spatially averaged bottom roughness experienced by the mean flow. Sorenson et al. (1995) found that the formula  $k_b = 6\eta[|\cos\phi_{cw}|]^{1.2}\beta_0$  was a better predictor for the field, where  $\beta_0$  is a constant with an average value equal to 0.19. For unidirectional flows, this gives  $k_b = 1.14\eta$ , which is lower than the typical value,  $k_b = 4\eta$ , quoted in the past (Wikramanayake and Madsen 1991). While the Sorenson et al. (1995) formula still maintains a linear relation between  $\eta$  and  $k_b$ , it also includes a term to describe the effects of waves and currents flowing at arbitrary angles, which is the case generally encountered in the field.

#### **4.6.2 Bottom roughness in the presence of a near-bed transport layer**

For stronger flows, ripples wash out so that ripple height is no longer a meaningful characteristic length scale. Under these conditions, studies have shown that a heavily concentrated near-bed transport layer develops, and that bottom roughness is proportional to the thickness of this layer (Smith and McLean 1977; Grant and Madsen 1982; Dietrich 1982). Based on analogies with saltating grains in the atmospheric boundary layer (Owen 1964), Grant and Madsen (1982) developed an semi-empirical model relating  $k_b$  to the thickness of the transport layer. To obtain an analytical expression they simply partition the bottom roughness into a contribution from the

ripples,  $k_r$ , and a contribution from the near-bed transport layer,  $k_t$ . The total roughness is then defined as  $k_b = k_r + k_t$ . In their model,  $k_t$  is proportional to the thickness of the near bed transport layer which is related to the bed shear stress based on a flow roughness proportional to grain size. Similar expressions for steady flows have been obtained by Smith and McLean (1977).

Based on a re-analysis of sheet flow data collected by Guy et al. (1966), Wiberg and Rubin (1989) showed that both the Grant and Madsen (1982) and Smith and McLean (1977) models overestimated  $k_t$  by as much as an order of magnitude. To obtain results that were consistent with the Guy et al. (1966) data, Wiberg and Rubin (1989) used a modified version of a  $k_t$  formulation originally developed by Dietrich (1982). Wilson (1989) found that the equivalent roughness,  $k/d$ , due to sheet flow was linearly proportional to the Shields parameter,  $\psi$ ,

$$\frac{k_t}{d} = 5 \psi' = \frac{5 |\tau_b'|}{\rho (s - 1) g d} \quad (4.25)$$

where  $\tau_b'$  is the bottom shear stress calculated using a roughness that is proportional only to grain size. The high quality of his linear fit implies the equivalent roughness is independent of grain size for the medium to coarse grains Wilson (1989) used. More recently, Tolman (1994) showed the  $k_t$  model of Wilson (1989) to be in qualitative agreement with the re-analysis of Wiberg and Rubin (1989). Because the Wilson (1989) model relates  $k_t$  to the independent wave parameters  $u_b$  and  $A_b$ ,

$$\frac{k_r}{d} = \frac{5 |\tau_b|}{\rho (s - 1) g d} = \frac{2.5 c_{fw} u_b^2}{(s - 1) g d} \quad (4.26)$$

where

$$c_{fw} = 0.114 \left( \frac{A_b}{(s - 1) g T_w^2} \right)^{0.4} \quad (4.27)$$

and not the shear stress like the Wiberg and Rubin (1989) and Dietrich (1982) models, it is adopted for this study. Correcting for misprints in Tolman's (1994) paper, the relative roughness for sediment transport is given by

$$\frac{k_r}{A_b} = 0.0655 \left( \frac{u_b^2}{(s - 1) g A_b} \right)^{1.4} \quad (4.28)$$

Because the individual contributions to the total roughness from ripples, individual grains, and the near-bed transport layer are expected to dominate for non-overlapping flow and sediment conditions, the three sources can be treated independently. Under this assumption, the full bottom roughness model is expressed as the sum of  $k_r$  and  $k_p$  which are defined in (4.24) and (4.28), respectively, and  $d$ .

#### 4.7 Field estimates for $k_b$

Because several models for both ripples and  $k_b$  have been presented, field measurements obtained at LEO-15 are used in conjunction with the BBLM to determine which combination of ripple and bottom roughness formulations are the most accurate.

This is an important issue since several of the methods used to arrive at the  $k_b$  formulas presented above are derived using the Grant and Madsen (1986) two layer eddy viscosity model, which is qualitatively different from the 3-layer model presented here.

#### 4.7.1 Flow data

Two flow data sets, both obtained using the BASS instrument, are chosen to determine  $k_b$ . The first includes the 1995 deployment described above and the second is during a 17-day period in August 1994. The 1994 deployment is chosen because the experiment captured an early northeaster, and the 1995 deployment is chosen because ripple height and length were measured in conjunction with the current.

#### 4.7.2 Bottom roughness estimates for the 1994 experiment

Figure 4.11 shows time series of  $u_b$  and  $u_r$  for the 1994 deployment obtained from BASS pod 1 located 55 cm above the bottom. The obvious features are the passage of three events centered on year day 227, 231 and 235 which coincide with Tropical Storm Beryl, Hurricane Chris and an early northeaster, respectively. In order to limit the confidence band on  $u_{*c}$  to  $\pm 25\%$ , Grant et al. (1984) showed that  $R^2$  must be greater than 0.993 at the 95% level of significance using a four current meter BASS array similar to the one used in this study. Drake and Cacchione (1986), using a different measuring system but one also equipped with four current meters, used as their limiting criteria  $R^2 > 0.98$ , which gives a confidence band of  $\pm 43.5\%$  at the 95% level of significance. For this study, a minimum  $R^2$  value of 0.99 is chosen, giving a confidence band on  $u_{*c}$  of  $\pm 31\%$  at the 95% level of significance. For each 15 minute burst,  $R^2$  values were calculated to identify profiles that were highly logarithmic. Again the data were checked

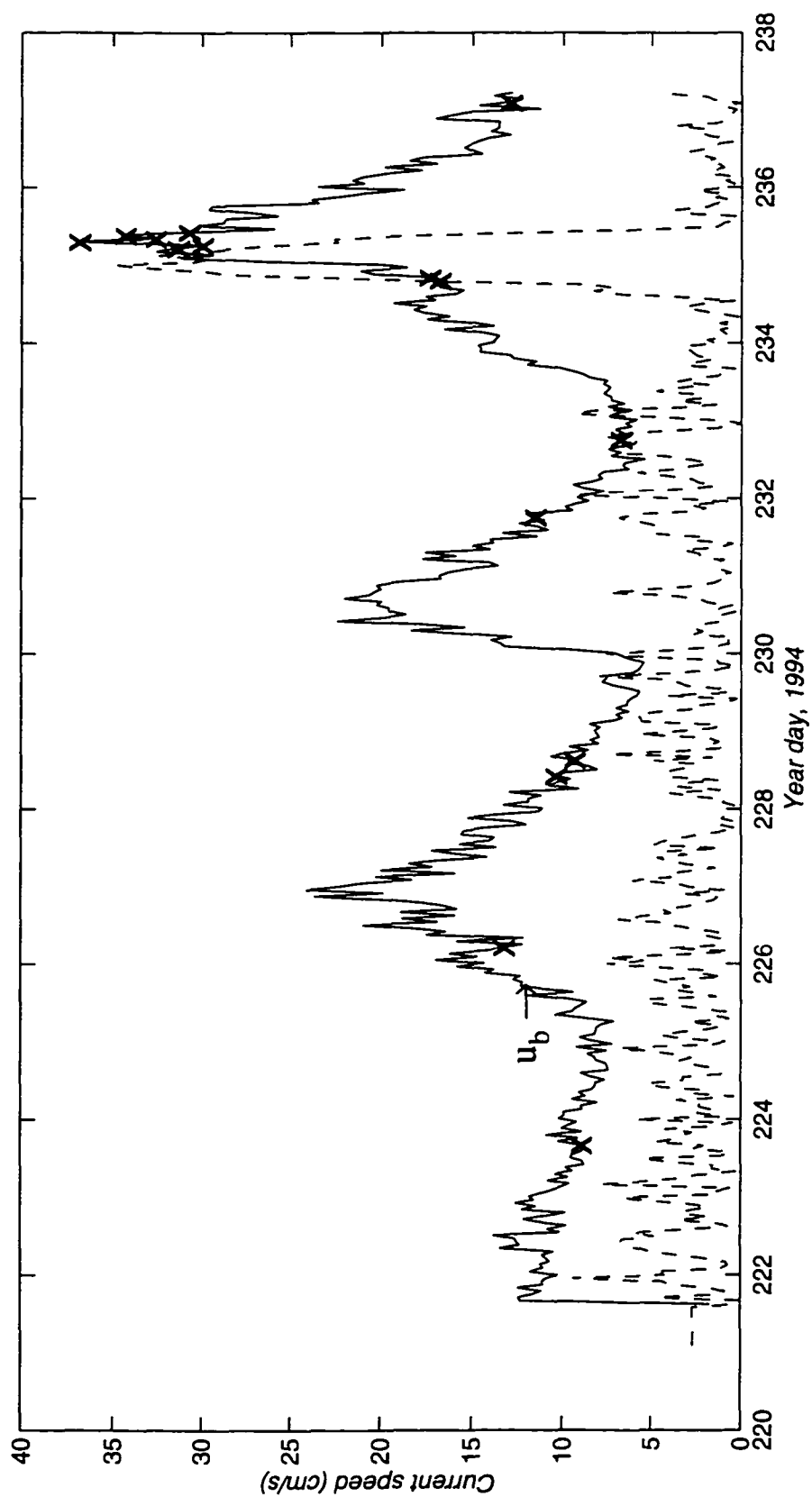


Figure 4.11 Time series of  $u_b$  and  $u_r$  for the 1994 deployment. The X's identify bursts with  $R^2 > 0.99$

for tripod settling, which was determined to be negligible. From the full record, a total of 15 produced  $R^2 \geq 0.99$ , which are also identified in Figure 4.11.

Figure 4.12 shows  $u_{*c}$  and  $z_{0c}$  calculated from the neutral version of the BBLM, as described in Section 3, and the ripple geometry model (4.24). Also shown are the shear stress and apparent roughness measured by the BASS for the 15 chosen bursts. It is seen that the bottom roughness formula of Sorenson et al. (1995) under estimates the bed roughness in all cases. In order to obtain results that better agree with the data,  $\beta_0$  was set equal to 0.5 for the modified Wikramanayake and Madsen (1991) model. After this modification, the model accurately predicts the shear stress and apparent hydraulic roughness for most of the storm (Figure 4.13c, d) but still under estimates during the other time periods (Figure 4.13a, b).

The fact that the model consistently under estimates  $u_{*c}$  during the pre-storm time period (Figures 4.12 and 4.13) can be explained through the model's inability to represent the bottom roughness. A necessary condition for the ripple geometry model to accurately predict ripple height is that the boundary stress be great enough to move sediment. During times of low wave and current activity, the minimum shear stress for the initiation of sediment motion will not be exceeded. Under these conditions, the ripples cannot be considered in equilibrium and the ripple geometry models will fail to provide an accurate estimate of  $\eta$ . For all chosen bursts prior to year day 235 and after year day 236, the minimum shear stress for the initiation of sediment motion is not exceeded. Because  $z_{0c}$  is under estimated during these bursts, so is the bottom roughness. One possible explanation is that ripples formed during some past event strong enough to move sediment, and thus create equilibrium conditions, are acting as relic roughness elements.

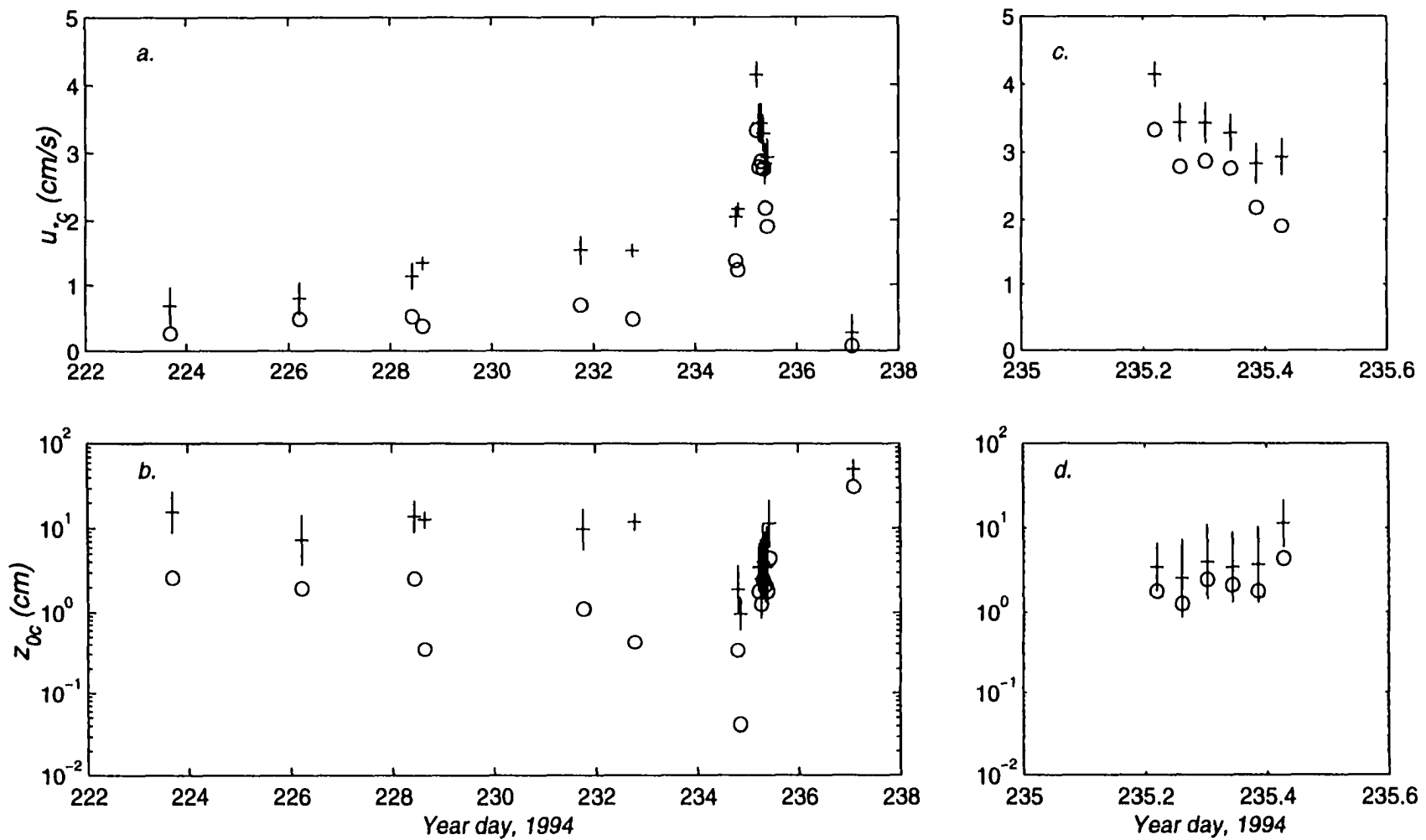


Figure 4.12 Comparison of measured and modeled  $u_{*c}$  and  $z_{0c}$  for bursts that indicate  $R^2 > 0.99$  for the 1994 deployment using the Sorenson et al. (1995) bottom roughness equation. (a) measured (+) and modeled (open circles)  $u_{*c}$ . (b) same as (a) showing  $z_{0c}$ . (c) and (d) are enlargements of (a) and (b), respectively during the storm. Error bars indicate 95% confidence.

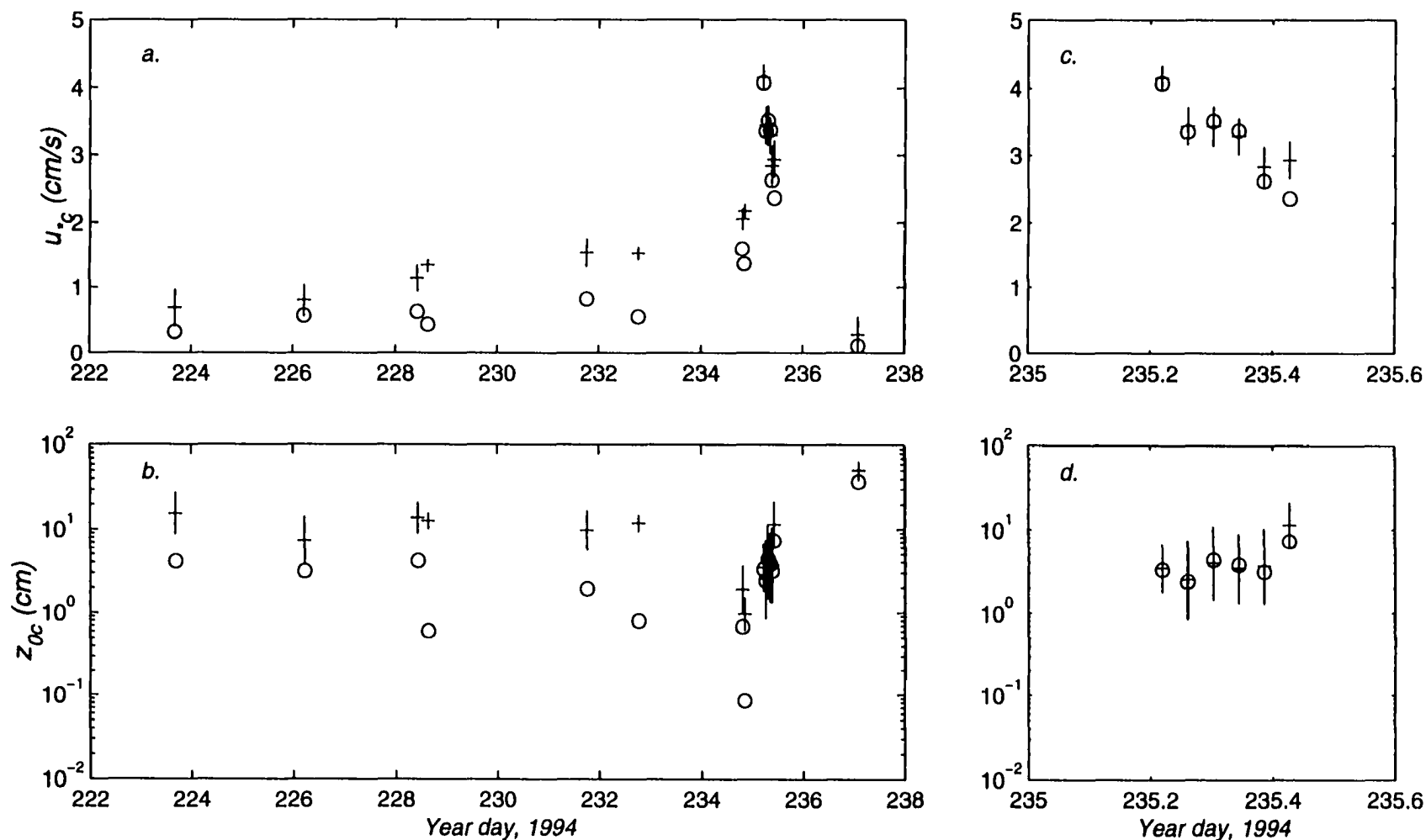


Figure 4.13 Same as Figure 4.12 but with the parameter  $\beta_0$  set equal to 0.5 to give a better comparison between the model and data during the storm.



These relic ripples could be larger than the ripples predicted by the model for the time periods indicated and subsequently could be responsible for generating a larger bed roughness. Inspection of Figure 4.11 indicates that bursts on days 228.4, 228.6, 231.8 and 232.8 are on the trailing side of two wave events, so the existence of relic ripples is likely. If  $\eta$  values derived from the peak of the two events just prior to year day 228.4 and 231.8, respectively, are input into the model,  $u_{*c}$  estimates are increased but are still not as accurate as during the final storm on year day 235. Because the ripple geometry model is not valid for flow conditions too weak to move sediment, and the fact that no direct measurements of the bed forms during this experiment are available, it is not possible to unequivocally establish from this data set alone why the model tends to under estimate  $u_{*c}$  during these times. It is highly likely, however, that the existence of relic ripples plays an important role in determining bottom roughness during times of relatively weak combined wave and current activity.

#### **4.7.3 Bottom roughness estimates for 1995 experiment**

Although the 1994 data indicate the model is accurate during a small storm, a more extensive set of measurements obtained during the second deployment in 1995 are used to further gauge the predictive capabilities of the model for a wider variety of flow conditions. Figure 4.14 shows  $u_b$  and  $u_r$  calculated from pod 1, which for this deployment is located 45 *cm* above the bottom. An interesting feature of this data set are the relatively high  $u_b$  values for nearly half of the deployment beginning on year day 240 and continuing until year day 255. Examination of weather records (WXP, Purdue University 1997) indicate a period of extended hurricane activity in the North Atlantic during this time period. Although none of these storms reached the New Jersey coast,

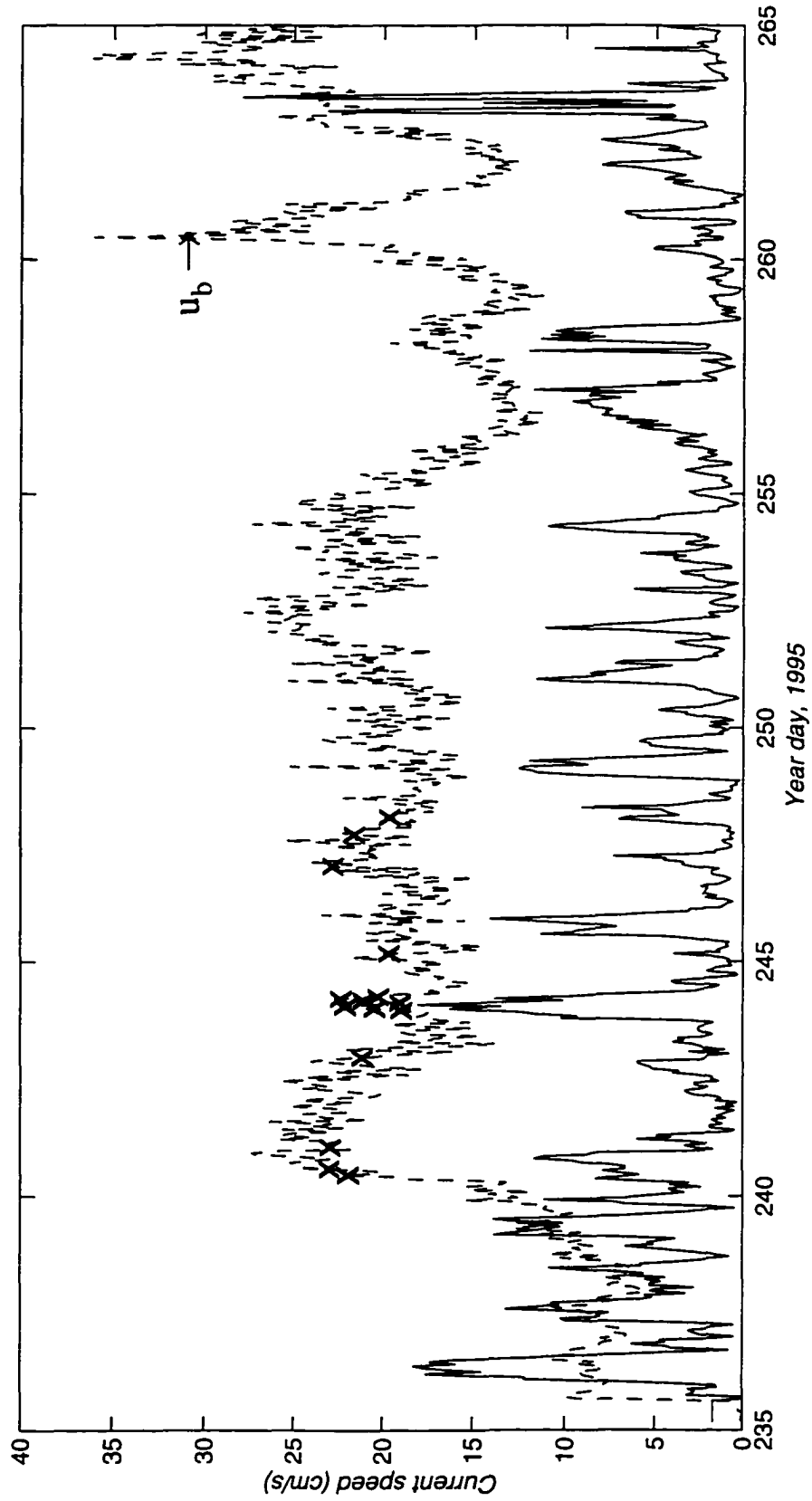


Figure 4.14 Time series of  $u_b$  and  $u_r$  for 1995 deployment. The X's identify bursts with  $R^2 > 0.99$

swell associated with these events did increase wave activity at LEO-15, giving a fortuitous opportunity to examine boundary layer flows for an extended period of wave dominated conditions.

Figure 4.15 shows time series of modeled and measured  $u_{*c}$  and  $z_{0c}$  using the same  $R^2$  criteria established for the 1994 data. Because the ripple geometry model is accurate only when sediment is in motion, the comparison is restricted to time periods that the model indicates sediment resuspension. From the figure it is seen that the modeled and measured  $u_{*c}$  and  $z_{0c}$  values agree relatively well for a majority of the time periods shown. Major exceptions include bursts on day 242.9, 247.0 and 248.1, where the model consistently under estimates both  $u_{*c}$  and  $z_{0c}$ . During these bursts, the direction between the wave and current are 64, 83 and 88 degrees, respectively, which indicates that the wave induced and mean current on year day 247.0 and 248.1 are at near right angles. Because these three bursts represent the greatest direction between the wave and current for the whole record, it is suspected that the directional dependence may not be properly accounted for. If a directionally independent bottom roughness model ( $k_r = 3\eta$ ) for these three bursts is used, then the comparison between the measured and modeled  $u_{*c}$  and  $z_{0c}$  is improved (Figure 4.16). This suggests that the modified Sorenson et al. (1995) model may not accurately represent bottom roughness during these time periods. One possible explanation is that when the wave and current are at near right angles, the effects of the wave-formed ripples are not properly accounted for.

The reasoning which suggests bottom roughness is directionally dependent is based on a description of the mean flow where individual water particle trajectories are not taken into account. If all that is present is a mean flow parallel to the ripple crests,

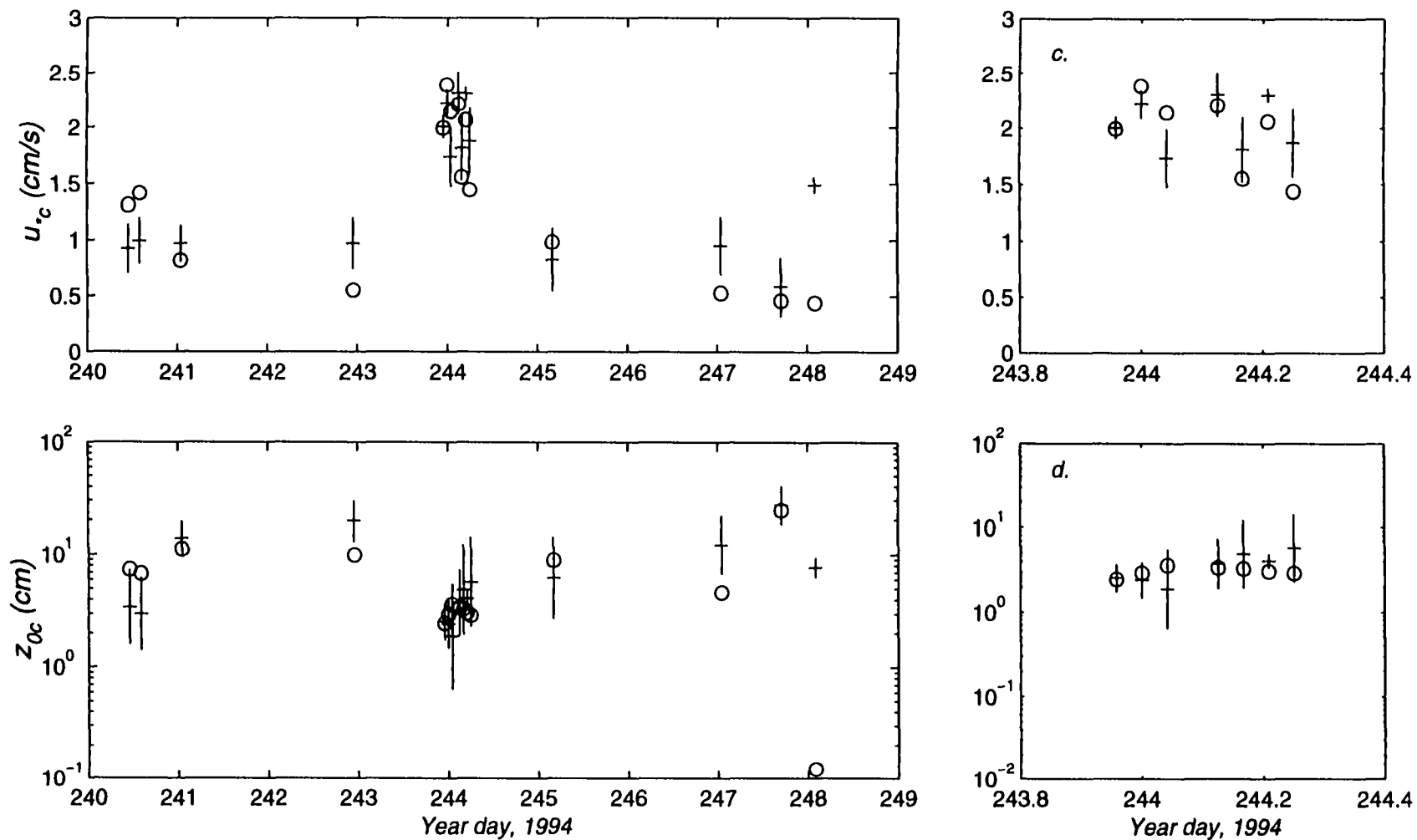


Figure 4.15 Comparison of  $u_{*c}$  and  $z_{0c}$  for the 1995 deployment using the modified Sorenson et al. (1995) bottom roughness equation. (a), measured (+) and modeled (open circles)  $u_{*c}$ . (b) same as (a) showing  $z_{0c}$ . (c) and (d) are enlargements of (a) and (b), respectively, during a small event clustered around year day 244. Error bars indicate 95% confidence.

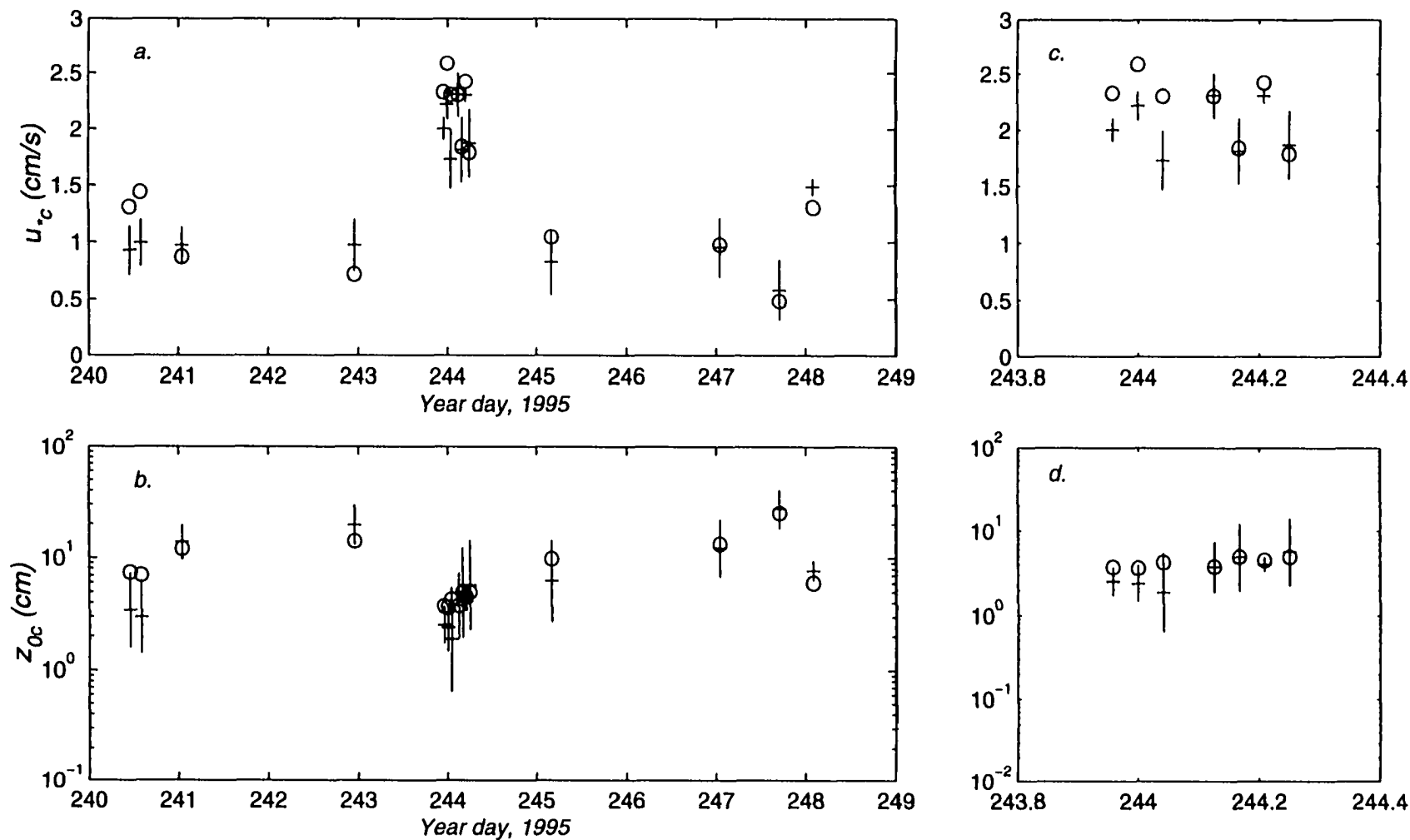


Figure 4.16 Same as Figure 4.15 using the directionally independent bottom roughness model ( $k_r = 3\eta$ ). Note the higher correlation between measured and modeled values for year day 242.9, 247.0 and 248.1 as compared to those shown in Figure 4.15.

an individual water particle traveling along a ripple crest, or trough, will sense a roughness due primary to the individual grains. In flows where the wave and current are at near right angles, and in the usual case where the ripple crests are aligned with the wave crests, a water particle will be advected back and forth along lines running perpendicular to the ripple crests due to the superimposed wave motion. While the mean motion may be along the ripple crest, the water particles actually are carried at right angles to the mean flow direction and, during the first half of the wave cycle, may cross over a neighboring ripple trough or even as far as an adjacent ripple crest before it returns to its center point. During the second half of the wave cycle the particle will be carried in the opposite direction, again passing over adjacent ripple troughs and crests. The effect of the ripples will be maximized if the relative strength of the wave is much greater than the current, and minimized if the current is the same order of magnitude or greater than the wave. This means that wave-formed ripples, during wave dominated conditions, may influence the spatially averaged mean current roughness even when  $\phi_{cw}$  is near 90 degrees.

#### **4.7.4 Reevaluation of bottom roughness for a rippled bed**

In light of the need to adjust the parameter multiplying  $\eta$  in the bottom roughness model, combined with the fact that the directionally dependent model of Sorenson et al. (1995) does not appear to be universally applicable, a reevaluation of  $k_b$  using the data sets discussed above is presented.

One weakness in the Sorenson et al. (1995) model may be the explicit dependence of the bottom roughness on the angle between the wave and current. As shown above, during wave dominated conditions, the time average shear velocity is more accurately

described in terms of a directionally independent model rather than as a function of  $\phi_{cw}$ . The idea, however, that  $k_b$  should be a function of both the wave and current is probably more in tune with the underlying physical principles. One possibility that takes into account both the direction and the relative strength of the wave and current is to express  $k_b$  in terms of the angle between the ripples (i.e., the wave direction) and the combined flow. For periods when the wave is much stronger than the current, and the direction between the two is near 90 degrees, the roughness felt by the mean flow, as water particles advect back and forth across lines running perpendicular to the ripple crests, will be substantially influenced by the stronger wave. If, however,  $\phi_{cw}$  is near 90 degrees but the current stress is strong relative to the wave, then the roughness will be more accurately described using the individual grains, as the height of wave-formed ripples are probably in a state of decay. With this in mind, the angle which defines the direction between  $\tau_{wm}$  and  $\tau_{cw}$ ,  $\phi_\tau$ , replaces  $\phi_{cw}$  in the Sorenson et al. (1995) bottom roughness model.

In order to reevaluate bottom roughness using the data sets from the 1994 and 1995 deployments, it is necessary to obtain  $k_b$  independent of ripple height. This is achieved by running the BBLM with  $u_{*c}$  and  $z_{0c}$  estimates derived from the data, and back calculate  $k_b$ . As was done to determine the values of  $\alpha$ ,  $u_{*c}$  and  $z_{0c}$  are given and  $k_b$  is the initially unknown parameter which is solved through iteration until  $z_{0c}$  calculated from the model matches that measured by the BASS. For both the 1994 and 1995 data,  $k_b$  is determined from the BBLM along with  $\phi_\tau$  and  $\phi_{cw}$ . Taking the ratio of  $k_b/\eta$ , where  $\eta$  is derived from (4.24), and plotting as a function of  $\cos\phi_{cw}$  and  $\cos\phi_\tau$  gives the results shown in Figure 4.17. A discernable pattern in which  $k_b/\eta$  is a function of either  $\cos\phi_{cw}$

or  $\cos\phi_\tau$  is not apparent in the plot. A more accurate statement would be that  $k_b/\eta$  is independent of either parameter with an average value of about 2.3. It should be noted, however, that  $\cos\phi_\tau$  is near 1 for all cases shown. This means that for both data sets, the relative strength of the wave, as expressed by  $\phi_\tau$ , is much greater than the current. Under these circumstances, it is not possible from this data set alone to determine the directional dependence of the bottom stress. Therefore, the functional form of the directionally dependent model of Sorenson et al. (1995) cannot be determined here and will remain unchanged with the exception that  $\phi_{cw}$  is replaced by  $\phi_\tau$ , and the constant multiplying  $\eta$  is set to 2.3.

Figure 4.18 shows  $u_{*c}$  and  $z_{0c}$  calculated using both  $k_r = 2.3\eta[|\cos\phi_{cw}|]^{1.2}$  and  $k_r = 2.3\eta[|\cos\phi_\tau|]^{1.2}$ . The estimates obtained using  $\phi_\tau$  are a slight improvement over those obtained using  $\phi_{cw}$ . A similar trend occurs for the 1995 data (Figure 4.19), where the estimates obtained using  $\phi_\tau$  are much more accurate for the two cases on year day 247.0 and 248.1 where  $\phi_{cw}$  is 83 and 88 degrees, respectively. The limited model/data comparisons presented here supports the use of  $\phi_\tau$  over  $\phi_{cw}$ , yet emphasize the strong need for controlled studies on movable bed roughness for waves and currents flowing at arbitrary angles.

In summary, the model proposed here uses the modified Sorenson et al. (1995) bottom roughness formula ( $k_r = 2.3\eta[|\cos\phi_\tau|]^{1.2}$ ) to calculate  $k_r$  and (4.24) to calculate  $\eta$ . Although this model is formally limited for flows in which  $\eta$  is the dominant roughness parameter, the extension beyond the equilibrium range is probably not a significant violation of the theory due to the findings of Wikramanayake and Madsen (1991), and Sorenson et al. (1995), who claim that using  $\eta$  as the only roughness length



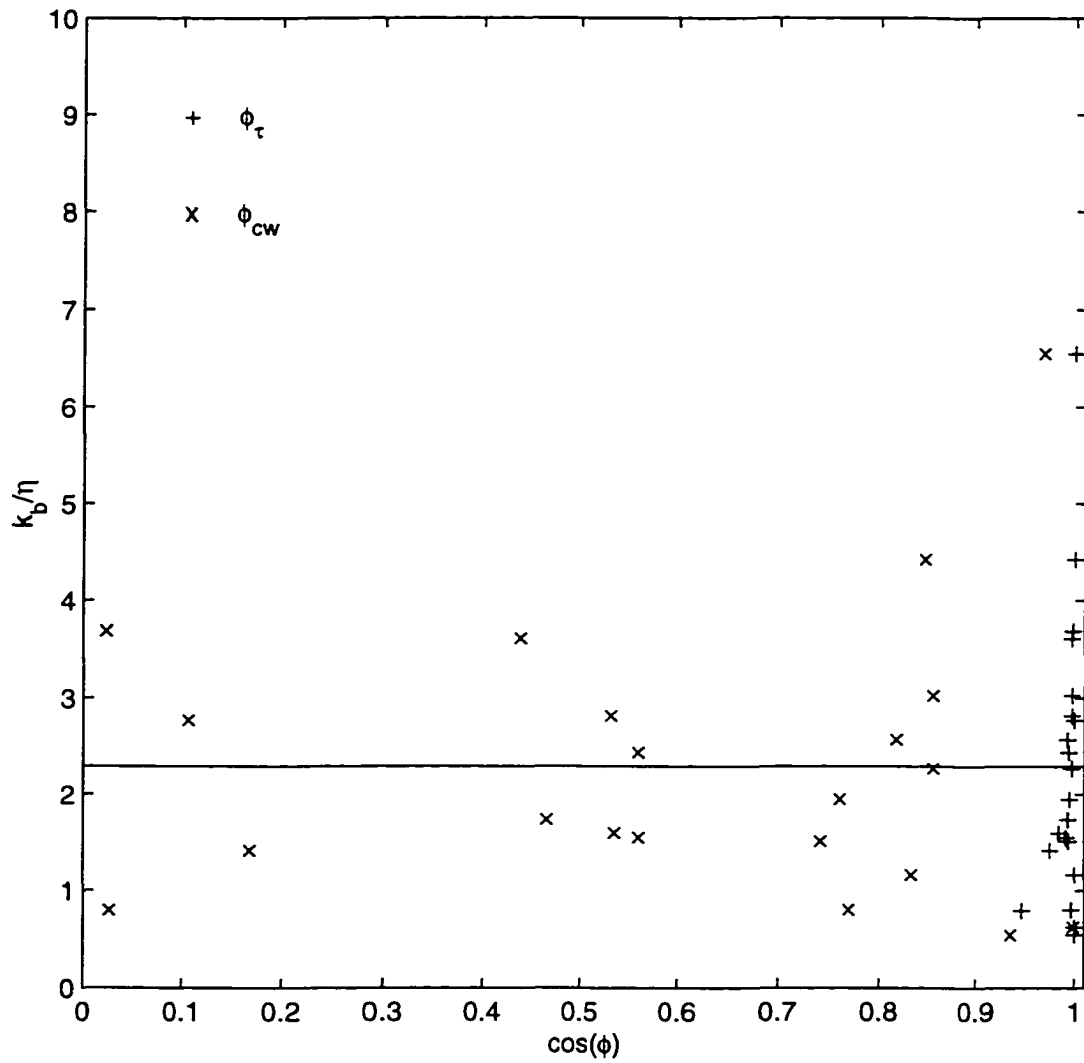


Figure 4.17 Non-dimensional bottom roughness  $k_b/\eta$  as a function of  $\cos\phi$  derived from chosen bursts in 1994 and 1995.  $\phi_\tau$  is the angle between the wave and the combined wave and current shear stress components, and  $\phi_{cw}$  is the angle between the current and wave velocities.

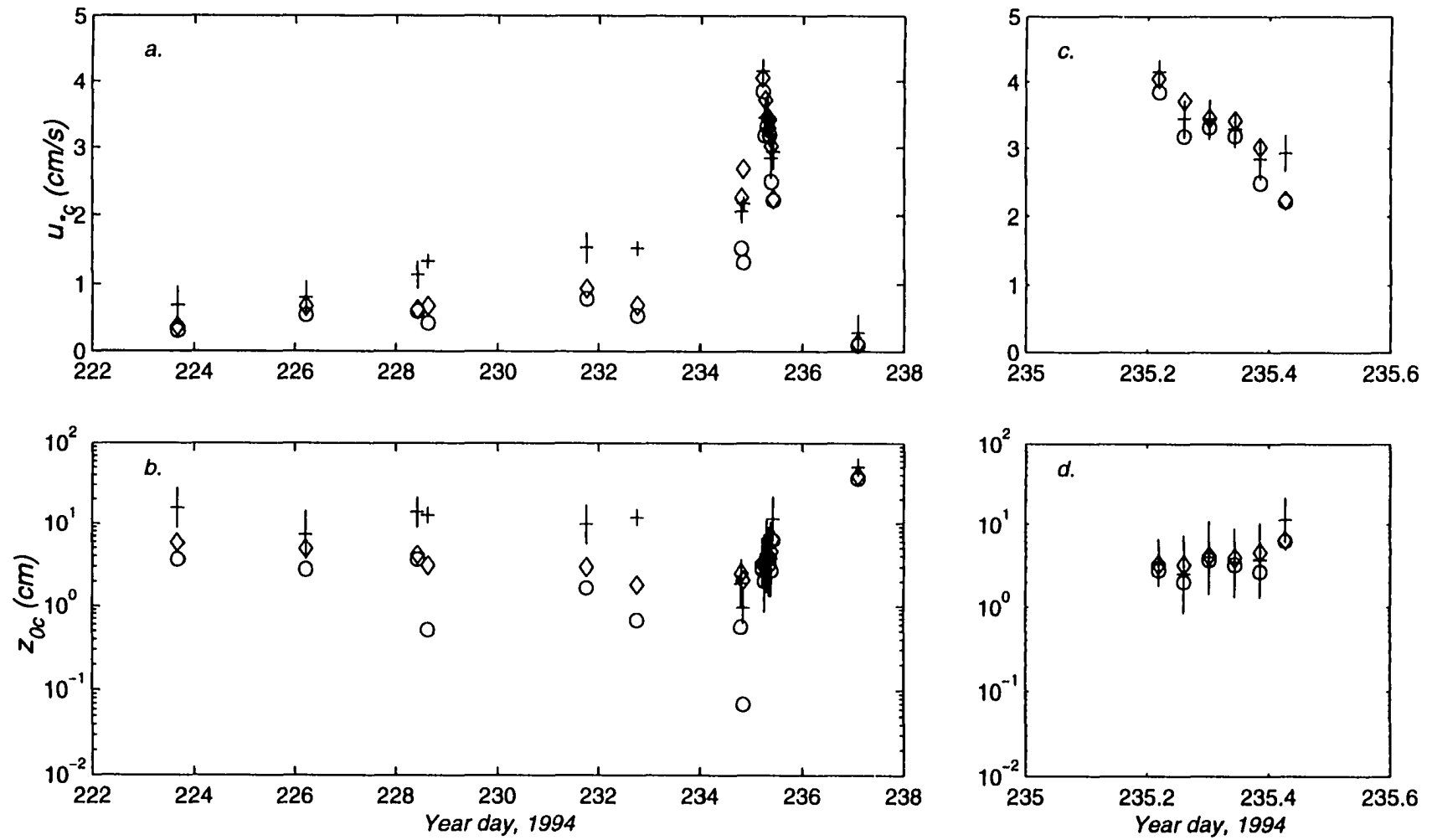


Figure 4.18 Reevaluation of (a)  $u_{*c}$  and (b)  $z_{0c}$  estimates for 1994 using the modified ripple roughness described in the text. Open circles indicate bottom roughness calculated using  $\phi_{cw}$  and diamonds using  $\phi_t$ . Error limits are the same as described in Figure 4.12

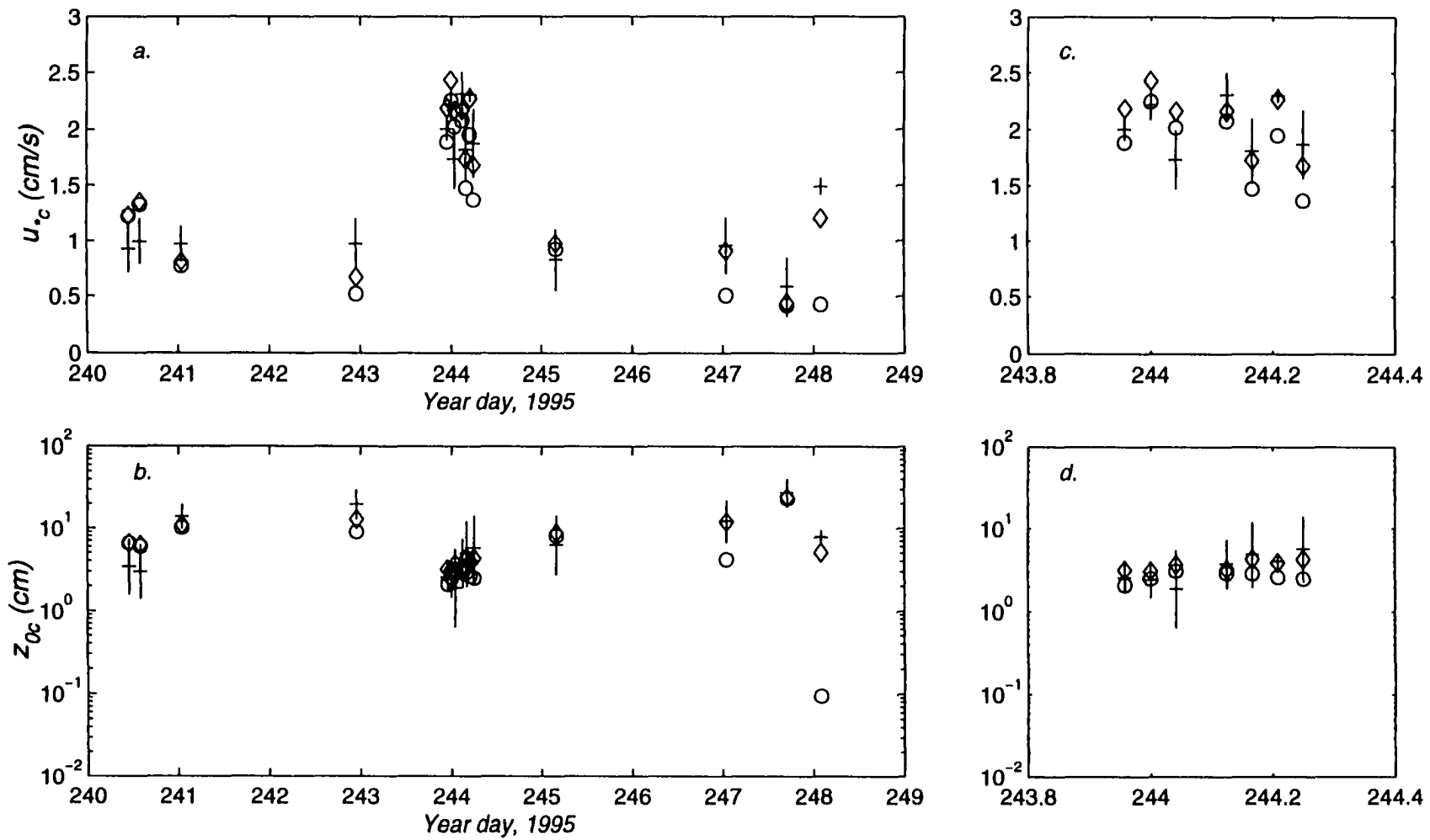


Figure 4.19 Same as Figure 4.18 for the 1995 experiment.

was valid for the variety of flows they studied. For extreme flow conditions, the ripples will disappear and  $k_b$  will be a function of the near-bed transport layer. For these conditions, the sheet-flow roughness model of Wilson (1989) is included in the BBLM.

#### 4.7.5 Summary and discussion of $k_b$ estimates

The previous analysis also showed that, after reevaluation of the Sorenson et al. (1995) bottom roughness model with the aid of the data sets described here,  $k_r = 2.3 \eta [|\cos \phi_r|]^{1.2}$  was superior to the original Sorenson et al. (1995) model for flows categorized as wave dominated. This was illustrated for bursts obtained during the 1995 deployment where the Sorenson et al. (1995) model under estimated  $u_{*c}$  when  $\phi_{cw}$  was near 90 degrees. Similar results were obtained during the small storm during the 1994 deployment. It should be noted, however, that the Sorenson et al. (1995) data possessed an appreciable contribution from the current, so that the directional dependence was more likely to appear in their data set.

Another factor that may affect the bottom roughness calculation is the existence of a near-bed transport layer. At the onset of sheet flow conditions,  $k_t$  may be on the same order of magnitude as  $k_r$ , making it difficult to separate the individual contributions from these two parameters to the total bottom roughness. Bed roughness calculated using (4.28) for all bursts examined, however, indicate  $k_t$  is at least two orders of magnitude less than  $k_r$ . These low values are consistent with the findings of Wilson (1989) who suggests that sheet flow conditions occur when

$$\frac{2.5 \pi^2 c_{fw} A_b^2}{(s - 1) g d T_w^2} > 1 \quad (4.29)$$

where the ratio represents the threshold for sheet flow conditions and is based on Wilson's (1989) empirical analysis using sheet flow data under waves. For the 1994 and 1995 data, this ratio is always less than 0.33 and 0.21, respectively, so the existence of a near-bed transport layer, and an associated contribution to the total bottom roughness from the parameter  $k_r$ , are both unlikely.

Finally, it must be mentioned that the above analysis was conducted using the neutral boundary layer model. This was justified based on comparison of  $u_{*c}$  predicted from both the stratified and neutral models which showed for all bursts in 1994 that the maximum difference between the two was less than 4.2%. For 1995 this difference was less than 0.07%. Both these error percentages are much less than the minimum criteria of  $\pm 31\%$  at the 95% confidence level established for the  $u_{*c}$  estimates from the BASS profiles. As a result, the potential errors associated with the effects of suspended sediment-induced stratification are noted and neglected.

## **4.8 Directions for future research**

### **4.8.1 Estimates for $\gamma_0$ , $\gamma$ and $\alpha$**

Although the limited model and data comparison suggests that the values reported for  $\gamma_0$ ,  $\gamma$  and  $\alpha$  represent reasonable estimates for use in applications, it is important to address a few related issues that should be considered in future calibration studies. Traykovski et al. (1998) show that the calibration curve that plots acoustic intensity as a function of grain size for a given concentration is near a maximum and almost constant for the grain sizes measured at LEO-15. Thus, sediment with grain sizes that fall within a small range of that used to calibrate the instrument will register very similar concentration values. This means the concentration measurements may actually represent

a small distribution of particle sizes that will have different fall velocities and different vertical profiles. It is possible that grains ranging within a small distribution around 0.04 *cm* could represent the dominant class for an individual burst and that the grain diameter used to calibrate the coefficients is not representative of the actual sediment. As a result, calibrating the model with either the 0.05 or 0.03 *cm* grains would probably change the values of  $\gamma$ ,  $\alpha$  and  $\gamma_0$ .

Additionally, if the exact size and distribution of the sediment is not well defined, three other problems can emerge. First, because of the time scales involved, it is not evident that a single surface sediment sample will accurately represent bed composition throughout the entire deployment. This is especially true during storms when the surface layer may be eroded. For the LEO-15 study site, this is probably not an issue due to a comprehensive grain size analysis which concluded that surface sediments at Node A are indicative in composition and distribution to sediment just below the surface (Craghan 1995). In order to reach older deposited, and possibly finer, sediment, it would be necessary to erode at least 1 *m* of the surface layer. This is not likely for the time scales involved during the 1995 deployment. It must be noted, however, that bed armoring, which removes the fines leaving only the coarser sediment at the top, would cutoff the supply of finer sediment for resuspension. Second, estimates of the settling velocity of the grains, which are also dependent on grain size, are still a relatively unknown for the field (Yogesh Agrawal, Sequoia Scientific, personal communication). As a result, virtually all sediment transport models rely on empirical relationships, like (4.13), which are determined in controlled settings using known sediment grain diameters and distributions. Third, non-local processes such as advection may lead to errors in

estimates of sediment grain size since the analysis here assumes the only sediment source is local resuspension. Problems associated with advection will also depend on grain size since smaller sized grains can be more easily advected than larger sized grains. The ABS, however, which is much more sensitive to the larger grains and is calibrated using bed sediment, is not likely to sense the advected fines. Overall, the inaccuracies in both  $d_n$  and  $w_{f_n}$  must be considered when modeling suspended sediment concentration profiles for heterogeneous sediment beds. Instruments designed to make these high-resolution measurements (Yogesh Agrawal, Sequoia Scientific, personal communication) should be used in conjunction with instruments like the ABS to begin to answer some of these questions.

The statistical models used in the calibration procedure implicitly assume that stratification is negligible. Because the interest here is to study stratified flows, the use of the neutral models in the calibration procedure needs justification. The neutral models are used because the chosen method to calculate the shear stress and other model parameters is based on the logarithmic profile technique which implicitly assumes that stratification is negligible. The degree to which this method is valid is determined from the regression analysis, which is why such a high  $R^2$  threshold is chosen to calibrate the model parameters. It is hypothesized that the stringent  $R^2$  criteria, even though it eliminates a majority of the available profiles, is necessary since the main objective is to calibrate important model coefficients, which either have a history of varying over several orders of magnitude or have never been properly validated in the field. Additionally, comparisons of  $u_{*c}$  from the stratified and neutral version of the model

showed relative differences of less than 1% for the 2 bursts that produced a non-zero reference concentration.

With these concerns in mind, the main quantitative statement concerning the parameter calibration is that the selected high-quality data suggest the 1-dimensional diffusive model is adequate for field conditions similar to those examined in this study. Based on this reasoning, the following values are suggested for use with the BBLM:  $\alpha = 1.5$ ,  $\gamma = 0.43$  and  $\gamma_0 = 3.1 \times 10^{-3}$ , which are determined by averaging the individual values shown in Table 4.3. Clearly, the model calibration study has revealed the need for comprehensive measurements of particle size spectra and settling velocity, and has sparked a new focus on additional calibration methods and statistical procedures.

#### **4.8.2 Bottom roughness**

Two important issues regarding bottom roughness on the continental shelf have been addressed - the existence of relic ripples and the need for a better understanding of the spatially averaged bottom roughness for waves and currents at arbitrary angles. If the model indicates flow conditions too weak to suspend sediment, then it is not possible to accurately determine ripple height, which, in turn, is needed to calculate bed roughness. This is a concern since the ripple roughness model is a function of wave parameters only and will predict a finite ripple height during periods if it is not first checked to see if sediment is in motion.

For long-term modeling studies that include extended periods of weak flow where bed reworking by biological activity and the existence of relic ripples are both likely, conditions will exist where it is not possible to obtain accurate estimates of the ripple roughness. During these time periods, two options are available to determine  $k_r$ . First,



the model can be run with  $\eta$  values obtained from the instantaneous wave parameters even when the model indicates conditions too weak to move sediment. This could either over-estimate or underestimate  $k$ , since there is no way to quantify the size of the relic ripples. Second,  $\eta$  values obtained from the most recent time step that indicate equilibrium conditions can be used for successive time steps until equilibrium conditions are again reached. If the period between two successive equilibrium flow events is relatively long, this method will over estimate  $\eta$  due to eventual ripple erosion caused by the rounding out of the ripple crest as the lesser flow moves grains off the ripple peak, and other influences such as bed reworking by biological organisms. Because the majority sediment flux is probably confined to storms with sufficient energy to resuspend sediment, problems associated with relic ripples are not a concern. During weaker flow events, however, small-scale processes like ripple migration may be a significant source of long-term transport (Traykovski et al. 1998). Ultimately, the need to address the influence of relic ripples on flow and sediment dynamics for studies of up to several years is important, since a significant fraction of this time will consist of relatively weak flow conditions.

## **5.0 MODEL APPLICATIONS: LONG-TERM SEDIMENT TRANSPORT AT LEO-15**

It is generally known that storms are a primary cause of sediment resuspension and transport on the continental shelf. It is also known that the frequency of storms usually increases during the winter months. Data obtained by Drake and Cacchione (1985) and Cacchione et al. (1987), during a winter deployment off the northern California coast in 85 *m* of water, indicated that four storms with a combined duration of approximately 12 days were responsible for between 30 and 50% of the annual sediment transport. Field studies designed to measure near bottom flow and sediment transport such as STRESS have capitalized on this fact, and have provided valuable information on the conditions that lead to these energetic transport events during the winter months (Sherwood et al. 1994). Less understood is the seasonal variation in sediment transport and the corresponding potential for summer-time storm events to mobilize and transport bed material. A major obstacle hindering such studies is a lack of sufficiently long time series of near-bed wave and current observations to drive bottom boundary layer models. This lack of long-term information has forced investigators to rely on sporadic measurements obtained as part of intense but short-term boundary layer studies such as CODE or STRESS, or non-local measurements, such as wave data obtained from surface NOAA buoys and statistical models of near-bed mean flow, to infer long-term flow and sediment transport conditions at the bottom. Such measurements have neither the temporal coverage nor the near-bed mean flow information to characterize long-term patterns of sediment movement.

Due to a recently initiated multi-year field program on the Eel shelf off the northern coast of California, this historic lack of long-term in situ measurements is no longer a major limiting factor (Nittrouer and Kravitz 1996). Initiated in 1995, this long range study consists of a series of heavily instrumented intense short-term experiments to measure wave and current velocities, suspended sediment concentration profiles and bottom elevation at various cross-shelf locations, embedded within a long-term study that includes a minimum 3-year investigation at mid-shelf to record flow and sediment patterns (Wiberg et al. 1996). The study site is located in 60 *m* of water, and overlays a transition region where shallower deposited sand gradually gives way to silt as the water deepens and direct forcing by waves and winds becomes less energetic.

Although this experiment provides some of the first available high-resolution long-term data sets to drive boundary layer models, general inferences on shelf sediment dynamics from results obtained during this study will be restricted to areas that have similar sediment types, water depths, and wave and current conditions. In areas such as the Middle Atlantic Bight (MAB), which includes the continental shelf offshore of New Jersey, long-term wind patterns and shelf characteristics are strikingly different. Throughout the summer and fall, hurricanes in the Atlantic Ocean form a significant source of long-period energetic swell and strong winds. Equivalent systems off the coast of northern California are practically non-existent, since eastern Pacific hurricanes rarely make landfall north of the Mexican-United States border (WXP, Purdue University 1998). As a result, most direct summer-time wind and wave forcing is caused by either local subtropical storm systems or long-period swell associated with distant storms. In addition, mid shelf water depths off the northern California shelf are  $O(100\text{ m})$ , with a

bed composition primarily composed of fine sand to silt. Typical mid shelf depths offshore of New Jersey are  $O(10\text{ m})$ , with a substrate of mostly medium sand. Therefore, there are likely to be differences in sediment transport patterns off the northern California coast compared to offshore New Jersey.

With these concerns in mind, the primary objectives in this section are to utilize nearly two years of S4 wave and current data to drive the BBLM, and to investigate long-term sediment flux at LEO-15 based on model predictions. After a description of available long-term data sets and model input parameters, model results are examined. Processes found to influence long-term transport, which include seasonal variability, event duration and storm intensity are discussed, followed by a narrower focus on the mechanisms of cross-shore transport patterns, emphasizing the coupling between atmospheric forcing and local bathymetry. Finally, the major findings of this study are summarized.

## **5.1 Input model data**

As previously mentioned, LEO-15 is the center-piece of a multi-platform observational network designed for long-term monitoring of coastal processes. In accordance with the long-term monitoring strategy, a pair of S4 current meters equipped with salinity, pressure, temperature and OBS sensors have been deployed episodically over the past five years at LEO-15. Because one of the primary interests is to obtain current data to drive bottom boundary layer models, both S4's are programmed to sample at  $2\text{ Hz}$  for a total 18-minute burst each hour. To provide optimal long-term coverage of near-bottom current and wave patterns, the S4's are deployed in series at Node A (74.26W-39.46N) 1 to 2  $m$  off the bottom (Figure 4.1). Initially, the S4s were placed

at a height of 2 *m* off the bottom, and then were lowered to 1 *m* in early November 1994 due to the construction of a new mooring system. As battery power and storage capacity on one S4 runs low, it is recovered and replaced with the other fully charged unit. Since the initial test deployment in 1993, the most continuous set of measurements were collected in 1994 and 1995. During this time period the S4 flow and pressure data were used to calculate model input parameters as described in Section 4.

### 5.1.1 Input wave and current data

The 1/2-second record for each 18-minute burst was Fast Fourier Transformed and converted to the near-bottom orbital velocity spectrum, which was then converted into equivalent maximum near-bottom wave orbital velocity,  $u_b$ , using (4.8). Figures 5.1 and 5.2 show  $u_b$  for 1994 and 1995, respectively. For both years,  $u_b$  is sharply peaked with a variable range from around 5 *cm/s* to over 70 *cm/s*. With few exceptions, the larger peaks ( $u_b \geq 30$  *cm/s*) cluster around the winter months. The distribution between the two years shows 1995 having fewer peaks over 40 *cm/s* than in 1994, indicating generally stronger wave conditions for 1994. Equally apparent are episodic data gaps scattered throughout the 2-year period. These gaps reflect unavoidable S4 down time for maintenance and the commitment of these instruments to overlapping field experiments. These few data gaps notwithstanding, the combined S4s were operational 78% of the time during the first year and 70% during the second, and gave at least partial coverage for all seasons. Figures 5.3 and 5.4 show equivalent wave radian frequency,  $\omega_r$ , which was calculated using (4.14) as described in Section 4.4. The patterns mimic  $u_b$  in that  $\omega_r$  is also very peaked. For both years,  $\omega_r$  is confined between a narrow band of frequencies that range from about 0.5 to 1 *s*<sup>-1</sup>. Within this band, however,  $\omega_r$  is highly

variable. The 0.5 and 1  $s^{-1}$  limits translate to a wave period range of about 6 to 12 s, which represent typical short period storm generated waves (6 s) and lower frequency ocean swell (12 s). Figures 5.5 and 5.6 show mean current,  $u_r$ , derived from the combined S4 data sets. The time series represents hourly averages calculated from the mean of each 18-minute burst. The height  $z_r$  at which the mean current is recorded is taken as the height of the S4s. Prominent features in the record include the strong semi-diurnal tidal signal embedded within lower frequency motion associated with synoptic weather systems and other subtidal forcing. Finally, Figures 5.7 and 5.8 show the angle between the wave and current,  $\phi_{cw}$ , which is highly variable throughout the 2-year time period.

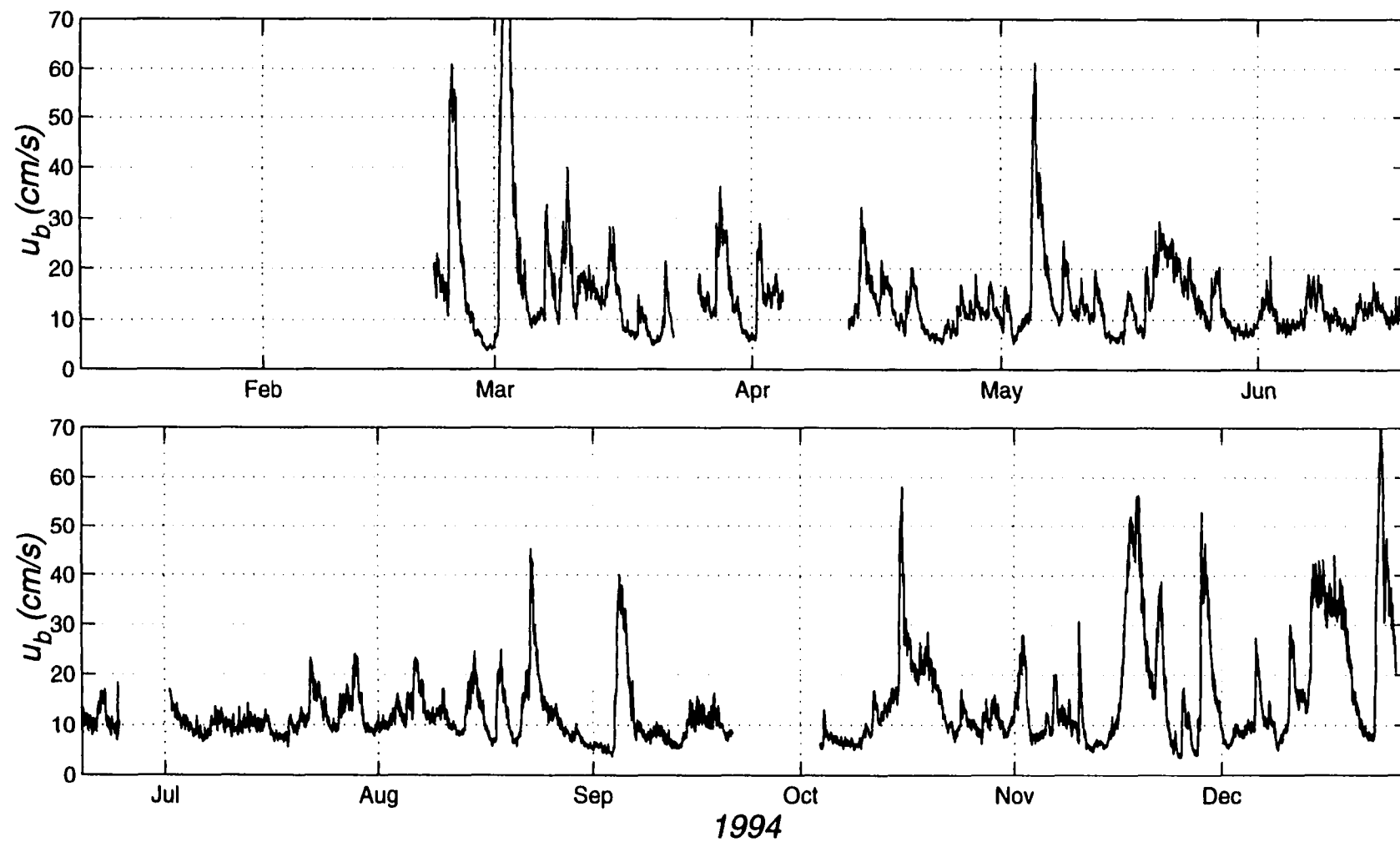


Figure 5.1 Maximum near-bottom wave orbital velocity,  $u_b$ , derived from S4 current meters for 1994. Noticeable are sporadic data gaps indicating S4 downtime.

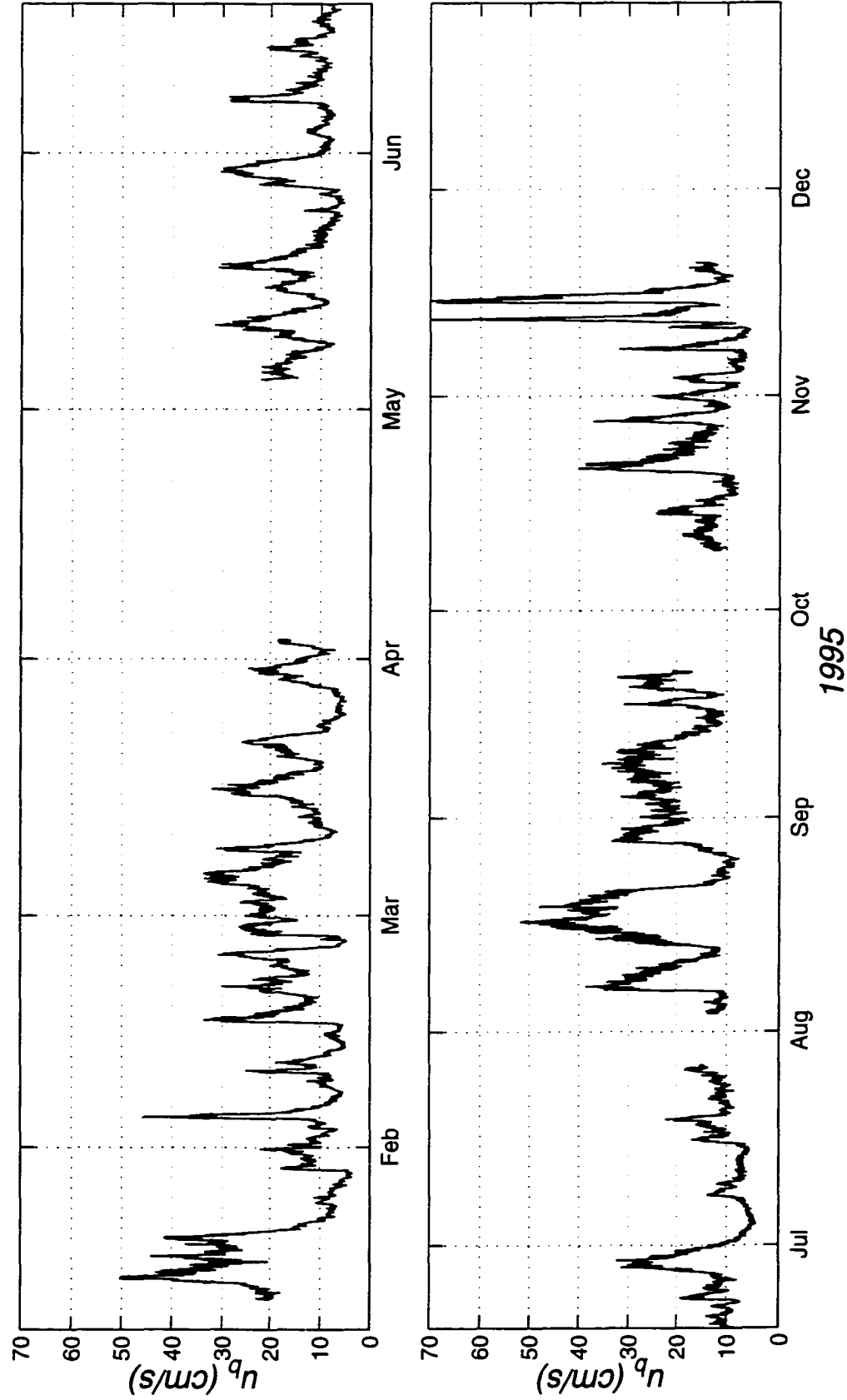


Figure 5.2 Same as Figure 5.1 for 1995.



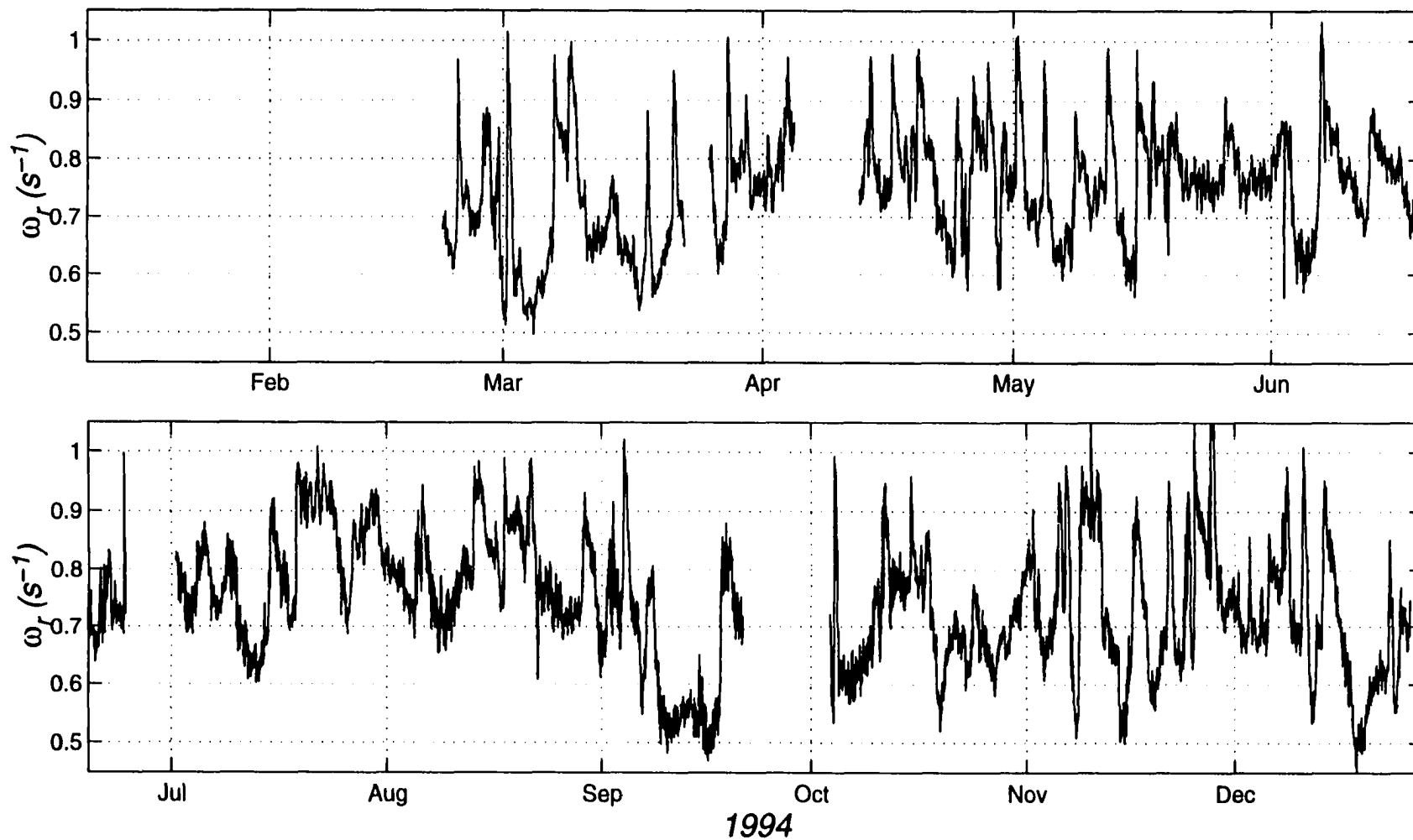


Figure 5.3 Equivalent wave radian frequency,  $\omega_r$ , calculated using the 1994 S4 current data. For the most part,  $\omega_r$  is bracketed between 0.5 and 1  $s^{-1}$ , which represents typical swell ( $\omega_r = 0.5s^{-1}$ ) and higher frequency waves associated with local storms ( $\omega_r = 1.0s^{-1}$ ).

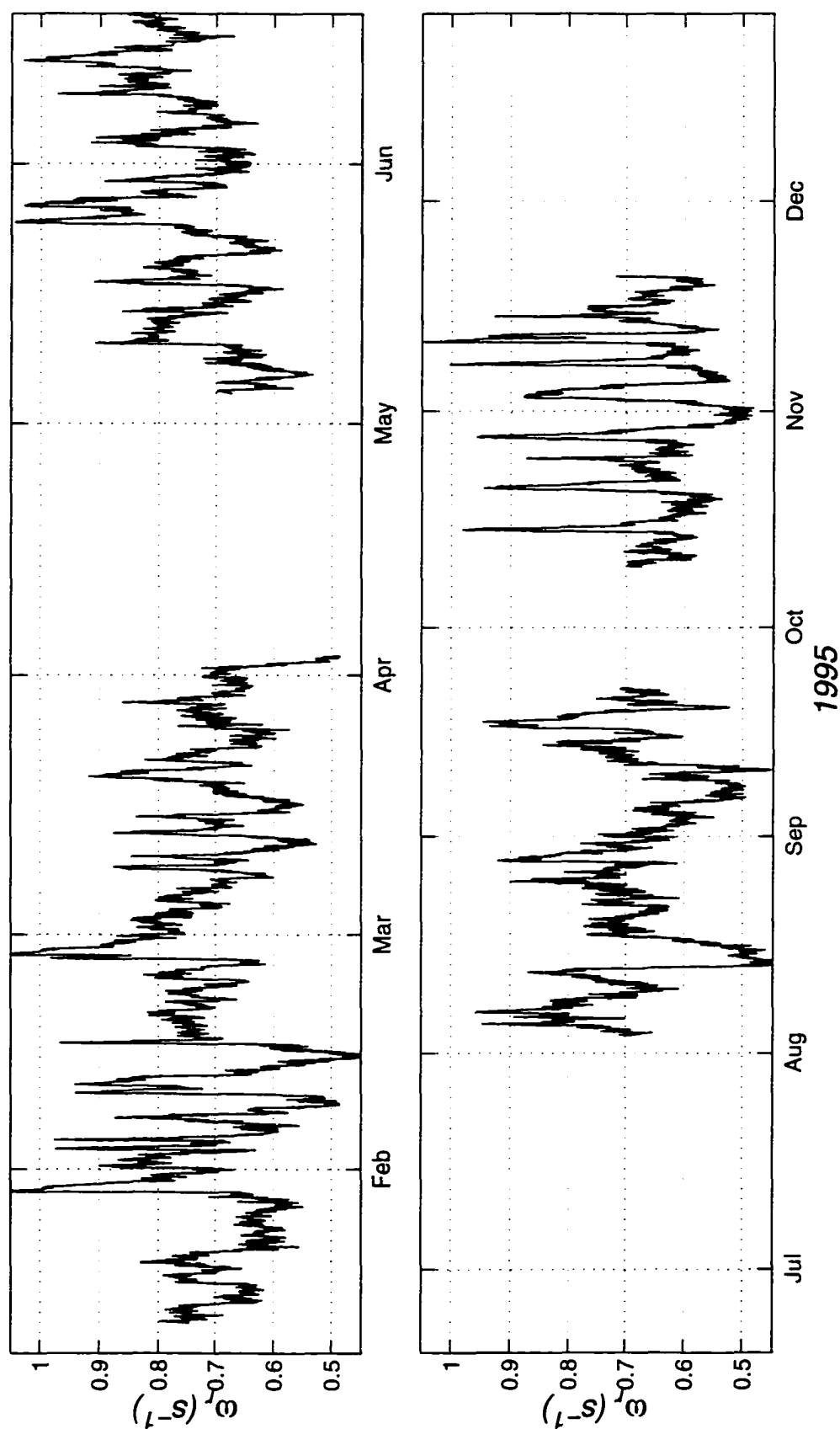


Figure 5.4 Same as Figure 5.3 for 1995

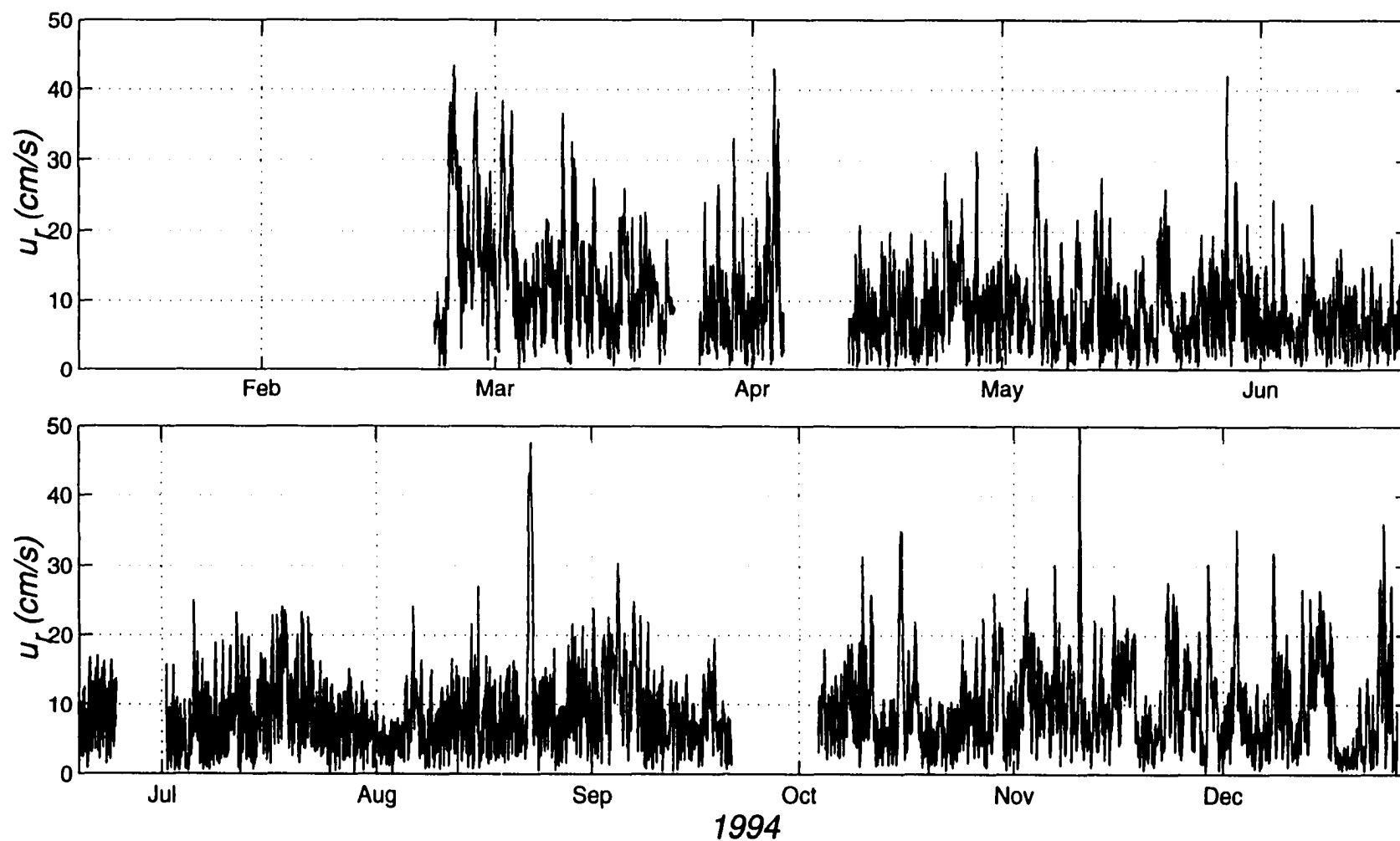


Figure 5.5 18-minute average current speed,  $u_r$ , derived from S4 current meters for 1994. Current speed is variable, containing both higher frequency tidal constituents and lower frequency motion associated with atmospheric forcing and other low-frequency sources.

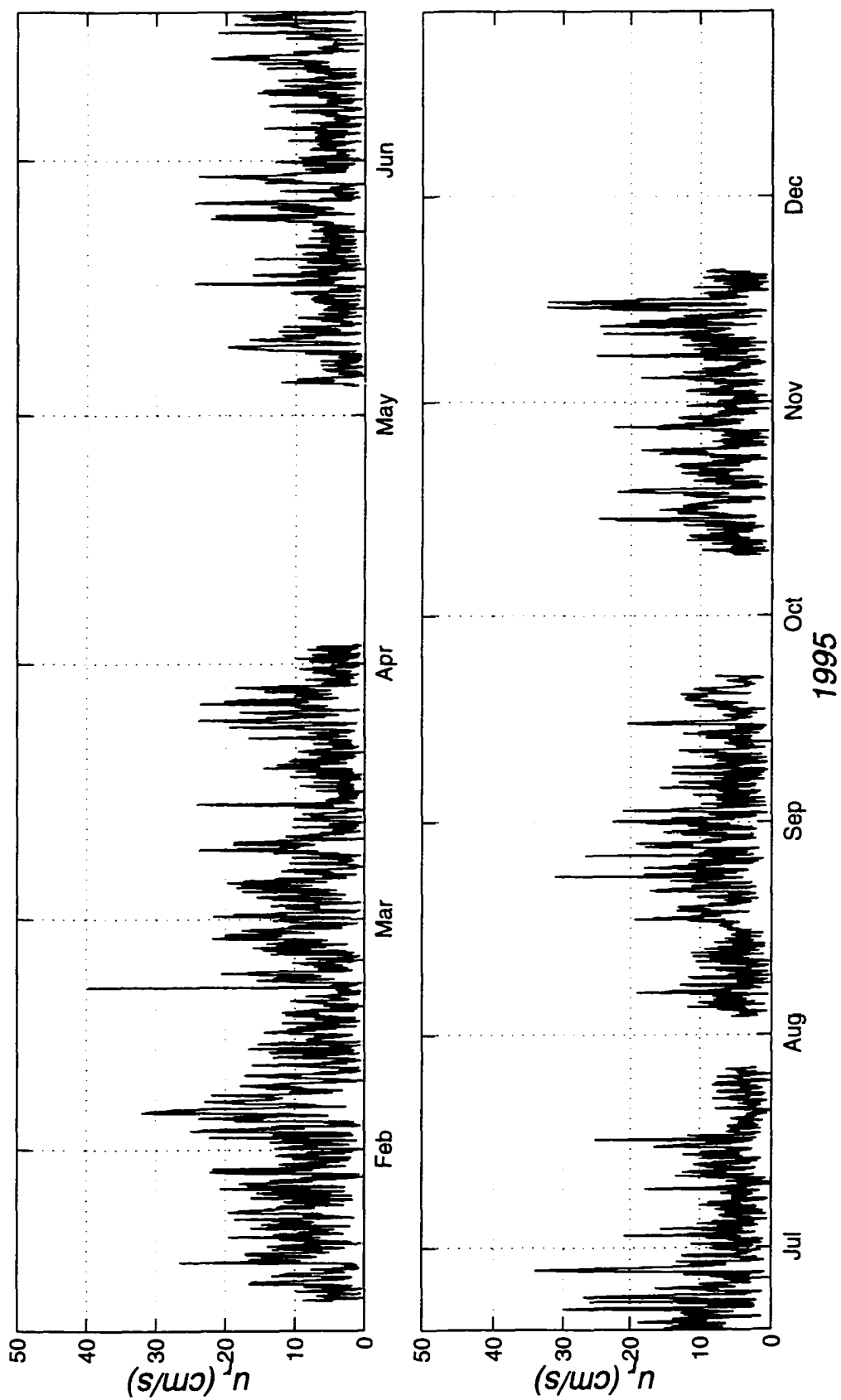


Figure 5.6 Same as Figure 5.5 for 1995

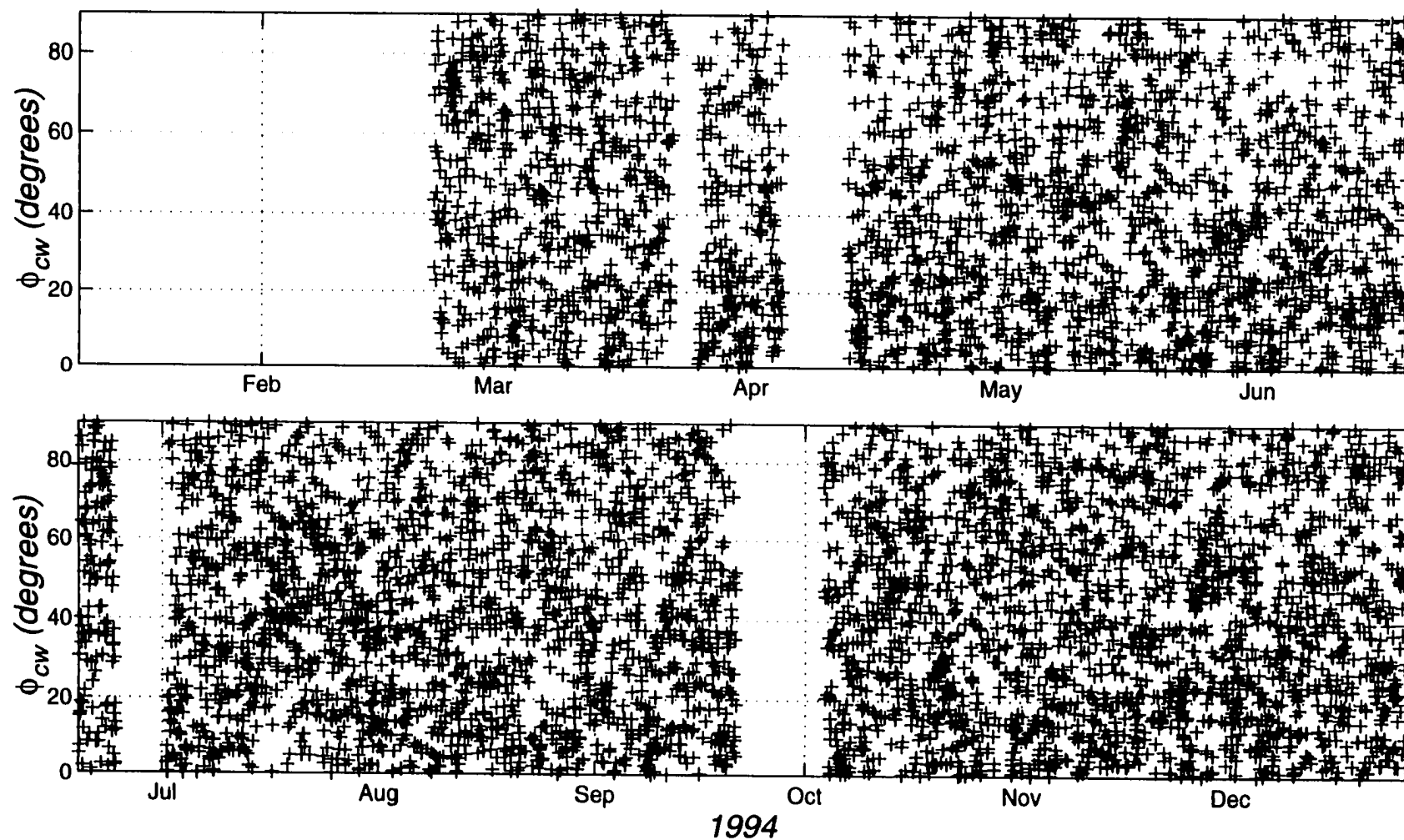


Figure 5.7 Angle between the wave and current,  $\phi_{cw}$ , derived from S4 records during 1994. The angle is highly variable during the year.

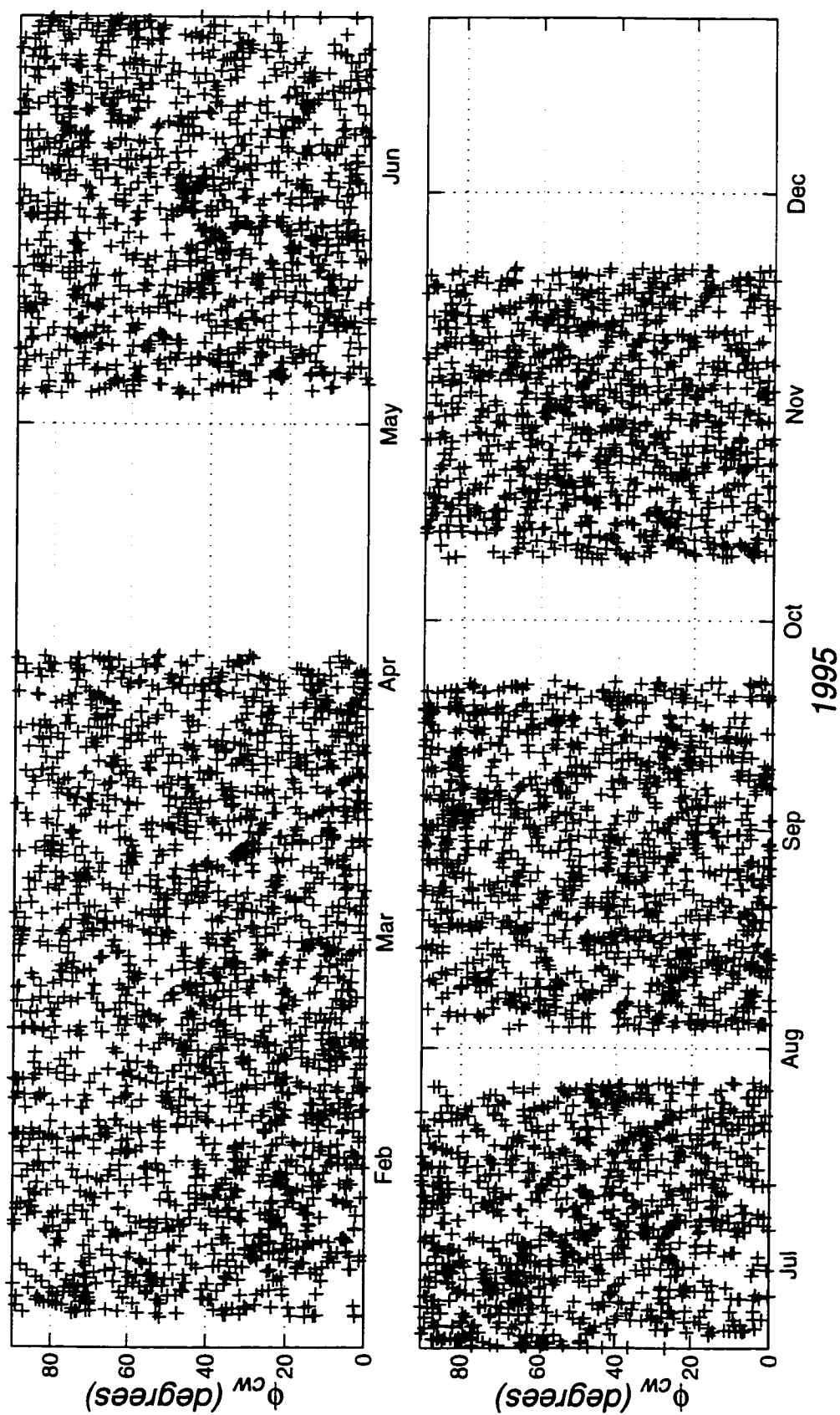


Figure 5.8 Same as Figure 5.7 for 1995.

### 5.1.2 Input sediment data

In addition to wave and current data, the BBLM requires as input sediment grain size, sediment density and sediment distribution in the bed. Surface sediment samples obtained by divers at LEO-15 in the summer of 1994 were analyzed for grain size distribution and type. The predominant sediment type consisted of noncohesive medium sized quartz sand with a density of  $2.65 \text{ gm/cm}^3$ . Grain size distribution was determined by dry sieve using a total of eight mesh sizes ranging from 0.1 to  $0.01 \text{ cm}^2$ . The results from the dry sieve indicated that the dominant size class consisted of  $0.05 \text{ cm}$  grains, constituting  $\sim 35\%$  of the bed total. With the medium sized grains contributing only  $1/3$  of the total, a more accurate representation of the true bed composition is obtained using multiple grain size classes. Because it was shown in Section 3 that the stratification correction is more sensitive to the smaller grains, it was determined that a small distribution, weighted by the relative contributions from grains both smaller and larger than the mean, would be used as input to the model. Based on the particle size distribution obtained from dry sieve analysis, sediment concentrations were grouped into three representative grain size classes to define the distribution in the bed. The three size classes represent small ( $0.024 \text{ cm}$ ) medium ( $0.050 \text{ cm}$ ) and large ( $0.083 \text{ cm}$ ) sized grains with relative concentrations of 48%, 35% and 17%, respectively, of the total bed concentration. This modifies the reference concentration for each grain size class since  $c_b$  defines the total concentration in the bed. For each grain size class, the reference concentration is multiplied by the fraction that each particular size class contributes to  $c_b$ . Additionally, the model parameters  $\alpha$ ,  $\gamma$  and  $\gamma_0$  are set with values 1.5, 0.43 and  $3.1 \times 10^{-3}$ , based on the results from the calibration study in Section 4.

### 5.1.3 Sediment transport event criteria

The model was run for the 2-year time period using the input wave, current and sediment parameters just discussed. Output time series of relevant sediment parameters to be discussed were generated and used to identify sediment transport events. Because sediment resuspension is episodic, there will be periods when the model will skip through several days or even weeks before identifying the next sediment transport occurrence. Clearly, these occurrences will have a distribution that can be used to identify dominant forcing agents responsible for entraining and transporting sediment. Time series of the sediment concentration output from the model were used to identify the duration of each sediment resuspension occurrence, which was then ranked according to the number of consecutive hours that showed resuspension. The results are displayed in Figure 5.9(a). The vertical axis signifies the number of times the model predicted sediment resuspension, and the horizontal axis shows the division of these resuspension occurrences grouped by duration. For example, the first vertical bar indicates the total number of occurrences whose combined total lasted 1, 2 or 3 hours. The last vertical bar indicates all occurrences with durations greater than 22 hours. Obviously, the short resuspension occurrences make up the majority. When these values are weighted by the number of hours per occurrence, however, it is clear that occurrences with a duration greater than 22 hours account for the majority of sediment transporting time periods (Figure 5.9b). Interestingly, a well defined spectral gap occurs around 17 hours separating the large scale transport occurrences from the short-term occurrences. Using this spectral gap as a guide, a sediment transport *event* is defined as any 17 consecutive hours or greater of non-zero sediment in suspension. The event will further be defined



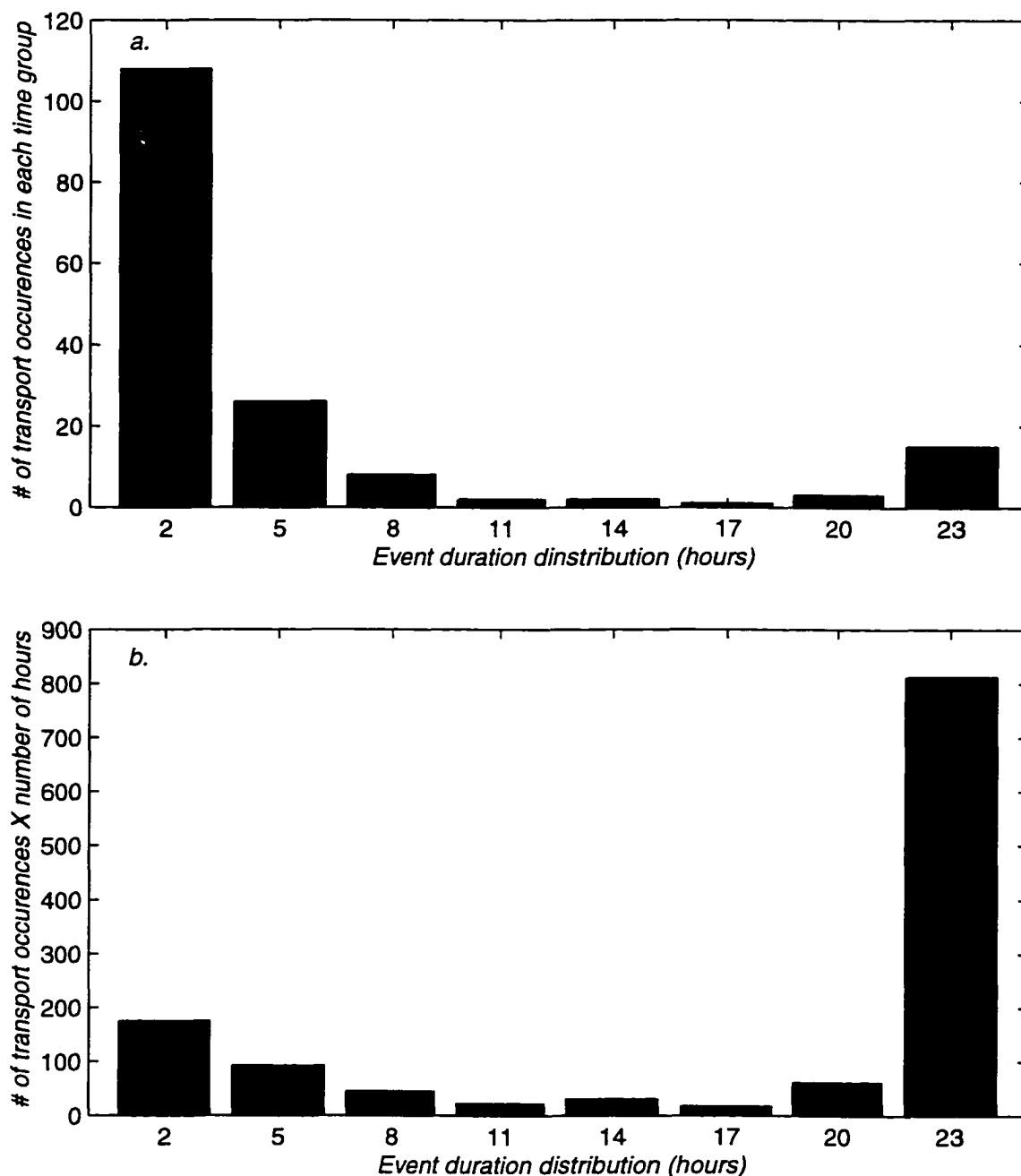


Figure 5.9 (a) Distribution of sediment transport occurrences for the two-year time period. Vertical axis indicates the total number of occurrences, grouped by occurrence duration, for the corresponding temporal bands identified on the horizontal axis. For example, the number 2 on the horizontal axis represents all transport occurrences with a duration of either 1, 2 or 3 hours. (b) same as (a), but each occurrence is weighted by occurrence duration. All transport occurrences with durations greater than 22 hours are grouped in the final column.

as having ended when 17 consecutive hours of zero sediment resuspension is calculated by the model. This definition of a sediment transport event establishes a consistent and logical event criteria, where, presumably, large synoptic atmospheric systems are considered the primary impetus for driving sediment motion on the shelf. Tables 5.1 and 5.2 list the number of transport events along with sediment statistics to be discussed. Eleven transport events were identified in 1994 and 8 were identified in 1995 with durations ranging from a minimum of 20 hours to a maximum of 151 hours.

#### **5.1.4 Qualitative assessment of sediment transport events**

Qualitative estimates of suspended particulate matter deduced from OBS time series can be used to help determine if the resuspension events predicted by the model accurately reflect conditions at LEO-15. For reasons to be discussed, the OBS cannot give quantitative estimates of the suspended sediment concentration for sediment typical of LEO-15. It is expected, however, that the OBS record will reflect changes in the concentration of suspended material, as higher OBS values indicate lower optical transmission. Figures 5.10 and 5.11 show OBS time series in formazin turbidity units (FTU) (D & A Instruments 1989) derived from the S4s. Individual sediment transport events identified by the BBLM correspond to the shaded regions in the plots. Noticeable is the saturation of the sensor various times during each year, which is usually due to biofouling after extended periods of exposure to a highly productive coastal marine environment. Sharp increases in OBS values during the first two sediment transport events for 1994 provide encouraging evidence that the model is able to identify periods of active sediment resuspension. Similar peaks, although not as dramatic when contrasted with background scattering levels, occur during the last five events in 1994.

Table 5.1 Sediment transport model results categorized by transport events for 1994.

Event	Date (1994)	Event Duration (hrs)	$\Gamma_{\beta-x}$ ( $cm^2$ )	$\Gamma_{\beta-y}$ ( $cm^2$ )	$\Gamma_{\beta}$ ( $cm^2/s$ )	$\Gamma_{\beta}$ ( $cm^2$ )	$\Gamma_{\beta}$ for each grain size class ( $cm^2$ )		
							0.083 cm	0.05 cm	0.024 cm
1	23-Feb	33	-0.433	-3.612	0.451	3.781	0.277	0.336	3.168
2	1-Mar	51	-2.705	-5.051	0.382	6.392	0.687	0.568	5.138
3	4-May	32	-0.355	-1.106	0.195	1.208	0.119	0.149	0.941
4	23-Aug	20	-0.106	-1.682	0.361	1.701	0.047	0.388	1.265
5	4-Sep	34	-0.032	-0.424	0.066	0.436	0.010	0.088	0.338
6	15-Oct	40	-0.270	-1.246	0.218	1.298	0.105	0.174	1.019
7	16-Nov	74	-0.302	-1.356	0.110	1.477	0.125	0.439	0.914
8	21-Nov	20	-0.022	0.037	0.008	0.047	0.002	0.014	0.031
9	28-Nov	33	0.081	0.625	0.118	0.657	0.022	0.172	0.463
10	14-Dec	123	0.006	-1.571	0.077	1.665	0.062	0.511	1.092
11	23-Dec	64	-0.239	-5.631	0.941	5.717	0.490	0.520	4.708
Annual totals:		524	-4.379	-21.016	2.927	24.380	1.944	3.358	19.077

Table 5.2 Sediment transport model results categorized by transport events for 1995.

Event	Date (1995)	Event Duration (hrs)	$\Gamma_{\beta-x}$ ( $cm^2$ )	$\Gamma_{\beta-y}$ ( $cm^2$ )	$\Gamma_{\beta}$ ( $cm^2/s$ )	$\Gamma_{\beta}$ ( $cm^2$ )	$\Gamma_{\beta}$ for each grain size class ( $cm^2$ )		
							0.083 cm	0.05 cm	0.024 cm
1	15-Jan	142	-0.176	-0.118	0.061	1.063	0.038	0.319	0.706
2	4-Mar	39	0.020	-0.316	0.041	0.333	0.002	0.027	0.303
3	6-Aug	58	-0.070	-0.026	0.034	0.198	0.004	0.039	0.155
4	15-Aug	151	-0.638	-0.251	0.033	1.013	0.059	0.457	0.497
5	28-Aug	54	-0.151	-0.183	0.028	0.273	0.002	0.028	0.243
6	21-Oct	28	-0.061	0.103	0.022	0.128	0.005	0.042	0.081
7	11-Nov	21	0.073	0.853	0.203	0.882	0.097	0.120	0.664
8	14-Nov	34	-0.732	-1.372	0.619	3.947	0.415	0.403	3.130
Annual totals:		527	-1.734	-1.310	1.041	7.836	0.622	1.435	5.779

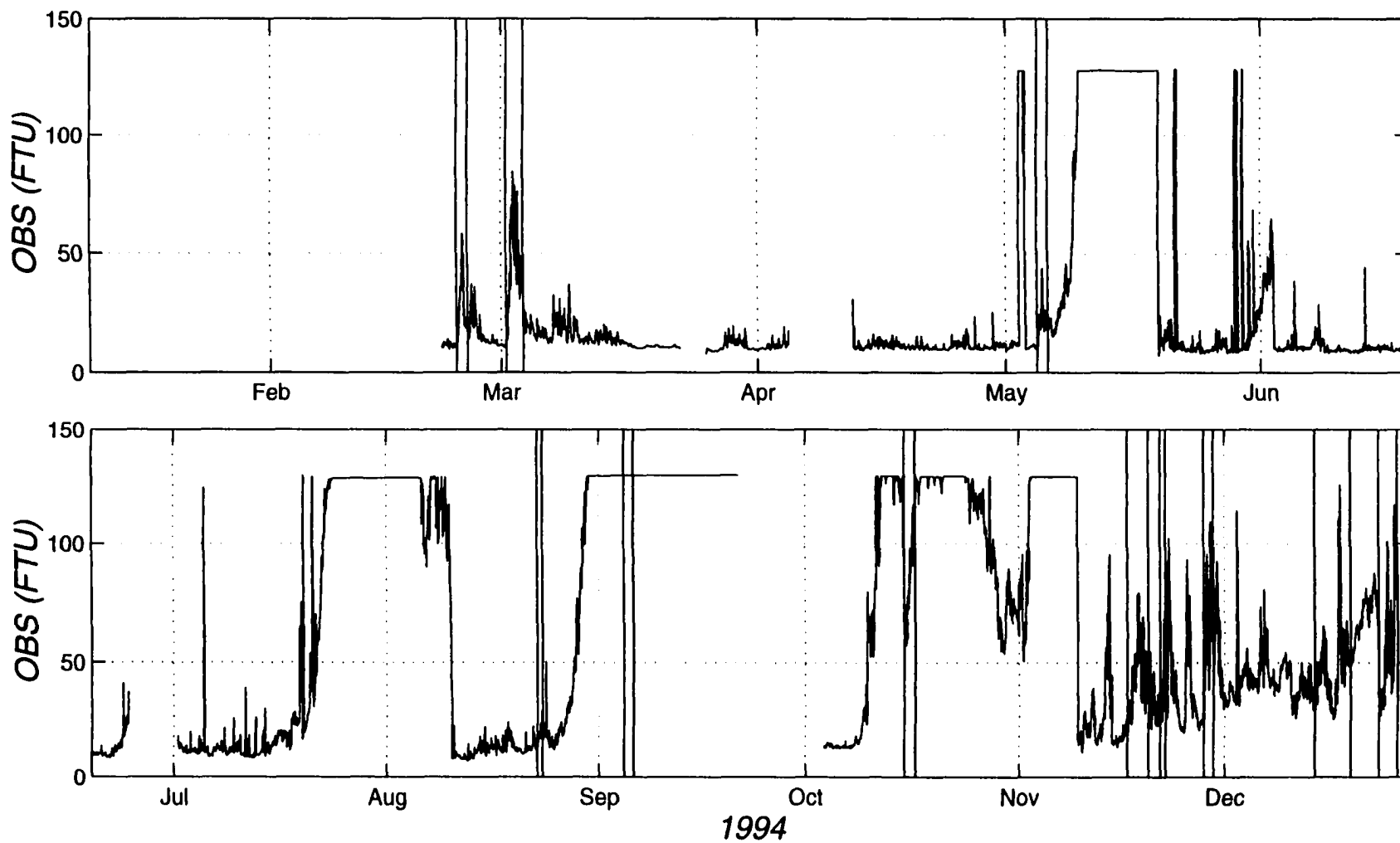


Figure 5.10 Backscatter time series in formazin turbidity units (FTU) derived from S4 OBS sensor for 1994. Sharp, narrow peaks indicating reduced optical transmission correlate well with predicted sediment transport events. Saturation is also present several times during the year and may indicate severe biofouling of the detector.

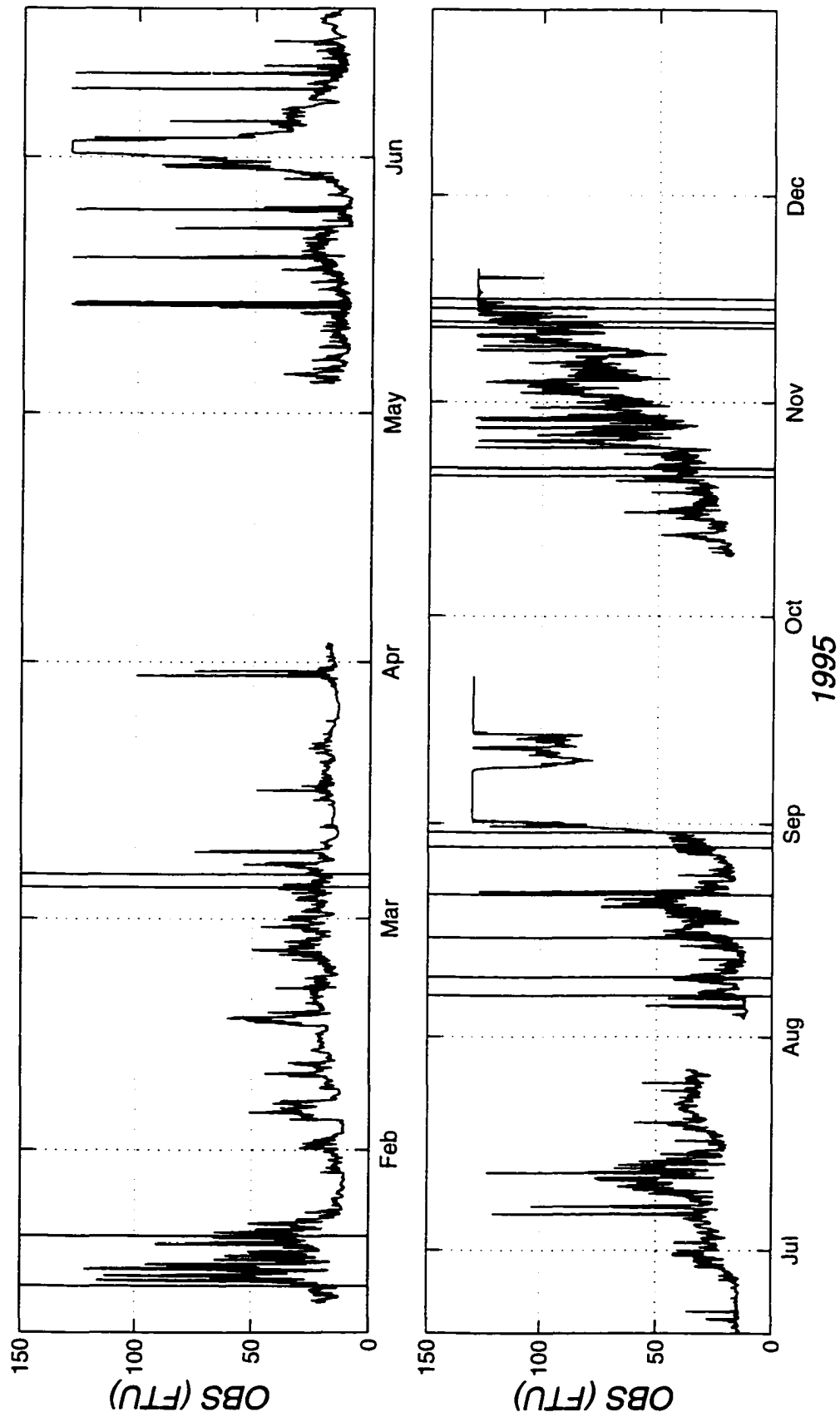


Figure 5.11 Same as Figure 5.10 for 1995.

In 1995, noticeable increases in OBS levels during the first and fourth events provide additional evidence that the event criteria and model predictions are identifying active sediment resuspension. Other peaks not identified with either sediment transport events or biofouling are numerous throughout the record. These peaks may represent transport associated with storms lasting less than 17 hours, or may be a result of the calibration and sensitivity of the OBS sensor. Background noise levels for OBS sensors generally increase with increasing particle size (D & A Instruments 1989). As a result, most factory-calibrated OBS sensors are more sensitive to particle sizes on the order of  $10^{-3}$  cm, which are an order of magnitude smaller than the medium sized sand indicative of LEO-15. This explains why it is extremely difficult to relate sediment concentration at LEO-15 to OBS time series. It further suggests the OBS sensor may be detecting advected particles that wash-over the study site. Finer particles, including marine aggregates associated with biological productivity, can stay in suspension much longer than medium size sand. These particles also register on the OBS detector, and are indistinguishable from finer sand particles presumed to be suspended locally.

#### **5.1.5 Dominant forcing agents driving sediment resuspension**

The near-bed flow is comprised of both low-frequency currents and waves, which combine to entrain and transport sediment. It is generally believed that on storm-dominated shelves, waves are the primary impetus for initiating motion. This issue is briefly explored for the New Jersey shelf using the 2-year modeled and measured data. Figures 5.12 and 5.13 show significant wave height,  $H_s$ , calculated from the S4 pressure data, along with individual sediment transport events. An unmistakable pattern relating higher  $H_s$  to transport is easily discerned. For at least some portion of all events,  $H_s$ ,

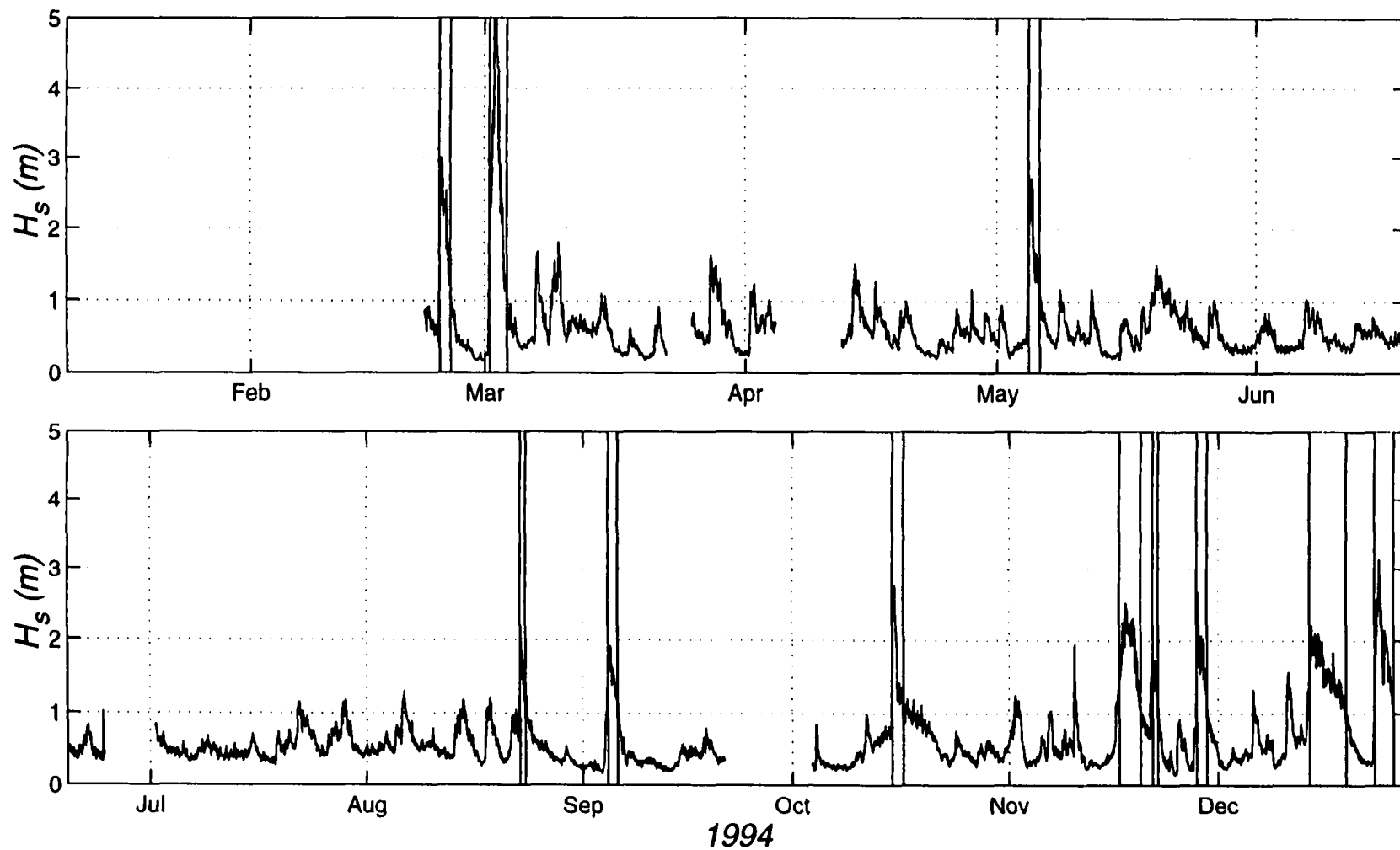


Figure 5.12 Significant wave height,  $H_s$ , derived from S4 pressure sensor for 1994. Shaded regions indicate sediment transport events. An unmistakable pattern relating sediment transport events to high  $H_s$  is clearly evident.

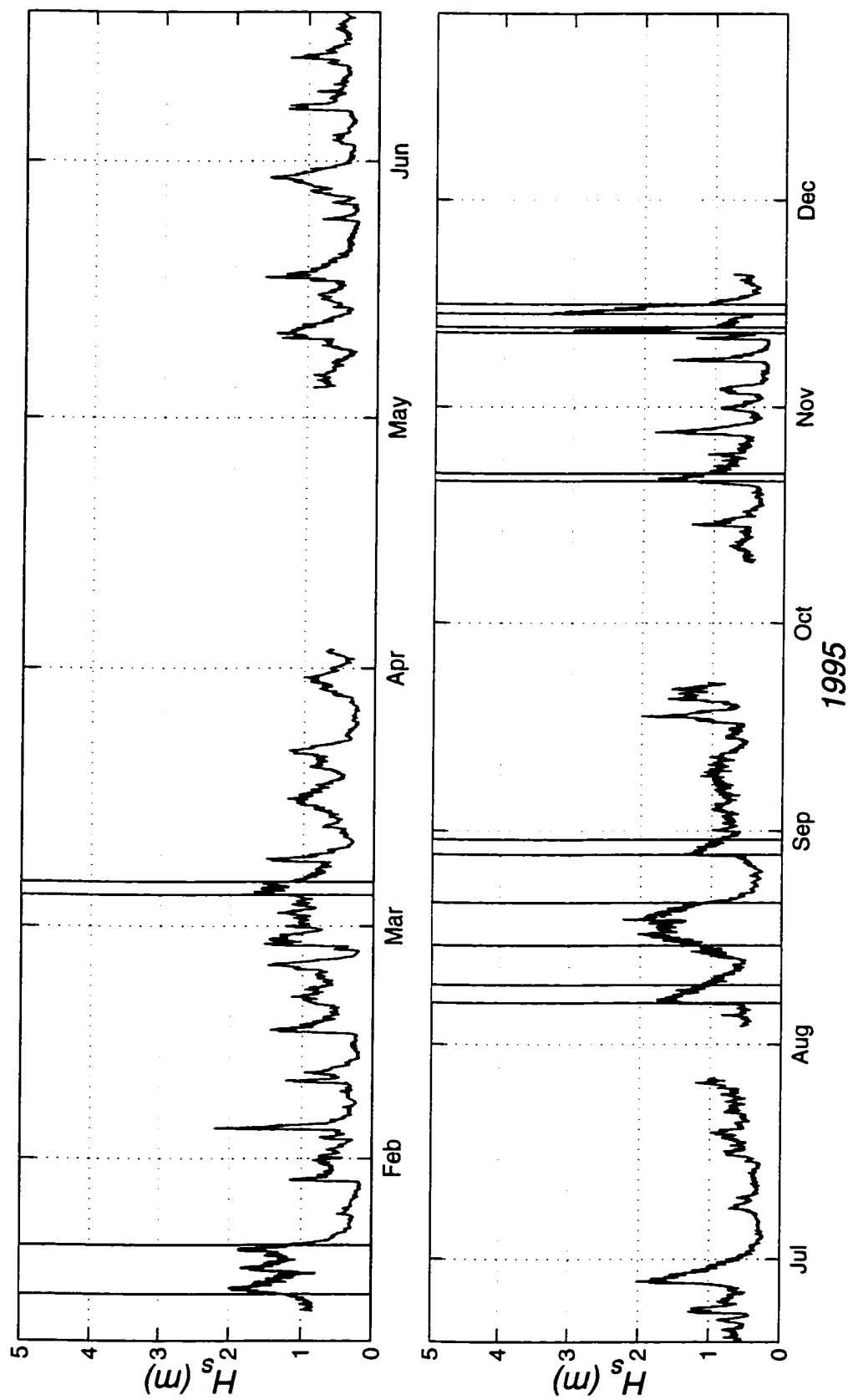


Figure 5.13 Same as Figure 5.12 for 1995



exceeds 1.5  $m$  and possesses a distinctive narrow peaked shape. Also noted are a number of weaker events where  $H_s$  extends above 1.5  $m$  that do not correspond to sediment transport events. Some of these represent transport occurrences that are less than 17 hours in duration and are neglected under the present event criteria threshold. But generally, it appears that the modeled transport events correspond to time periods with higher wave events.

To distinguish the effects of waves and currents, time series of the maximum instantaneous shear velocity for the wave,  $u_{*cw}$ , and the time average shear velocity,  $u_{*c}$ , predicted by the model are shown in Figures 5.14 through 5.17. Figure 5.14 and 5.15 show  $u_{*cw}$  for 1994 and 1995. Patterns of  $u_{*cw}$  mimic  $H_s$ , where larger  $u_{*cw}$  clearly correspond to the transport events. The time average shear velocity shown in Figures 5.16 and 5.17, however, is generally much weaker than  $u_{*cw}$  and mimics the mean current records depicted in Figures 5.5 and 5.6. Because sediment entrainment is directly related to the shear stress, it is clear that waves dominate the total stress and are responsible for initiating and maintaining sediment resuspension.

## 5.2 Model results: Annual sediment transport at LEO-15

In the following discussion, the primary function to describe sediment motion at LEO-15 is the instantaneous depth-integrated sediment transport defined as

$$\Gamma_f = \sum_{n=1}^N \int_{z_0}^h C_{nm}(z) u(z) dz \quad (5.1)$$

where  $h$  is the water depth and  $N$  denotes the total number of grain size classes. As was

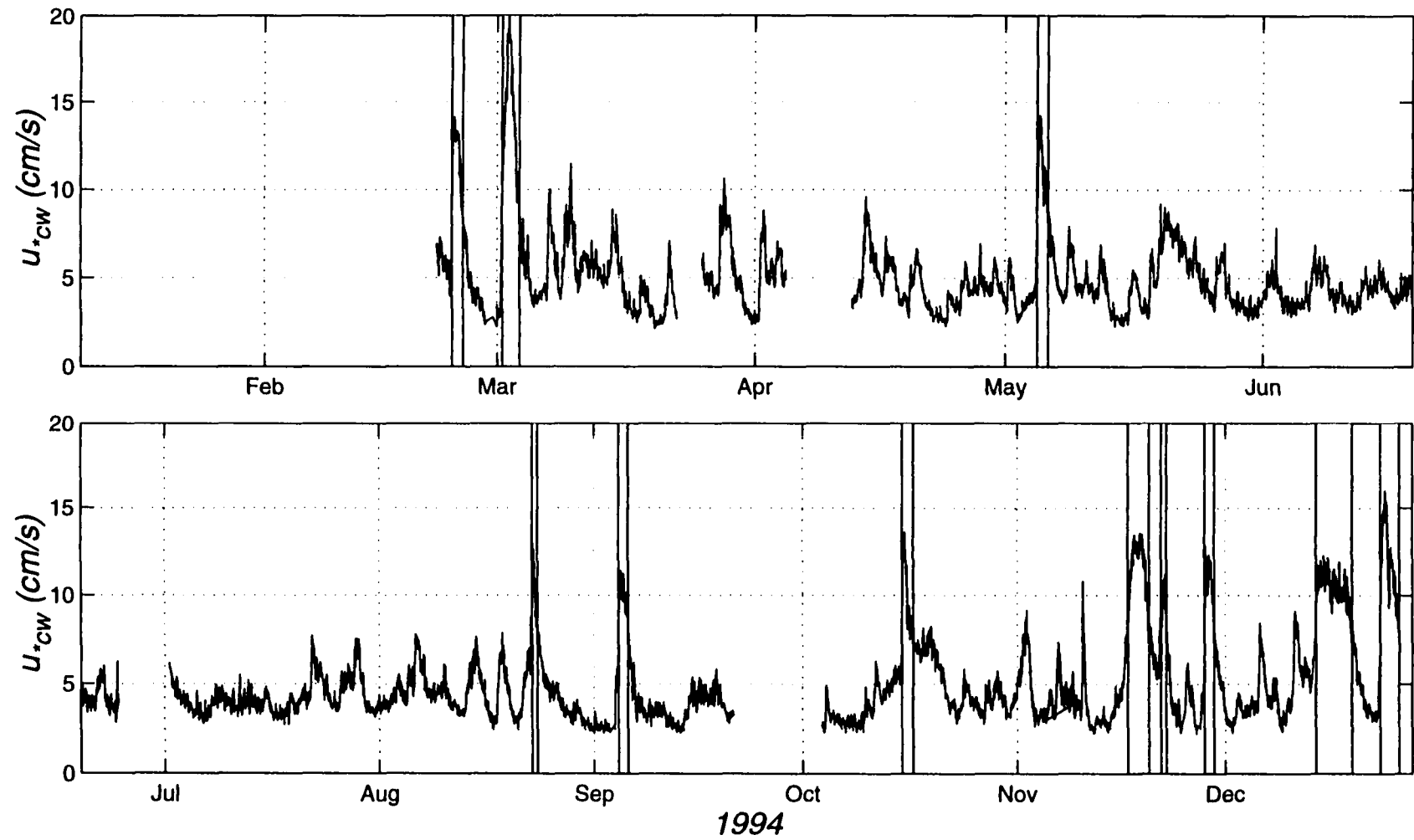


Figure 5.14 Predicted combined wave and current shear velocity,  $u_{cw}$ , for 1994 model run. Patterns mimic those of  $H_s$  and show a clear correlation between transport events and high  $u_{cw}$ .

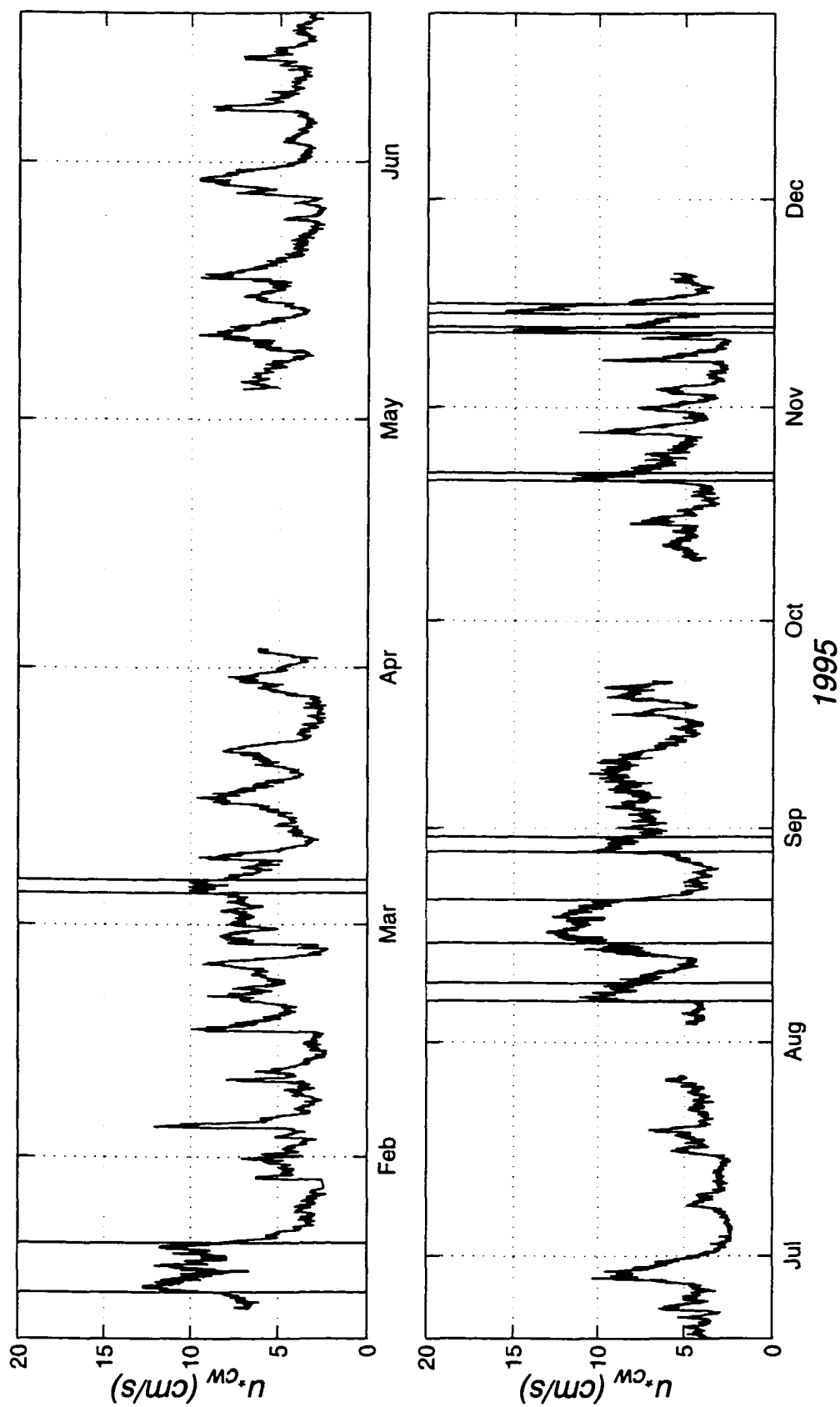


Figure 5.15 Same as Figure 5.14 for 1995

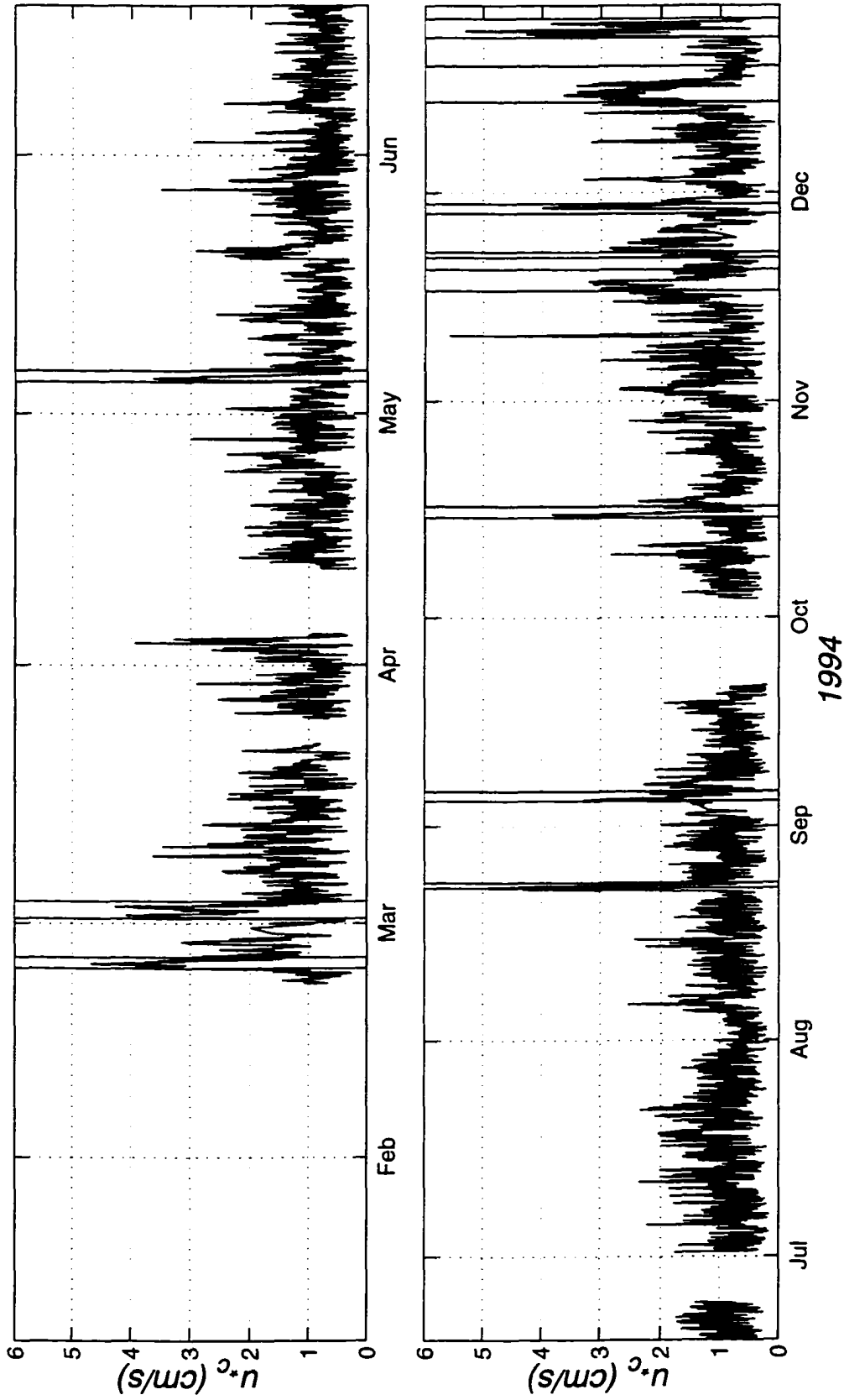


Figure 5.16 Predicted time average shear velocity,  $u_*c$ , for 1994 model run. Patterns are similar to the mean current shown in Figure 5.5.

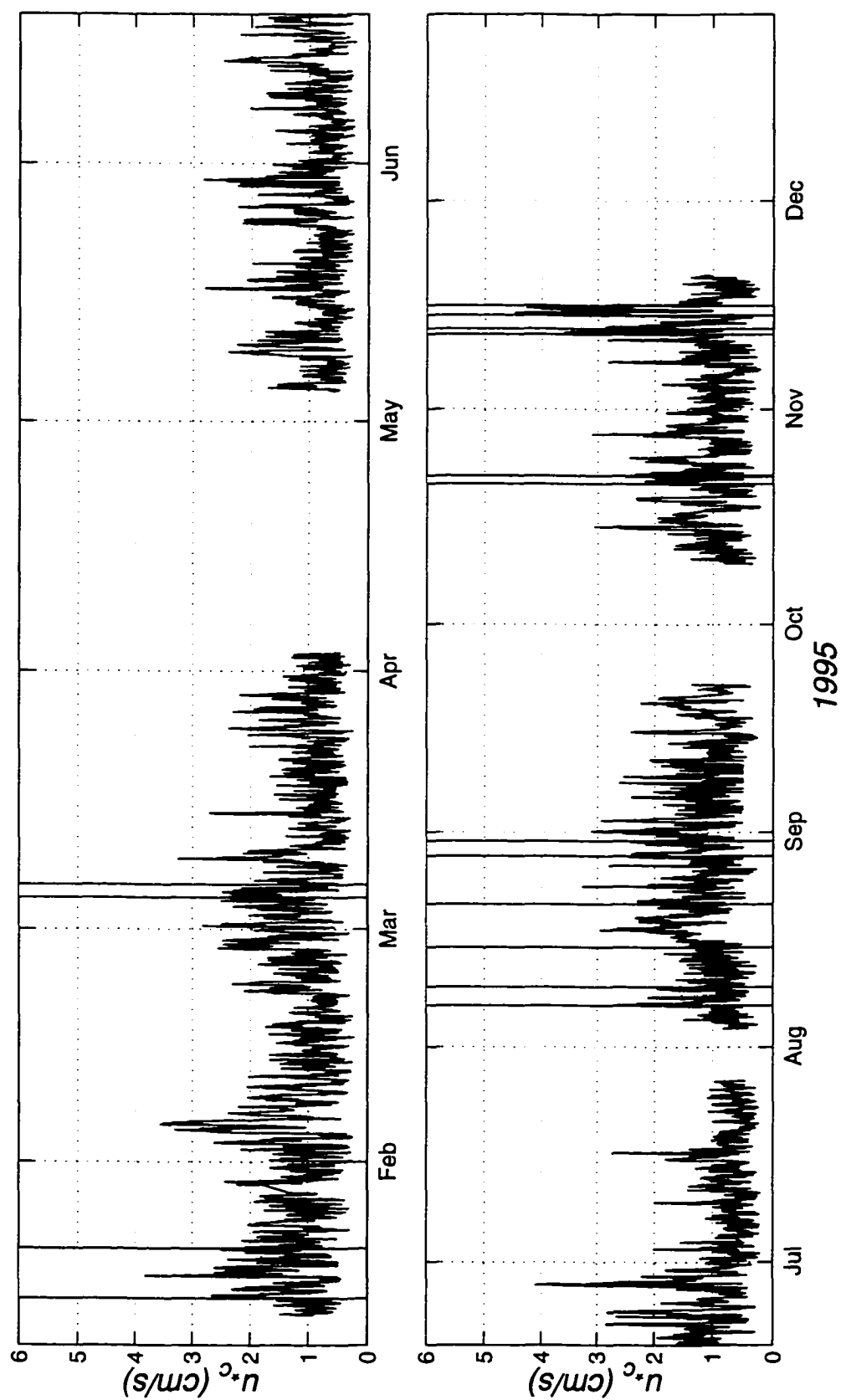


Figure 5.17 Same as Figure 5.16 for 1995

shown in Section 3.7, the product  $C_{nm}(z)u(z)$  rapidly decreases with height for  $z \geq z_2$ , so that (5.1) mostly reflects sediment transport near or within the wave boundary layer. Another useful variable to described sediment transport in terms of individual events is the total depth-integrated sediment transport defined as

$$\Gamma_{ft} = \int_{T_0}^{T_e} \Gamma_f dt \quad (5.2)$$

where the limits  $T_0$  and  $T_e$  denote the beginning and end of an event. Within each event,  $\Gamma_f$  will take on a maximum value defined as  $\Gamma_{fm}$ . Tables 5.1 and 5.2 list relevant statistics for the transport events identified in 1994 and 1995. Included are the start dates of each event, event duration, total depth-integrated cross-shore,  $\Gamma_{ft-x}$  and longshore,  $\Gamma_{ft-y}$ , transport, maximum depth-integrated transport,  $\Gamma_{fm}$ , and  $\Gamma_{ft}$  for each grain-size class.

Conveniently defining the winter storm season as any period between 1-October and 31-March indicates that 8 out of the 11 events for 1994 are classified as winter sediment transport events. Additionally, event duration is highly variable with the shortest event lasting only 20 hours and the longest 123 hours. The seasonal distribution, however, shows that the three summer events are comparable in duration to events in February and late November. The number of event hours for the entire year totals 524 hours. Dividing this by the number of hours the S4s were in operation (6768), translates to 8% active sediment transport for the recorded time period.

For 1995, a total of 8 transport events are identified, but only 5 are counted as winter events. The range in event duration for 1995 is even greater than 1994 with the shortest event lasting 21 hours and the longest 151 hours. Like 1994, 3 events occur

during the summer, and account for nearly 19% of the yearly total  $\Gamma_f$ . The number of event hours for 1995 totals 527 hours, which translates to active sediment transport nearly 9% of the year.

### 5.2.1 Estimates of $\Gamma_f$ and erosion depth

As an initial illustration of the capabilities of the sediment transport model, Figures 5.18(a) and 5.19(a) show time series of  $\Gamma_f$  for all events. The instantaneous depth-integrated sediment transport varies in intensity, duration and distribution throughout the year. For 1994, maximum transport occurs in late December followed by a weaker event in March. Although these can be characterized as winter events, two other events, one in late August and one in early May, rank fourth and seventh, respectively, out of the total 11 events. For 1995,  $\Gamma_f$  is, on average, much less than for 1994, but still exhibits strong seasonal variability with the greatest flux during the end of the year. In addition,  $\Gamma_f$  tends to be weaker during the longer events. The seasonal distribution depicted for both years supports the general statement that most energetic sediment transport events tend to cluster around the winter storm season. Summer storms, however, cannot be dismissed in contributing to the annual transport budget, as illustrated by  $\Gamma_f$  values during May and August of 1994 and June and July 1995. Another important quantity often used to characterize sediment transport is the erosion depth, defined as the change in bed height that would occur assuming all eroded material goes into suspension. For this study, it is calculated by dividing the depth-integrated concentration over all grain size classes,

$$\sum_{n=1}^N \int_{z_0}^h C_{nm}(z) dz \quad (5.3)$$

by the assumed bed concentration ( $c_b = 0.65$ ). Figures 5.18(b) and 5.19(b) show erosion depth calculated from the suspended sediment concentrations predicted by the model. Interestingly, erosion depth for most events tends to peak at about 0.01 *cm*. This indicates that peak values of sediment resuspension tends to be independent of event duration or  $\Gamma_f$ .

### 5.2.2 Relationship between event duration, $\Gamma_{fm}$ and $\Gamma_f$

Intuitively, the degree to which an individual transport event contributes to the yearly total can be categorized according to event duration and  $\Gamma_{fm}$ . Obviously, longer events combined with higher average sediment transport will lead to larger total depth-integrated sediment transport. The question then naturally arises, do the longest events result in the greatest transport? Figure 5.20 illustrates the relationship between  $\Gamma_{fm}$ , event duration and  $\Gamma_f$  for events identified in 1994. All three variables are normalized to 1 so that the relative value across any one variable is proportional to the height of the corresponding vertical bar. The events identified with the greatest  $\Gamma_f$  are closely correlated with  $\Gamma_{fm}$ . For example, events on 23-December, 23-February and 1-March rank first, second and third in  $\Gamma_{fm}$  and events on 1-March, 23-December and 23-February rank first, second and third in  $\Gamma_f$ . Event duration, however, does not correlate well with either of these, with the longest event associated with the sixth greatest  $\Gamma_f$  and eighth greatest  $\Gamma_{fm}$ . For 1995, the relationship between event duration,  $\Gamma_{fm}$  and  $\Gamma_f$  follows



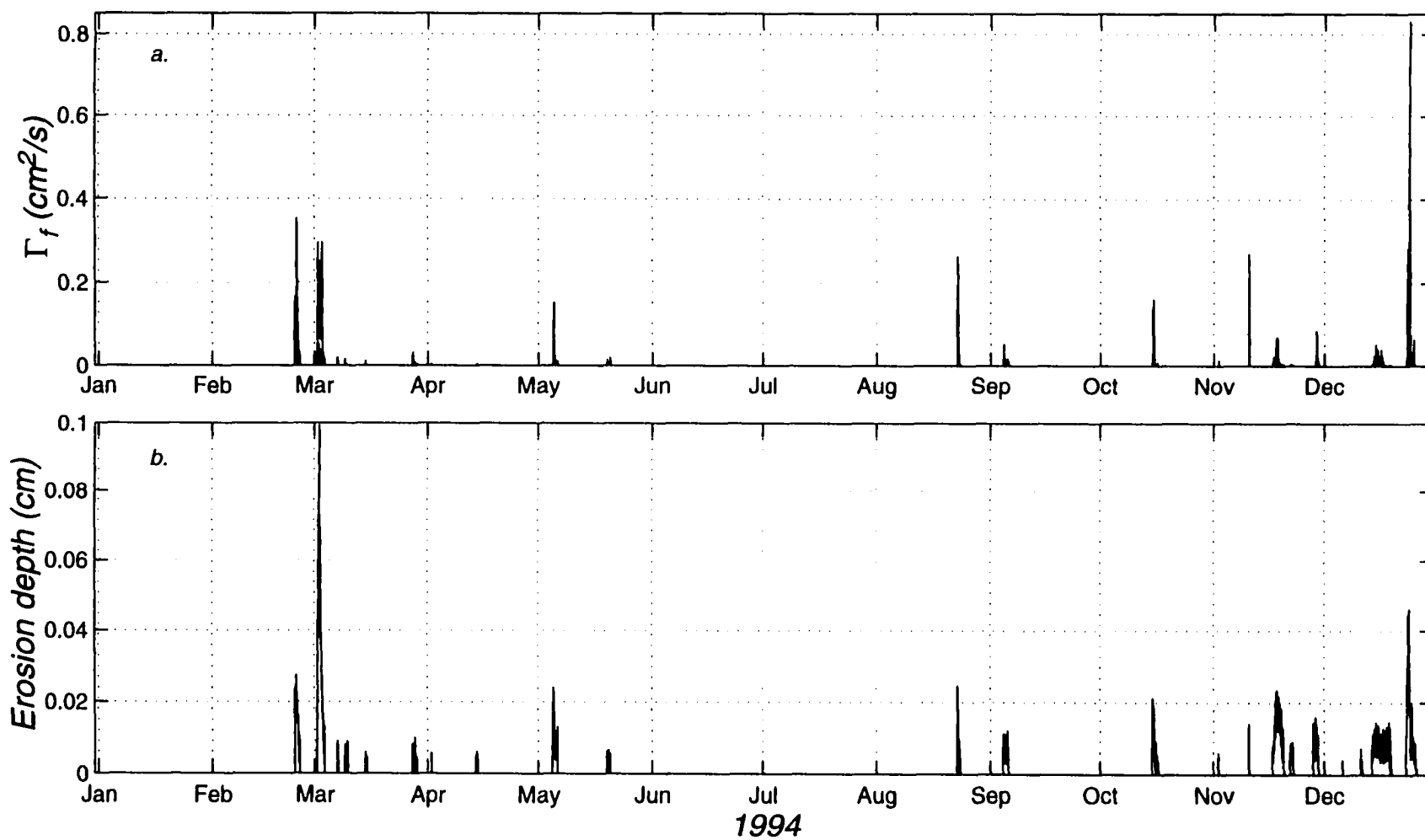


Figure 5.18 Predicted maximum depth-integrated transport (a) and erosion depth (b) for the 1994 sediment transport study. The greatest transport occurs during the beginning and end of the year, but significant transport is seen during August.

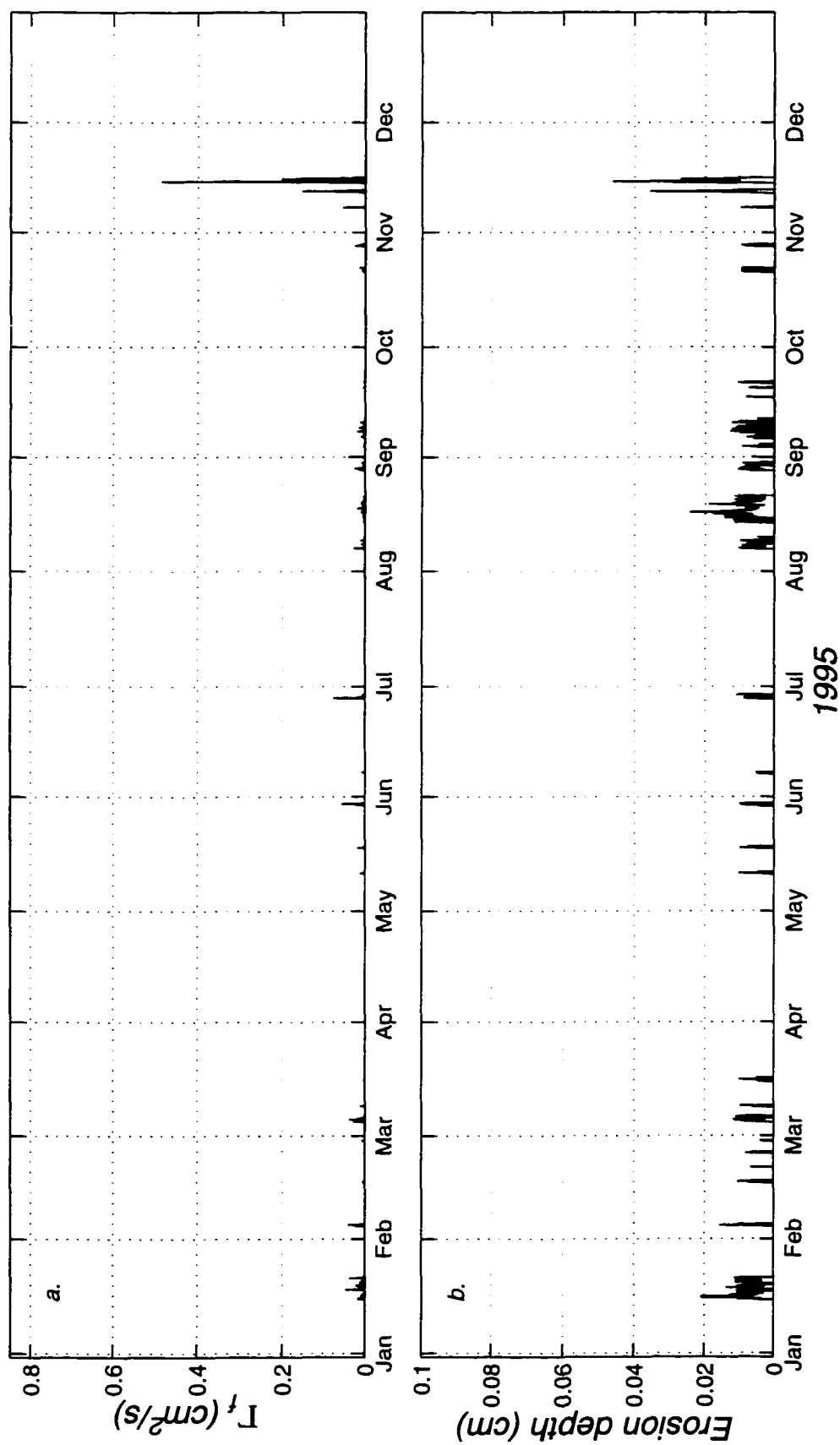


Figure 5.19 Same as Figure 5.18 for 1995.

patterns similar to those in 1994, with  $\Gamma_{ft}$  more closely correlated with  $\Gamma_{fm}$  than with event duration. This is illustrated in Figure 5.21 where the longest event corresponds with the third largest  $\Gamma_{ft}$  and the fifth largest  $\Gamma_{fm}$ .

### 5.2.3 Cross-shore and longshore transport

Figure 5.22 shows progressive trajectories of  $\Gamma_f$  for the 1994 events. The  $x$ - and  $y$ -axes are in units of  $\Gamma_f$  ( $cm^2/s$ ) and are of equal length to reflect accurately the advancing motion of the transport through an event. The lines are drawn from the origin which represents the start of each event, and the crosses indicate an advancement of one hour. With the exception of 21- and 28-November, the strong southward alongshore component is clearly illustrated. Figure 5.23 shows the same for the 1995 events. A similar strong alongshore flux is observed but is interrupted in August and replaced by a relatively substantial onshore component. Interestingly, the instantaneous alongshore components for 15-January, 6-August and 15-August show a reversal in direction partway through the event.

In the vicinity of the LEO-15 study area, the New Jersey coastline is oriented approximately  $20^\circ$  clockwise from true north ( $27^\circ$  magnetic). The total depth-integrated sediment transport is decomposed into shore-normal,  $\Gamma_{ft-x}$  (+ indicates offshore flow) and shore-parallel,  $\Gamma_{ft-y}$  (+ indicates alongshore flow toward the north, north-east) components. Results from the cross-shore and longshore decomposition are depicted in Figures 5.24 and 5.25. For 1994, the predominant transport is alongshore to the south for all but two weak events in late November, and one event in mid December. The cross-shore component is weakly onshore for nearly all events. For 1995, cross- and longshore transport also exhibit strong southerly and slightly onshore components for most of the

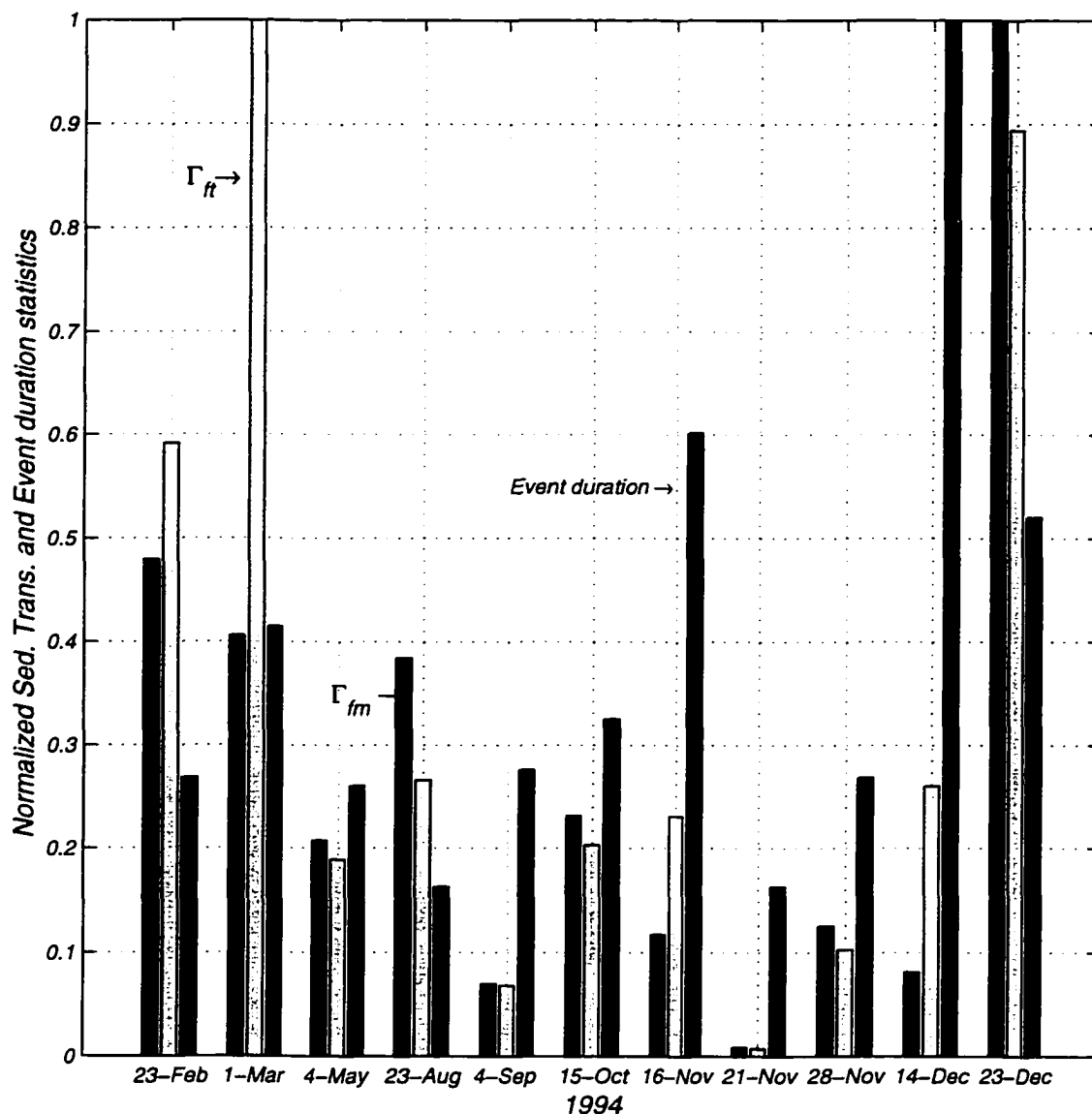


Figure 5.20 Maximum instantaneous depth-integrated transport,  $\Gamma_{fm}$ , total depth-integrated transport,  $\Gamma_{ft}$ , and event duration for the 11 events identified in 1994. For each of the three variables, values shown are normalized by the maximum value obtained across all events. Thus, the 23-December event shows the greatest  $\Gamma_{fm}$  and the 1-March event shows the greatest  $\Gamma_{ft}$ , since for both variables, their normalized value is one. For individual variables, comparing the heights of the vertical bars identifies the rank of that event against all 11 events for that particular variable. Because of the normalization procedure adopted here, comparing the relative heights of all three variables for any one event does not accurately reflect the relationship between the three variables for that event.

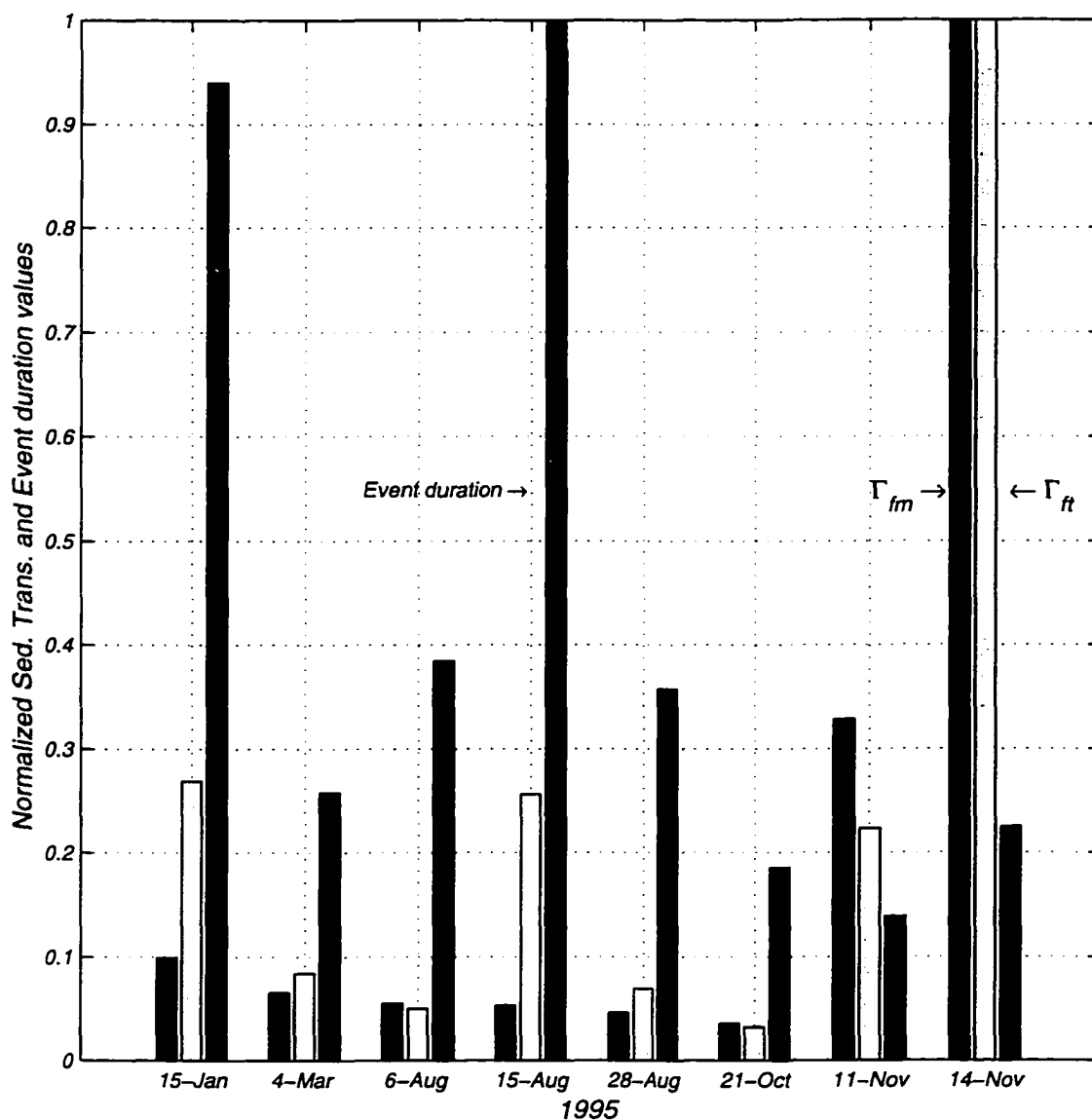


Figure 5.21 Maximum instantaneous depth-integrated transport,  $\Gamma_{fm}$ , total depth-integrated transport,  $\Gamma_{ft}$ , and event duration for the 8 events identified in 1995. The format is the same as 1994. Again,  $\Gamma_{fm}$  correlates well with  $\Gamma_{ft}$ . Event duration, however, is not well correlated with either  $\Gamma_{ft}$  or  $\Gamma_{fm}$ .

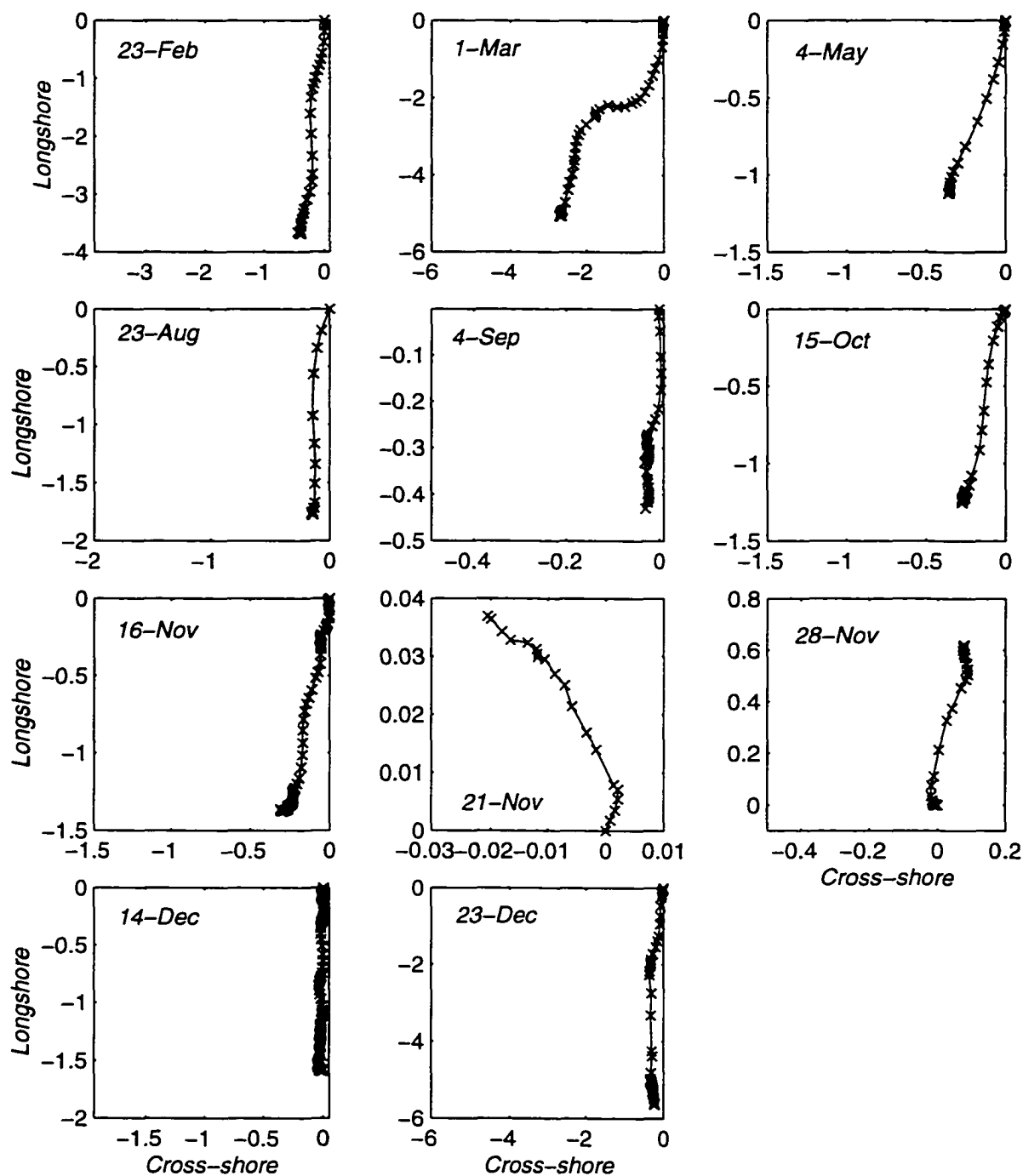


Figure 5.22 Progressive trajectories of sediment transport for events identified in 1994. Axes are drawn on the same scale to emphasize the strong alongshore component during most transport events. Note change of scale.

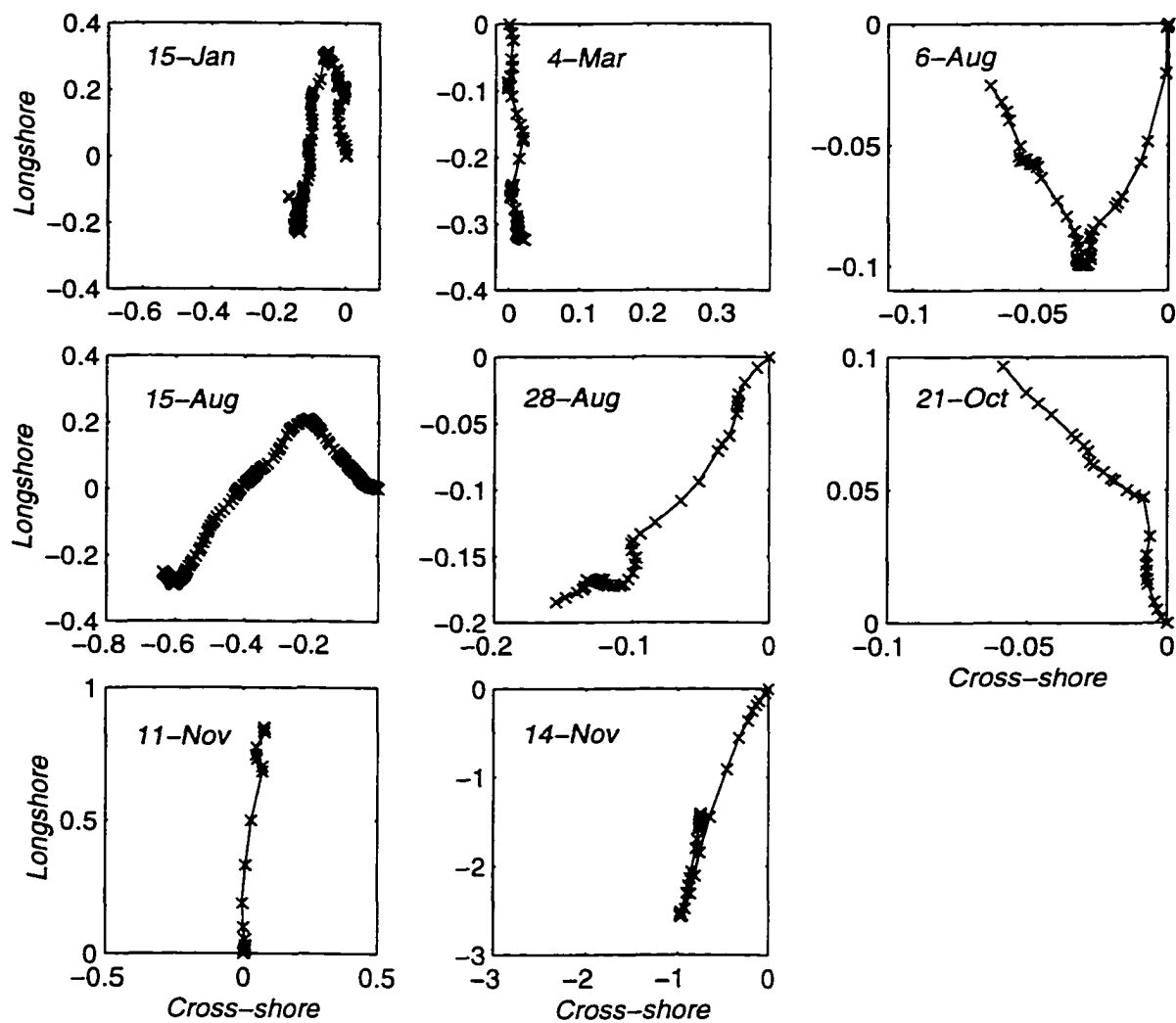


Figure 5.23 Hodograph showing transport trajectories for events identified in 1995. Axes are equal to emphasize the predominant alongshore transport. Note change of scale.

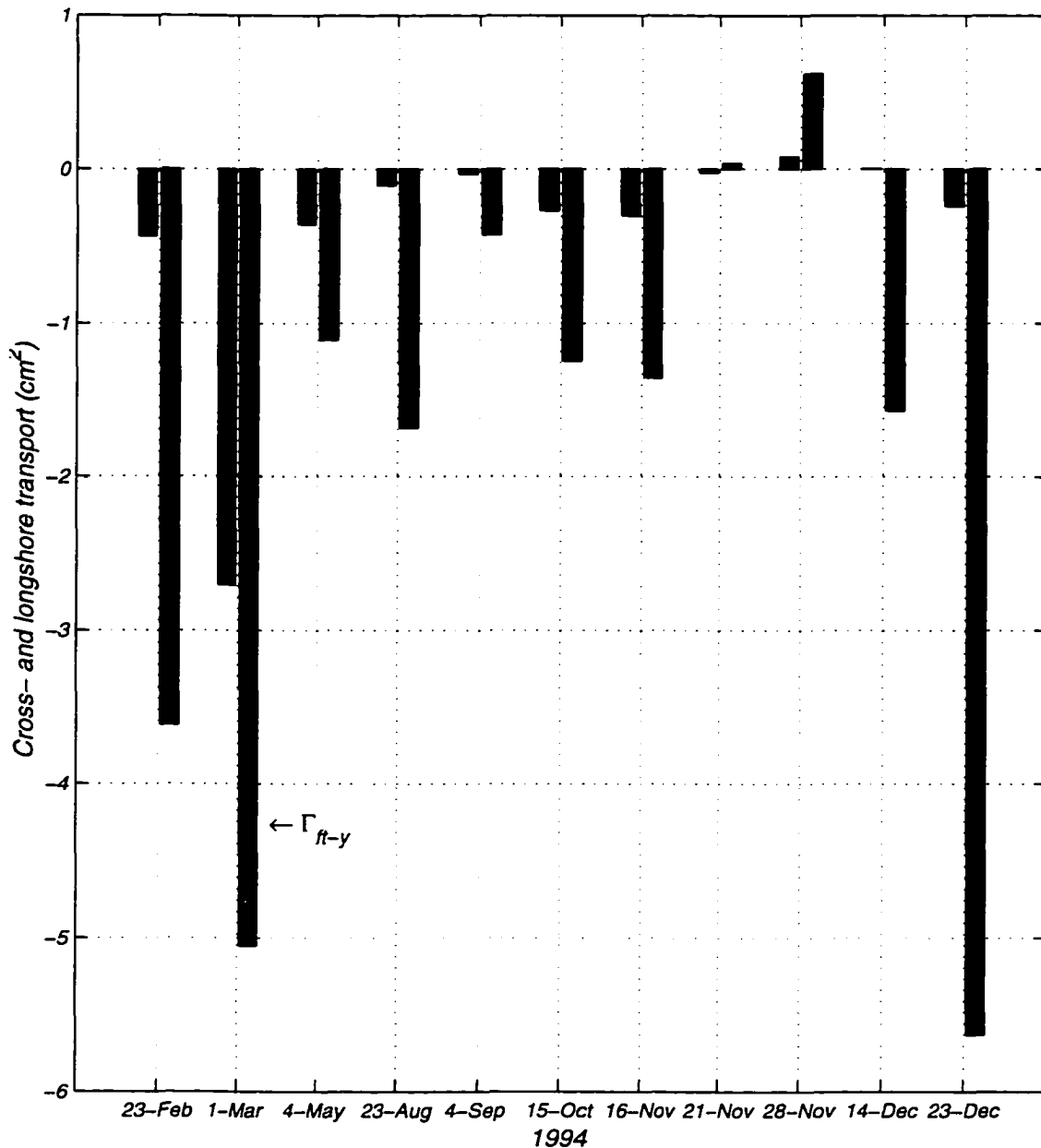


Figure 5.24 Cross-shore,  $\Gamma_{ft-x}$ , and longshore,  $\Gamma_{ft-y}$ , total depth-integrated sediment transport for each of the 11 events identified for 1994. For each event, identified by day and month, the left vertical bar indicates the cross-shore component and the right the longshore component. The magnitude of  $\Gamma_{ft-x}$  and  $\Gamma_{ft-y}$  is indicated by the height of the corresponding vertical bar. Negative values indicate flow toward the south and onshore. For most events, the transport is directed alongshore to the south and slightly onshore.



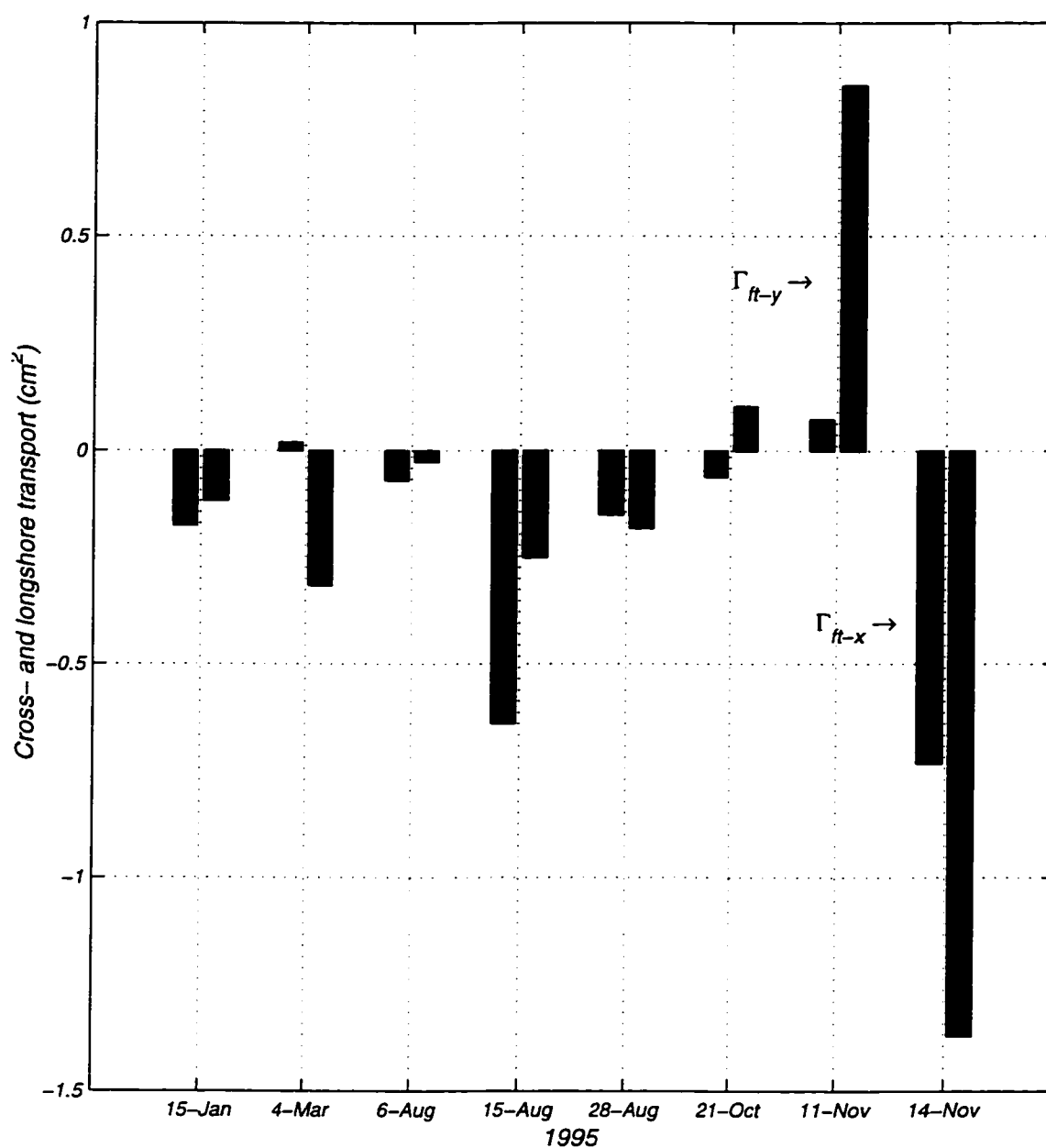


Figure 5.25 Cross-shore,  $\Gamma_{ft-x}$ , and longshore,  $\Gamma_{ft-y}$ , total depth-integrated sediment transport for 1995. The graph is organized the same way as for 1994, with negative values indicating flow toward the south and onshore. Again, the majority transport is alongshore to the south and slightly onshore.

year (Figure 5.25). Relatively strong northward  $\Gamma_{f-y}$ , however, does occur in early November, followed by weaker transport in October. Weak offshore  $\Gamma_{f-x}$  is similarly seen in March and early November, but countered by strong onshore transport in August. The strong southerly, alongshore component for both years is in agreement with measured patterns of flow in the MAB during strong northeast storms (Niederoda et al. 1984). The slight, yet persistent, onshore component, however, is generally not recognized as the predominant direction for net long-term cross-shelf transport. The figures also illustrate the seasonal distribution of  $\Gamma_{f-x}$  and  $\Gamma_{f-y}$  with stronger events near the beginning and end of the year bracketing generally weaker events during the summer and early fall.

#### **5.2.4 The relationship between $\Gamma_f$ and sediment grain size.**

The last category in Tables 5.1 and 5.2 list  $\Gamma_f$  according to sediment grain-size class denoted  $\Gamma_{fn}$ . As expected, the smaller grains show the largest values, as these particles are preferentially mixed higher into the water column due to their lower settling velocities. This leads, on average, to correspondingly larger  $\Gamma_{fn}$ . Interestingly, typical values between the largest and smallest grains span an order of magnitude, reflecting the sensitivity of sediment flux to particle size.

#### **5.2.5 Comparison of neutral and stratified models**

As a final look at results for both years, comparisons of sediment transport between the neutral and stratified versions of the model are presented. The neutral model is run using the same input wave, current and sediment parameters, and results of time integrated sediment transport are matched with corresponding values obtained from the stratified version. Figure 5.26 shows  $\Gamma_f$  obtained from both the neutral and stratified

models. In all cases the neutral model predicts at least 78% greater total depth-integrated transport than the stratified model, with a maximum of 88%. Averaging these percentages over all events implies that neglecting the suspended sediment correction can lead to over-predictions by as much as 82%. Because it has been demonstrated in Section 3 that smaller grains,  $O(0.01 \text{ cm})$ , influence the stratification solution to a much greater degree than grains typical of LEO-15, correct parameterization of the stratification correction for arbitrary sediment conditions becomes crucial. In addition, the neutral and stratified boundary layer models for 1995 show similar trends as in 1994, with the neutral model predicting on average 86% greater total depth-integrated sediment transport for the entire year (Figure 5.27).

### 5.3 Discussion

The definition of a sediment transport event lasting at least 17 hours has eliminated a number of short sediment transport occurrences, and it is instructive to determine the consequences of ignoring the contribution from these events in describing annual totals. A quantitative estimate of the contribution from these lesser events is achieved by taking the sum of  $\Gamma_f$  over all events and dividing by the total calculated for the entire year. For 1994, the sum of  $\Gamma_f$  over all events totals  $24.587 \text{ cm}^2/\text{s}$ , and the total from the year is  $25.598 \text{ cm}^2/\text{s}$ . This translates to ~96% coverage based on the 17-hour event criterion established for this study. For 1995, this percentage is ~82%. When these numbers are categorized according to grain size class, the 1994 percentages are 99.5% for the  $0.08 \text{ cm}$  grains, 97% for the  $0.05 \text{ cm}$  grains and 95% for the  $0.024 \text{ cm}$  grains. Similar statistics for 1995 show 97% for the  $0.08 \text{ cm}$  grains, 88% for the  $0.05 \text{ cm}$  grains and 79% for the  $0.02 \text{ cm}$  grains. Thus, the criterion used to define

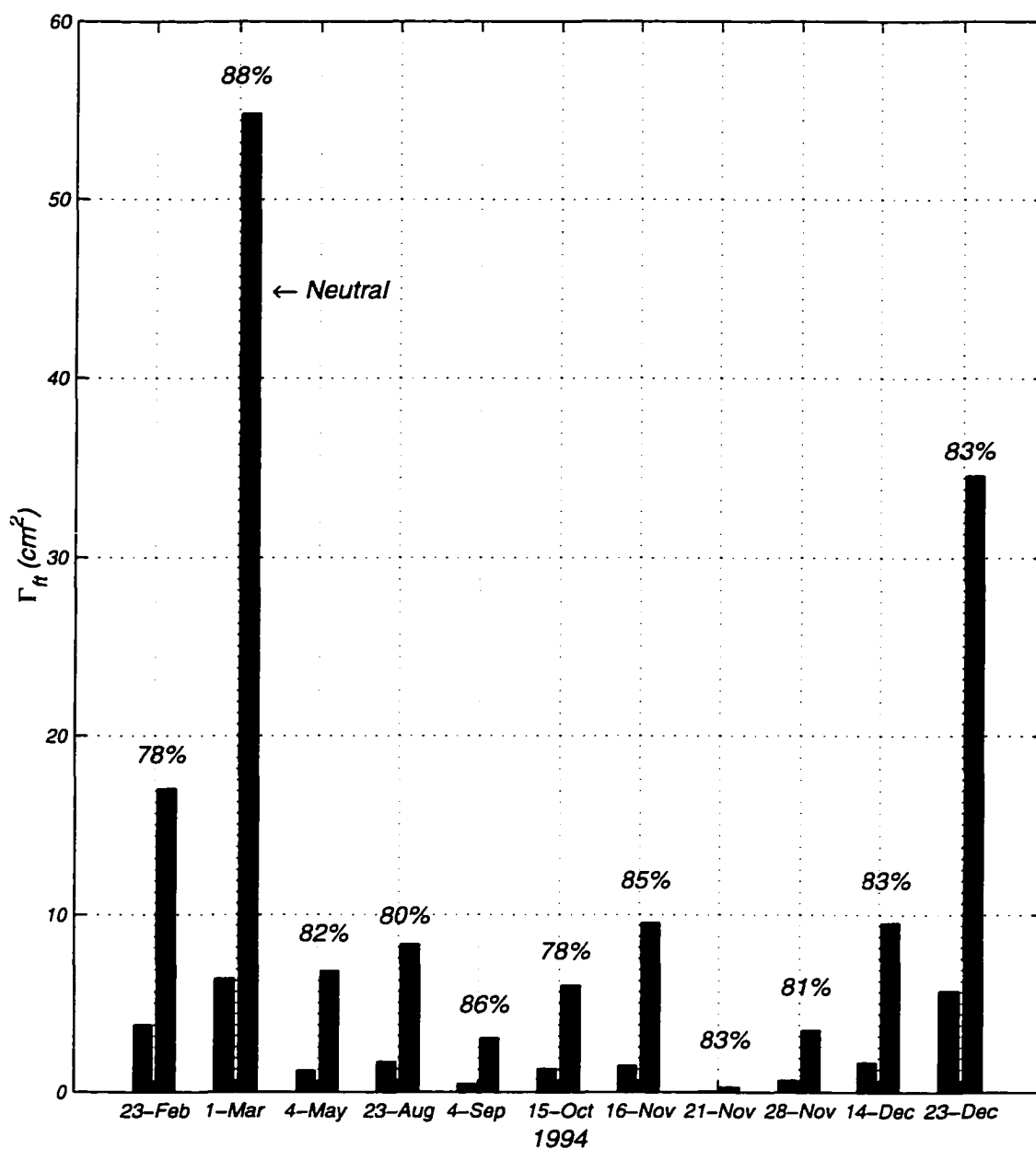


Figure 5.26 Comparison of total depth-integrated transport,  $\Gamma_t$ , for neutral and stratified versions of the model for 1994. Percentages show 1 minus the ratio of the stratified to neutral model. The stratified version, on average, predicts 82% less transport than the neutral. Note that during the most active sediment transport event, the neutral model over estimates by 88%.

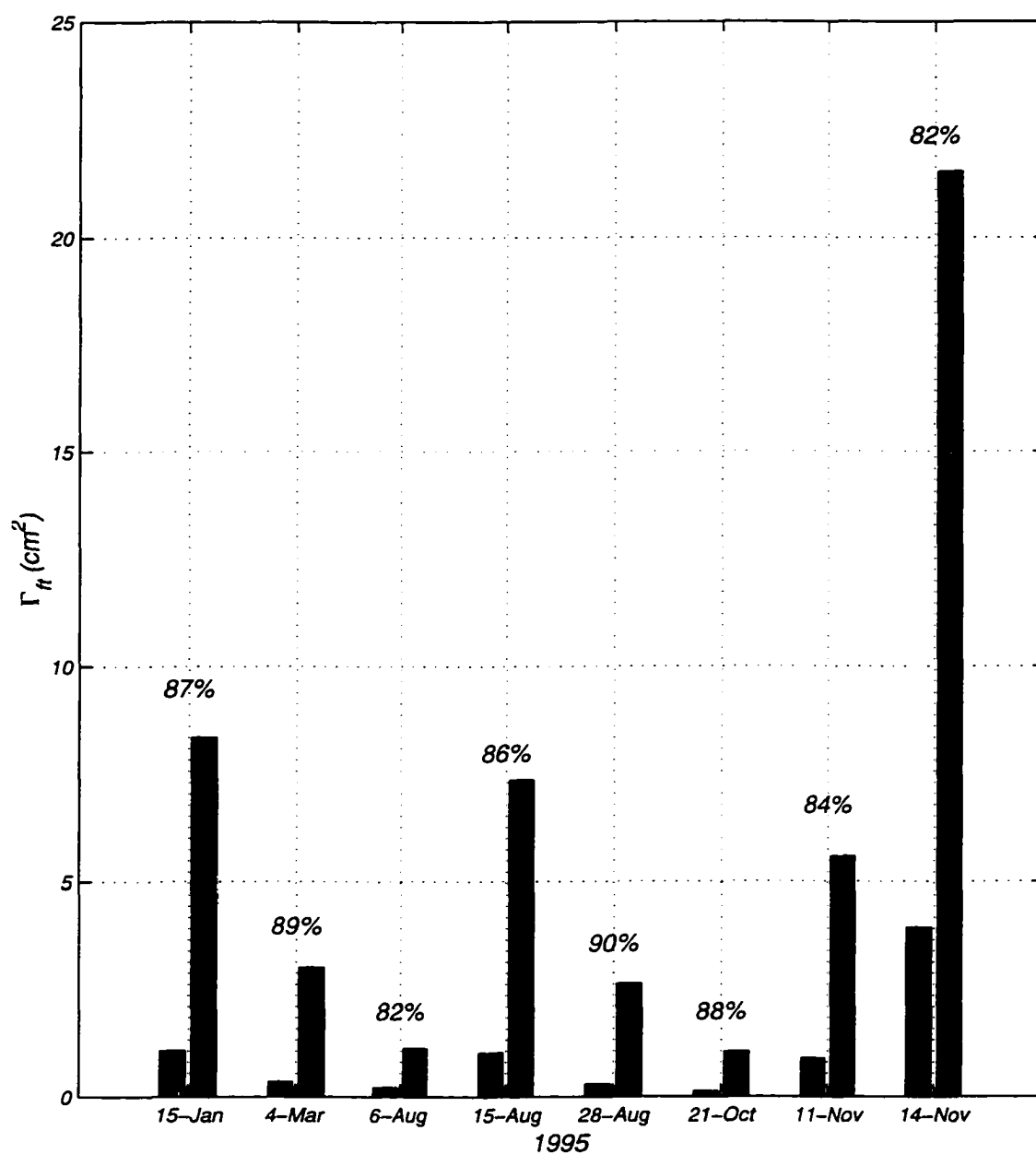


Figure 5.27 Same as Figure 5.26 for 1995. In this case, the stratified version, on average, predicts 86% less transport than the neutral.

sediment transport events for 1994 and 1995 captures most of the annual sediment transport, and is especially representative of the larger sized grains.

When comparing time series of  $u_{*c}$  with  $u_{*cw}$  (Figures 5.14–5.17) it is obvious that the wave shear stress constitutes most of the total. Recalling that sediment resuspension is directly related to shear stress, it is suspected that the wave is primarily responsible for sediment entrainment during the transport events. Figure 5.28 shows mean and maximum  $u_{*c}$  and  $u_{*cw}$  for events identified in 1994. In both cases,  $u_{*cw}$  values are nearly triple corresponding  $u_{*c}$  values. Similar results hold for 1995 where  $u_{*cw}$  is again nearly triple  $u_{*c}$  (Figure 5.29). Examination of Tables 5.1 and 5.2 show that annual totals of  $\Gamma_{fm}$  and  $\Gamma_f$  for 1994 are substantially greater than for 1995. The mean of the maximum  $u_{*cw}$  over all events is 13.8 *cm/s* for 1994 and 12.4 *cm/s* for 1995. Computing the same for the mean  $u_{*cw}$  gives 11.1 *cm/s* for 1994 and 10.4 *cm/s* for 1995. This translates to about 10% greater maximum  $u_{*cw}$  and about 7% greater average  $u_{*cw}$  for 1994 than 1995. In both cases,  $u_{*cw}$  is greater for 1994 when annual totals of sediment transport are highest. Model predictions, supported by the available data, have clearly identified waves as the dominant forcing mechanisms responsible for entraining sediment at LEO-15. Although  $u_{*c}$  for both years is much less, it is the mean current that is crucial in transporting sediment suspended by the wave. For 1994, the mean values across all events for both maximum and average  $u_{*c}$  are 3.8 *cm/s* and 2.1 *cm/s*. For 1995, these values are 3.1 *cm/s* and 1.7 *cm/s*. This translates to about 10% greater maximum  $u_{*c}$  for 1994 than 1995, and 10% greater average  $u_{*c}$ .

Because longer events mean greater exposure of the suspended material to the current, it is tempting to associate  $\Gamma_f$  with event duration. Surprisingly though for both

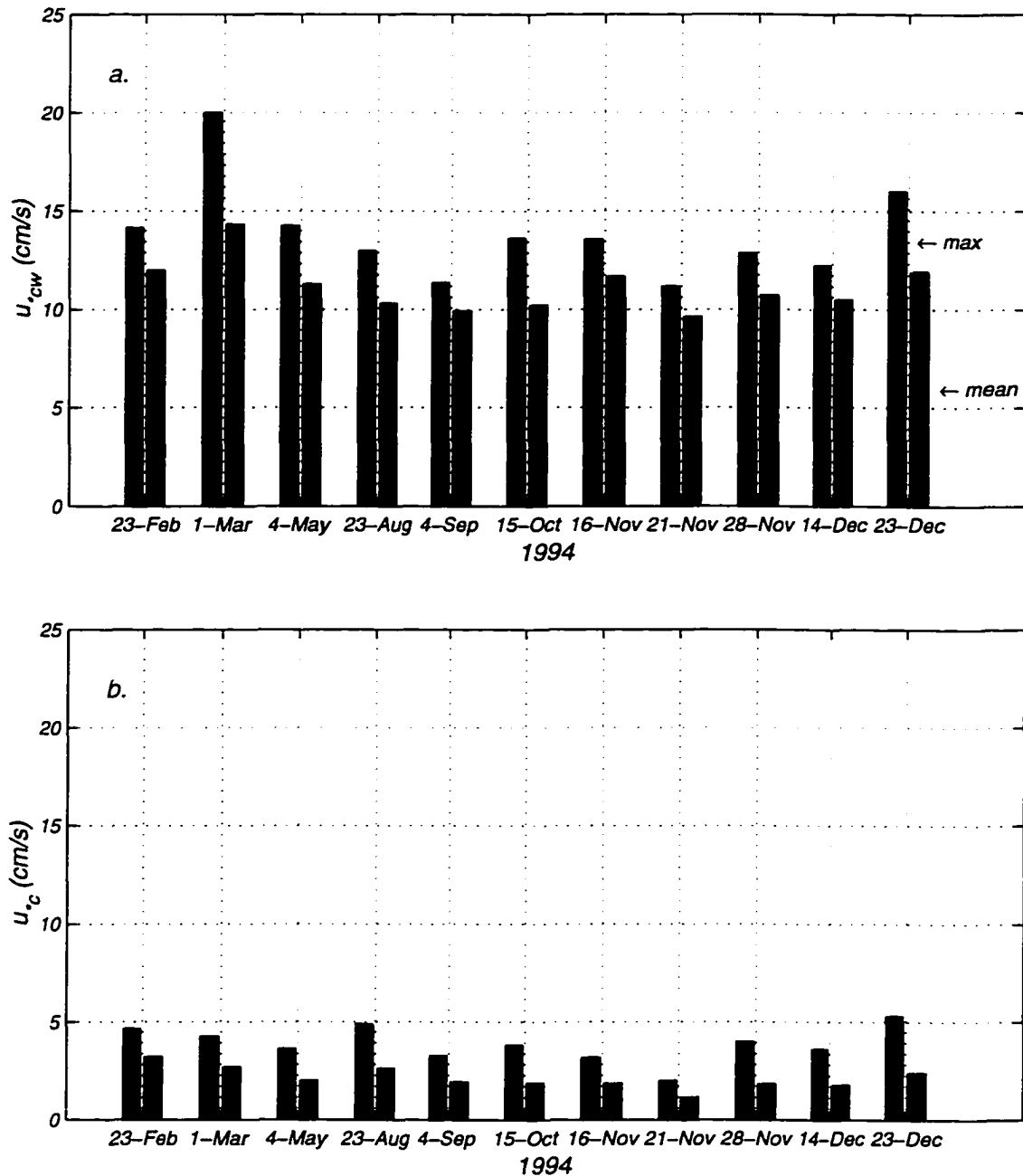


Figure 5.28 (a) Combined wave and current,  $u_{*cw}$ , and (b) time average,  $u_{*tc}$ , shear velocities calculated by the model for 1994. Shear velocities are categorized by maximum over each event and the mean for each event. The fact that  $u_{*cw}$  is much greater than  $u_{*tc}$  indicates that the wave portion of the shear stress makes a significant contribution to the total, reemphasizing the importance of waves on sediment transport at LEO-15.

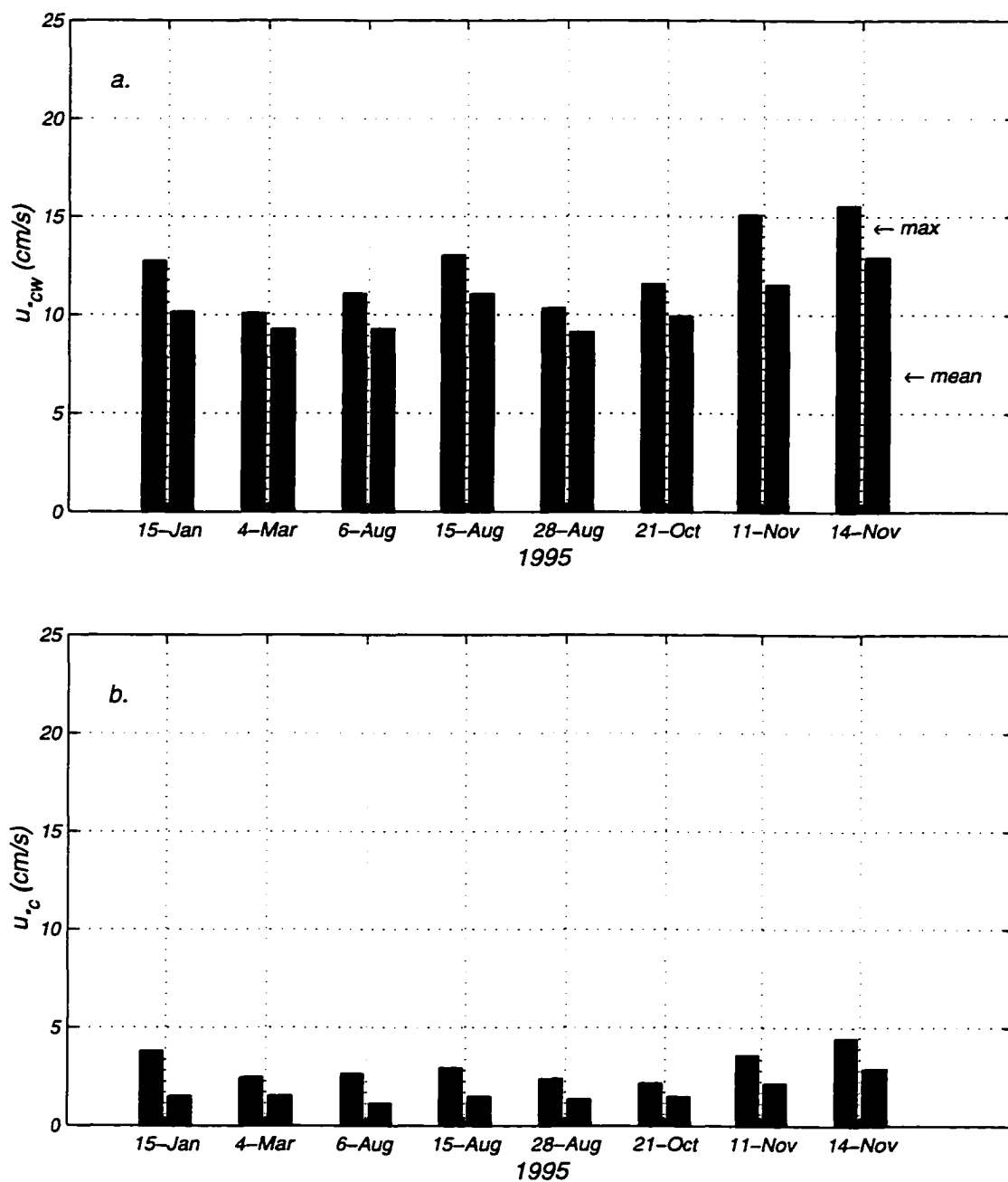


Figure 5.29 Same as Figure 5.28 for 1995. Note the generally weaker combined wave and current shear stress for this year compared to 1994.



years,  $\Gamma_{ft}$  is more correlated with  $\Gamma_{fm}$  than event duration. A formal expression describing the mutual relationship between  $\Gamma_{fm}$ ,  $\Gamma_{ft}$  and event duration can be formed by constructing a matrix of correlation coefficients representing the normalized covariance between these three variables (Bendat and Piersol 1986). Treating the events as independent observations and the three parameters as variables produces the matrix of correlation coefficients depicted in Tables 5.3 and 5.4. Individual matrix values can be interpreted as representing the correlation between any two pair of variables. As an illustration, the diagonal elements in Table 5.3 show a correlation of one since event duration correlates perfectly with event duration,  $\Gamma_{ft}$  correlates perfectly with  $\Gamma_{ft}$  etc... The off-diagonal elements indicate correlations between variables on the left-hand side and the

Table 5.3 Cross-correlation coefficient relating total depth-integrated sediment flux, maximum instantaneous depth-integrated sediment flux and event duration derived from 1994 sediment transport events.

1994	$\Gamma_{ft}$	$\Gamma_{fm}$	Event duration
$\Gamma_{ft}$	1.00	0.81	0.02
$\Gamma_{fm}$	0.81	1.00	0.20
Event duration	0.02	0.20	1.00

Table 5.4 Cross-correlation coefficient relating total depth-integrated sediment flux, maximum instantaneous-depth integrated sediment flux and event duration derived from 1995 sediment transport events.

1995	$\Gamma_{ft}$	$\Gamma_{fm}$	Event duration
$\Gamma_{ft}$	1.00	0.95	-0.32
$\Gamma_{fm}$	0.95	1.00	-0.04
Event duration	-0.32	-0.04	1.00

corresponding elements across the top. The correlation coefficient between  $\Gamma_{fm}$  and  $\Gamma_{ft}$  is found by matching  $\Gamma_{fm}$  on the left-hand side with  $\Gamma_{ft}$  across the top. Because correlations between two variables are symmetric, selecting  $\Gamma_{ft}$  on the left-hand side and  $\Gamma_{fm}$  along the top is the same as before. Thus,  $\Gamma_{fm}$  is well correlated with  $\Gamma_{ft}$  with a correlation coefficient of 0.81 for 1994, and 0.95 for 1995. The correlation coefficient between  $\Gamma_{ft}$  and event duration is 0.02 for 1994, and -0.32 for 1995. Similarly weak correlation coefficients between  $\Gamma_{fm}$  and event duration are seen for both years with values of 0.20 for 1994, and -0.04 for 1995. If the results depicted here are indicative of transport conditions on the New Jersey shelf, then the greatest sediment transport occurs during short energetic storms.

The seasonal distribution of sediment transport reflects established patterns of energetic winter storms driving major transport events, countered by less frequent summer events with a range of transport magnitudes. When the 2-year transport budget is considered, however, summer storms make up a significant fraction of the total. For 1994 and 1995, a total of 6 summer transport events were identified. When separated by annual contributions, 3 events in 1994 were responsible for 14% of the total annual  $\Gamma_{ft}$  and 3 events in 1995 were responsible for 19% of the total. A few summer storms produced transport rates comparable to several moderate winter storms. In fact, the 23-August-94 event ranked fourth in  $\Gamma_{fm}$  for that year, while the 15-August-1995 event ranked third in  $\Gamma_{ft}$  the following year. Thus, it is clear that an accurate assessment of long-term sediment transport patterns must include more than winter storms.

The availability of the S4 data set has made it possible to obtain a preliminary glimpse into long-term patterns of sediment transport at LEO-15. These patterns,

however, are a direct consequence of the bottom boundary layer model which is most limited in its description of the long-term variability of bed forms. Relatively little is known about the seabed's response to extended periods of weak wave and current conditions, or to reworking of bed material due to biological activity. In regions where wave-formed ripples are present, models that incorporate bed reworking by biological organisms usually assume that after a significant sediment transport event the ripples are continuously smoothed or distorted by the activities of the organisms. Physical models usually assume an exponential decay, with a rate proportional to the assumed efficiency of these organisms in reworking the sediment bed (Sherwood 1995). Obviously, the efficiency will be a function of the number and types of organisms present, which is difficult to quantify, and a function of geographical location and season. In addition, through bed armoring and grading, the storm itself can rework the bed, leaving the vertical distribution of bed sediment after a storm very different from pre-storm conditions.

Although attention to these interesting and potentially important factors influencing long-term transport must eventually be considered, it should be noted that the present model is designed to reflect accurately local conditions during sediment transport events. As discussed in Section 4, studies have shown that the initiation of sediment motion in wave dominated environments has an intermediate stage where wave-formed ripples are accurately described in terms of wave excursion amplitude and maximum near-bottom orbital velocity. It was hypothesized that when ripples are in this equilibrium state, the model accurately predicts bedform geometry and bottom roughness. For stronger flows, the ripples may washout leaving a near-bed transport layer for which

the model is also able to calculate the bottom roughness and reference concentration. During storm conditions, the leading order state of the seabed that most influences sediment transport is assumed to be adequately described by the BBLM. This assertion is probably more justified at LEO-15 Node A since the ridge consists of a reasonably well mixed layer of medium sized sand. In other areas where the vertical distribution is more heterogeneous, or the bed mixture consists of finer material such as mud that is more easily reworked by biological organisms, pre- and post-storm bed characteristics may need to be taken into account to form an adequate description of long-term patterns of sediment transport.

#### **5.3.1 Mechanisms influencing cross-shore transport**

As noted for both 1994 and 1995, the predominant cross-shore transport is directed weakly onshore. This pattern occasionally is interrupted by substantial onshore transport several times during the 2-year time period. To help explain the causes of this predominant onshore transport, a brief examination of the local winds and LEO-15 bathymetry is presented.

For this study, the primary source of wind data is the meteorological tower located at the Rutgers University Marine Field Station (RUMFS) located in Tuckerton, NJ. The field station is equipped with a 70 *m* meteorological tower that supports a wind sensor at the 10 *m* level. The sensor logs wind speed and direction each minute which is stored on disk at the field station. For the present analysis, the 1-minute winds were vector averaged to form 1-hour winds, which then were rotated into long- and cross-shore components and averaged over each event. During 1994, the wind sensor was fully operational, but in January 1995 the wind sensor was taken down to refurbish the

tower and was not reinstalled until the end of that year. To fill data gaps left by the Tuckerton wind sensor, hourly wind data were obtained from NOAA Buoy 44009, Delaware Bay (NDBC 1998) located approximately 100 miles south of LEO-15. Unfortunately, the NOAA buoy was out of service during the beginning and end of 1995, so that only 4 of the 8 events for 1995 are supplemented by wind data. Despite these unresolvable data gaps, it is still possible to infer seasonal current patterns as they relate to local wind forcing. Before presenting wind and current comparisons, Figure 5.30 shows 24-hour low pass filtered cross- and longshore wind components obtained from both the Delaware Bay buoy and the Tuckerton wind sensor for selected days in 1994. Both the longshore and cross-shore decomposition tend to indicate favorable agreement between the two wind sources. The major differences are associated with the extreme values, where the Delaware Bay buoy generally indicates greater magnitudes. The overall trends, however, suggest the Delaware Bay buoy is a reasonable substitute for the Tuckerton wind sensor.

Figure 5.31 shows wind and current speed and direction for the 11 events in 1994. The plots represent vector averages over the entire event for both the wind and current. Each pair of polar grids represent wind and current data for each of the sediment transport events. The events are depicted in chronological order so that the first pair of polar grids show the 23-February, 1-March, 4-May and 23-August events. A similar chronological pattern applies to the second and third set of plots (see Figure 5.31 caption). For most events, the wind is out of the north directed along the coast or slightly offshore. Noticeable exceptions include flows toward the north on 21- and 28-November, and flows towards the south slightly onshore on 1-March and less so on

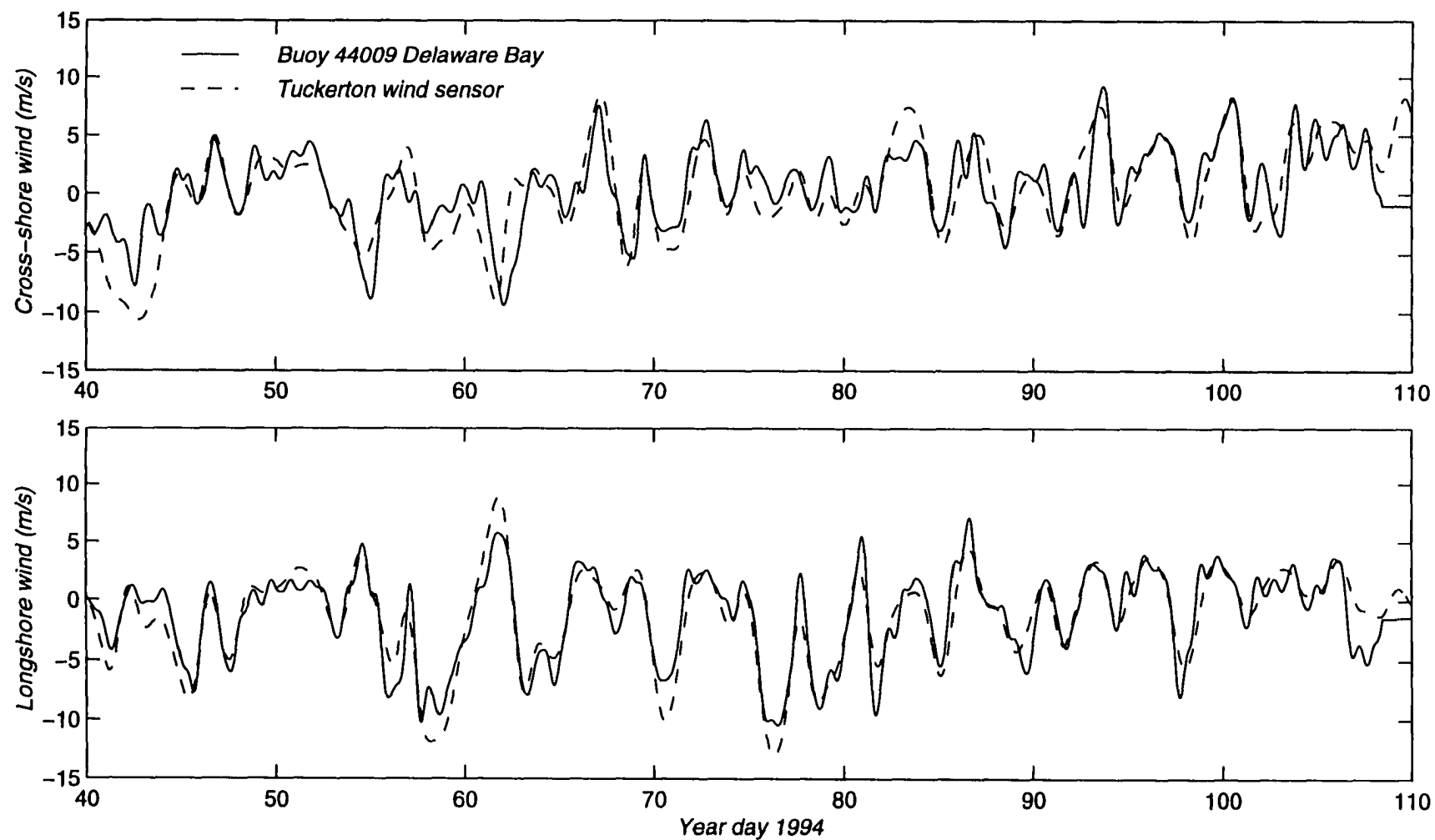


Figure 5.30 Comparison of filtered longshore and cross-shore wind speeds between Tuckerton wind sensor and Delaware Bay buoy. The Delaware Bay buoy captures the general trends of the Tuckerton wind sensor.

16-November. For all south or southeast wind directions, the mean current is either slightly onshore or directed almost perfectly alongshore down the coast. For the northward winds, the pattern shows onshore bottom currents on 21-November and nearly alongshore flow on 28-November. The general pattern seen in all these current diagrams mimics the results for the sediment flux study in that most of the cross-shore flow is directed onshore. It is surprising that this pattern appears to be independent of cross-shore wind direction which exhibits both on- and offshore movement during the various transport events. For 1995, the Tuckerton wind sensor only was operational through the end of January, so that all wind data from February on is from the Delaware Bay buoy (Figure 5.32). For the 4 events shown, the wind and current vectors strongly resemble patterns observed during the 1994 events. For both on- and offshore winds, the current is directed entirely onshore. Of special interest are current patterns for 6- and 15-August, which possess strong onshore components in the presence of strong alongshore winds.

The available empirical evidence suggests a working hypothesis where the observed flow patterns result from three-dimensional effects caused by the presence of variable topography. Off the New Jersey coast topographic variations on several scales alter the flow from idealized patterns generally attributed to coasts with straight and parallel contours. For example, large 50 *km* topographic variations which correspond to drowned river deltas are more or less uniformly distributed along the New Jersey coastline, and are believed to be responsible for the observed upwelling patterns observed during the summer (Glenn et al. 1996). Model results have shown that a meandering jet forms over these topographic highs that is shifted northward by the ambient alongshelf current as the event progresses. These meandering jets can cause net on/offshore flow

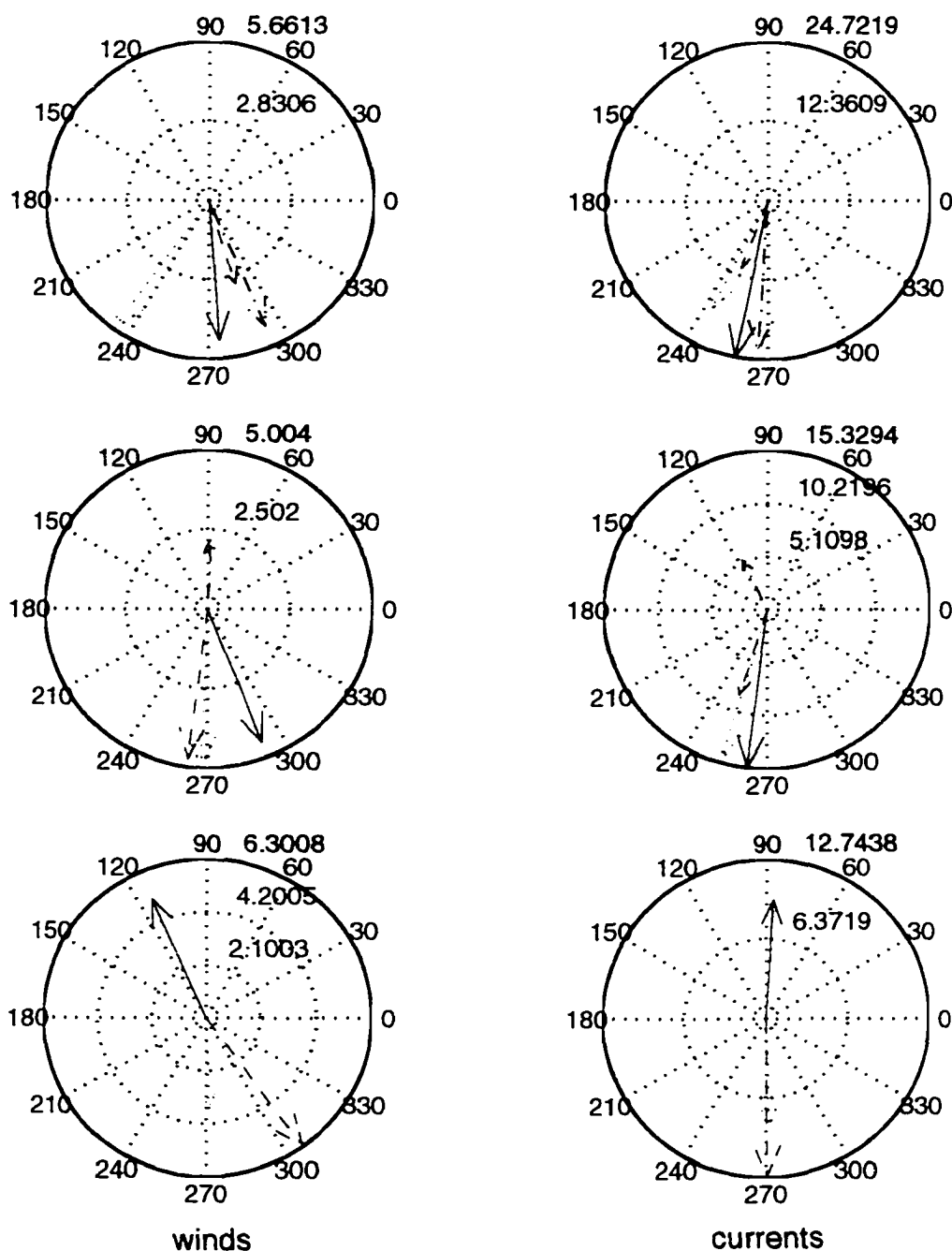


Figure 5.31 Polar grid depicting wind and current vectors for 1994 transport events. The first row, or pair, of grids represent the first 4 transport events. The first pair indicate (red) 23-Feb, (blue) 1-Mar, (green) 4-May and (black) 23-Aug. The second pair indicate (red) 4-Sep, (blue) 15-Oct, (green) 16-Nov and (black) 21-Nov. The final pair of polar grids indicate (red) 28-Nov, (blue) 14-Dec and (green) 23-Dec. All arrows indicate the direction the current or wind is moving. The compass is oriented into long- and cross-shore directions so that  $90^\circ$  is alongshore toward the north and  $180^\circ$  is cross-shore toward the coast.



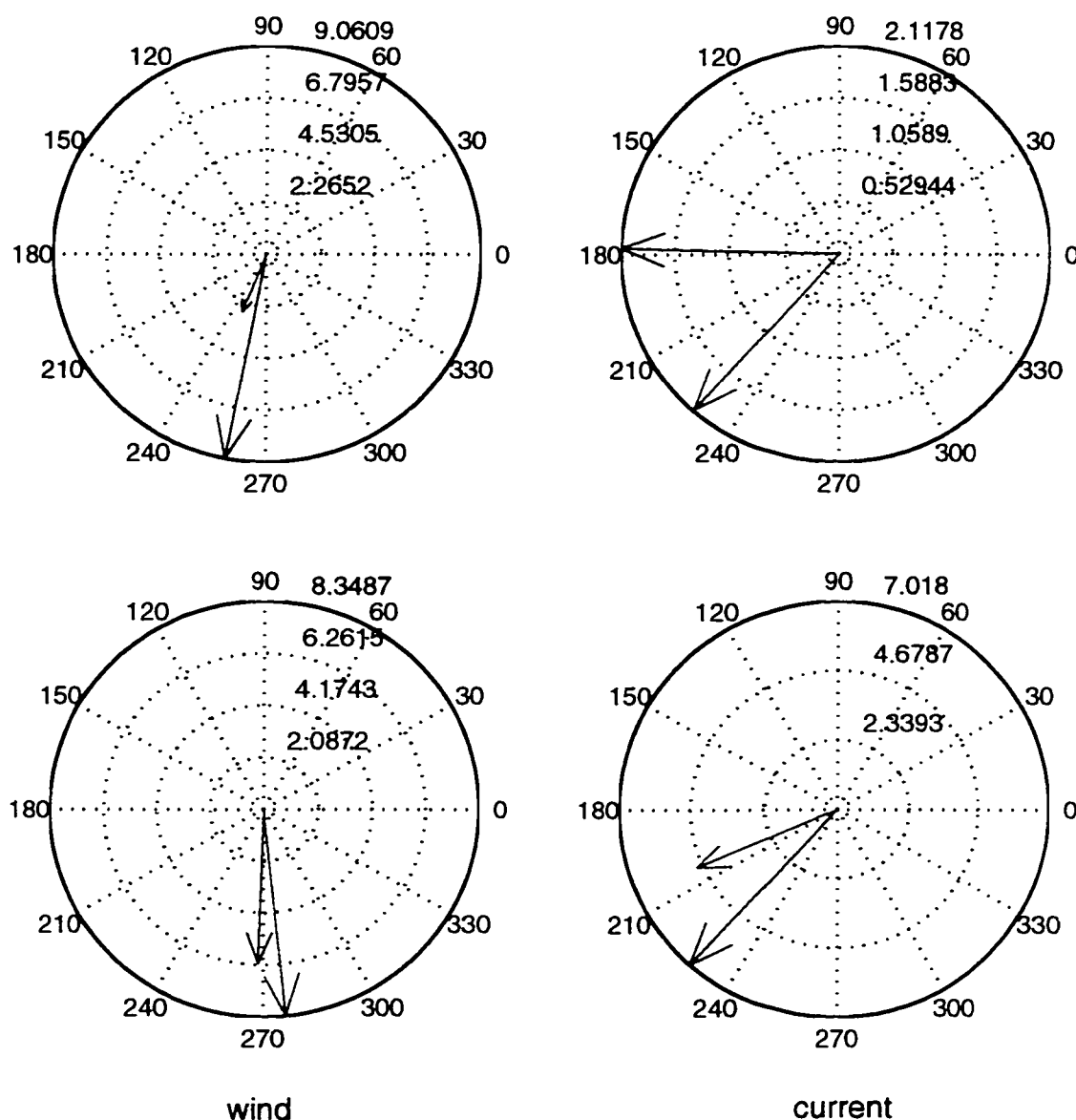


Figure 5.32 Polar grid depicting wind and current vectors for 4 of the 1995 transport events. The first row indicates (red) 15-Jan, (blue) 6-Aug. The second row indicates (red) 15-Aug and (blue) 28-Aug. For 1995, only 4 of the 8 events are shown because of a lack of sufficient local wind data.

as the jet steers away from the coast on the upstream side, and back toward the coast on the downstream side. It is possible that downwelling favorable winds will produce a reverse effect, that may explain the persistent onshore movement in the S4 current measurements at Node A. Alternatively, small scale topographic features are also prevalent in the LEO-15 study area. Node A is located at the landward extension of a shore oblique sand ridge oriented approximately  $20^\circ$  clockwise from shore-parallel, and extending 2 *km* to the northeast (Figure 4.1). The presence of this distinctive feature alters the local bathymetry and also may steer the flow in a manner consistent with the predicted onshore flux. Similar flow patterns in the vicinity of shore oblique sand ridges have been measured off the southern coast of Long Island, New York (Han and Mayer 1981). Han and Mayer's (1981) figure 3b indicates distinct near-bottom onshore flow in a trough separating two sand ridges during downwelling favorable conditions. Slight near-bottom onshore flow is also seen on the landward side of the sand ridges, which is somewhat more representative of the bathymetry where the S4s at LEO-15 are moored. Preferential cross-shore flow is also common around headlands in stratified estuaries (Chant and Wilson 1997) and in tidal channels (Lu 1997). In addition, models of near-bottom flow over these sand ridges during downwelling favorable conditions show a slight onshore component in the trough separating ridge peaks (Trowbridge 1995). Thus, independent flow measurements and model predictions provide additional evidence that directionally bias lateral flow can in part be influenced by local variations in topography.

Another possibility could be related to the dynamical balance associated with Ekman's elementary current system in shallow water. In this barotropic model, downwelling favorable winds drive surface currents onshore with an offshore return flow

at the bottom. Given the extreme shallow depths at Node A, however, it is more likely that the horizontal current vectors in the absence of sloping topography would line up in the direction of the wind excluding any turning with depth. A quick examination of the typical thickness of the Ekman layer,

$$D_E = \frac{u_{*c}}{f} = \frac{3 \text{ cm/s}}{9.25 \times 10^{-5} \text{ s}^{-1}} = 3.24 \times 10^4 \text{ cm} = 324 \text{ m}$$

where  $u_{*c}$  is chosen from Figure 5.28 and the latitude at LEO-15 is approximately  $39.5^\circ$ , shows that  $D_E$  is much greater than the typical water depth (10 m). Ekman layer dynamics, therefore, indicate this is well within the depth-limited range, and pure alongshore flow is expected in the absence of 3-dimensional bottom variations.

#### 5.4 Summary

The unique availability of long-term wave and current measurements obtained over a wide shallow continental shelf has furnished a glimpse into processes driving sediment motion at LEO-15. Model predictions based on these long-term data sets has further provided an insightful look into annual sediment flux patterns and how sediment transport events relate to these dominant forcing agents. Common to all sediment transport events was an unmistakable dominance by waves in initiating and maintaining sediment motion. This was clearly revealed in  $u_b$  and  $H_s$  time series as well as model predictions of bottom wave and current shear stresses. Because storm intensity and duration are crucial factors in describing sediment flux, correlation coefficients were constructed to see how event duration and maximum depth integrated flux relate to sediment transport events. Interestingly, the largest transport events were highly

correlated with maximum depth integrated flux, with event duration relatively weak by comparison. This suggests that over the 2-year time period, short energetic storms are more efficient transport mechanisms than longer weaker storms. In agreement with established patterns common to storm-dominated continental shelves, the most energetic transport events occurred during the winter storm season. Summer storms, however, contributed significantly to the overall transport budget, with several summer transport events possessing flux values comparable to moderate winter storm events.

Modes of longshore transport also followed established patterns for the near-shore region of a wide, gently sloping continental shelf. For nearly all transport events, sediment transport and currents were directed primarily alongshore in the direction of the prevailing wind. Regardless of wind direction, a bias toward onshore transport was common to most events. It was hypothesized that the first order description of cross-shore flow and sediment transport was controlled by variations in topography that lead to three-dimensional flow effects. The various scales of bathymetric variability along the inner New Jersey continental shelf, however, makes it difficult to isolate which features drive the observed flow.

## 6.0 SUMMARY AND CONCLUSIONS

A continental shelf bottom boundary layer model was presented for use in combined wave and current flows over a non-cohesive, movable sediment bed. Principal model features include: profile estimates of the mean current and suspended sediment concentration, calculation of bottom roughness for plane and rippled beds and for sheet flow, inclusion of a stability parameter to model the effects of suspended sediment-induced stratification, determination of skin friction to define the reference concentration, and calculation of the shear stress for the wave, current, and combined wave and current. To describe how these features are incorporated into the BBLM, a systematic and careful derivation of the governing equations, emphasizing limiting assumptions and specific mathematical procedures, was presented. Key features noted during the analysis include: (a) a 3-layer eddy viscosity, (b) inclusion of a stability parameter for the entire water column, (c) sensitivity tests on the importance of  $\epsilon$ ,  $\alpha$  and  $\phi_{cw}$  in determining the wave friction factor and bottom shear stress, (d) representation of the decay of turbulence kinetic energy in the region  $z_1 < z < z_2$  through a modification of the kinematic flux using a function with the same functional form as the wave stress, (e) modification of the vertical coordinate using a logarithmic coordinate transformation to enhance numerical stability and efficiency, and (f) representation of the stability parameter using a discrete set of Chebyshev polynomials. To gauge BBLM performance in the context of similar boundary layer models, comparisons of mean horizontal current and suspended sediment concentration profiles with the GG model were presented. The GG model was chosen since the two share similar turbulence closure schemes, especially with respect to modeling suspended sediment-induced stratification. Sensitivity of the current and

suspended sediment profile solutions to changes in the free parameters  $\alpha$ ,  $\beta$  and  $\gamma$ , and to changes in the number of sediment size classes, were also performed.

Field data collected at LEO-15 during the summer months of 1994 and 1995 were used to calibrate crucial model coefficients and to gauge the accuracy of the BBLM at predicting natural flows. The primary instruments relevant to the BBLM calibration included the BASS, SSS, ABS and ADCP, and information on the spatial and temporal sampling schemes of these instruments and general technical information on how they operate was discussed. Detailed suspended sediment profile measurements obtained from the ABS were used in conjunction with current data from the BASS and statistical models to obtain field estimates of  $\gamma_0$ ,  $\alpha$  and  $\gamma$ . Examination of the data identified 5 potentially useful concentration profiles for calculating these crucial parameters. It was determined that  $\gamma = 0.43$  for the sediment and flow conditions measured at LEO-15. Further statistical analysis revealed that 4 of the profiles were obtained during periods when the bottom roughness was very large. It was determined that under these conditions the eddy viscosity used in the model should be adjusted in a manner that made the model independent of  $\alpha$ . As a result,  $\alpha$  was determined using only 2 of the original 5 profiles. This gave an average value of  $\alpha = 1.55$ . The resuspension coefficient was also calculated from these two profiles, with a geometric average of  $\gamma_0 = 3.1 \times 10^{-3}$ . Existing reference concentration models were modified according to the theoretical and empirical findings of Wikramanayake and Madsen (1992) and integrated into the BBLM. Ripple geometry measurements obtained from the SSS and near-bed flow and wave parameters obtained from the BASS were used to distinguish

existing ripple geometry and bottom roughness models, and to identify the most accurate for modeling wave-formed ripples and flow roughness.

The fortuitous availability of near bed current measurements collected during 1994 and 1995 made it possible to obtain a preliminary glimpse into long-term sediment transport offshore New Jersey. A total of 19 sediment transport events were identified during the 2-year time period that varied in duration, peak transport and seasonal distribution. During all events, measurements and model predictions clearly established waves as the primary impetus for initiating sediment motion. Comparisons between event duration and maximum transport during individual events showed that most of the short, energetic storms produced the greatest transport. Although most energetic storms occurred during the winter months, several storms of moderate sediment transport potential occurred in the summer or early fall.

Modes of cross- and longshore transport were consistent with what is expected in a near-shore environment with the majority transport directed alongshore and in the direction of the wind. Cross-shore transport exhibited an unusual onshore bias during nearly all events. It was suspected that local variations in topography, which could lead to 3-dimensional flow effects, were responsible for the observed cross-shore transport.

The major results from this dissertation are summarized as follows:

- For the mean current and concentration in stratified flows, it is necessary to include the stability parameter at all levels in the boundary layer.
- The number and distribution of grain size classes significantly affects the stability parameter profile and resulting stratification correction for the eddy viscosity.
- Bottom roughness is directly proportional to  $\eta$  for all flows investigated.

- A modified version of the Sorenson et al. (1995) directionally dependent bottom roughness model adequately describes the flow roughness for both unidirectional flows and when the current is near  $90^\circ$  to the wave.
- The ripple geometry model of Wikramanayake and Madsen (1991) is physically unreasonable for equilibrium conditions and is adjusted for use in the field.
- For a rippled bed, existing theories and experimentally determined values for the parameter  $\gamma_0$  are consistent with the model and data comparisons presented here.
- For the field, the value  $\alpha = 1.55$  produces the best overall correlation between measured and modeled current.
- The estimate  $\gamma = 0.43$  is lower than the value 0.74 reported in the past, and may suggest that  $\gamma$  is grain size dependent.
- Long-term sediment transport on the continental shelf is linked to waves.
- The greatest transport occurs during short, energetic storms.

## **6.1 Direction of future research**

In light of the limited, yet favorable, model and data comparisons presented here, the BBLM is a promising tool for investigating the first order solution of flow and sediment transport on the continental shelf. It is equally evident, however, that more studies, both theoretical and experimental, are needed to further advance the present knowledge base on flow and sediment transport in the boundary layer. Specifically, this study has identified 3 major deficiencies in our present understanding of boundary layer physics.

- 1) Field measurements of the current within the wave boundary layer need to be collected and carefully analyzed. In the past, such measurements were not possible due



to a lack of suitable instrumentation for use in this unforgiving environment. Trowbridge and Agrawal (1995), however, using state-of-the-art current measuring systems have begun to make these crucial, high-resolution measurements. Although this preliminary study shows that such measurements are now possible, it hardly possesses the needed temporal and spatial coverage to establish a significant statistical description or provide a fundamental basis to test bottom boundary layer models. Additionally, measurements within the wave boundary layer are critical if the bottom roughness is to be accurately calculated.

2) Alternative statistical methods to identify appropriate bursts for model and data comparisons also must be explored. From the 1995 data set less than 11% of the available bursts indicated  $R^2$  values greater than 0.99, implying that a majority of the available profiles were considered inappropriate for calibration studies. The lack of a sufficient number of adequate bursts reveals an even greater problem for determining the still elusive parameter  $\gamma_0$ , which requires high-resolution, simultaneous current and suspended sediment concentration profile measurements very near the bed. To address some of these concerns, it is suggested that suitable non-linear statistical methods be employed which can identify a greater number of measured current and suspended sediment concentration profiles that conform to the model.

3) Grain size spectra and particle settling velocity need to be accurately determined. Because estimates of these variables are crucial for validating sediment transport models, the extreme sensitivity of the calculated suspended sediment concentration profile and the stability parameter to grain size distribution cannot be overemphasized. Along these same lines, measurements of the still settling velocity of grains in a marine environment

are severely lacking. This information is needed to create empirical expressions, like those developed from laboratory studies, on the relation between settling velocity and grain size for use in models.

4) A comparison of model results and suspended sediment concentration data during at least some portion of the 2-year time period that encompassed the long-term study needs to be conducted. This will provide some validation of the model beyond the qualitative verification provided by the OBS data. Such a comparison would also provide a systematic measure of the extended predictive capabilities of the present model when modified for use in other areas with conditions similar to those found at LEO-15.

From the ideas summarized in this final section, it is clear that a primary focus of future boundary layer research efforts are to acquire accurate, high-resolution spatial and temporal measurements of the flow, sediment and bed forms, and use results from these studies to improve existing boundary layer models and to further the theoretical understanding of boundary layer mechanics.

## APPENDIX: LIST OF PRINCIPAL SYMBOLS

$A_b$	- maximum near-bed excursion amplitude for the wave
$A_{brms}$	- root-mean-square maximum excursion amplitude for the wave
$a_1$	- measured $\kappa/u_{*c}$
$b_1$	- measured Rouse parameter
$c_b$	- bed sediment concentration
$c_f$	- volumetric concentration of fluid
$c_{fw}$	- friction factor used to define $k_t$
$c_n$	- concentration in volume of sediment per volume of fluid-sediment mixture
$C_n$	- Reynolds averaged concentration for each grain size class $n$
$C_{nm}$	- mean concentration for each grain size class $n$
$C_{np}$	- periodic concentration for each grain size class $n$
$c_n'$	- turbulent concentration fluctuation for each grain size class $n$
$c_p$	- wave phase speed
$C_R$	- ratio of $u_{*cw}^2/u_{*wm}^2$
$D(\omega, \theta)$	- directional spreading function
$D_E$	- scale height of the bottom Ekman layer
$d_n$	- sediment grain size for each grain size class $n$
$d_0$	- maximum semi-excursion amplitude for the wave
$f$	- Coriolis parameter
$f_w$	- wave friction factor
$g$	- acceleration due to gravity

$H$	- wave height
$H_s$	- significant wave height
$h$	- water depth
$i$	- imaginary unit
$K$	- neutral eddy viscosity for momentum
$K_s$	- neutral eddy diffusivity for sediment mass
$K_{strat}$	- stratified eddy viscosity for momentum
$K_{s\ strat}$	- stratified eddy diffusivity for sediment mass
$k$	- wave number
$k_b$	- bottom roughness length
$k_r$	- bottom roughness length due to ripples
$k_t$	- bottom roughness length due to a near-bed transport layer
$L$	- Monin-Obukov length
$L_w$	- wavelength
$l_{cw}$	- scale height of wave boundary layer in the presence of a mean current
$l_w$	- scale height of the wave boundary layer
$P$	- Reynolds averaged fluid pressure
$p$	- fluid pressure
$p'$	- turbulent pressure fluctuation
$p_c$	current pressure
$p_w$	- wave pressure
$Q$	- vertical dependent solution for the wave in the wave boundary layer

$q$	- sediment transport
$R_s$	- Rouse parameter
$R$	- correlation coefficient
$R_e$	- wave Reynolds number
$s_n$	- relative sediment density $\rho_{sn}/\rho$
$\overline{S}_n$	- normalized excess skin friction for steady flows
$\overline{S}_n'$	- normalized excess skin friction for combined flows
$S(\omega)$	- frequency spectrum
$S(\omega, \theta)$	- directional wave spectrum
$S_{u_b}$	- near-bottom orbital velocity spectrum
$S_s$	- non-dimensional sediment parameter
$T_n$	- Chebyshev polynomial of degree $n$
$T_w$	- wave period
$t$	- time
$U$	- Reynolds averaged horizontal component of velocity in the $x$ -direction
$U_0$	- solution for the magnitude of the current
$u$	- horizontal component of velocity in the $x$ -direction
$u'$	- turbulent velocity fluctuation in the $x$ -direction
$u_b$	- maximum near-bottom wave orbital velocity
$u_c$	- fluid velocity in the $x$ -direction associated with the current
$u_p$	- horizontal component of particle velocity in the $x$ -direction
$u_r$	- current speed at a known height $z_r$

$u_w$	- fluid velocity in the $x$ -direction associated with the wave
$u_0$	- characteristic velocity scale for the wave and current
$u_\infty$	- wave velocity at the outer edge of the wave boundary layer
$u_{*c}$	- shear velocity derived from time average shear stress
$u_{*cw}$	- shear velocity derived from maximum boundary shear stress
$u_{*f}$	- shear velocity derived from time average shear stress over one wave period in the absence of a current
$u_{*wm}$	- shear velocity derived from maximum instantaneous boundary shear stress for the wave
$V$	- Reynolds averaged horizontal component of velocity in the $y$ -direction
$v$	- horizontal component of velocity in the $y$ -direction
$v'$	- turbulent velocity fluctuation in the $y$ -direction
$v_c$	- fluid velocity in the $y$ -direction associated with the current
$v_p$	- horizontal component of particle velocity in the $y$ -direction
$v_w$	- fluid velocity in the $y$ -direction associated with the wave
$W$	- Reynolds averaged vertical component of velocity
$w$	- vertical component of velocity with $z$ positive upwards
$w'$	- vertical velocity turbulent fluctuation
$w_c$	- fluid velocity in the $z$ -direction associated with the current
$w_{f_n}$	- particle settling velocity for each grain size class $n$
$w_p$	- vertical component of particle velocity
$w_w$	- fluid velocity in the $z$ -direction associated with the wave

$w_0$	- characteristic velocity scale for the vertical velocity
$x$	- horizontal Cartesian coordinate
$y$	- horizontal Cartesian coordinate
$z$	- vertical Cartesian coordinate
$z_r$	- height of specified reference current velocity
$z_0$	- hydraulic roughness
$z_{0c}$	- apparent hydraulic roughness
$z_1$	- arbitrary cutoff point marking the lower boundary where the eddy viscosity is constant with height
$z_2$	- cutoff height for the eddy viscosity defined as $z_1 u_{*cw}/u_{*c}$
$z/L$	- stability parameter
$\alpha$	- free non-dimensional parameter regulating the height $z_1$
$\beta$	- non-dimensional parameter used to define the stratification correction in the eddy viscosity
$\beta_0$	- factor multiplying the ripple height in the Sorenson et al. (1995) bottom roughness equation
$\eta$	- ripple height
$\lambda$	- ripple length
$\Gamma$	- depth-integrated sediment transport
$\Gamma_f$	- instantaneous depth-integrated sediment transport
$\Gamma_{fm}$	- maximum instantaneous depth-integrated transport
$\Gamma_{ft}$	- total depth-integrated sediment transport
$\Gamma_{ft-x}$	- $x$ -component of $\Gamma_{ft}$

$\Gamma_{fr,y}$	- y-component of $\Gamma_{fr}$
$\Gamma_w$	- non-dimensional parameter used to define $\tau_{wm}$ in (3.76)
$\gamma$	- ratio of neutral eddy viscosity to neutral eddy diffusivity
$\gamma_0$	- resuspension coefficient
$\Delta_w$	- non-dimensional parameter used to define $\tau_{wm}$ in (3.86)
$\delta_l$	- height at which the eddy viscosity reaches a maximum defined in (3.25)
$\delta \tau_w$	- difference between the neutral and stratified wave shear stresses
$\delta_w$	- wave boundary layer height
$\epsilon$	- ratio of $u_{*cw}$ to $u_{*c}$
$\epsilon_{N_i}$	- point-wise error for stability parameter convergence tests
$\epsilon_N$	- maximum error for stability parameter convergence tests
$\theta$	- logarithmic coordinate defined as $\theta = \ln(z/z_0)$
$\theta_m$	- mobility number
$\kappa$	- von Karmans constant
$\nu$	- kinematic viscosity of water
$\xi$	- non-dimensional vertical coordinate = $z/l_{cw}$
$\xi_0$	- non-dimensional hydraulic roughness = $z_0/l_{cw}$
$\xi_1$	- non-dimensional height = $z_1/l_{cw}$
$\xi_2$	- non-dimensional height = $z_2/l_{cw}$
$\rho$	- fluid density
$\rho_{sn}$	- sediment density in each size class $n$
$\rho'$	- turbulent density fluctuation
$\overline{\rho}$	- Reynolds averaged density



$\rho_T$	- total density for the fluid/sediment mixture
$\rho'_T$	- turbulent density fluctuation for the fluid/sediment mixture
$\overline{\rho}_T$	- Reynolds averaged density for the fluid/sediment mixture
$\tau$	- shear stress
$\tau_b$	- bottom turbulent shear stress
$\tau_c$	- shear stress associated with the time average current
$\tau_{wm}$	- maximum instantaneous shear stress
$\tau_{cw}$	- maximum combined wave and current shear stress
$\tau'_b$	- bottom shear stress based on skin friction
$\tau'_n$	- steady shear stress based on skin friction
$\tau'_{bn}$	- instantaneous shear stress for combined flows based on skin friction
$\tau'_{cm}$	- critical shear stress based on skin friction
$\phi_{cw}$	- angle between the wave and current
$\phi_\tau$	- angle between the maximum wave stress and the combined stress
$X$	- non-dimensional wave and sediment parameter
$\psi'$	- Shields parameter
$\psi'_{cm}$	- critical Shields parameter based on skin friction for each size class $n$
$\omega$	- wave radian frequency
$\omega_r$	- equivalent wave radian frequency

## REFERENCES

- Abramowitz, M., Stegun, I. A., eds. 1964: *Handbook of Mathematical Functions*, Natl. Bur. Stand. Appl. Math. Ser. No. 55. Washington, DC: US Govt. Print. Off., 1046 pp.
- Allen, J. S., R. C. Beardsley, W. S. Brown, D. A. Cacchione, R. E. Davis, D. E. Drake, C. Friehe, W. D. Grant, A. Huyer, J. D. Irish, M. M. Janopaul, A. J. Williams and C. D. Winant, 1982: A preliminary description of the CODE-1 field program, *CODE Tech. Report No. 9*, WHOI Tech. Rep. No. 82-51, 47 pp.
- Atkinson, K. E., 1989: *An Introduction to Numerical Analysis*, John Wiley & Sons, Inc., 693 pp.
- Bagnold, R. A., 1946: Motions of waves in shallow water: Interaction of waves and sand bottoms. *Proc. Roy. Soc. Lond*, **187**, 1-15.
- Bedford, K. W., O. Wai, R. Van Evra, P. Velissariou, J. Lee and C. Libicki, 1990: The local near-bottom response of a dredged material placement site to wind and tide effects. Report prepared for the U.S. Army Corps of Engineers, Waterways Experiment Station, Coastal Engineering Research Center.
- Bendat, J. S. and A. G. Piersol, 1986: *Random Data: Analysis and Measurement Procedures*. John Wiley & Sons, 566 pp.
- Bowden, K. F. and R. A. White, 1966: Measurements of the orbital velocities of sea waves and their use in determining the directional spectrum. *Geophys. J. R. Astr. Soc.*, **12**, 33-54.
- Businger, J. A., J. C. Wyngaard, Y. Izumi and E. F. Bradley, 1971: Flux-profile relationships in the atmospheric surface layer. *J. Atmos. Sci.*, **28**, 181-189.
- Cacchione, D. A., W. D. Grant, D. E. Drake and S. M. Glenn 1987: Storm-dominated bottom boundary layer dynamics on the northern California continental shelf: measurements and predictions. *J. Geophys. Res.*, **92**, 1817-1827.
- Carstens, M. R., F. M. Neilson, and H. D. Altinbilek, 1969: Bed forms generated in the laboratory under an oscillatory flow: Analytical and experimental study. *Tech. Memo*, **28**, 39 pp., U.S. Corps of Engineers, Coastal Engineering Research Center, Washington, D. C.
- Chant, R. J. and R. E. Wilson, 1997: Secondary circulation in a highly stratified estuary. *J. Geophys. Res.*, **102**, 23,207-23,215.

- Christoffersen, J. B. and I. G. Jonsson, 1985: Bed friction and dissipation in a combined current and wave motion. *Ocean Engng.*, **12**, 387-423.
- Craghan, M., 1995: Topographic changes and sediment characteristics at a shoreface sand ridge- Beach Haven Ridge, New Jersey. M. Sc. thesis, Rutgers University, New Jersey, 123 pp.
- Davies A. G. and C. Villaret, 1997: Oscillatory flow over rippled beds: Boundary layer structure and wave-induced Eulerian drift. *Gravity Waves in Water of Finite Depth*, M. Rahman, Ed., Vol. 10, Computational Mechanics, 215-254.
- Dean, R. G. and R. A. Dalrymple, 1991: *Water Wave Mechanics for Engineers and Scientists*. World Scientific, 353 pp.
- Dietrich, W. D., 1982: Flow, boundary shear stress, and sediment transport in a river meander. Ph.D. thesis, Univ. of Wash., Seattle, 261 pp.
- Dingler, J. R., 1974: Wave-formed ripples in nearshore sands. Ph.D. thesis, University of Calif., San Diego, 136 pp.
- Drake, D. E. and D. A. Cacchione, 1985: Seasonal variation in sediment transport on the Russian River shelf, California. *Cont. Shelf Res.*, **4**, 495-514.
- and -----, 1986: Field observations of bed shear stress and sediment resuspension on continental shelves, Alaska and California. *Cont. Shelf Res.*, **6**, 415-429.
- and -----, 1989: Estimates of the suspended sediment reference concentrations ( $C_d$ ) and resuspension coefficient ( $\gamma_0$ ) from near-bottom observations on the California shelf. *Cont. Shelf Res.*, **9**, 51-64.
- , D. A. Cacchione and W. D. Grant, 1992: Shear stress and bed roughness estimates for combined wave and current flows over a rippled bed. *J. Geophys. Res.*, **97**, 2319-2326.
- Dyer, K. R., 1980: Velocity profiles over a rippled bed and the threshold of movement of sand. *Estuarine Coastal Mar. Sci.*, **10**, 181-199.
- Gibbs, R. J., M. D. Mathews and D. A. Link, 1971: The relationship between sphere size and settling velocity. *J. Sed. Petrology*, **41**, 7-18.
- Glenn, S. M., 1983: A continental shelf bottom boundary layer model: The effects of waves, currents, and a movable bed. Sc.D. thesis, Mass. Inst. of Technol., Cambridge, 237 pp.

- and W. D. Grant, 1987: A suspended sediment correction for combined wave and current flows. *J. Geophys. Res.*, **92**, 8244-8246.
- , M. F. Crowley, D. B. Haidvogel and Y. T. Song, 1996: Underwater observatory captures coastal upwelling events off New Jersey. *Eos, Trans. Amer. Geophys. Union*, **77**, 233, 236.
- Grant, W. D., 1977: Bottom friction under waves in the presence of a weak current: Its relationship to coastal sediment transport. ScD thesis., Mass. Inst. of Technol., Cambridge, 275 pp.
- and O. S. Madsen, 1979: Combined wave and current interaction with a rough bottom, *J. Geophys. Res.*, **84**, 1797-1808.
- and -----, 1982: Movable bed roughness in unsteady oscillatory flow. *J. Geophys. Res.*, **87**, 469-481.
- and -----, 1986: The continental-shelf bottom boundary layer. *Ann. Rev. Fluid Mech.*, **18**, 265-305.
- , L. Boyer, L. P. Sanford, 1982: The effects of bioturbation on the initiation of motion of intertidal sands. *J. Mar. Res.*, **40**, 659-677.
- , A. J. Williams, III, and S. M. Glenn, 1984: Bottom stress estimates and their prediction on the Northern California continental shelf during CODE-1: The importance of wave-current interaction. *J. Phys. Oceanogr.* **14**, 506-527.
- Gross, T. F. and A. R. M. Nowell, 1983: Mean flow and turbulence scaling in a tidal boundary layer. *Cont. Shelf Res.*, **2**, 109-126.
- Guy, H. P., D. B. Simons and E. V. Richardson, 1966: Summary of alluvial channel data from flume experiments, 1956-1961. *U. S. Geol. Surv. Prof. Pap.*, 462-I, 96 pp.
- Han, G. C. and D. A. Mayer, 1981: Current structure on the Long Island inner shelf. *J. Geophys. Res.*, **86**, 4205-4214.
- Hanes, D. M., 1991: Suspension of sand due to wave groups. *J. Geophys. Res.*, **96**, 8911-8915.
- Hay, A. E., and D. J. Wilson, 1994: Rotary side scan images of near-shore bedform evolution during a storm. *Marine Geology*, **119**, 57-65.

- Hill, P. S., A. R. M. Nowell and P. A. Jumars, 1988: Flume evaluation of the relationship between suspended sediment concentration and excess boundary shear stress. *J. Geophys. Res.*, **93**, 12,499-12,509.
- Hinze, J. O., 1975: *Turbulence*. McGraw-Hill, 790 pp.
- Högström, U., 1988: Non-dimensional wind and temperature profiles in the atmospheric surface layer: A re-evaluation. *Boundary-Layer Meteorol.*, **42**, 55-78.
- Inman, D. L., 1957: Wave generated ripples in nearshore sands, *Tech. Memo*, 100, 66 pp., U.S. Army Corps of Engineers, Beach Erosion Board, Washington, D. C.
- Jensen, B. L., B. M. Sumer and J. Fredsoe, 1989: Turbulent oscillatory boundary layers at high Reynolds numbers, *J. Fluid Mech.*, **106**, 265-298.
- Jonsson, I. G., and N. A. Carlsen, 1976: Experimental and theoretical investigations in an oscillatory turbulent boundary layer. *J. Hydraul. Res.*, **14**, 45-60.
- Lee, T. H. and D. M. Hanes, 1996: Comparison of field observations of the vertical distribution of suspended sand and its prediction by models. *J. Geophys. Res.*, **101**, 3561-3572.
- Kennedy, J. F. and M. Falcon, 1965: Wave generated sediment ripples. *Rep. 86*, Mass. Inst. of Technol. Hydrodyn. Lab., Cambridge.
- Longuet-Higgins, M. S., D. E. Cartwright and N. D. Smith, 1963: *Ocean Wave Spectra*, Prentice-Hall, 111-132 pp.
- Lu, Y. 1997: Flow and turbulence in a tidal channel. Ph. D. thesis, Univ. of Victoria, Victoria.
- Lumley, J. L., 1976: Two-phase and non-Newtonian flows. *Topics in Applied Physics*, P. Bradshaw, Ed., Springer, **12**, 289-324.
- Lundgren, H., 1972: Turbulent currents in the presence of waves. *Proc. Coastal Eng. Conf.*, *13th*, 623-634.
- Lynch, J. F., J. D. Irish, C. R. Sherwood and Y. C. Agrawal, 1994: Determining suspended sediment particle size information from acoustical and optional backscatter measurements. *Cont. Shelf Res.*, **14**, 1139-1165.
- , T. F. Gross, P. L. Wiberg, A. E. Newhall, P. A. Traykovski and J. D. Warren, 1997: Acoustic measurements of the spatial and temporal structure of the near-bottom boundary layer in the 1990-1991 STRESS experiment. *Cont. Shelf Res.*, **17**, 1271-1295.

- Madsen, O. S., 1991: Mechanics of cohesionless sediment transport in coastal waters. *Coastal Sediments '91 Proc.*, Seattle, WA., ASCE WR Div., 15-27.
- and W. D. Grant, 1977: Quantitative description of sediment transport by waves. *Proc. Coastal Eng. Conf.*, 15th, 2, 1093-1112.
- and P. N. Wikramanayake, 1991: Simple models for turbulent wave-current bottom boundary layer flow. Contract report DRP-91-1. Final Report for the Dredging Research Program. U.S. Army Corps of Engineers, Coastal Engineering Research Center.
- , Y. K. Poon and H. C. Graber, 1988: Spectral wave attenuation by bottom friction: Theory. *Proc. Coastal Eng. Conf.*, 21st, 492-504.
- , L. D. Wright, J. D. Boon and T. A. Chisholm, 1993: Wind stress, bed roughness and sediment suspension on the inner shelf during an extreme storm event. *Cont. Shelf Res.*, 13, 1303-1324.
- Mathisen, P. P. and O. S. Madsen, 1996a: Waves and currents over a fixed rippled bed, 1, Bottom roughness experienced by waves in the presence and absence of currents. *J. Geophys. Res.*, 101, 16,533-16,542.
- and -----, 1996b: Waves and currents over a fixed rippled bed, 2, Bottom and apparent roughness experienced by currents in the presence of waves. *J. Geophys. Res.*, 101, 16,543-16,550.
- McClennen, C. E., 1973: Sands on continental shelf off New Jersey move in response to waves and currents. *Maritimes*, 14-16.
- McLean, S. R., 1992: On the calculation of suspended load for noncohesive sediments. *J. Geophys. Res.*, 97, 5759-5770.
- Mei, C. C., 1989: *The Applied Dynamics of Ocean Surface Waves*. World Scientific, 740 pp.
- Mogridge, G. R., and J. W. Kamphuis, 1972: Experiments on bedform generation by wave action. *Coastal Eng.*, Proc. 13th Conf., Vancouver, B. C., 1123-1142, Am. Soc. Civil Eng., New York.
- National Data Buoy Center, Climate Summary Tables, Feb. 1995, <ftp://seaboard.ndbc.noaa.gov/data/climatic/44009.txt.gz> (28 Jan. 1998)
- Neter, J., W. Wasserman and M. H. Kutner, 1989: *Applied Linear Regression Models*. Irwin, 667 pp.

- Niedoroda, A. W., D. J. P. Swift, T. S. Hopkins and C. M. Ma, 1984: Shoreface morphodynamics of wave-dominated coasts. *Mar. Geol.*, **60**, 331-354.
- Nielsen, P., 1981: Dynamics and geometry of wave generated ripples. *J. Geophys. Res.*, **86**, 6467-6472.
- , 1984: Field measurements of time-averaged suspended sediment concentrations under waves. *Coastal Eng.*, **8**, 51-72.
- , 1992: *Coastal Bottom Boundary Layers and Sediment Transport*. World Scientific, 324 pp.
- Nittrouer, C. A. and J. H. Kravitz, 1996: STRATAFORM: a program to study the creation and interpretation of sedimentary strata on continental margins. *Oceanography*, **9**, 146-152.
- Nowell, A. R. M., P. A. Jumars and J. E. Eckman, 1981: Effects of biological activity on the entrainment of marine sediments. *Mar. Geol.*, **42**, 133-153.
- Owen, P. R., 1964: Saltation of uniform grains in air. *J. Fluid Mech.*, **20**, 225-242.
- Press, W. H., S. A. Teukolsky, W. T. Vetterling and B. P. Flannery, 1986: *Numerical Recipes*, Cambridge University Press, 933 pp.
- Rankin, K. L., 1997: Shear plate measurements of bottom shear stress for a moveable bed. Ph.D. thesis, Stevens Inst. of Technology, Hoboken.
- Rhodes, D. C. and L. F. Boyer, 1982: The effects of marine benthos on physical properties of sediments. *Animal-Sediment Relations*, P. L. McCall, M. J. S. Teresz, Eds., Plenum, 3-57.
- Rouse, H. 1937: Modern conceptions of the mechanics of turbulence. *Trans. American Soc. Civil Eng.*, **102**
- Sherwood, C. R., 1995: Measurements and modeling of suspended-sediment transport on the Northern California continental shelf. Ph.D. thesis, Univ. of Washington, Seattle, 175 pp.
- , B. Butman, D. A. Cacchione, D. E. Drake, T. F. Gross, R. W. Sternberg, P. L. Wiberg and A. J. Williams III, 1994: Sediment-transport events on the northern California continental shelf during the 1990-1991 STRESS experiment. *Cont. Shelf Res.*, **14**, 1063-1099.
- Simons, R. R., A. J. Grass and A. Kyriacou 1988: The influence of currents on wave height attenuation. *Proc. 21st Int. Conf. Coastal Eng.*, Malaga.

- Sleath, J. F. A., 1987: Turbulent oscillatory flow over rough beds, *J. Fluid Mech.*, **182**, 369-409.
- , 1991: Velocities and shear stresses in wave-current flows. *J. Geophys. Res.*, **96**, 15,237-15,244.
- Smith, J. D., 1977: Modeling of sediment transport on continental shelves. *The Sea*, E. D. Goldberg, I. N. McCave, J. J. O'Brien, J. H. Steele, Eds., Vol. 6, Interscience, 538-577.
- and S. R. McLean, 1977: Spatially averaged flow over a wavy surface. *J. Geophys. Res.*, **82**, 1735-1746.
- Sorenson, K. S., O. S. Madsen, and L. D. Wright, 1995: Evidence of directional-dependence of moveable bottom roughness in inner shelf waters. *EOS Supplement*, November 1995, p. F281.
- Stull, R. B., 1988: *An Introduction to Boundary Layer Meteorology*. Kluwer Academic, 666 pp.
- Tennekes, H. and J. L. Lumley, 1972: *A First Course in Turbulence*. The MIT Press, 300 pp.
- Thorne, P. D., C. E. Vincent, P. J. Hardcastle, S. Rehman and N. Pearson, 1991: Measuring suspended sediment concentrations using acoustic backscatter devices. *Mar. Geol.*, **98**, 7-16.
- Tolman, H. L., 1994: Wind waves and moveable-bed bottom friction. *J. Phys. Oceanogr.*, **24**, 994-1009.
- Traykovski, P., J. D. Irish, A. Hay, and J. F. Lynch, 1998: Geometry, migration, and evolution of wave orbital ripples at LEO-15. *J. Geophys. Res.*, submitted.
- Trowbridge, J., 1995: A mechanism for the formation and maintenance of shore-oblique sand ridges on storm-dominated shelves. *J. Geophys. Res.*, **100**, 16,071-16,086.
- and Y. C. Agrawal, 1995: Glimpses of a wave boundary layer. *J. Geophys. Res.*, **100**, 20,729-20,743.
- and O. S. Madsen, 1984a: Turbulent wave boundary layers 1. Model formulation and first-order solution. *J. Geophys. Res.* **89**, 7989-7997.
- and -----, 1984b: Turbulent wave boundary layers 2. Second order theory and mass transport. *J. Geophys. Res.* **89**, 7999-8007.



- Turner, J. S., 1979: *Buoyancy effects in fluids*. Cambridge Univ. Press, 368 pp.
- Villaret C. and J. H. Trowbridge, 1991: Effects of stratification by suspended sediments on turbulent shear flows. *J. Geophys. Res.*, **96**, 10,659-10,680.
- Vincent, C. E. and M. O. Green, 1990: Field measurements of the suspended sand concentration profiles and fluxes and of the resuspension coefficient  $\gamma_0$  over a rippled bed. *J. Geophys. Res.*, **95**, 11,590-11,601.
- von Alt, C. J., and J. F. Grassle, 1992: LEO-15, An unmanned long term environmental observatory. *Proc. Oceans* 92, **2**, 849-854.
- , M. P. DeLuca, S. M. Glenn, J. F. Grassle and D. B. Haidvogel, 1997: LEO-15: Monitoring & managing coastal resources. *Sea Technology*, **38**, 10-16.
- Wiberg, P., and C. K. Harris, 1994: Ripple geometry in wave-dominated environments. *J. Geophys. Res.*, **99**, 775-789.
- and J. M. Nelson, 1992: Unidirectional flow over asymmetric and symmetric ripples. *J. Geophys. Res.*, **97**, 12,745-12,761.
- and D. M. Rubin, 1989: Bed roughness produced by saltating sediment. *J. Geophys. Res.*, **94**, 5011-5016.
- and J. D. Smith, 1983: A comparison of field data and theoretical models for wave-current interactions at the bed on the continental shelf, *Cont. Shelf Res.*, **2**, 126-136.
- and -----, 1985: A theoretical model for saltating grains in water. *J. Geophys. Res.*, **90**, 7341-7354.
- , D. E. Drake and D. A. Cacchione, 1994: Sediment resuspension and bed armoring during high bottom stress events on the northern California inner continental shelf: measurements and predictions. *Cont. Shelf Res.*, **14**, 1191-1219.
- , D. A. Cacchione, R. W. Sternberg and L. Donelson Wright, 1996: Linking sediment transport and stratigraphy on the continental shelf. *Oceanogr.*, **9**, 153-157.
- Wieringa, J., 1980: A revaluation of the Kansas mast influence on measurements of stress and cup anemometer overspeeding. *Boundary-Layer Meteorol.*, **18**, 411-430.
- Wikramanayake, P. N., and O. S. Madsen, 1991: Calculation of movable bed friction factors. Technical report DACW-39-88-K-0047. Technical progress report for the Dredging Research Program. U.S. Army Corps of Engineers, Coastal Engineering Research Center, Vicksburg, MS, 105 pp.

- and -----, 1992: Calculation of suspended sediment transport by combined wave-current flows. Contract report DRP-92-. Final report for the Dredging Research Program. U.S. Army Corps of Engineers, Coastal Waterways Research Center, Vicksburg, MS, 148 pp.
- Williams, A. J., J. S. Tochko, R. L. Koehler, W. D. Grant, T. F. Gross, and C. V. R. Dunn, 1987: Measurements of turbulence in the ocean bottom boundary layer with and acoustic current meter array. *J. Atmos. Oceanic Tech.*, **4**, 312-327.
- Wilson, K. C., 1989: Friction of wave-induced sheet flow. *Coast. Engng.*, **12**, 371-379.
- Wright, L. D., J. D. Boon, S. C. Kim and J. H. List, 1991: Modes of Cross-shore sediment transport on the shoreface of the Middle Atlantic Bight. *Mar. Geolog.*, **96**, 19-51.
- WXP, Purdue University Hurricane and Tropical Data, Apr. 1998, <http://wxp.atms.purdue.edu/hurricane/index.html>

## Curriculum Vita

### RICHARD STYLES

#### *Education:*

1991 B.S. in Physics, University of Tennessee, Knoxville, Tennessee.

1993 M.S. in Physical Oceanography, Florida Institute of Technology, Melbourne, Florida.

#### *Employment:*

1994-Pres Graduate Research Assistant, Rutgers University, New Brunswick, NJ.

1991-1993 Graduate Research Assistant, Florida Institute of Technology, Melbourne, FL.

1991 Undergraduate Research Assistant, University of Tennessee, Knoxville, TN.

#### *Professional societies:*

Member, American Geophysical Union since 1994.

#### *Reviewed Publications:*

**Styles, R.**, 1996: Long-term variability of sea surface temperature and atmospheric pressure along the equatorial Pacific. *Bull. N. J. Acad. Sci.*, **41(1)**, 25-29.

#### *Published abstracts:*

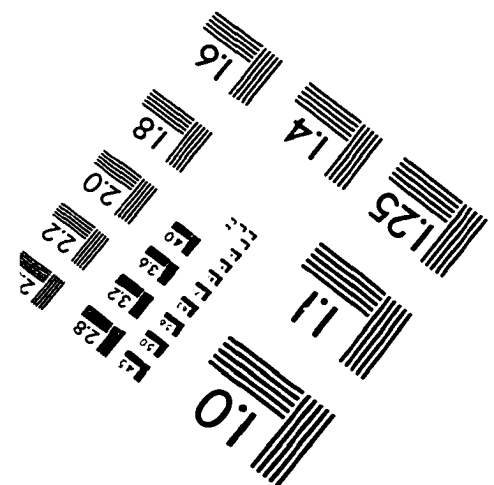
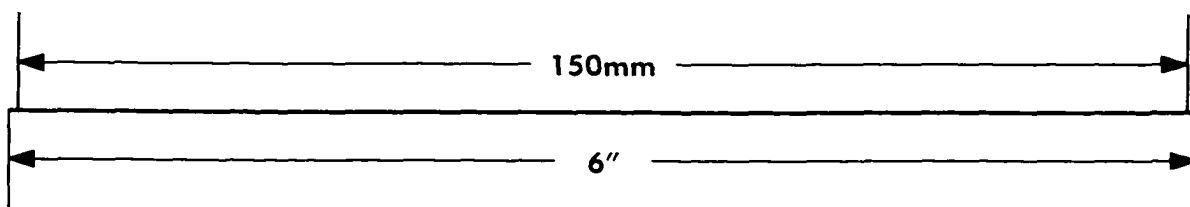
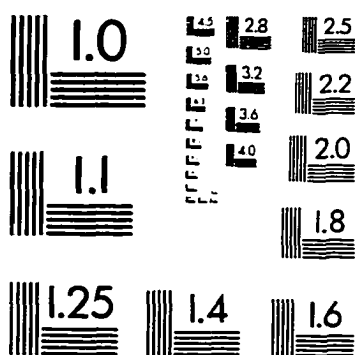
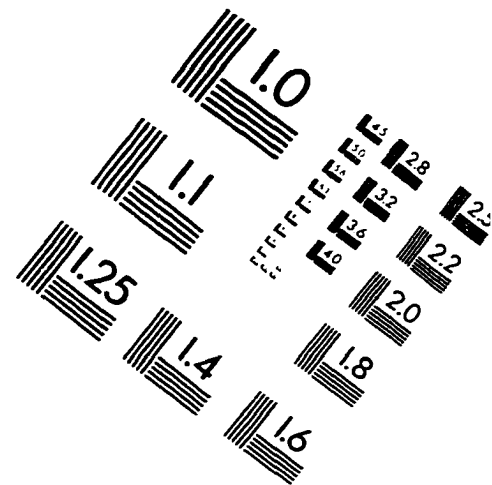
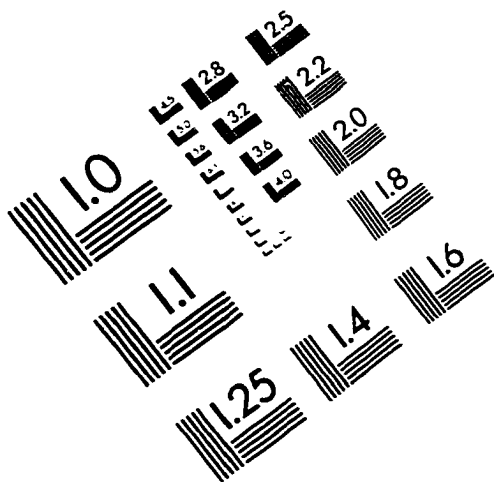
**Styles, R.**, S.M. Glenn, E. Creed and L. Henderson, 1996: Monitoring bottom boundary layer processes with implications for sediment transport modeling. Published as a supplement to *EOS*, Transactions, AGU, **77**, Number 17, S148.

**Styles, R.** and S.M. Glenn, 1996: Observations and modeling of sediment transport offshore New Jersey. Published as a supplement to *EOS*, Transactions, AGU, **77**, Number 46, F371.

#### *Conference presentations:*

**Styles, R.**, S.M. Glenn, 1995: Observations of a late summer mixing storm: Implications for sediment transport. Middle Atlantic Bight Physical Oceanography and Meteorology (MABPOM) Workshop.

# IMAGE EVALUATION TEST TARGET (QA-3)



APPLIED IMAGE, Inc  
1653 East Main Street  
Rochester, NY 14609 USA  
Phone: 716/482-0300  
Fax: 716/288-5989

© 1993, Applied Image, Inc., All Rights Reserved

